Transport of electrons in two-dimensional lateral surface superlattices

Md. Sujaul Haque Chowdhury

**A thesis submitted for the degree of
Doctor of Philosophy to
Physical Sciences Graduate School of
The University of Glasgow,
United Kingdom.
01 May 2001**

To
My wife Kanak for her sacrifice.

Acknowledgements

First of all, I acknowledge my supervisors Dr. Andrew R. Long and Professor John N. Chapman, FRSE. As to Andrew, it is his interest in the project that benefited me most. His dedication and vigilance kept the measurement systems working for all the time. He has been easily accessible informally that helped the discussion of every detail of every idea whenever necessary. I am grateful to Andrew for offering me the project which I enjoyed thoroughly. John Chapman has been sympathetic to my predicaments. His recommendations were invaluable in different occasions. He also bothered to keep himself informed of my progress from Andrew and from myself on some occasions. I am grateful that he admitted me in his Solid State Physics Group as I applied for.

Then comes Professor John H. Davies who bothered to put in his theoretical expertise alongside Andrew's that together with my experiments significantly clarified the semi-classical aspect of the Physics for transport of electrons in two-dimensional lateral surface superlattices.

I note my special gratitude to Professor Colin R. Stanley and Dr. Giovanni Pennelli who supplied the high quality semiconductor heterostructures essential for the project.

On the experimental side, I acknowledge that Dr. C. J. Emeleus had introduced me to the fabrication of Hall bars and the measurement systems in my early days working here and B. Milton had introduced me to scanning electron microscopy. I had to gather ideas from Dr. Elef Skuras to learn to fabricate high quality superlattices. He has been an excellent guy. It was enjoyable to have him as a co-worker. Dr. K. Lister supported the milli-Kelvin experiments that were necessary for part of the project.

Special thanks to David E. Grant for taking the trouble to do the simulations that provided vital clues which together with my experimental results ultimately enabled John Davies and Andrew Long to track down the trajectories of guiding centre in two-dimensional superlattices and clarify the semi-classical aspect of transport.

Stephen G. Hamill introduced me to the use of the surface profiler that was necessary to calibrate the etchant used in the project.

Jamie Scott and Agne Kundrotaite helped in obtaining the AFM images of superlattices.

Special gratitude to staff and technicians of the Ultra-Small Structure Laboratory (USSL) of the Nanoelectronics Research Centre of the University of Glasgow for taking the trouble to run my jobs in the electron beam-writer. Special

thanks to Douglas Macintyre, Stephen Thoms, David Gourlay and others of the USSL for their sincere efforts in keeping the fabrication facilities working all the time. Thanks to Derek McQuade for technical assistance on some occasions.

Thanks to Dr. Patrick Nicholson and Dr. Sam McFadzean for taking the trouble in providing the group with excellent computing facilities.

A stimulating discussion with Professor Peter C. Main regarding the amplitude modulation of Weiss oscillations and some correspondence with Professor Rolf R. Gerhardts supportive of our theoretical efforts are gratefully acknowledged. I am grateful to Professor F. M. Peeters for sending a copy of a conference paper of him that helped in understanding the Weiss oscillations of symmetric two-dimensional superlattices.

I am grateful to the University of Glasgow for providing me a Postgraduate Scholarship. I am also grateful to the British Government for providing me an ORS Award and for renewing it twice. I note my gratitude to Professor Robert P. Ferrier for recommending my application for an ORS Award. The Engineering and Physical Sciences Research Council (EPSRC) supported our measurement systems.

I would note with gratitude the hospitality of Dr. Mahfuzur Rahman and his wife Latika Rahman.

I note with gratitude the research training I had got in the undergraduate level from Professor Dr. M. Habibul Ahsan, Professor Dr. M. A. Zaman and Professor Dr. M. Salimullah which helped me in different aspects of this project. Some crucial advice of Prof. Dr. M. Khalilur Rahman (in my undergraduate level) regarding research kept me collected during some of the eventful days of the project.

Finally, I thank my parents, father and mother-in-laws, brother-in-law Dr. Arif Murshed Khan and sister-in-law Rasheda Rawnak Khan for their encouragement. I note the sacrifice of my wife Zobada Kanak Khan (Kanak) who bore the brunt of loneliness as I stayed in the laboratories most of the time.

Declaration of originality

I, Md. Sujaul Haque Chowdhury, hereby do solemnly declare that this thesis has been composed fully by myself and all the results reported are original (except where explicitly stated otherwise and appropriately referenced) and are the results of my research in the University of Glasgow and do not form part of any previous work for any other degree.

Abstract

The transport of electrons in two-dimensional periodic potentials and a perpendicular magnetic field has been studied experimentally at low temperature to gather understanding of the mechanisms governing conduction of electrons in such a situation. Hall bars were fabricated from GaAs-AlGaAs heterostructures containing a high mobility two-dimensional electron gas (2DEG) 53 nm below the unpatterned surface. Some of the heterostructures contained a 6 nm thick strained layer of $In_{0.2}Ga_{0.8}As$ 10 nm below the surface. High resolution electron beam lithography was used to obtain patterns of holes 50 nm or 40 nm in diameter in a resist layer coating Hall bars. The holes were arranged on square lattices in some cases and rectangular lattices in others. Superlattices were realised by shallow etching of material through the holes for typically 100 seconds by an extremely slow wet etching using a suitable mixture of citric acid and hydrogen peroxide. The resist pattern was removed after etching and about 200 nm thick continuous Ti-Au Schottky gate was obtained by evaporation covering the etched areas on the Hall bars. Square superlattices of both 80 nm and 100 nm periods and rectangular superlattices of 100 nm by 130 nm and 100 nm by 170 nm periods were fabricated. The Hall bars studied were oriented along four directions: [010], [011], [001] and [01$\bar{1}$] on (100) GaAs substrate. The principal axes of the patterns were always aligned along and across each Hall bar. Devices fabricated using the heterostructures containing the strained layer are called *stressed* devices while those fabricated using the heterostructures lacking the strained layer are called *unstressed* devices.

Some of the devices were kept without a gate. Magnetoresistances of both ungated and gated devices were studied at 4 K, and at 30 mK in some cases. Because of the fluctuation in the laboratory conditions, in particular the dose of electron beam-writer used in the lithography, in most cases the main features of the data were confirmed from the ungated devices. This is because the quality of the etched patterns of the ungated devices could be ascertained by microscopy. Moreover, just before obtaining gates on each set of devices, a group of devices was removed by cleaving and kept without a gate. The quality of the etched patterns of these ungated devices was also ascertained by extensive microscopy. Both scanning electron microscopy (SEM) and atomic force microscopy (AFM) were used in investigating the quality of the etched patterns. SEM revealed if the etched patterns were uniform and correct over the entire extent of the pattern on the Hall bars. AFM revealed if the holes were etched through to uniform depths and the depth of the etched holes was close to 20 nm in all

cases. This confirms that in the case of stressed devices, the holes completely passed through the strained layer of InGaAs and hence brought about stress modulation at the 2DEG.

There are two sources of modulation at the 2DEG. Periodic removal of material from the heterostructure surface brings about a periodic potential at the 2DEG which is isotropic and is the only source of modulation in unstressed devices. In stressed devices, besides the surface effect, there is periodic stress modulation at the 2DEG, which is anisotropic. On (100) GaAs surface, stress modulations along [011] and [01$\bar{1}$] are equal but opposite in sign and are zero along [010] and [001]. In stressed devices, the combination of the two sources of modulation turns the potential landscape of even square superlattices asymmetric. Rectangular superlattices provide asymmetric potential landscapes even in absence of stress. In stressed rectangular superlattices, the combination of the isotropic and the anisotropic modulation enables a change in the dominant Fourier component by changing the electrostatic bias on the overlying gate. Etched superlattices of square symmetry after removal of the resist and without gate obtained using unstressed heterostructures provide symmetric potential landscapes, as there is no distinction between the modulations in any two orthogonal directions in the plane of the 2DEG in this case. Also, in short period stressed square superlattices of 80 nm period, the small surface effect could be eliminated by applying a large forward gate bias leaving only the stress modulations along the cleavage directions. As the stress modulations in these two directions are equal in magnitude but opposite in sign, an anti-symmetric two-dimensional periodic potential and hence a symmetric potential landscape is obtained. The potential distribution in one principal lattice direction is displaced by half a period relative to the lithographic pattern. The magnetoresistances were measured in a wide range of asymmetric and symmetric two-dimensional lateral surface superlattices (2D LSSLs) and the detailed studies of the data using the existing models lead to the following conclusions.

1) In cases of strongly broken symmetry, different Fourier components do *not* independently contribute to the commensurability oscillations (COs) in *striking* agreement with the guiding centre drift model of D. E. Grant, A. R. Long and J. H. Davies [Physical Review B **61** (2000) 13127]. Moreover, it is found that the characteristics of the COs are defined by the asymmetry of the potential landscape as envisaged by this model. A previous semi-classical model [R. R. Gerhardts; Physical Review B **45** (1992) 3449] and a corresponding quantum mechanical calculation [F. M. Peeters and P. Vasilopoulos; Proceedings of 20th International

Conference on the Physics of Semiconductors (ICPS-20), 1990, p.1589] are both found to be unable to account for the data.

2) In stressed rectangular superlattices, for transport along the cube axes, change of gate bias from large positive to less positive changed the dominant Fourier component in the 2D periodic potential from a diagonal to an axial Fourier component and accordingly the guiding centre drift direction *switched* from a diagonal to the appropriate axial direction manifested by the change of the period of COs from that of diagonal Fourier component to that of the dominant axial Fourier component. When the dominant diagonal and axial Fourier components were nearly equal in amplitude, the *switching* was observed by change of magnetic field at a constant gate bias, as change in the magnetic field changed the dominant Fourier component in the magnetic field dependent effective potential. These results are in complete accord with the guiding centre drift model of D. E. Grant, A. R. Long and J. H. Davies [Physical Review B **61** (2000) 13127]. Again, the previous semi-classical model [R. R. Gerhardts; Physical Review B **45** (1992) 3449] and a corresponding quantum mechanical calculation [F. M. Peeters and P. Vasilopoulos; Proceedings of 20th International Conference on the Physics of Semiconductors (ICPS-20), 1990, p.1589] are both found to be unable to account for the data, particularly the phenomenon of *switching*.

3) In 2D LSSLs containing symmetric potential landscapes, different Fourier components *do* independently contribute to COs confirming the quantum mechanical calculation of F. M. Peeters and P. Vasilopoulos [Proceedings of 20th International Conference on the Physics of Semiconductors (ICPS-20), 1990, p.1589]. An interplay between the semi-classical model of D. E. Grant, A. R. Long and J. H. Davies [Physical Review B **61** (2000) 13127] and the said quantum mechanical model is found to be necessary to account for the suppression of the amplitude of COs.

4) Asymmetry suppresses quantum mechanical effects in asymmetric 2D LSSLs.

5) Symmetric, stressed, short period and high mobility 2D LSSLs showed a characteristic amplitude modulation of COs whenever one flux quantum h/e passed through 1, 2, 3, ... unit cells of the lattice. This phenomenon is found to be related to flux quantization.

Title of the thesis:

Transport of electrons in two-dimensional lateral surface superlattices

Section   *Page*

Chapter I   1
Introduction and low dimensional semiconductors

Chapter II   14
Review of literature

Chapter III   59
Design of experiments, fabrication of devices and experimental procedure

Chapter IV   111
Transport in stressed square and unstressed rectangular lattices: commensurability oscillations of two-dimensional lateral surface superlattices are defined by asymmetry

Chapter V   155
Transport in stressed rectangular superlattices: manifestations of switching of guiding centre drift direction in asymmetric two-dimensional lateral surface superlattices

Chapter VI   177
Transport in unstressed and stressed symmetric two-dimensional lateral surface superlattices: interplay between semi-classical and quantum mechanical Physics

Chapter VII
Summary of the results, conclusions and suggestion for future work

Appendix I

Appendix II

Appendix III

List of Tables

List of Figures

of the lattice.

of period a plotted against magnetic field showing that the magnetic field dependent switching of dominance occurred in a complicated fashion. The parameters used are $V_x = V_d = 1$, carrier density 4×10^{15} m^{-2}, $a = 100$ nm.

Chapter I: Introduction and low dimensional semiconductors

1.1 Semiconductor heterostructures

The term semiconductor heterostructure refers to semiconductors composed of more than one material. A well-known example is a GaAs-$Al_xGa_{1-x}As$ heterostructure (Figure 1.1). Here x stands for fraction of Al atoms on the group III sites. The junction between the two materials is called a heterojunction.

GaAs

heterojunction
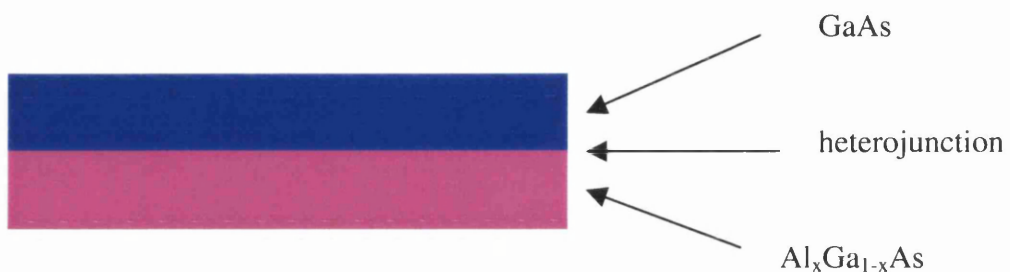
$Al_xGa_{1-x}As$

Figure 1.1
A schematic diagram of a semiconductor heterostructure consisting of GaAs and $Al_xGa_{1-x}As$.

Carriers are introduced at the heterojunction for realising devices of practical importance. The two materials in a heterostructure must be joined in a seamless manner so that the surface roughness scattering does not reduce the (low temperature) mobility of the carriers. Such a requirement is met by growth of material by the molecular beam epitaxy (MBE).

MBE is a method by which semiconductors are grown usually at high temperature, typically 600°C, in an ultrahigh vacuum environment by supplying molecular and / or atomic beams of, for example Ga, As and other constituents onto a cleaned crystalline substrate. Depending on substrate, semiconductor films of high quality can be grown by MBE with a precision in thickness of one atomic layer or better. The surface of the grown semiconductor layer is known to be very flat. Often a superlattice buffer layer consisting of alternating thin layers of GaAs and AlGaAs is grown on the substrate followed by a thick, typically ~3 μm, GaAs buffer layer before growing the active heterostructure layers. This is to prevent the propagation of defects and impurities from the substrate to the active layers.

For the heterojunction to be perfect, the materials involved should have the same crystal structure or at least symmetry that is satisfied by the common III-V compounds. Here III and V refer to the 3rd and 5th column respectively of the periodic

table. The semiconductors involved should also have nearly the same lattice constant. In general there is no problem in growing high quality heterostructures with lattice-matched pair of materials. High quality means free of any lattice imperfections such as dislocations, interface defects etc. Such imperfections, if present, result in widespread degradation of the heterostructure. GaAs-$Al_xGa_{1-x}As$ is an example of a lattice-matched heterostructure. The system has a very small mismatch of the lattice constants, about ~0.1%, over the entire range of possible values of x in $Al_xGa_{1-x}As$.

Many purposes are not met by the lattice-matched heterostructures. For example, the difference between the energy gaps in the two materials in a heterostructure may not be large enough to provide an adequate barrier for retaining energetic carriers. Moreover, a much wider choice of materials opens up if the equality of the lattice constants is relaxed.

A lattice-mismatched heterostructure is characterised by a finite difference in the lattice constants between the two materials. If one tries to match these lattices, the thinner layer will be forced to adjust its lattice constant with that of the underlying thick substrate. Hence, strain in the plane of growth and distortion along the growth axis arise in the thinner layer. The question if this deformation is expected to lead to the formation of imperfections depends on the characteristic energies of the heterostructures. The thinner top layer being lattice-mismatched, the resulting strain causes elastic energy E_e to build up which depends on the thickness of the layer and increases with increasing thickness. Generation of misfit dislocations or defects on the other hand, requires some energy E_i. If the elastic energy exceeds that required for the generation of imperfections, i.e. if $E_e > E_i$, the system will relax to a new state with a lower energy and imperfections will be generated. If the strained layer is thin enough, there will not be sufficient elastic energy and hence imperfections will not be generated. For each heterostructure, there is a critical thickness determined by the Matthews-Blakeslee criterion [1]. For thickness less than the critical thickness, the thinner layer is strained and the heterostructures are free from any imperfections. Such heterostructures are called pseudomorphic heterostructures. Examples of such systems include $In_xGa_{1-x}As$-$Al_yGa_{1-y}As$ and $In_xGa_{1-x}As$-GaAs.

It is sometimes possible to grow defect-free heterostructures with layer thickness exceeding the said critical thickness. Such heterostructures are metastable and may degrade due to effects such as temperature, external stress and processing.

In this project, a 6 nm thick pseudomorphic strained layer of $In_{0.2}Ga_{0.8}As$ is used on GaAs-$Al_xGa_{1-x}As$ heterostructure containing the carriers to utilise the strain present in the InGaAs layer, as will be discussed later.

1.2 Modulation doping

As already mentioned, carriers must be introduced at the heterojunction of a heterostructure for realising devices. The obvious way of introducing carriers is to dope the regions where electrons or holes are desired. When the carriers are released however, charged donors or acceptors are left behind which scatter the carriers by the Coulomb interaction, the so called ionised impurity scattering. This greatly diminishes the mobility of carriers, which is generally undesirable.

The solution to this problem is to place the dopant in a region away from the region to which the carriers subsequently migrate. Such introduction of carriers spatially separated from their donors is called modulation doping. The idea is illustrated in the following.
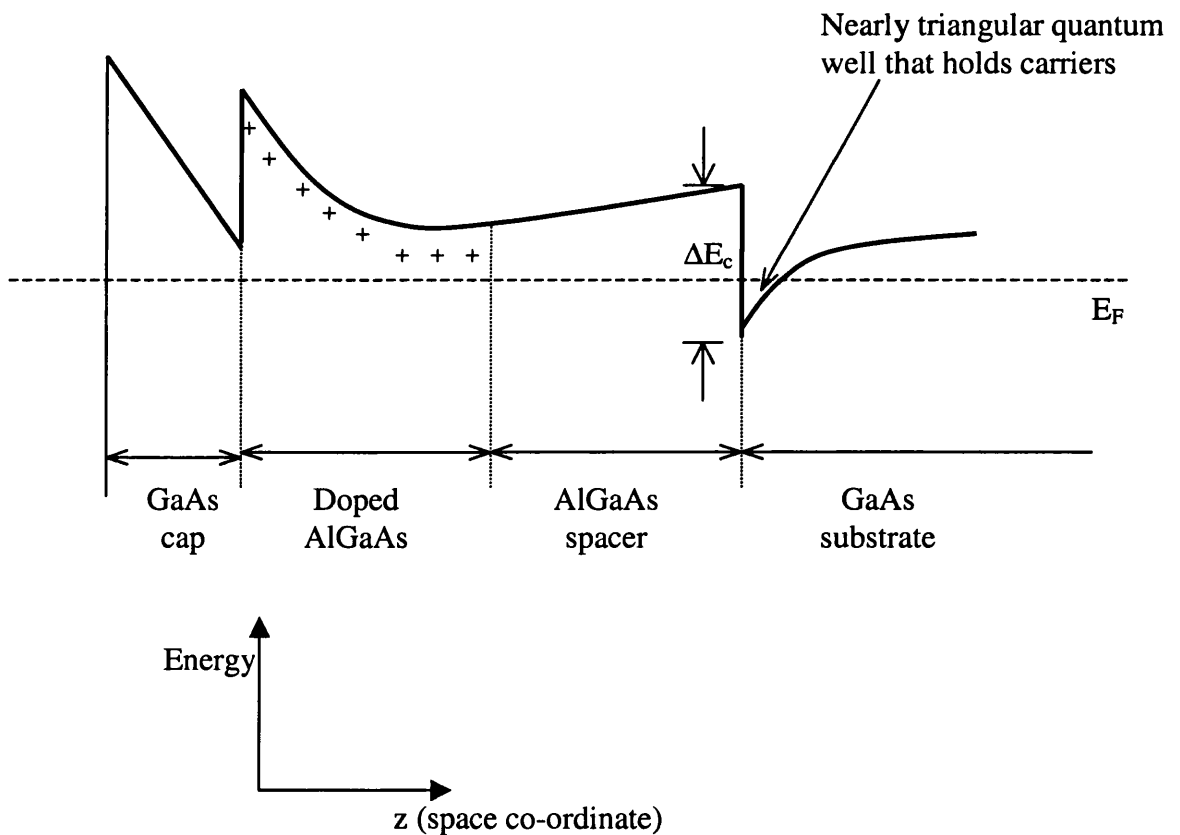
Figure 1.2
A schematic description of modulation doping, showing the conduction band edges (thick curves) after charge transfer. An approximately triangular quantum well is formed that holds the carriers spatially separated from the donors. Here ΔE_c is the discontinuity of conduction band edge between GaAs and AlGaAs and E_F is the Fermi energy. The + signs indicate ionized donors.

Figure 1.2 illustrates the scheme of modulation doping for a GaAs-AlGaAs heterostructure. Before charge transfer takes place, both the materials are neutral and the edges of the energy bands are flat. The discontinuity of ΔE_c arises as the energy gaps between valence and conduction bands are different for the two materials. Charge transfer takes place and some carriers migrate to the lower energy band of GaAs until the electrostatic potential brought about by the redistribution of charge makes the Fermi level constant across the material. This potential energy adds to the kinetic energy of electrons, and as such the band edges which represent the total energy of the electrons bend as shown in Figure 1.2. The nearly triangular quantum well thus formed holds the carriers.

In most cases, an undoped layer of AlGaAs, the so called spacer, is used between the donors and heterojunction where carriers reside, which raises the separation between the carriers in the triangular well and the donors. This reduces scattering by the ionised donors and hence higher mobility can be obtained which is vital in many physics experiments.

The example of modulation doping discussed above is often referred to as slab doping in contrast with δ doping. The δ doping involves doping within an atomic layer thickness. Such a doping with δ function like profile is routinely achieved by MBE by which dopant atoms can be inserted into an atomic mono-layer of the host crystal. The δ doping enables one to achieve a very high level of doping. Such doping is characterised by a sheet concentration of dopant atoms. δ-doped heterostructures are used in this project.

The above discussion is very crude, qualitative and introductory. The determination of the actual form of the bent energy band is a self-consistent problem, because one needs to know the charge density to solve Poisson's equation and deduce the energy bands, but the density of free carriers cannot be calculated until the energy bands are known.

1.3 Two-dimensional electron gas (2DEG)

As already noted, the carriers introduced at the heterojunction of a heterostructure reside in a roughly triangular quantum well. The energy band gap discontinuity on one side and electrostatic potential on the other form the well. The well is typically ~10 nm wide along the z direction (see Figure 1.2) at the energy of the electrons. Thus the energy for motion along the z direction is quantized as in a particle-in-a-well problem of elementary quantum mechanics. Hence the well is referred to as

quantum well. Often the number of carriers is such that only the lowest allowed energy level of the well is occupied. This is often desirable, as is the case in this project. In this case all the carriers occupy the same energy level for motion in the z direction while they are free to move in the plane perpendicular to z, i.e. in the x-y plane. In other words, the electrons in the quantum well are confined to move in two dimensions and hence are called two-dimensional electron gas (2DEG). An alternative name is the two-dimensional electron system (2DES). 2DEG is the basis of majority of the electronic devices in semiconductor heterostructures.

1.4 Shubnikov de Haas (SdH) oscillations

The solution of the Schrödinger equation in a uniform magnetic field along the z direction using the Landau gauge for the vector potential shows that for electrons free in the x-y plane, the energy is quantized and the allowed energy levels are given by

$$E_n = (n - 1/2)\hbar\omega_c$$

$$(1.1)$$

where $n = 1, 2, 3, \ldots$ $\hbar = \dfrac{h}{2\pi}$ where h is Planck's constant and $\omega_c = \left|\dfrac{eB}{m}\right|$ where B is the

magnetic field in SI unit, e is the charge of an electron and m is the effective mass of an electron. These energy levels are called Landau levels. The quantized energy due to the potential confining the electrons in the z direction has to be added to the expression of Equation (1.1).

Each Landau level contains a large number of degenerate states and the allowed number of such states in each Landau level per unit area is eB/h (considering the two spins as not degenerate).

The density of states of the Landau levels as Equation (1.1) implies consists of sharp δ functions; but this picture holds only for an ideal system where the electrons get infinite time between scattering events. In reality, however, there are always scattering events due to various reasons. According to the uncertainty principle, there is therefore always a broadening of the Landau levels. Hence the density of states of a 2DEG in a uniform magnetic field may be described by a set of Lorentzian or Gaussian profiles as in Figure 1.3, although the exact shape is controversial.

The most important point to note is that the number of states in each Landau level per unit area eB/h depends on magnetic field. Also the energy gap between consecutive Landau levels, $\hbar\omega_c$, increases with increasing magnetic field. As the magnetic field is raised, each Landau level can accommodate more electrons. Thus higher Landau levels gradually become depopulated, as the total number of electrons

remains unchanged. Again, the Fermi energy is the maximum energy of the occupied states. Thus change in magnetic field forces the Fermi energy to sweep through the system of Landau levels. In other words, the Landau levels pass through the Fermi energy as the magnetic field is changed. In this process, as the Fermi energy lies in the energy gap between two Landau levels, the resistance drops (to zero if there is clear energy gap between Landau levels which is the case at higher magnetic fields). This is because in such a case there are no carriers at the Fermi level for the conduction to take place and, peculiarly enough, the resistance is proportional to conductance in this case. As the Fermi energy moves inside a Landau level, the resistance increases. Thus the resistance of a 2DEG oscillates as a function of magnetic field. This is called Shubnikov-de Haas effect. The oscillating magnetoresistance (resistance as a function of magnetic field) is known as Shubnikov-de Haas (SdH) oscillations (Figure 1.4).
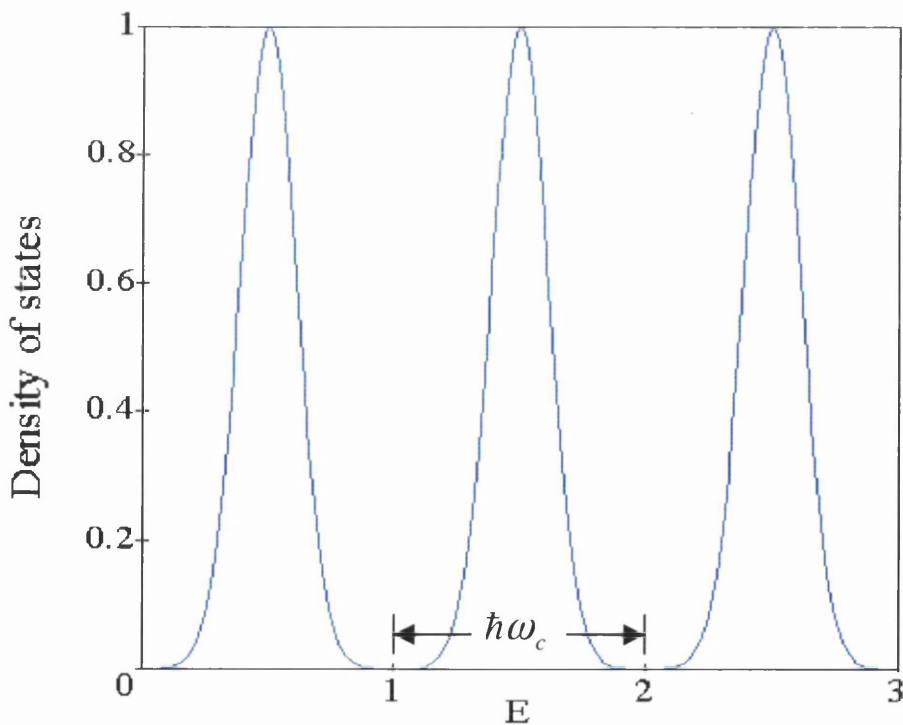
Figure 1.3
Schematic profile of broadened Landau levels showing density of states (DOS) against energy (E). DOS is shown on arbitrary scale, while E is shown in unit of $\hbar\omega_c$.
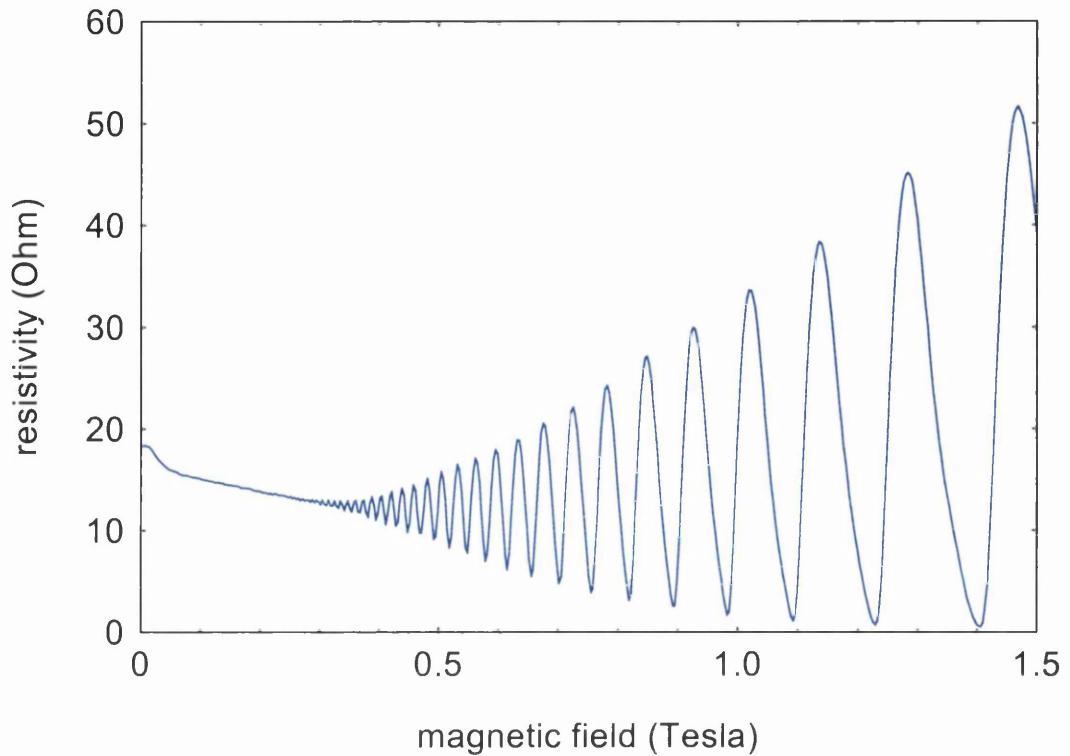
Figure 1.4
Resistivity (resistance per unit area) of a two-dimensional electron gas measured at 1.6 K as a function of a perpendicular magnetic field showing Shubnikov-de Haas oscillations. The sample used is a δ-doped GaAs-Al$_{0.3}$Ga$_{0.7}$As heterostructure with a 20 nm thick spacer, while the 2DEG is 53 nm below the surface. There is a 6 nm thick strained layer of In$_{0.2}$Ga$_{0.8}$As 10 nm below the surface.

Since the energy gaps between Landau levels are resolved at low temperature, the SdH oscillations are observed in experiments at low temperature, typically 4 K. An important feature of SdH oscillations is that these are periodic in inverse magnetic field as in Figure 1.5 and this periodicity is related with the carrier density as

$$\Delta(1/B)^{-1} = \frac{h}{2e}n_{2D}$$

(1.2)

where $\Delta(1/B)^{-1}$ is the inverse of $1/B$ periodicity of the SdH oscillations, n_{2D} is the density of 2DEG per unit area. Equation (1.2) is used as a standard equation for determining the carrier density of a 2DEG.

That there is only one peak in the FFT in Figure 1.5 reveals that there is only one frequency in the data corresponding to only one occupied sub-band. If more than

one sub-band is occupied in the quantum well containing the 2DEG, then SdH oscillations consist of more than one frequency interfering with each other. Each frequency is related to the carrier density of the sub-band in question by an equation of the form of Equation 1.2.
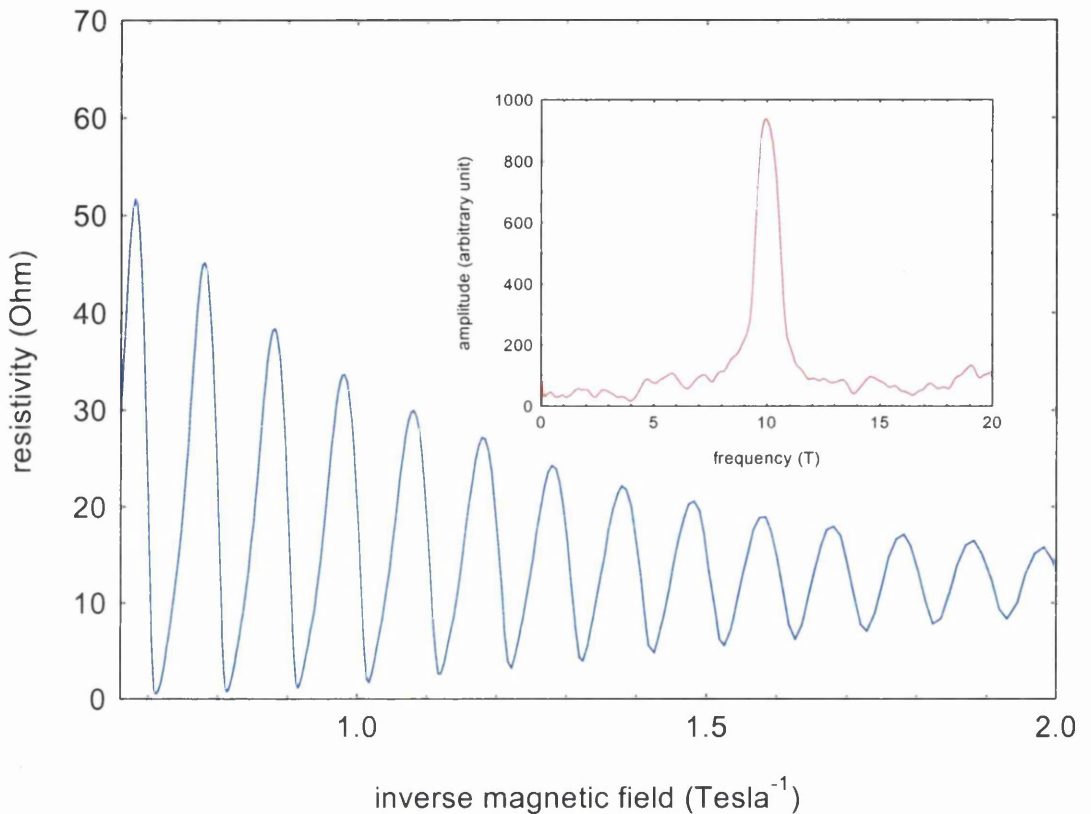
Figure 1.5
Resistivity of a two-dimensional electron gas as a function of inverse magnetic field showing that the Shubnikov-de Haas oscillations are periodic in inverse magnetic field. Data of Figure 1.4 are shown here against inverse magnetic field. Inset shows fast Fourier transform (FFT) of the data in inverse magnetic field for low magnetic field range of 0 to 0.8 T.

1.5 Hall effect

If a specimen containing charged particles is subjected to an electric field and a magnetic field at the same time, perpendicular to each other, then a voltage drop occurs across the sample in the direction perpendicular to both the directions of the electric field and the magnetic field. This effect was discovered by Hall and is called Hall effect.
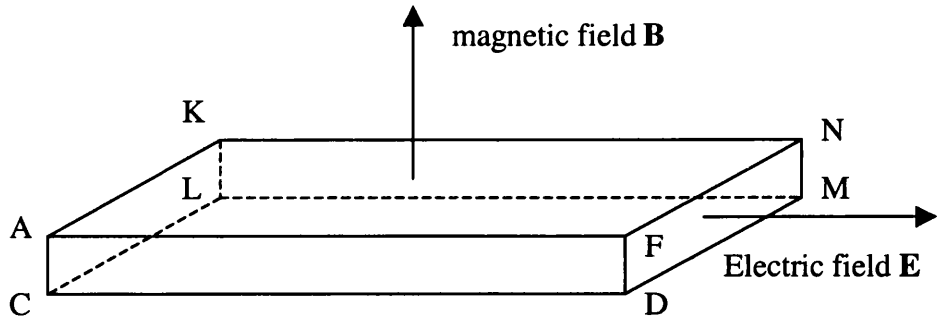
Figure 1.6
A schematic diagram for Hall effect in three-dimensions. In the limit of
AC→ 0, the figure illustrates Hall effect in two-dimensions.

Referring to Figure 1.6, if an electric field **E** is applied along AF and a magnetic field **B** along CA, then a voltage drop occurs across the faces ACDF and KLMN. This has been explained by the Lorentz force which deflects the moving charged particles and accumulates opposite types of charge at the faces ACDF and KLMN, which causes the voltage drop. One curious thing to note as a passing remark is that positive charge moving along AF and negative charge moving along the opposite direction FA results in opposite polarity of the Hall voltage. Thus the Hall effect has got the unique feature that motion of opposite charge in opposite directions leads to a physically different effect. In the limit of AC→ 0, Figure 1.6 illustrates Hall effect in two-dimensions applicable to 2DEG.

At low magnetic field, the Hall resistance shows a linear dependence on magnetic field and agrees with the classical expectations. Hence the low field Hall resistance is used as another standard means of calculating the carrier density in a 2DEG. The equation used in this regard is

$$\frac{dR_H}{dB} = \frac{1}{n_{2D}|e|}$$

(1.3)

where $\dfrac{dR_H}{dB}$ is the gradient of the Hall resistance versus magnetic field trace at low

magnetic fields and $|e|$ is the absolute value of the charge of an electron.

In high magnetic field the Hall resistance of a 2DEG shows plateaus unlike what is expected from the classical treatment. These plateaus occur at the minima of the SdH oscillations (Figure 1.7). The Hall resistances at the plateaus are h/ne^2 where n is integer. This effect is referred to as quantum Hall effect [2]. There is a vast expanse of

literature available regarding the quantum Hall effect, which is outside the scope of this dissertation.
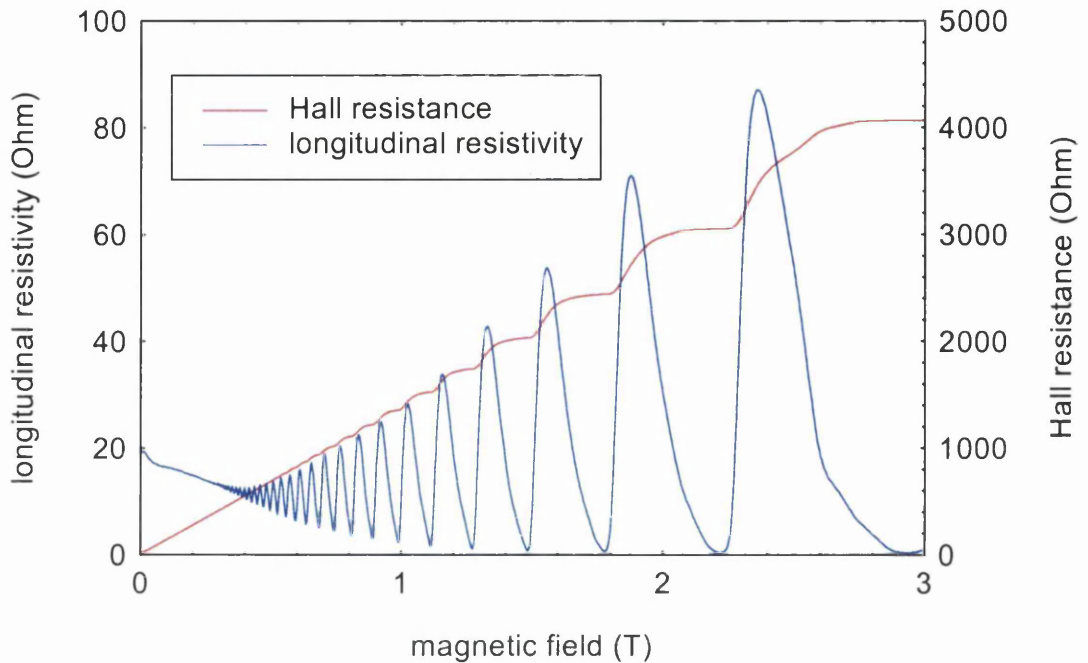
Figure 1.7
The red curve shows quantized Hall effect while the blue curve shows SdH oscillations. Plateaus in the Hall resistance occur at the SdH minima. Data were obtained at 1.6 K for the sample of Figure 1.4. The carrier density obtained from the SdH oscillations using Equation (1.2) is about 4.37×10^{15} m^{-2}, while that obtained from the low field Hall resistance using Equation (1.3) is about 4.46×10^{15} m^{-2} in close agreement with each other.

1.6 Lateral surface superlattices (LSSLs): one and two-dimensional

The term superlattice means artificially realised periodic potential. Lateral surface superlattices (LSSLs) are based on semiconductor heterostructures containing a 2DEG close to the surface. The idea is to modulate this 2DEG with a periodic potential imposed from the top. Depending on whether the periodic potential varies in one lateral direction or two, the LSSLs are called one-dimensional (1D) LSSLs or two-dimensional (2D) LSSLs respectively.

The periodic potential can be introduced in several ways. It can involve a maskless technique or lithographic techniques. An example of a maskless technique [3, 4] is the use of a light beam of spatially modulated intensity to modulate the density of 2DEG utilising the persistent photoconductivity effect of the heterostructure material.

The lithographic techniques involve realising a pattern in a resist mask on the surface of the heterostructure first and then utilising it to produce potential modulation at the 2DEG in one of the following ways.

1) Depositing metal on the patterned resist with the thickness of the metal smaller than that of the resist, followed by lift off to get rid of the resist and be left with a pattern of metal only on semiconductor surface. Electrostatic bias on this pattern of metal provides modulation at the 2DEG. This method was used in the early days of investigations for realising both 1D [5] and 2D LSSLs [6]. E. Skuras et al. [5] showed that there is modulation at the 2DEG even in absence of any gate bias due to the stress effect of the gate.

2) Depositing metal on the patterned resist with the thickness of the metal larger than that of the resist. In this case, the resist under the patterned metal remains and a patterned Schottky gate is realised [7, 8]. Application of an electrostatic bias to the gate produces a potential modulation at the 2DEG. The patterned resist puts significant stress and this modulates the 2DEG even in absence of any electrostatic bias at the gate [9].

3) Transferring the resist pattern by etching, which involves modification of the surface of the heterostructure. The periodic removal of the material brings the surface states closer to the 2DEG and thus brings about a periodic modulation at the 2DEG [10, 11]. This method has relatively rarely been used for obtaining weak 2D modulation at the 2DEG. For reasons described in section 3.1, it is this third method that has been used in this project.

1.7 Commensurability oscillations (COs)

Experimental studies of 1D LSSLs in a perpendicular magnetic field led to the discovery that for a 2DEG having mean free path larger than the period of the potential, the magnetoresistance at liquid helium temperature (4 K) for current flow perpendicular to the direction of modulation shows pronounced oscillations at low magnetic field [3].

These oscillations are caused by the interference of the cyclotron orbits with the periodic potential. These oscillations are called commensurability oscillations (COs) or Weiss oscillations after their discoverer [3], as these occur whenever the cyclotron radius is commensurate with the period of the potential. Several theoretical analyses of COs are available which are discussed in Chapter II. In contrast with 1D LSSLs, magnetotransport in 2D LSSLs generally shows COs of amplitude about an order of magnitude smaller [4] than that of 1D LSSLs.

As to 1D LSSLs, data for transport along the direction of modulation is usually referred as ρ_{xx} data while that for transport along the equi-potentials is referred as ρ_{yy} data. This convention is used in this thesis in referring to the data of 1D LSSLs.

1.8 Aim

The aim of the project is to study the transport of electrons in weakly modulated 2D LSSLs with a perpendicular magnetic field at low temperature in a systematic manner and to gather understanding of the mechanism of electron transport in two-dimensional periodic potential and a perpendicular magnetic field.

1.9 Organisation of chapters

This thesis is organised as follows. A basic introduction has been presented in Chapter I. For further details of some of the topics, see reference [12]. Chapter II contains a review of the relevant literature of both 1D (only essential works) and 2D LSSLs, evaluation of the literature and a summary of what remained to be done when the project was started. The contrast between two semi-classical models for predicting magnetoresistance characteristics of weakly modulated 2D LSSLs is also presented in considerable detail. Chapter III contains details of the design and fabrication of devices and a brief outline of the experimental procedure. Details of the development of an etching process for the realisation of superlattices is also presented. In Chapter IV, data for magnetotransport in stressed square and unstressed rectangular superlattices are discussed which confirm the role of asymmetry in defining the observed magnetoresistance characteristics. As demonstrated, the characteristics of the COs are in striking agreement with the guiding centre drift model of Grant, Long and Davies [13]. In Chapter V, magnetotransport data of stressed rectangular superlattices are discussed which provide striking experimental confirmation of *switching* of guiding centre drift direction in asymmetric two-dimensional lateral surface superlattices, a phenomenon predicted by the guiding centre drift model of Grant, Long and Davies [13]. In Chapter VI, data for both unstressed and stressed symmetric 2D LSSLs are discussed. While symmetric unstressed devices showed weak COs, symmetric, short period, high mobility stressed devices showed a magnetoresistance feature involving inverse flux quantum periodicity. Moreover, as also discussed in Chapter VI, an interplay between semi-classical dynamical effect in the symmetric potential landscape [13] and quantum mechanical effect involving modulation of the density of states [14] turns out to be necessary to account for the data. Finally, a summary of all the results,

conclusions reached and suggestions for future work are presented in Chapter VII. There are three appendices. Appendix I contains the Maple worksheets used to produce the resistivity traces presented in section 2.3.1. Appendix II contains a list of the contributions made by this project along with the copies of some of these, while the prizes received in recognition of the work are listed in Appendix III with copies of award letters enclosed. The references are presented at the end of every chapter.

1.10 References of Chapter I

[1] J. W. Matthews and A. E. Blakeslee; Journal of Crystal Growth **27** (1974) 118

[2] K. von Klitzing, G. Dorda and M. Pepper; Physical Review Letters **45** (1980) 494

[3] D. Weiss, K. v. Klitzing, K. Ploog, G. Weimann; Europhysics Letters **8** (1989) 179

[4] R. R. Gerhardts, D. Weiss and U. Wulf; Physical Review B **43** (1991) 5192

[5] E. Skuras, A. R. Long, I. A. Larkin, J. H. Davies and M. C. Holland;
    Applied Physics Letters **70** (1997) 871

[6] C. T. Liu, D. C. Tsui, M. Shayegan, K. Ismail, D. A. Antoniadis and H. I. Smith;
    Applied Physics Letters **58** (1991) 2945

[7] R. W. Winkler, J. P. Kotthaus and K. Ploog;
    Physical Review Letters **62** (1989) 1177

[8] T. Schlösser, K. Ensslin, J. P. Kotthaus and M. Holland;
    Semiconductor Science and Technology **11** (1996) 1582

[9] C. Albrecht, J. H. Smet, D. Weiss, K. von Klitzing, R. Hennig, M. Langenbuch,
    M. Suhrke, U. Rössler, V. Umansky, H. Schweizer;
    Physical Review Letters **83** (1999) 2234

[10] Y. Paltiel, D. Mahalu, H. Shtrikman, G. Bunin and U. Meirav;
    Semiconductor Science and Technology **12** (1997) 987

[11] C. J. Emeleus, B. Milton, A. R. Long, J. H. Davies, D. E. Petticrew and
    M.C. Holland; Applied Physics Letters **73** (1998) 1412

[12] J. H. Davies (1998). The Physics of Low-dimensional Semiconductors: An
    Introduction. Cambridge University Press.

[13] D. E. Grant, A. R. Long and J. H. Davies; Physical Review B **61** (2000) 13127

[14] F. M. Peeters and P. Vasilopoulos; In the Proceedings of the 20th International
    Conference on the Physics of Semiconductors (ICPS-20), edited by E. M.
    Anastassakis and J. D. Joannopoulos, (World Scientific, Singapore, 1990); p.1589

Chapter II: Review of literature

Although the project is restricted to the study of two-dimensional lateral surface superlattices (2D LSSLs), it is very useful to summarise some of the important experimental and theoretical work on one-dimensional lateral surface superlattices (1D LSSLs) first. This is important primarily because it introduces one to the research area. The other importance of this is, as will be seen later, that many ideas originated from the studies of 1D LSSLs are borrowed in the quest for understanding the conduction mechanism of electrons in 2D LSSLs. As to 2D LSSLs, mainly the information of interest or relevance to the project has been summarised. As noted in section 1.8, the aim of the project is to study the transport of electrons in weakly modulated 2D LSSLs. Hence antidot superlattices, usually formed by drilling a 2D array of holes right through the 2DEG, in which the modulation amplitude of the 2D periodic potential is larger than Fermi energy have been de-emphasised in the review. There is a quite large expanse of literature available on magnetotransport in antidot superlattices. Magnetotransport features of antidot lattices are mainly resistance peaks corresponding to pinned cyclotron orbits round given number of antidots [1].

2.1 1D LSSLs: basic introduction to experiments and theories

The literature available on 1D LSSLs is quite large. Following is a survey of some important experimental and theoretical work in this area. The survey shows that overall agreement between theories and experiments on 1D LSSLs is quite good and the experimental position is well established.

D. Weiss et al. [2] pioneered the study of two-dimensional electron gas (2DEG) subject to a weak one-dimensional (1D) periodic density modulation and a magnetic field perpendicular to the plane of the 2DEG. With the period of modulation smaller than the electron mean free path, they discovered that the magnetoresistance at low temperature, typically 4 K, contains a novel set of $1/B$ periodic oscillations, where B is the magnetic field. They obtained the modulation by illuminating the surface of a GaAs-AlGaAs heterostructure (containing a 2DEG) by an interference fringe pattern realised using two laser beams obtained from one laser source by a beam-splitting technique. This caused density modulation at the 2DEG by the persistent photoconductivity effect. After the illumination, they measured the resistance of the 2DEG both perpendicular (ρ_{xx}) and parallel (ρ_{yy}) to the 1D modulation at low temperature as a function of a magnetic field perpendicular to the plane of the 2DEG. At magnetic fields higher than about 0.3 T, they observed Shubnikov de Haas (SdH)

oscillations in both ρ_{xx} and ρ_{yy} data as a fingerprint of the 2DEG. Below 0.3 T, pronounced oscillations were observed in ρ_{xx} while weaker anti-phase oscillations were observed in the ρ_{yy} data. The low field oscillations in both the directions were found to be $1/B$ periodic with the period different from that of the SdH oscillations. The pronounced oscillations in the ρ_{xx} data were accompanied with a remarkable positive magnetoresistance (PMR) at low magnetic field. The new oscillations were found to be much less temperature sensitive than the SdH oscillations. Using a semi-transparent gate, they varied the carrier density and found change in the $1/B$ period of the novel oscillations. They plotted, for two different periods of the modulation, namely 294 nm and 382 nm, the inverse of the $1/B$ period of the novel oscillations in unit of $h/2e$ against the carrier densities. Here h is Planck's constant and e is the charge of an electron. They found that the data agree very well with the calculated curves based on the assumption that the classical cyclotron orbit diameter is commensurate with the period of the potential modulation. The commensurability condition used is that the said diameter is integer multiple of the period of the modulation as $2R_c = (m + \varphi)a$ where R_c is the cyclotron radius at the Fermi energy, a is the period of the modulation, $m = 1, 2, 3, \ldots$ and φ is a dimensionless quantity often called the phase factor. Hence the oscillations are called commensurability oscillations (COs). This equation was found to agree with the minima and maxima of the oscillations in the ρ_{xx} data with $\varphi = -0.25 \pm 0.06$ and 0.17 ± 0.06 respectively. They could not, however, present a detailed mechanism that gave rise to minima in the ρ_{xx} and maxima in the ρ_{yy} data for the same cyclotron radius.

Following the discovery of COs [2], there have been several theoretical efforts to understand the conduction mechanism involved alongside novel ways of realising 1D LSSLs involving lithographic techniques. Both quantum mechanical and semi-classical theories were put forward regarding both the COs and the PMR as noted below.

R. R. Gerhardts, D. Weiss and K. v. Klitzing [3] summarized the results of their experimental observation of COs in 1D LSSLs [2] with the additional observation that no additional structure appeared in the Hall resistance. They also explained the observations by a quantum mechanical picture assuming weak modulation, i.e. $V_0/E_F \approx 0.1$ where V_0 is the amplitude of the modulation and E_F is the Fermi energy. For 1D potential modulation of the 2DEG as $V(x) = V_0 \cos(Kx)$ with $K = 2\pi/a$, they showed that the potential lifts the degeneracy of the Landau levels and yields

eigenstates which carry current in the y direction. They noted this as the origin of the anisotropy of transport coefficients. Within the first order perturbation theory, they found that the width of the Landau levels oscillates as a function of Landau band index for a fixed magnetic field. The so-called flat-band condition, which refers to zero value of the perturbation term in energy, was obtained as $2R_c = (\lambda - 1/4)a$ where $\lambda = 1$, 2, 3, ... Their numerical calculations assuming $V_0 = 0.3$ meV lead to an excellent fit with the magnetoresistance curve for ρ_{xx} but they could not reproduce the weak oscillations in ρ_{yy}. They also calculated the Hall resistance and found no noticeable structures in agreement with their experimental observation. They remarked (a) the magnetic field strongly couples states of different energetically overlapping bands leading to strong magnetic breakdown effects, which may be the reason for the strong PMR in the ρ_{xx} data, (b) commensurability oscillations also occur in the scattering rate, which may be the reason for the weak anti-phase oscillations in the ρ_{yy} data.

R. W. Winkler, J. P. Kotthaus and K. Ploog [4] presented their study of 1D LSSLs realised using a patterned Schottky gate on the surface of GaAs-AlGaAs heterostructures as a gate electrode. The gate was patterned in that metal was evaporated to cover a resist pattern followed by no lift off. They demonstrated that the magnetoresistance oscillations reflect the formation of Landau bands in the 2DEG under the influence of the periodic potential. They also showed that the width of the Landau bands at the Fermi energy oscillates periodically with period $2R_c/a$ and this gives rise to an oscillatory band conductivity. Their calculation of the magnetoresistance caused by this mechanism provided good agreement with the observed oscillations in the ρ_{xx} data. They presented only the ρ_{xx} data for different gate biases and noted that the oscillations in ρ_{yy} are much smaller. Their calculations show that the modulation along x direction causes an extra conductivity called band conductivity along y direction, which gives rise to the oscillatory magnetoresistance in ρ_{xx}. They could not account for the oscillations in the ρ_{yy} data. They observed the third harmonic in their ρ_{xx} data.

C. W. J. Beenakker [5] presented an extremely elegant semi-classical theory for the COs discovered [2] in 1D LSSLs. The COs were explained as a resonance between the cyclotron orbit motion and the oscillating $\mathbf{E} \times \mathbf{B}$ drift of the orbit centre, called the *guiding centre*, induced by the periodic potential. Here $\mathbf{E}$ and $\mathbf{B}$ are electric field and magnetic field respectively. Such resonance is known from plasma Physics. He presented both a simplified physical picture and a systematic transport theory in this regard. The magnetoresistance oscillations for transport in the direction of modulation

were reproduced with accurate phase and amplitude without any adjustable parameter apart from the amplitude of the modulation. The reproduction of the locations of the maxima and minima of the oscillations on the magnetic field axis without any adjustable parameters, as he noted, is a "significant support" for the theory. But as he also noted, no oscillation was found for transport in the direction of the equipotentials, neither any effect was found on the Hall resistance in this theory. The PMR and the SdH oscillations are also beyond the scope of the theory, as he noted. His analytical expression for the fractional change in the magnetoresistance due to COs

$$\frac{\Delta\rho}{\rho} = \left(\frac{eV_0}{E_F}\right)^2 \left(\frac{l^2}{aR_c}\right) \cos^2\left(\frac{2\pi R_c}{a} - \frac{\pi}{4}\right),$$

(2.1)

is used as a standard means of determining the amplitude of potential modulation from the COs of the magnetoresistance data of 1D LSSLs. Here l is the mean free path of electrons.

P. Vasilopoulos and F. M. Peeters [6] and C. Zhang and R. R. Gerhardts [7] presented quantum mechanical theories which could explain both the pronounced oscillations in ρ_{xx} and weak anti-phase oscillations in ρ_{yy} in the magnetoresistances of 1D LSSLs. R. R. Gerhardts and C. Zhang [8] presented quantum mechanical calculations which could explain the anti-phase oscillations in ρ_{xx} and ρ_{yy} data observed in the magnetoresistances of 1D LSSLs. The basic premise is the oscillatory width of the modulation broadened Landau levels. P. Vasilopoulos and F. M. Peeters [9] presented a full quantum mechanical calculation for the resistivity tensor of a 2DEG in a weak 1D LSSL. Besides accounting for the data at that time, new oscillations in the Hall resistance, the cyclotron resonance frequency and the cyclotron resonance line-width are predicted. R. Menne and R. R. Gerhardts [10] showed that for 1D LSSLs whereas electric or magnetic modulation along x direction affects *only* ρ_{xx} data if the mobility is homogeneous, a mobility modulation along x direction in absence of electric and magnetic modulation affects only ρ_{yy} data. P. Streda and A. H. MacDonald [11] reported a semi-classical theory that could account for the PMR. Their arguments are based on the idea of 'magnetic breakdown' i.e. the tunneling of electrons through the Brillouin zone boundary.

P. H. Beton et al. [12, 13] made a significant contribution in the study of the PMR. They [12] studied the gate bias dependence of the magnetoresistances of 1D LSSLs realised by a patterned Schottky gate [4]. They performed simulations of the electron trajectories by numerical integration of semi-classical equation of motion and found both guiding centre drift and open runaway trajectories along the equipotentials.

They related the open runaway electron trajectories to positive magnetoresistance (PMR) at low magnetic field. In a subsequent paper, P. H. Beton et al. [13] presented the experimentally observed dependence of the critical field of PMR, the magnetic field at which PMR saturates, on the period of 1D LSSLs. They also presented a quantum mechanical description of the PMR and concluded that their semi-classical model [12] is valid if the kinetic energy of a free electron with a wavelength equal to the period of the applied potential is greater than the amplitude of the applied potential. Assuming a sinusoidal periodic potential, they presented an equation relating the critical magnetic field of the PMR B_c with the period a and the amplitude of the modulation V_0 as

$$B_c = \frac{2\pi V_0}{a v_F}$$

(2.2)

where v_F is the Fermi velocity. They obtained this result from the observation that the lateral streaming orbits responsible for the PMR, that are dominant at low magnetic field, are no longer possible when the Lorentz force on an electron at the Fermi level due to the applied magnetic field exceeds the maximum force resulting from the periodic electrostatic field. That is

$$-e v_F B_c = -e E_{max}$$

(2.3)

with E_{max} given by the amplitude of $-\frac{\partial}{\partial x}(V_0 \cos(2\pi x/a))$ reduces to equation (2.2).

Equation (2.2) is used as another standard means of determining potential amplitude from (the low field PMR in) the magnetoresistance data of 1D LSSLs.

P. H. Beton et al. [14] also studied the temperature dependence of the COs of 1D LSSLs (of 150 nm period). They provided the following explicit expression for the temperature dependence of COs.

$$\frac{\Delta\rho_{xx}}{\rho_0} = \left(\frac{eV_0}{E_F}\right)^2 \left(\frac{l^2}{aR_c}\right) \cos^2\left(\alpha E_F^{1/2} - \frac{\pi}{4}\right) \times \left(\frac{T}{T_a(B)}\right) \Bigg/ \sinh\left(\frac{T}{T_a(B)}\right)$$

(2.4)

where ρ_0 is the resistivity at zero magnetic field, $\Delta\rho_{xx}$ is the amplitude of CO, T is temperature, $\alpha = 2\pi(2m^*)^{1/2}/eBa$ and $T_a(B) = \hbar\omega_c k_F a/(4\pi^2 k_B)$ is the effective temperature. Here m^* is the effective mass of electron, $\hbar = h/2\pi$, ω_c is the cyclotron frequency, k_F is the Fermi wave-vector and k_B is the Boltzmann constant. They compared Equation (2.4) with their data and found excellent agreement. They also discussed some limitations of Equation (2.4).

There have been observations of harmonics in the COs of 1D LSSLs. As already noted, R. W. Winkler, J. P. Kotthaus and K. Ploog [4] observed third harmonic

in the COs. R. Cuscó et al. [15] studied metal gated 1D LSSLs of period 270 nm with an aspect ratio of 130:140. They realised metal gratings on heterostructures by evaporating metal to cover a resist pattern followed by lift off. The lattice was fabricated on shallow heterostructures containing 2DEG only 28 nm below the surface and showed second harmonic in the COs, while an identical lattice fabricated on heterostructures containing 2DEG 90 nm below the surface showed no second harmonic at all. They found that, for shallow heterostructures, the shape of the potential inferred from the magnetoresistance data is best explained by a strain field due to differential contraction between metal gate and semiconductor. R. Cuscó et al. [16] in another study of 1D LSSLs made the observation that the superlattices with equal aspect ratio (mark to space ratio) show only the fundamental frequency in COs whereas those with unequal aspect ratio (1:2) show significant second harmonic in the COs. M. Kato et al. [17] noted the observation of third harmonic in the magnetoresistances of 1D LSSLs. They also noted that appearance or non-appearance of higher harmonics presumably depends on specific wafer used, materials of gates, details of sample preparation, crystallographic orientation of the wafer with respect to the grating that can greatly affect the strain induced effect.

The strain introduced in LSSLs has been identified as a source of significant modulation at the 2DEG in several studies of 1D LSSLs. As already noted, R. Cuscó et al. [15] could best explain the shape of the potential by a strain field.

P. D. Ye et al. [18] studied the low field magnetoresistances (ρ_{xx}) of 1D LSSLs of metal grating. They found that the strain connected with the patterned gate results in a periodic potential that can lead to pronounced electrostatic modulation of the 2DEG. They observed different harmonics of the potential in the data depending on the aspect ratio of the grating. For superlattices of 950 nm period with metal stripes of width 1/3 of the period, they observed electrostatic modulation of 317 nm period corresponding to the third harmonic. Again, for lattices of 500 nm period with the metal stripes of width 1/2 of the period, they observed electrostatic modulation of 250 nm period corresponding to the second harmonic.

E. Skuras et al. [19] in their studies of 1D LSSLs realised by metal stripes [15] demonstrated that the strain from the gates modulates the 2DEG by the anisotropic piezoelectric effect. They experimentally showed that the piezoelectric modulation under a (100) GaAs wafer varies as $sin2\theta$ where θ is the angle between the direction of current flow and [010] direction towards [001]. They found that for current flow along [011] and [01$\bar{1}$], the piezoelectric modulations are equal but opposite in sign. They

noted that if the piezoelectric modulation is not wanted, it can be eliminated by orienting the superlattice so that the modulation is along [010]. They also noted that the piezoelectric modulation offers a valuable tool for modulating a 2DEG in both one and two-dimensions.

The realization that strain can introduce significant modulations at the 2DEG led to the use of a lattice mismatched intrinsic stressor layer to induce potential modulations at the 2DEG. R. J. Luyken et al. [20] studied the magnetotransport in 670 nm period 1D LSSLs obtained by realising a grating of an epitaxial 10 nm thick strained $In_{0.1}Ga_{0.9}As$ layer on top of GaAs-AlGaAs heterostructures. They patterned the stressor layer by wet etching up to a depth of 10 and 13 nm for two samples of two aspect ratios of the superlattice. Their work demonstrates that heterostructures with a coherently strained InGaAs top layer can be used to create lateral potential modulation. They noted that contrary to the conventional evaporated or sputtered strained structures, epitaxial stressors offer the possibility to accurately control the amount of stress and allow for a precise theoretical analysis starting from the well-known material parameters and matching conditions.

C. J. Emeleus et al. [21] in their studies of 300 nm period 1D LSSLs demonstrated that a patterned heteroepitaxial strained layer of $In_{0.2}Ga_{0.8}As$ close to the surface of GaAs-AlGaAs heterostructures is very useful in providing a strong and anisotropic potential modulation at the 2DEG without diminishing the electron mobility very much. They patterned the stressor layer by dry etching. They accounted for the anisotropic magnetoresistances using the previous result [19] that the stress couples to the 2DEG by the anisotropic piezoelectric effect. They also identified that in the superlattices lacking the stressor layer, there is modulation due to the surface pattern which is isotropic unlike the piezoelectric modulation. They named it the surface effect. They further noted that there is no piezoelectric modulation along [010] and [001] while (for 300 nm period) the surface effect and piezoelectric effect add to each other in [011] and cancel each other in the [$01\bar{1}$] direction on a (100) GaAs wafer. They could realise a potential modulation amplitude typically 1 to 2 meV, while the Fermi energy is about 10 meV. They noted 60% difference between the magnitudes of PMR and COs in [010] and [001] directions but could not account for it. This difference is presumably because of a non-uniform etch-depth. In a later paper [22], they presented the temperature dependence of the COs as well and noted that the patterned stressor should provide a powerful tool for the design and fabrication of a two-dimensional periodic potential.

B. Milton et al. [23] in their studies of 100 nm period 1D LSSLs realised by patterning an epitaxial InGaAs stressor layer close to the surface of GaAs-AlGaAs heterostructure noted that the surface effect and the piezoelectric effect add to each other in [01$\bar{1}$] direction unlike [011] for 300 nm period [21]. They obtained potential modulation amplitude of 1.5 meV from both the PMR and the COs of the data at 5 K and +0.3 V gate bias. At 45 mK they found strong interference between SdH oscillations and COs. They explained the low field data at 45 mK by a quantum mechanical analysis.

That periodic removal of material from heterostructure surface introduces a periodic potential at the 2DEG [21] was also observed by Y. Paltiel et al. [24]. They studied magnetotransport in etched 1D LSSLs of period 100 and 200 nm. They used GaAs-AlGaAs heterostructures with a 2DEG lying 70 nm below the surface in each case. They realised samples with two different etch depths, namely 10 and 20 nm, for each period. They noted that the etched profile brought about potential modulation at the 2DEG and the modulation is determined primarily by the etch depth and little can be added by biasing the gate. The COs they observed are quite large even for a 10 nm etch depth with the 2DEG lying 70 nm below the surface.

There have been theoretical studies on the strain in inducing potential modulation at the 2DEG. J. H. Davies and I. A. Larkin [25] calculated analytically the potential generated in a 2DEG by a LSSL formed by an array of parallel metal striped gates on the surface of GaAs-AlGaAs heterostructures. They found that the strain field produced by differential contraction between the metal gates and the semiconductor fits the data [15] within a factor of two. I. A. Larkin et al. [26] calculated the piezoelectric coupling between a 2DEG and the stress field due to a LSSL of striped metal gates. Their calculations show that the piezoelectric effect provides the dominant interaction between the strain under a LSSL and the electrons in the 2DEG and it is several times larger than the deformation potential coupling. The piezoelectric contribution to modulation was noted to depend on orientation and on a (100) GaAs surface, it vanishes for current flow along the crystal axes and it has maxima for that along the cleavage directions.

There is a detailed study of 1D LSSLs available. A. R. Long et al. [27] presented in detail their studies of 1D LSSLs of a wide range of periods realised by metal gratings [15] as gates on top of GaAs-AlGaAs heterostructures. They found modulations of the 2DEG even in absence of any gate bias, which they attributed to the gate induced strain that couples to the 2DEG by piezoelectric modulation. For non-zero

gate bias, electrostatic contribution added to the piezoelectric contribution of modulation. They calculated the magnitude of the potential modulations by studying amplitudes of COs [5] and also PMR steps [13] and found that both the magnitude of the modulations and the harmonic content of the potential are in reasonable agreement with theoretical calculations over the full range of periods and for all structures studied.

2.2 2D LSSLs: introduction to relevant experiments and theories

The magnetotransport features of 2D LSSLs depend on the potential amplitude relative to the Fermi energy. In the following, mainly the literature on weakly modulated 2D LSSLs is surveyed in appreciable detail with emphasis on information that is of interest or relevance to the project. The review has been presented in two sections: experiments and theories.

2.2.1 Experiments on 2D LSSLs

The experimental position on weakly modulated 2D LSSLs is less certain compared with that of 1D LSSLs. Early experimental work revealed COs much weaker in amplitude compared with that of the COs in the ρ_{xx} data of 1D LSSLs and with different phase factors.

R. R. Gerhardts, D. Weiss and U. Wulf [28] studied the contrast between the amplitudes of COs obtained from 1D and 2D LSSLs. They realised the superlattices by a maskless technique, by illuminating twice the heterostructure surface by an interference grating pattern of two coherent laser light beams, rotating the sample by 90° after first exposure. The most notable features of their data are (a) COs of 2D LSSLs are about an order of magnitude weaker or suppressed in amplitude than that of the COs in the ρ_{xx} data of 1D LSSLs [2] realised also by holographic illumination, (b) in 2D LSSLs the COs in ρ_{xx} and ρ_{yy} are *in phase* with each other. Moreover, they found the COs of both ρ_{xx} and ρ_{yy} of 2D LSSLs to be in anti-phase with those of the ρ_{xx} data of 1D LSSLs. They attributed the suppression in the amplitude of the COs of 2D LSSLs to suppression of band conductivity due to possible, implicit resolution of minibands in the modulation broadened Landau levels. In line with this argument, they suggested that in low mobility samples the collision broadening is expected to exceed the sub-band splitting and hence the band conductivity will be of the same order of magnitude for both 1D and 2D LSSLs. Similar data were reported by D. Weiss et al. [29] in an earlier paper in which they noted that the order of exposure whether to produce modulation along x direction first and then along y direction and vice-versa

should produce the same magnetoresistances. In view of the similarity of the magnetoresistance data of 2D LSSLs with the ρ_{yy} data of 1D LSSLs, D. Weiss et al. [29] speculated that the COs in 2D LSSLs also reflect the oscillating scattering rate.

E. S. Alves et al. [30] studied 145 nm period 2D LSSLs and observed weak COs. They realised superlattices by obtaining about 60 nm diameter holes in a resist layer and evaporating metal on top to get a patterned gate. At zero gate bias, they studied the $1/B$ periodicity of COs for various carrier densities of the 2DEG, changing the density by illuminating the sample and exploiting the persistent photoconductivity effect. They plotted the inverse of $1/B$ period of the COs, $1/\Delta(1/B)_{co}$, for different carrier densities obtained from the SdH oscillations and found that the data fit well with the curve $1/\Delta(1/B)_{co} = 2\hbar(2\pi n_{2D})^{1/2}/(ea)$ which corresponds to the magnetic frequency given by $2R_c = (\lambda + \phi)a$. Thus they argued that the COs they observed in 2D LSSLs are due to commensurability between the cyclotron orbit diameter at Fermi energy and the period of the superlattice, as in 1D LSSLs. They admitted that they could not identify a consistent value of the phase factor ϕ. They compared the result with that of a 1D LSSL of 106 nm period.

H. Fang and P. J. Stiles [31] studied the magnetotransport in 2D LSSLs of hexagonal symmetry with two different degrees of modulations. They realised the weakly modulated lattice by shallow etching a hexagonal pattern up to the depth of the GaAs cap of the conventional GaAs-AlGaAs heterostructures. They obtained the strongly modulated lattice by etching the pattern through the 2DEG. They completed the fabrication by removing etch mask and evaporating metal to get a Schottky gate. Their magnetoresistance data show weak oscillations at low magnetic field for both types of samples. For deeply etched samples, the peaks of these oscillations follow the commensurability condition $2R_c = (\lambda + \phi)a$ with $\phi \approx -0.21\pm0.02$, whereas for 1D LSSLs it is around +0.25 [2, 3, 5]. For the shallow etched samples of different periods and gate voltages, the maxima in the low field magnetoresistances were found to appear with $\phi \approx 0.27\pm0.04$. The phase was found to change slightly with gate bias and the period a was found to have half of the expected value. They noted that these differences in the oscillation period and the phase factor in the two types of samples correlate with different geometries due to the difference in the degree of depletion. They studied lattices of 330, 364 and 394 nm periods. They found the low field oscillations to be $1/B$ periodic for all three periods of lattices, for both shallow and deep etched case and different gate biases.

A. Lorke, J. P. Kotthaus and K. Ploog [32] in their studies of antidot lattices observed COs at positive gate bias when the modulation is weaker than in the antidot regime. At sufficiently large negative gate bias, the potential amplitude exceeds the Fermi energy giving rise to what is called anti-dot regime. They realised a pattern of 170 nm radius voids on a grid of 460 nm period in a resist coating Hall bars by photolithography and covered the resist pattern by a thin layer of metal to get a modulated gate. Modulation at the 2DEG was realised by applying a voltage to the patterned gate. The maxima of the COs they observed agree with the commensurability condition $2R_c = (\lambda + \phi)a$ with $\phi = 0$ instead of 1/4. They accounted for the data by a simulation involving a semi-classical diffusion model based on ballistic transport in a 2D periodic potential under the influence of a Lorentz force and invoking ad hoc a cross term, $\cos(kx)\cos(ky)$ in the potential $\cos(kx) + \cos(ky)$.

C. T. Liu et al. [33] fabricated 200 nm period 2D LSSLs with a metal grid by X-ray nano-lithography and lift off. Magnetotransport at zero gate bias showed no COs at all. At positive bias the COs are just visible while the COs are present at very large negative values of the gate bias. The minima of the COs they observed agree almost unequivocally with the phase factor of $\varphi = -0.25$ in $2R_c = (\lambda + \varphi)a$. They noted that as the phase factor was ambiguous in the previous experimental studies of 2D LSSLs, they for the first time observed guiding centre drift resonance in 2D LSSLs, as the phase they observed agrees with what is predicted by the guiding centre drift model [5].

There are several experimental work available in which the magnetotransport features of weakly modulated 2D LSSLs were attributed to quantum mechanical effects. O. Steffens et al. [34] studied 215 nm period 2D LSSLs. They fabricated the superlattices by realising holes in a resist layer coating the Hall bars and then laying a metal blanket thicker than the resist layer followed by no lift off, thus getting a patterned Schottky gate. They reported magnetotransport data at 4.2 K for gate biases from 0.2 V to –0.75 V. They observed weak COs for positive gate biases that decreased in amplitude as the bias was made less positive. At negative biases they observed antidot features related to pinned electron trajectories round one and four antidots. For intermediate biases, they observed weak PMR followed by very weak oscillations that they could not relate to specific commensurability conditions. At negative bias, one of the anti-dot peaks (peak in the magnetoresistance corresponding to pinned electron trajectories round a given number of maxima of the periodic potential) appeared near the magnetic field where there was a PMR at intermediate gate bias. Hence it appeared as if the PMR developed into an antidot peak as the gate bias was made more negative.

They tried a detailed quantum mechanical treatment involving minigaps and minibands to account for the data at intermediate biases. The decrease of COs in amplitude with more negative gate bias was also observed by T. Schlösser et al. [35]. They studied 139 nm period 2D LSSLs of patterned Schottky gates [34]. At 4.2 K they observed that the amplitude of COs decreased as the gate bias was made more negative.

C. Albrecht et al. [36] reported data obtained at 1.5 K and 50 mK from 120 nm period 2D LSSLs of patterned Schottky gate [34]. They observed large COs for both the temperatures. There are traces of splitting of SdH peaks into two or three peaks in the data. With the heterostructures containing a 2DEG with a very high mobility (210 $m^2V^{-1}s^{-1}$), they observed at 50 mK a novel set of very regular oscillations at low magnetic field at the saturation of the PMR. This set of oscillations was found to have a $1/B$ periodicity distinctly different from those of the COs and the SdH oscillations. The amplitude of the novel oscillations was found to be modulated by the COs. They explained these novel oscillations by periodic potential induced modification of contours of constant energy of the free electrons in k-space. They reported the observations earlier [37] in which they included the gate bias dependence of the magnetoresistance features and called for explanations.

There have been observations of deviations of the minima of COs from flat-band condition, which were attributed to quantum mechanical effects. D Weiss et al. [38] studied 150 nm period 2D LSSLs of patterned Schottky gate [34]. At 50 mK they found that as the gate bias is made positive, the maxima of the envelope of the SdH maxima coincide with the flat-band condition, which they attributed to suppression of band conductivity. At 4.2 K they found this anomaly at magnetic fields higher than 0.25 T, which they also attributed to suppression of band conductivity. They noted that a small inhomogenity in the carrier density could prevent the direct observation of the internal structure of Landau levels.

A similar magnetoresistance feature was observed by T. Schlösser et al. [39] as well. They reported data obtained at 30 mK from 139 nm period 2D LSSLs of patterned Schottky gates [34]. They observed weak COs superimposed on SdH oscillations. They reported the observation of systematic deviation of the minima of the envelope of the SdH maxima from the magnetic fields corresponding to flat-band condition. They found no such deviation for the minima of the envelope of the SdH minima. As the gate bias was made more and more negative, the minima of the envelope of the SdH maxima started to deviate from the flat-band condition at higher magnetic field first. Eventually, at large negative gate bias, the maxima of the envelope of the SdH maxima coincided with the flat-band condition. They have attributed this

observed phenomenon to suppression of band conductivity and noted it as a sign of resolution of the internal structure of Landau bands and increasing dominance of scattering conductivity with increasing potential modulation.

There have been several observations at mK temperature of splitting of SdH peaks into multiple peaks [35, 40, 41], which have been attributed to the passage of Fermi energy through the internal structures of Landau levels according to Hofstadter's butterfly (discussed below in section 2.2.2). There have been observations [40] of splitting of a SdH peak into two peaks at 2.15 flux quanta per unit cell, another into four peaks at 4 flux quanta per unit cell of 139 nm period superlattices. In the same paper the authors reported the observation of splitting of a SdH peak into three peaks for 3/2 flux quanta per unit cell of 105 nm period superlattices. They observed further splitting at lower magnetic field, which they could not account for but asserted that these are "certainly" due to internal structure of Landau levels. In another paper [35], they reported the observations of splitting of a SdH peak into three peaks for 3 flux quanta per unit cell and another into two peaks for 2/3 flux quantum per unit cell of 139 nm period superlattice. For 80 nm period superlattices, they observed [41] splitting of a SdH peak into two peaks for 2/3 flux quantum per unit cell.

As an advance in the search for internal structure of Landau levels, C. Albrecht et al. [42] studied at 50 mK both 100 nm and 120 nm period 2D LSSLs of patterned Schottky gate [34] containing 2DEG of very high mobility. They observed, besides splitting of SdH peaks, quantized Hall conductance corresponding to splitting of SdH peaks. They related the observations to the internal structures of Landau levels as envisaged by Hofstadter's butterfly.

Several other works on 2D LSSLs are available and of interest as well. These are summarised below. A. Soibel et al. [43] studied magnetotransport in lateral superlattices formed by a honeycomb gate pattern on GaAs-AlGaAs heterostructures. The patterns had a pitch of 200 or 150 nm with the hexagons having sides of length 115 and 87 nm respectively. For both the samples they observed weak magnetoresistance oscillations at low magnetic field and different gate biases. Some of their samples had back gate which allowed them to change the density of the 2DEG keeping the bias on the patterned gate fixed. They presented a simple picture based on the idea that the potential at the vertices of the hexagons in the lattice is larger than elsewhere and hence there can be pinned cyclotron orbits round the vertices that avoid these locations. They have sketched such orbits and found that these are centered at lattice symmetry points: either on a vertex or at the centre of a hexagon or at the centre of a segment. Their

calculations show that the cyclotron radii for which they observed magnetoresistance peaks agree well with those of their intuitive picture.

E. Paris et al. [44] have studied magnetotransport of 2D LSSLs realised by a grid gate of 170 nm period on GaAs-AlGaAs heterostructures. Data at 1.4 K after illumination and without gate bias showed weak COs.

K. Y. Lee et al. [45] fabricated 100 nm and 150 nm period 2D LSSLs by etching a grid on GaAs-AlGaAs heterostructures using an array of 50 nm diameter dots of metal as etch mask and subsequently covering the etched area by metal to get a Schottky gate. They transferred the superlattice pattern in 10 seconds by a rather fast etchant ending up with a large resistivity of the 2DEG (without gate bias). In the magnetoresistances they found COs. They also observed some additional plateaus in the Hall resistance in the quantum Hall regime (which cannot be attributed to integer or fractional quantization) which have associated oscillations in the longitudinal resistances.

C. G. Smith et al. [46] showed that 40 nm period lateral surface superlattices of dots can be exposed in a resist layer. They realised a hexagonal lattice of exposed dots with a separation of both 40 nm and 60 nm. They obtained a patterned Schottky gate with the 60 nm case on heterostructures containing 2DEG of rather low mobility (33 $m^2V^{-1}s^{-1}$). They studied magnetotransport at mK temperature and noted that COs were not observed. They observed structures in high field SdH oscillations and corresponding detail in Hall resistance. They tried to compare these structures with the predictions of a calculation by F. H. Claro and G. H. Wannier [47]. These calculations are concerned with the effect of a hexagonal potential on a 2DEG in the presence of a magnetic field and led to miniband structure in Landau levels. They [46] found it "very difficult" to fit the data with the theory.

R. Schuster et al. [48] studied magnetotransport in 2D LSSLs of rectangular symmetry and a number of different ratios of the two lattice constants. They realised the superlattices by wet etching holes arranged on rectangular grids on the surface of GaAs-AlGaAs heterostructures. They completed the fabrication by covering the etched structure with metal to realise a gate. They did not mention if they removed the etch mask or not before gating. They discussed the data in terms of anti-dot lattices. The most notable feature of their data is that when the larger lattice constants of rectangular lattices were aligned along the direction of transport, they always observed oscillations commensurate with the shorter lattice constants, while for transport in the orthogonal direction they observed no oscillations commensurate with the lattice constants. They also studied the devices at mK, which brought out some more features in the data.

2.2.2 Theoretical work on 2D LSSLs

Much of the available theoretical work on 2D LSSLs is concerned with resolution of minigaps in the energy spectrum of an electron in a 2D periodic potential and a perpendicular magnetic field. This follows the work of D. R. Hofstadter [49] who calculated the energy spectrum of an electron in a two-dimensional periodic potential of square symmetry and a perpendicular uniform magnetic field. His plot of the energy of the electron as a function of a wide range of rational values of flux quanta per unit cell gives rise to a recursive spectrum, the large gaps of which form a pattern somewhat resembling a butterfly. This is known as Hofstadter's butterfly. He pointed out that experimental detection of this energy spectrum in natural crystals would require magnetic fields well beyond that accessible in laboratories. He indicated the possibility of using an artificial lattice to bring the magnetic field requirement to what is available in laboratories.

A. H. MacDonald [50] presented a proof of the statements used by Hofstadter to characterise the recursive structure of the energy spectrum of an electron in a two-dimensional periodic potential as a function of a perpendicular magnetic field. He showed how this recursive structure arises.

M. A. Andrade Neto and P. A. Schulz [51] presented a model that shows, within the same framework, the evolution of the electronic spectra of LSSLs as a function of a perpendicular magnetic field ranging from weak to strong potential modulation. They could identify Hofstadter-type spectra in every modulation strength regime.

H. Silberbauer [52] presented a quantum mechanical method for calculating the miniband structure in the energy spectrum and eigenstates of an electron in a 2D LSSL and a perpendicular magnetic field. He noted that the approach is capable of dealing with arbitrary potential shapes.

There has been much work on how the ideal single particle energy spectrum of Hofstadter gets modified by different effects. V. Gudmundsson and R. R. Gerhardts [53] studied the effects of electron-electron interaction on the energy spectrum of a 2DEG in a perpendicular magnetic field and a superlattice potential of square symmetry. They showed that the essential gap structure of the energy spectrum remains, although screening leads to quenching of Hofstadter butterfly at small values of inverse flux.

V. Gudmundsson and R. R. Gerhardts [54] studied the effect of Coulomb interaction between electrons on the Hofstadter butterfly. They found that the interactions essentially preserve the intricate gap structure in the energy spectrum but with a lower symmetry that depends on the filling of the Landau bands.

O. Kühn et al. [55] investigated the single particle energy spectrum in presence of a periodic potential of square symmetry and a perpendicular magnetic field. They showed that coupling between different Landau levels causes a strong modification of the spectra compared to the ideal Hofstadter case though the presence of gap regions survives. They did not consider the effect of disorder on the spectrum however.

D. Springsguth et al. [56] studied the energy spectrum and quantized Hall conductance of electrons in a 2D periodic potential in presence of a perpendicular magnetic field without neglecting the coupling of the Landau bands. They found modifications of the Hall conductance resulting from changes in the structure of the energy spectrum compared to the Hofstadter butterfly. They noted that such changes could be found even for weak Landau band coupling.

There have been studies on how classical chaos affects the Hofstadter butterfly. T. Geisel et al. [57] studied the effect of classical chaos in LSSLs on the Hofstadter butterfly. They found that the classical chaos can destroy the butterfly spectra completely and remarked that in the experimental search for Hofstadter butterfly in LSSLs, spectral modifications due to classical chaos should be expected. R. Fleischmann et al. [58] studied chaotic electron dynamics and could reproduce some of the results on the magnetotransport in antidot superlattices including the low magnetic field quenching of the Hall effect. They also studied the influence of classical chaos on Hofstadter butterfly and discussed on its observability in experiments.

There has been much work on the effect of Hofstadter butterfly on the magnetoresistivities of weakly modulated 2D LSSLs. R. R. Gerhardts and D. Pfannkuche [59] reported a detailed quantum mechanical treatment of conduction in 2D LSSLs. They found splitting of Landau bands into sub-bands and showed that if the collision broadening is smaller than the energy separation between adjacent sub-bands, the band conductivity is drastically reduced. Their numerical calculations also show that the dominance between band conductivity and scattering conductivity is determined by the relative strength of collision and modulation broadening even in the regime of resolved sub-bands. Their model calculations reflect the sub-band splitting of the Hofstadter's butterfly directly in the magnetoresistance curves.

D. Pfannkuche and R. R. Gerhardts [60] reviewed the literature available at that time and also collected the results on the single particle energy spectrum under a unified perspective and notation. They also presented detailed calculations for transport in 2D LSSLs with weak modulations. According to the calculations, if the collision broadening is so large that the internal sub-band structure of the Landau levels is not resolved, the magnetoresistances for 2D LSSLs are the same as those for (the ρ_{xx} data

of) 1D LSSLs of same period. If, however, the collision broadening is so small that the internal structure is resolved, at least partially, then the calculations predict a drastic suppression of the band conductivity observed in experiments. The authors attributed the experimentally observed [38] magnetic field dependent transition of COs from in-phase to anti-phase to a transition of dominance between band conductivity and scattering conductivity. They noted that the suppression of band conductivity is an indirect manifestation of Hofstadter's energy spectrum and asked for high mobility samples with lower carrier density ($<10^{15}/m^2$) and shorter period (~50 nm) for a direct resolution of the sub-band structure in the Landau levels. It should be noted that their calculated self-similar energy spectrum [60] has inverse flux quantum periodicity, while the original spectrum introduced by Hofstadter [49] is periodic in flux quantum per unit cell.

G. Petschel and T. Geisel [61] noted that for a potential of amplitude V_0 given by $h^2/mV_0a^2 \approx 4$, the observability of butterfly structures in a sufficiently wide magnetic field regime down to 1.5 T would require a lattice constant of 70 nm.

Several quantum mechanical calculations are available that are intended to explain the magnetotransport data. R. R. Gerhardts [62] presented a quantum mechanical picture which explains the large amplitude COs of 1D LSSLs as a result of band conductivity and the weak anti-phase COs along the equipotentials as due to quantum oscillations of the scattering rate. The weak COs in 2D LSSLs were explained as a consequence of suppression of band conductivity due to resolution of minibands.

Y. Tan [63] presented quantum mechanical calculations for the conductivity in both 1D and 2D LSSLs. As to 2D LSSLs, his arguments involve splitting of Landau levels into minibands and the relative role of band conductivity and scattering conductivity. He argued to explain the experimental observations of Weiss et al. [38] in terms of a change of dominance between band conductivity and scattering conductivity.

A. V. Vagov [64] presented a calculation of the electrical conductivity tensor of a 2DEG with a weak two-dimensional potential modulation in a perpendicular magnetic field. He calculated the energy spectrum with all finite lifetime effects in conformity with the high mobility samples tested in experiments. He took into account the collision broadening as well, before calculating the conductivity. He found that though both the number of sub-bands and the degree of spectra degeneracy depend irregularly on the magnetic field, all physically measurable quantities such as the density of states (DOS), chemical potential, and resistivity remain smooth functions of magnetic field. He found the oscillations in the DOS at the Fermi level to be connected

only with the oscillations of the strength of the modulations. He did not find any oscillations due to the sub-band structure itself.

F. M. Peeters and P. Vasilopoulos [65] presented a quantum mechanical calculation of the magnetoresistivity of a 2DEG in a weakly modulated 2D LSSL assuming for the first time ever that the splitting of the Landau levels, characteristic of the Hofstadter energy spectrum, is not resolved due to thermal broadening. This is an extension of their similar calculation for 1D LSSLs [6] to the case of 2D LSSLs. Their calculations predict that different Fourier components in a 2D LSSL independently contribute to the resistivity and give rise to their own series of COs of amplitude as large as in the ρ_{xx} data of 1D LSSLs.

Several remarkable works are available that show that magnetoresistivities of 2D LSSLs can be influenced by the number of flux quantum passing through a unit cell of the lattice. P. Rotter, M. Suhrke and U. Rössler [66] presented a quantum mechanical calculation of the resistivity of a 2DEG in a strongly modulated two-dimensional periodic potential and a perpendicular magnetic field. The main parameters used are 100 nm period, 5 meV potential amplitude, 4 to 12 meV Fermi energy. They observed two types of structures. One type of structure is most pronounced for 1, 3/2, 2 and 3 magnetic flux quanta per unit cell that does not change position with carrier density or temperature and decreases in amplitude with increasing carrier density. The other is SdH type structure that appeared mainly for magnetic fields above 1.2 T. The latter structure shifts to higher magnetic field with increasing carrier density and disappears at higher temperature. They identified the former type of structure as quantum oscillations and predicted the conditions for an experimental observation. For mobility of about 50 $m^2V^{-1}s^{-1}$, they asked for a lattice period of about 100 nm as the most important requirement. Not too low temperature is said to be required.

R. B. S. Oakeshott and A. MacKinnon [67] presented results for the density of states and band conductivity of strongly modulated LSSLs in a magnetic field. The band conductivity was found to show oscillations periodic in magnetic field with a period of one flux quantum per unit cell of the periodic potential related to Hofstadter's butterfly.

The role of strain in modulating 2DEG was explored in the case of 2D LSSLs as well. J. H. Davies et al. [68] calculated the potential energy induced in a 2DEG by a two-dimensional array of gates on the surface of a heterostructure. They calculated both the deformation and piezoelectric potential energy under a LSSL on arbitrary surface of a cubic III-V semiconductor. The electrostatic field from the gate and the deformation potential are independent of orientation but the piezoelectric potential varies strongly

with direction and is dominant. For example, the potential under a circular gate on a (100) surface varies as $sin2\theta$ where θ is the angle measured from [010]. For (111) surface, the piezoelectric potential is nearly isotropic however.

D. E. Petticrew et al. [69] calculated the deformation and piezoelectric potentials under square and circular gates on common III-V surfaces. The deformation potential was found to be an order of magnitude smaller and it does not break the symmetry. The piezoelectric potential is anisotropic however.

There are two semi-classical models, both of which extended the semi-classical model of C. W. J. Beenakker [5] for 1D LSSLs to the case of 2D LSSLs. R. R. Gerhardts [70] extended the semi-classical approach of Beenakker [5] to include higher harmonics in the potential. He also obtained an analytical expression for the (modulation induced extra) band conductivity tensor for 2D LSSLs as

$$\Delta\sigma_{\mu\nu} = \frac{\tau e^2}{\pi m (\hbar\omega_c)^2} \sum_g q_{\mu\nu} |V_g|^2 [J_0(gR)]^2$$

(2.5)

with $q_{xx} = g_y^2$, $q_{yy} = g_x^2$ and $q_{xy} = -g_x g_y$ for   a   potential   of   the   form

$$V(x,y) = \sum_g V_g \exp(i\vec{g}.\vec{r}) \text{ with } \vec{g} = 2\pi \left[\frac{n_x}{a_x}, \frac{n_y}{a_y} \right] \text{ with } n_x \text{ and } n_y \text{ integers, } a_x \text{ and } a_y \text{ the}$$

principal periods of the potential and $V_{-g} = V_g^*$ i.e. $V(x,y)$ real. For 1D LSSLs he showed that the same result can be obtained quantum mechanically while for 2D LSSLs he left such a proof for another paper [60]. The paper [70] contains examples of the use of the model for 1D LSSLs. As to 2D LSSLs, he noted that if the 2D potential is of the form $V(x,y) = V_x(x) + V_y(y)$ then $\Delta\sigma_{yy}$ is independent of $V_y(y)$ and depends only on $V_x(x)$. This means $V_x(x)$ and $V_y(y)$ independently contribute to $\Delta\sigma_{yy}$ and $\Delta\sigma_{xx}$ respectively. He noted that this cannot account for the suppression of the amplitude of the COs observed in experiments on 2D LSSLs [28]. He tried adding a diagonal Fourier component in the potential to account for the said suppression but with no success. He concluded that the experimentally observed [28] suppression of COs in amplitude in 2D LSSLs by an order of magnitude, which occur when the lateral superlattice potential is changed from one-dimensional to two-dimensional, "cannot be explained by the classical calculation". As elucidated in section 2.3.1, according to the model, different Fourier components in a 2D periodic potential independently contribute to the resistivity and give rise to their own series of COs as large in amplitude as in the ρ_{xx} data of 1D LSSLs. Formally this result is essentially the same as that of a quantum mechanical calculation of F. M. Peeters and P. Vasilopoulos [65].

D. Grant, A. R. Long and J. H. Davies [71] re-examined the way the semi-classical model of C. W. J. Beenakker [5] for 1D LSSLs was extended [70] to the case of 2D LSSLs. They [71] presented simulations and an extremely elegant theory for electron transport in weakly modulated 2D LSSLs. They presented the results of a numerical simulation that they explained by a theory. They showed the following.

(a) Guiding centre drift occurs along the contours of a magnetic field dependent effective potential.

(b) In symmetric 2D LSSLs in which orthogonal Fourier components are equal in amplitude, all guiding centre trajectories will be closed and hence COs will be very weak, if not absent in the limit of $\omega_c \tau >> 1$ where ω_c is the cyclotron frequency and τ is the mean interval between scattering events.

(c) In asymmetric 2D LSSLs, there can be only one direction of guiding centre drift under a given set of conditions, determined by the dominant Fourier component in the potential.

(d) If the conditions are changed by changing gate bias or magnetic field, resulting in change of the dominant Fourier component in the potential, the direction of guiding centre drift will change accordingly, which may change the period of the COs.

(e) In asymmetric 2D LSSLs in which orthogonal Fourier components are unequal in amplitude, there will be large COs reminiscent of those in the ρ_{xx} data of 1D LSSLs for transport along the larger potential only, while there will be no COs for that in the direction of the weaker potential. This will happen even if the weaker potential is comparable in amplitude with the larger potential.

(f) In the presence of a dominant diagonal Fourier component, magnetotransport features in both the "axial" directions will be identical and will contain COs of the period of the diagonal Fourier component.

(g) If the diagonal Fourier component ceases to be dominant, the direction of guiding centre drift will "switch" to the axial direction appropriate for the larger "axial" Fourier component and the period of the COs will change from that of the diagonal to that of the larger axial Fourier component. This is in accord with the point (d) above.

(h) If different Fourier components with different periods are comparable in amplitude, a change of magnetic field will change the dominant Fourier component and hence switching of guiding centre drift direction and consequent change of the period of COs will be observed as a function of magnetic field. This is also in accord with the point (d) above.

The most important premises of the formulation [71] are as follows.

1) Different Fourier components of the potential in a 2D LSSL do not independently contribute to the resistivity.

2) In asymmetric 2D LSSLs, the guiding centre drift can occur in *only* one direction for a given condition determined by the dominant Fourier component in the potential.

The predictions of the guiding centre drift model [71] are in sharp contrast with those of an earlier semi-classical model [70] and a corresponding quantum mechanical calculation [65] based on perturbation theory. It is interesting to note that the predictions of the said quantum mechanical calculation are formally the same as those of the previous semi-classical model [70].

The importance of asymmetry in 2D LSSLs was also pointed out by R. Ketzmerick et al. [72], but from the viewpoint of classical chaos. They presented a theoretical analysis for the magnetotransport in asymmetric 2D LSSLs in which two orthogonal Fourier components are unequal in amplitude. They found the electron transport to occur in the direction of stronger modulation and a localisation in the direction of weaker modulation.

Götz J. O. Schmidt [73] in his study of electron dynamics in (symmetric) two-dimensional (magnetic) periodic potential also found closed guiding centre trajectories. He noted that in the case of electrostatic 2D periodic potential, such pinning of the orbits leads to a reduction of conductivity.

2.3 Contrast between two semi-classical models

Of the two semi-classical models [70, 71] for the magnetotransport of electrons in weakly modulated 2D LSSLs, the former is very plausible and attractive while the latter is very elegant and revolutionary. As will be clear in subsequent chapters in the discussion of the experimental data obtained from weakly modulated 2D LSSLs, data obtained from a wide range of devices agree remarkably well with the latter model while contradict sharply with the former. It is therefore of considerable interest to discuss both the models in some detail before proceeding further.

2.3.1 Some details of the semi-classical model by R. R. Gerhardts [70]

There is a semi-classical model by Gerhardts [70], which is an extension of the guiding centre drift resonance model for 1D LSSLs of Beenakker [5] to 2D LSSLs. The former [70] provides an analytical expression for calculating the magnetoresistances of

2D LSSLs. In view of the success of the latter [5] regarding 1D LSSLs, it is of considerable interest to obtain the magnetoresistances of 2D LSSLs using Gerhardts' model [70] for various physical situations of interest.

For a 2D potential of the form

$$V(x,y) = \sum_g V_g \exp(i\vec{g}.\vec{r}) = \sum_{n_x,n_y} V_{n_x n_y} \exp\{i(g_x x + g_y y)\}$$

(2.6)

where $(g_x, g_y) = 2\pi \left(\dfrac{n_x}{a_x}, \dfrac{n_y}{a_y} \right)$ with n_x and n_y integers and $V_{-g} = V_g^*$ i.e. $V(x,y)$ real, he

obtained an analytical expression for the (modulation induced extra) band conductivity tensor as

$$\Delta\sigma_{\mu\nu} = \frac{\tau e^2}{\pi m (\hbar \omega_c)^2} \sum_g q_{\mu\nu} |V_g|^2 [J_0(gR)]^2$$

(2.7)

with $q_{xx} = g_y^2$, $q_{yy} = g_x^2$ and $q_{xy} = -g_x g_y$ where R is the cyclotron radius at the Fermi energy. Here τ is the scattering time. Thus

$$\Delta\sigma_{xx} = \frac{\tau e^2}{\pi m (\hbar \omega_c)^2} \sum_{n_x,n_y} g_y^2 |V_{n_x n_y}|^2 J_0^2\left(\sqrt{g_x^2 + g_y^2} R \right)$$

(2.8)

$$\Delta\sigma_{yy} = \frac{\tau e^2}{\pi m (\hbar \omega_c)^2} \sum_{n_x,n_y} g_x^2 |V_{n_x n_y}|^2 J_0^2\left(\sqrt{g_x^2 + g_y^2} R \right)$$

(2.9)

and
$$\Delta\sigma_{xy} = -\frac{\tau e^2}{\pi m (\hbar \omega_c)^2} \sum_{n_x,n_y} g_x g_y |V_{n_x n_y}|^2 J_0^2\left(\sqrt{g_x^2 + g_y^2} R \right).$$

(2.10)

For a potential of the form

$$V(x,y) = V_x \cos kx + V_y \cos ky + V_{d1} \cos k(x+y) + V_{d2} \cos k(x-y),$$

(2.11)

where $k = 2\pi/a$, $a_x = a_y = a$, and $(g_x, g_y) = \left(\dfrac{2\pi}{a}, \dfrac{2\pi}{a} \right)$. The first two terms on the right

hand side of Equation (2.11) are the two axial Fourier components which are orthogonal to each other while the last two terms are the two diagonal Fourier components which are also orthogonal to each other. Equation (2.11) can be given the

form of Equation (2.6) as follows to obtain the band conductivity tensors directly from Equation (2.8), (2.9) and (2.10).

$$V(x, y) = \frac{1}{2}V_x\left(e^{ikx} + e^{-ikx}\right) + \frac{1}{2}V_y\left(e^{iky} + e^{-iky}\right)$$

$$+ \frac{1}{2}V_{d1}\left[e^{ik(x+y)} + e^{-ik(x+y)}\right] + \frac{1}{2}V_{d2}\left[e^{ik(x-y)} + e^{-ik(x-y)}\right]$$

$$= V_{10}e^{ikx} + V_{-10}e^{-ikx} + V_{01}e^{iky} + V_{0-1}e^{-iky}$$

$$+ V_{11}e^{ik(x+y)} + V_{-1-1}e^{-ik(x+y)} + V_{1-1}e^{ik(x-y)} + V_{-11}e^{-ik(x-y)}$$

$$\text{(2.12)}$$

where $V_{10} = V_{-10} = \frac{1}{2}V_x$, $V_{01} = V_{0-1} = \frac{1}{2}V_y$, $V_{11} = V_{-1-1} = \frac{1}{2}V_{d1}$, $V_{1-1} = V_{-11} = \frac{1}{2}V_{d2}$.

The table below summarises the various parameters for the terms on the right hand side of Equation (2.12).

Table 2.1
Summary of the values of various parameters related to the terms of Equation (2.12).

Term	g_x	g_y	$\sqrt{g_x^2 + g_y^2}$	$V_{n_x n_y}$
$V_{10}e^{ikx}$	$2\pi/a$	0	$2\pi/a$	$V_{10} = \frac{1}{2}V_x$
$V_{-10}e^{-ikx}$	$-2\pi/a$	0	$2\pi/a$	$V_{-10} = \frac{1}{2}V_x$
$V_{01}e^{iky}$	0	$2\pi/a$	$2\pi/a$	$V_{01} = \frac{1}{2}V_y$
$V_{0-1}e^{-iky}$	0	$-2\pi/a$	$2\pi/a$	$V_{0-1} = \frac{1}{2}V_y$
$V_{11}e^{ik(x+y)}$	$2\pi/a$	$2\pi/a$	$2\pi/(a/\sqrt{2})$	$V_{11} = \frac{1}{2}V_{d1}$
$V_{-1-1}e^{-ik(x+y)}$	$-2\pi/a$	$-2\pi/a$	$2\pi/(a/\sqrt{2})$	$V_{-1-1} = \frac{1}{2}V_{d1}$
$V_{1-1}e^{ik(x-y)}$	$2\pi/a$	$-2\pi/a$	$2\pi/(a/\sqrt{2})$	$V_{1-1} = \frac{1}{2}V_{d2}$
$V_{-11}e^{-ik(x-y)}$	$-2\pi/a$	$2\pi/a$	$2\pi/(a/\sqrt{2})$	$V_{-11} = \frac{1}{2}V_{d2}$

Use of the tabulated values in Equation (2.8), (2.9) and (2.10) leads to the following analytical expressions for various elements of the band conductivity tensor.

$$\Delta\sigma_{xx} = \frac{\tau e^2}{\pi m(\hbar\omega_c)^2}\frac{1}{2}\left(\frac{2\pi}{a}\right)^2\left[V_y^2 J_0^2\left(\frac{2\pi R}{a}\right)+V_{d1}^2 J_0^2\left(\frac{2\pi R}{a/\sqrt{2}}\right)+V_{d2}^2 J_0^2\left(\frac{2\pi R}{a/\sqrt{2}}\right)\right]$$

(2.13)

$$\Delta\sigma_{yy} = \frac{\tau e^2}{\pi m(\hbar\omega_c)^2}\frac{1}{2}\left(\frac{2\pi}{a}\right)^2\left[V_x^2 J_0^2\left(\frac{2\pi R}{a}\right)+V_{d1}^2 J_0^2\left(\frac{2\pi R}{a/\sqrt{2}}\right)+V_{d2}^2 J_0^2\left(\frac{2\pi R}{a/\sqrt{2}}\right)\right]$$

(2.14)

$$\Delta\sigma_{xy} = -\frac{\tau e^2}{\pi m(\hbar\omega_c)^2}\frac{1}{2}\left(\frac{2\pi}{a}\right)^2\left(V_{d1}^2 - V_{d2}^2\right)J_0^2\left(\frac{2\pi R}{a/\sqrt{2}}\right).$$

(2.15)

Also,

$$\Delta\sigma_{yx} = -\Delta\sigma_{xy} = \frac{\tau e^2}{\pi m(\hbar\omega_c)^2}\frac{1}{2}\left(\frac{2\pi}{a}\right)^2\left(V_{d1}^2 - V_{d2}^2\right)J_0^2\left(\frac{2\pi R}{a/\sqrt{2}}\right).$$

(2.16)

One remarkable feature of Equation (2.13) and (2.14) is that $\Delta\sigma_{xx}$ is independent of V_x while $\Delta\sigma_{yy}$ is independent of V_y. This has important consequences as discussed later. The elements of the conductivity tensor are then given by

$$\sigma_{xx} = \frac{\sigma_0}{1+\omega_c^2\tau^2}+\Delta\sigma_{xx}$$

(2.17)

$$\sigma_{yy} = \frac{\sigma_0}{1+\omega_c^2\tau^2}+\Delta\sigma_{yy}$$

(2.18)

$$\sigma_{xy} = -\frac{\sigma_0\omega_c\tau}{1+\omega_c^2\tau^2}+\Delta\sigma_{xy}$$

(2.19)

$$\sigma_{yx} = \frac{\sigma_0\omega_c\tau}{1+\omega_c^2\tau^2}+\Delta\sigma_{yx}$$

(2.20)

with

$$\sigma_0 = \frac{ne^2\tau}{m}.$$

(2.21)

The two important components of the resistivity tensor are

$$\rho_{xx} = \frac{\sigma_{yy}}{\sigma_{xx}\sigma_{yy}-\sigma_{xy}\sigma_{yx}}$$

(2.22)

and

$$\rho_{yy} = \frac{\sigma_{xx}}{\sigma_{xx}\sigma_{yy}-\sigma_{xy}\sigma_{yx}}.$$

(2.23)

First of all, for a one-dimensional lateral surface superlattice $V(x) = V_x \cos kx$, Equation (2.13), (2.14), (2.15) and (2.16) show that only $\Delta\sigma_{yy}$ is non-zero and it is given by

$$\Delta\sigma_{yy} = \frac{\tau e^2}{\pi m(\hbar\omega_c)^2} \frac{1}{2}\left(\frac{2\pi}{a}\right)^2 V_x^2 J_0^2\left(\frac{2\pi R}{a}\right).$$

(2.24)

The resistivities, ρ_{xx} and ρ_{yy}, as a function of magnetic field are shown in the figure below.
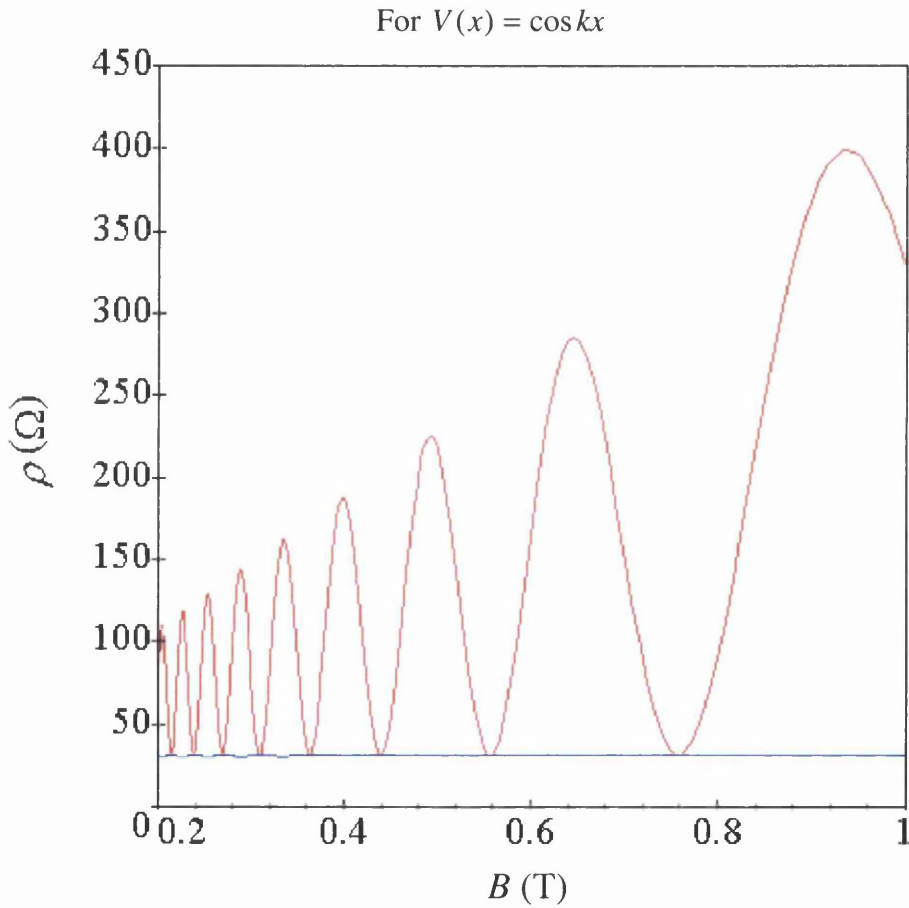
Figure 2.1
The resistivities as a function of magnetic field for 1D LSSLs $V(x) = V_x \cos kx$ calculated using the formulation as above. The red curve is for ρ_{xx} while the blue curve is for ρ_{yy}. The parameters used are carrier density 4×10^{15} m^{-2}, mobility 50 m^{2}V^{-1}s^{-1}, period 100 nm, $V_x = 1$ meV. The Maple worksheet used to produce the curves can be found in section AI.1 of Appendix I.

For a 2D LSSL in which the periodic potential is given by $V(x,y) = V_x \cos kx + V_y \cos ky$, Equation (2.13), (2.14), (2.15) and (2.16) show that only $\Delta\sigma_{xx}$ and $\Delta\sigma_{yy}$ are non-zero and are given by

$$\Delta\sigma_{xx} = \frac{\tau e^2}{\pi m (\hbar\omega_c)^2} \frac{1}{2} \left(\frac{2\pi}{a}\right)^2 V_y^2 J_0^2 \left(\frac{2\pi R}{a}\right)$$

(2.25)

and

$$\Delta\sigma_{yy} = \frac{\tau e^2}{\pi m (\hbar\omega_c)^2} \frac{1}{2} \left(\frac{2\pi}{a}\right)^2 V_x^2 J_0^2 \left(\frac{2\pi R}{a}\right).$$

(2.26)

The most important point to note is that $\Delta\sigma_{xx}$ is independent of V_x while $\Delta\sigma_{yy}$ is independent of V_y. These two contributions to the conductivity along X and Y axis respectively are thus independent of each other. For $V_x = V_y = 1$ meV, the magnetoresistances are as in Figure 2.2 below.

The most important points to note in Figure 2.2 are as follows.

- The COs in both ρ_{xx} and ρ_{yy} data of 2D LSSLs turned out to be as large in amplitude as that of the COs in ρ_{xx} data of 1D LSSLs (see Figure 2.1).

- ρ_{xx} and ρ_{yy} are indistinguishable confirming that V_x and V_y have independently given rise to COs in ρ_{xx} and ρ_{yy} respectively.

The two points contradict with the experimental observation that in symmetric 2D LSSLs in which $V_x = V_y$, the COs in both ρ_{xx} and ρ_{yy} are suppressed in amplitude [28] by about an order of magnitude compared with that of the COs in the ρ_{xx} data of 1D LSSLs realised in similar manner. This important observation that remained as a puzzle for nearly a decade is frequently referred to as "suppression of band conductivity" in the literature.

Further confirmation that in the framework of Gerhardts' model [70] different Fourier components independently contribute to the resistivity comes from Figure 2.3 which shows the magnetoresistances for $V(x,y) = V_x \cos kx + V_y \cos ky$ with $V_x = 1$ meV and $V_y = 0.5$ meV. The most important point to note in Figure 2.3 is that the amplitudes of the COs in ρ_{xx} and ρ_{yy} are in the ratio of the squared amplitudes of the modulations i.e. V_x^2 / V_y^2, i.e. 4:1.

If one of the diagonal Fourier components is dominant, the magnetoresistance characteristics turn out to be as in Figure 2.4. The most important points to note in Figure 2.4 are as follows.

- The magnetoresistance characteristics for transport along both the axial directions of a square lattice are identical.

- The period of the COs is not 100 nm but $100/\sqrt{2}$ nm.

- The amplitude of the COs is as large as in the ρ_{xx} data of a 1D LSSL of potential amplitude 0.25 meV and period $100/\sqrt{2}$ nm.

For $V(x, y) = \cos kx + \cos ky$
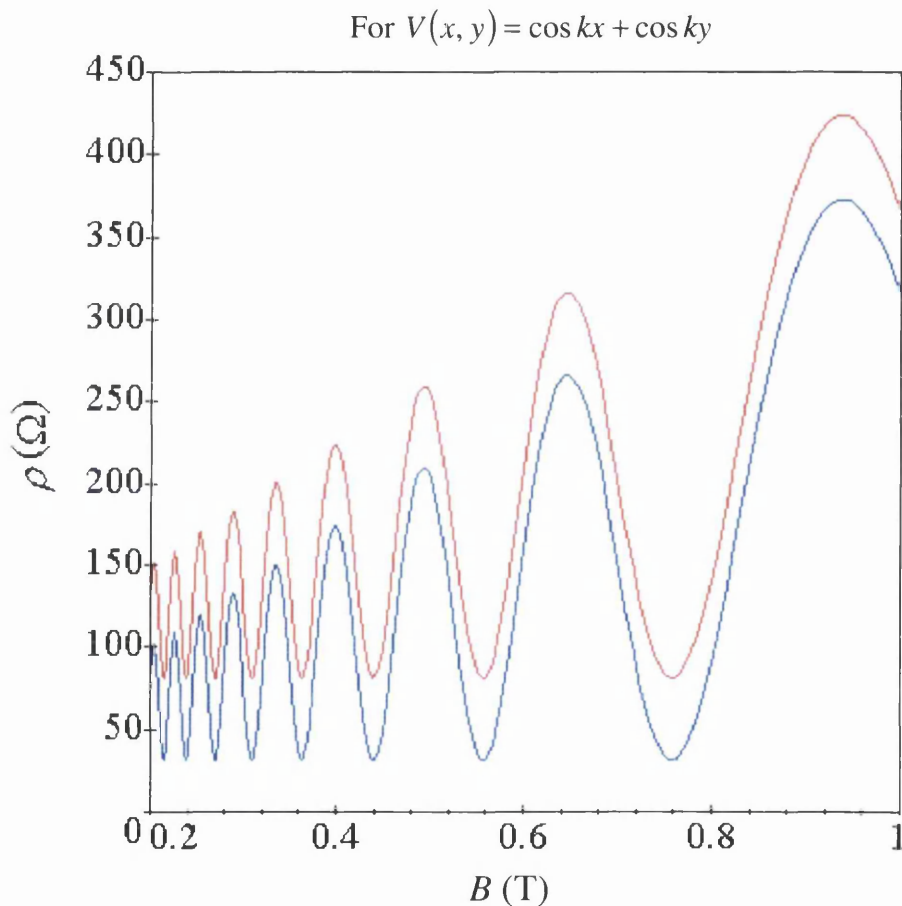
Figure 2.2
The resistivities as a function of magnetic field for 2D LSSLs of the form $V(x, y) = V_x \cos kx + V_y \cos ky + V_{d1} \cos k(x + y) + V_{d2} \cos k(x - y)$, calculated using the formulation as above. The red curve is for ρ_{xx} while the blue curve is for ρ_{yy}. 50 Ω offset has been added to ρ_{xx} to distinguish it from ρ_{yy}. The parameters used are carrier density 4×10^{15} m^{-2}, mobility 50 m^{2}V^{-1}s^{-1}, period 100 nm, $V_x = V_y = 1$ meV, $V_{d1} = V_{d2} = 0$. The Maple worksheet used to produce the curves can be found in section AI.2 of Appendix I.

For $V(x, y) = \cos kx + 0.5\cos ky$
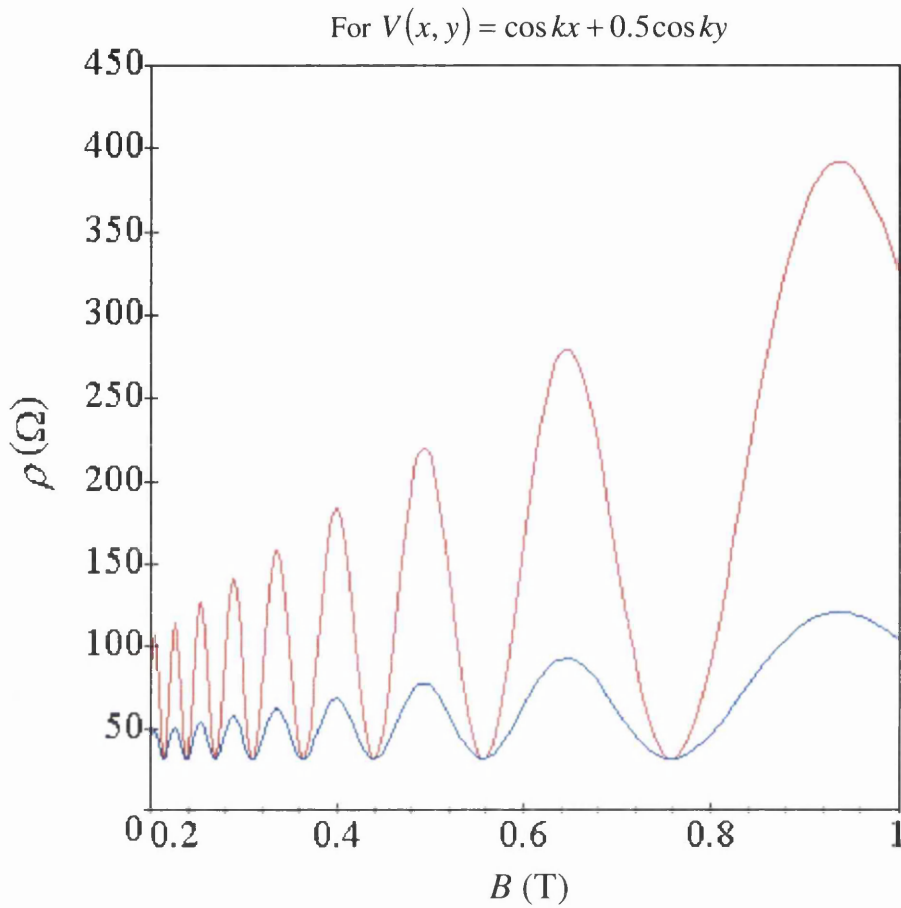
Figure 2.3

The resistivities as a function of magnetic field for 2D LSSLs of the form $V(x, y) = V_x \cos kx + V_y \cos ky + V_{d1} \cos k(x + y) + V_{d2} \cos k(x - y)$, calculated using the formulation as above. The red curve is for ρ_{xx} while the blue curve is for ρ_{yy}. The parameters used are carrier density 4×10^{15} m^{-2}, mobility 50 $m^2V^{-1}s^{-1}$, period 100 nm, $V_x = 1$ meV, $V_y = 0.5$ meV, $V_{d1} = V_{d2} = 0$. The Maple worksheet used to produce the curves can be found in section AI.3 of Appendix I.

For $V(x, y) = 0.25 \cos k(x + y)$
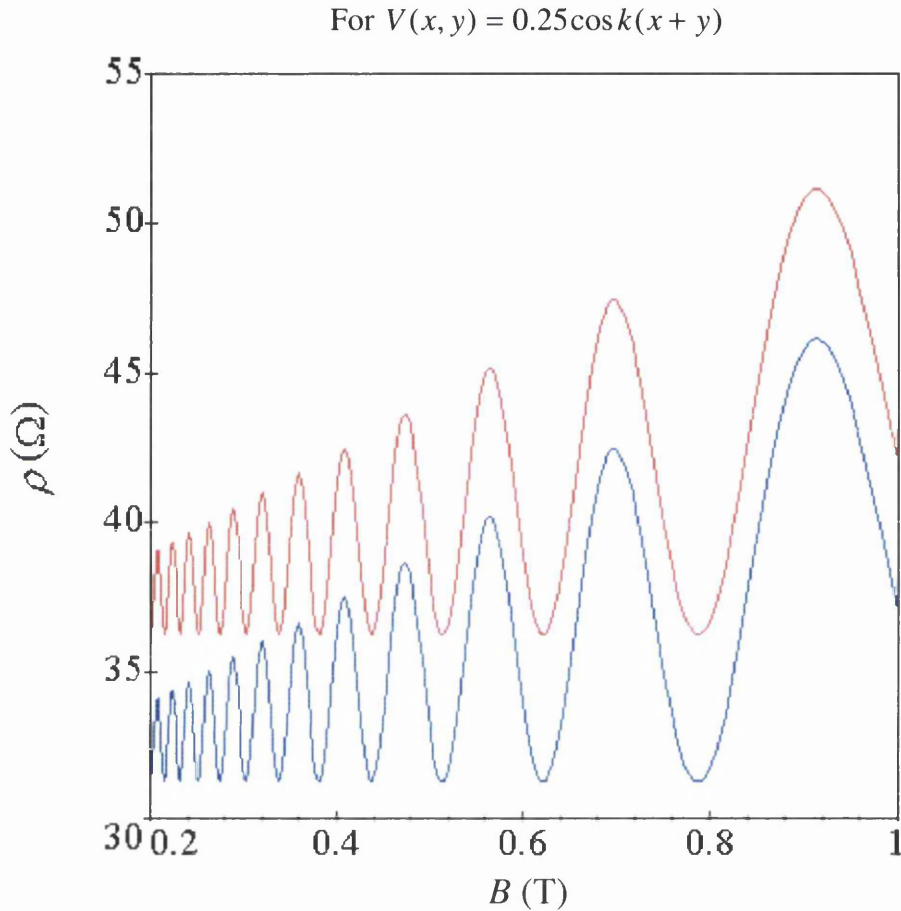
Figure 2.4
Resistivity as a function of magnetic field for 2D LSSLs of the form
$V(x, y) = V_x \cos kx + V_y \cos ky + V_{d1} \cos k(x + y) + V_{d2} \cos k(x - y)$,

calculated using the formulation as above. The red curve is for ρ_{xx} while the blue curve is for ρ_{yy}. 5 Ω offset has been added to ρ_{xx} to distinguish it from ρ_{yy}. The parameters used are carrier density 4×10^{15} m^{-2}, mobility 50 m^{2}V^{-1}s^{-1}, period 100 nm, $V_x = V_y = V_{d2} = 0$ and $V_{d1} = 0.25$ meV. The Maple worksheet used to produce the curves can be found in section AI.4 of Appendix I.

For
$$V(x, y) = 0.3\cos kx + 0.3\cos ky$$
$$+ 0.8\cos k(x + y) + 0.4\cos k(x - y)$$
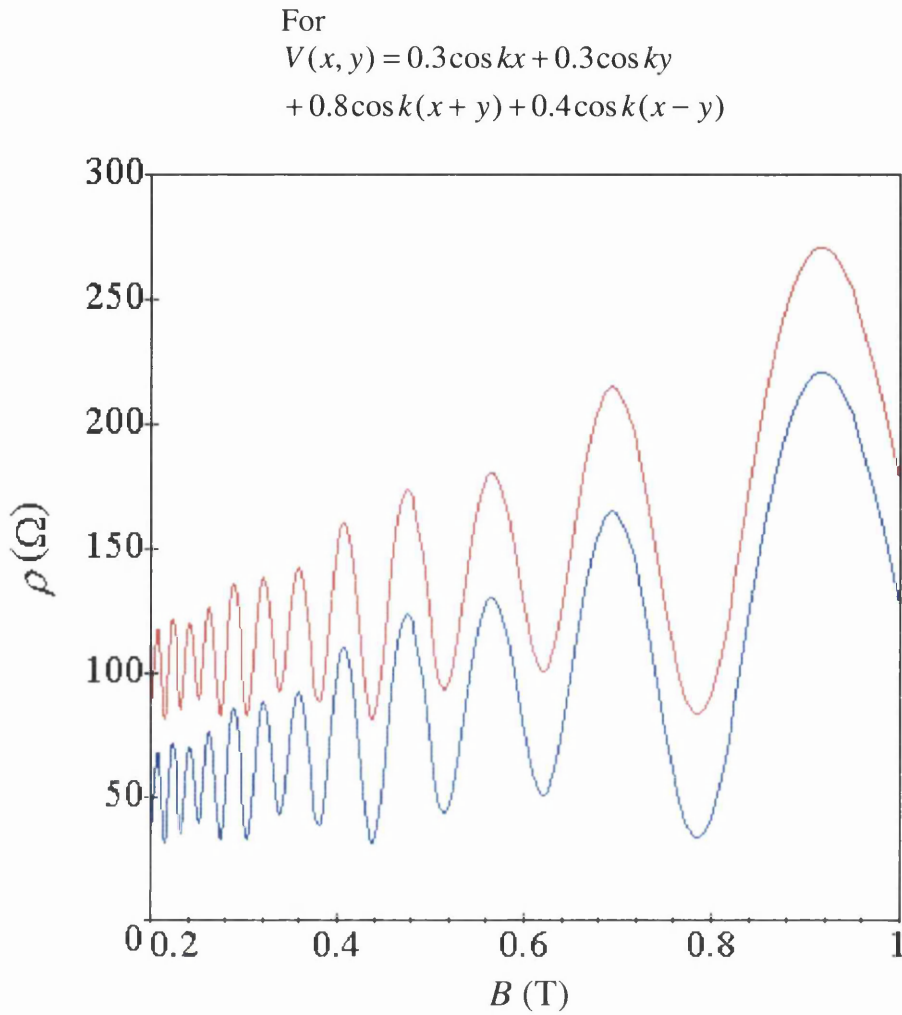
Figure 2.5
The resistivities as a function of magnetic field for 2D LSSLs of the
form $V(x, y) = V_x \cos kx + V_y \cos ky + V_{d1} \cos k(x + y) + V_{d2} \cos k(x - y)$,
calculated using the formulation as above. The red curve is for ρ_{xx} while
the blue curve is for ρ_{yy}. 50 Ω offset has been added to ρ_{xx} to distinguish
it from ρ_{yy}. The parameters used are carrier density 4×10^{15} m^{-2}, mobility
50 m^{2}V^{-1}s^{-1}, period 100 nm, $V_x = V_y = 0.3$ meV, $V_{d1} = 0.8$ meV, $V_{d2} = 0.4$
meV. The Maple worksheet used to produce the curves can be found in
section AI.5 of Appendix I.

One last example showing that within the semi-classical model [70] different
Fourier components in 2D LSSLs independently contribute to resistivity is shown in
Figure 2.5. The most important point to note in Figure 2.5 is that COs of both 100 nm
and $100/\sqrt{2}$ nm periods are present in the magnetoresistances interfering with each
other.

The above extensive studies of the semi-classical model [70] lead to the general conclusion that according to the model each Fourier component in a 2D LSSL independently contributes to the resistivity and gives rise to its own series of COs of amplitude equivalent to that predicted for the ρ_{xx} data of 1D LSSLs.

Before leaving the discussion on the semi-classical model [70], it is important to point out that the formulation [70] contains a conceptual difficulty. The independence of the contributions of different Fourier components in a 2D periodic potential implies the drift of a given guiding centre in different directions at the same time, which does not seem plausible unless the guiding centre drifts in a direction determined by the resultant displacement. The corresponding quantum mechanical formulation [65] predicts the simultaneous presence of current carrying states in different directions, associated with modulation induced extra band conductivity, for different Fourier components in the 2D periodic potential.

2.3.2 Some details of modified guiding centre drift model of Grant, Long and Davies [71]

As already mentioned, a wide range of data obtained in this project from a wide range of devices agrees remarkably well with the modified guiding centre drift model [71]. Moreover, as also already mentioned, the predictions of the model are in sharp contrast with those of a previous semi-classical [70] and a quantum mechanical formulation [65]. It is, therefore, worth digressing for a while to describe the formulation of the model [71] before discussing fabrication of devices, experiments, analysis of data and understanding obtained.

The semi-classical model [71] starts with the result of a simulation the major feature of which is that two orthogonal Fourier components in a 2D LSSL *do not* independently contribute to COs for transport in the two orthogonal directions unlike what is predicted by previous models [65, 70]. The authors [71] found that for a 1D LSSL $V(x) = V_x \sin(2\pi x / a)$ their results agree with the analytical expression of 1D guiding centre drift model [5] with strong COs in the ρ_{xx} data. They also found that introduction of another Fourier component in the orthogonal direction to get a 2D LSSL $V(x, y) = V_x \sin(2\pi x / a) + V_y \sin(2\pi y / a)$ *suppressed* the COs in ρ_{xx} and *did not* introduce any COs in ρ_{yy}.

They explained this revolutionary finding by an extremely elegant model based on the guiding centre drift concept [5]. The idea is that they tracked down the trajectories the guiding centre takes in various possible experimental situations being

imbued with the notion gathered from the studies of 1D LSSLs that in experiments there should be COs for transport in the direction orthogonal to that of the guiding centre drift. In the presence of a periodic potential, an electrostatic field $\vec{E}$ will be introduced by the spatial gradient of the potential. If a magnetic field $\vec{B}$ is applied, the presence of crossed electric and magnetic fields causes the guiding centre (of cyclotron motion) to experience a drift, the "$\vec{E} \times \vec{B}$ drift" well known from plasma physics. The instantaneous velocity $\vec{v}_i$ of the drift is given by

$$\vec{v}_i = \frac{\vec{E}(x,y) \times \vec{B}}{B^2}.$$

(2.27)

If this instantaneous drift velocity is averaged over a perimeter of the cyclotron orbit, using the relation (see Figure 2.6 below) between the co-ordinates of the electron (x,y) and those of the guiding centre (X,Y), for a 2D periodic potential of the form

$$V(x,y) = V_x \cos(2\pi x/a) + V_y \cos(2\pi y/a) + V_{11} \cos[2\pi(x+y)/a] + V_{1-1} \cos[2\pi(x-y)/a]$$

(2.28)

where the first two terms on the right hand side are the two axial Fourier components and the last two terms are the two diagonal Fourier components, one ends up with an average velocity of the guiding centre drift as

$$\vec{v}_{avg} = \frac{\vec{\nabla} V^{\textit{eff}}(X,Y) \times \vec{B}}{B^2}$$

(2.29)

where $V^{\textit{eff}}(X,Y)$ is called "effective potential" and is given by

$$V^{\textit{eff}}(X,Y) = V_x J_0 \left(2\pi R_c /a\right) \cos(2\pi X/a) + V_y J_0 \left(2\pi R_c /a\right) \cos(2\pi Y/a)$$
$$+ V_{11} J_0 [2\pi R_c /(a/\sqrt{2})] \cos[2\pi(X+Y)/a] + V_{1-1} J_0 [2\pi R_c /(a/\sqrt{2})] \cos[2\pi(X-Y)/a]$$

(2.30)

where J_0 is a Bessel function of first kind. The effective potential can be written in the form

$$V^{\textit{eff}}(X,Y) = V_x^{\textit{eff}} \cos(2\pi X/a) + V_y^{\textit{eff}} \cos(2\pi Y/a)$$
$$+ V_{11}^{\textit{eff}} \cos[2\pi(X+Y)/a] + V_{1-1}^{\textit{eff}} \cos[2\pi(X-Y)/a]$$

(2.31)

where $V_x^{\textit{eff}} = V_x J_0 \left(2\pi R_c/a\right)$, $V_y^{\textit{eff}} = V_y J_0 \left(2\pi R_c/a\right)$, $V_{11}^{\textit{eff}} = V_{11} J_0 [2\pi R_c/(a/\sqrt{2})]$ and $V_{1-1}^{\textit{eff}} = V_{1-1} J_0 [2\pi R_c/(a/\sqrt{2})]$.

Notable features of the effective potential are as follows.

- It looks as if it is derived from the actual potential with the amplitude of each Fourier component multiplied by a Bessel function of first kind (J_0).

- The effective potential depends on magnetic field as the Bessel functions involved are magnetic field dependent as these contain the cyclotron radius (which is proportional to $1/B$ where B is the magnetic field).

- The arguments of the Bessel functions associated with diagonal Fourier components are different from those of the axial Fourier components. Notably, whereas the axial Fourier components have a in the arguments of the Bessel functions, those of the diagonal Fourier components of a square lattice of period a have $a/\sqrt{2}$. Thus the dependence of the effective potentials of the axial and diagonal Fourier components on magnetic field are different.
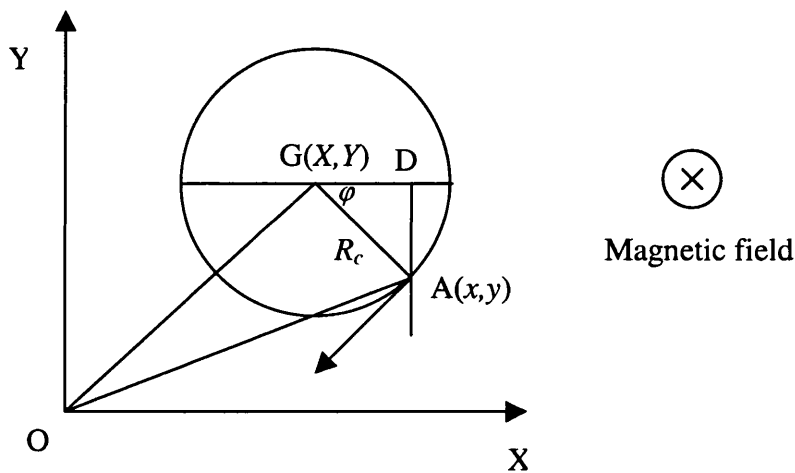
Figure 2.6

A snapshot of an electron executing cyclotron motion in an orbit of radius R_c with a velocity shown by the arrow in a magnetic field directed into the page. A is the instantaneous location of the electron in orbit. (x,y) is a set of co-ordinates for the location of the electron. The guiding centre is located at G. (X,Y) is another set of co-ordinates for the location of the guiding centre. Let us denote $\angle AGD$ as φ. Then it is trivial to obtain the relations between the two sets of co-ordinates as $x = X + R_c \cos\varphi$ and $y = Y - R_c \sin\varphi$.

The most revolutionary idea of the theory can be embodied in the following equation.

$$\vec{v}_{avg} \bullet \vec{\nabla}V^{eff} = 0.$$

(2.32)

This equation can be readily obtained from equation (2.29) with a little manipulation of the triple product. What this dot product means is that guiding centre drift occurs along the direction orthogonal to the gradient of the effective potential. Stated in another way, *the guiding centre drifts along the contours of the effective potential.* The problem of tracking down the trajectories of the guiding centre is thus reduced to plotting the contours of the effective potentials relevant to physical situations in experiments. The characteristics of the COs, notably the period and the strength, can be understood from the trajectories of the guiding centre. Comparison with experiments should indicate the validity of the theory. Trajectories of guiding centre (potential contours) for a few situations of interest in experiments are shown in the following figures.

Figure 2.7 below makes it evident that all the trajectories of guiding centre are closed in the case of *symmetric* 2D LSSLs. As there is no net drift of the guiding centre in any direction, there should be *no COs* at all for magnetotransport in symmetric 2D LSSLs. However, this picture holds strictly for the case of infinite lifetime of carriers, i.e. if $\omega_c\tau \gg 1$ where ω_c is the cyclotron frequency and τ is the mean interval between scattering events. In experimental systems, τ is always finite and hence there may be small drifts of guiding centre even in the case of symmetric 2D LSSLs. Thus in symmetric 2D LSSLs, any COs present should be *weak.* It is important to emphasise that only semi-classical transport is considered here; no quantum mechanical effect is included.

Figure 2.8 shows clearly that besides closed trajectories, there are open bands of trajectories of the guiding centre in *asymmetric* 2D LSSLs. This leads to guiding centre drift for a significant fraction of the total number of carriers. Moreover, it can be gathered from Figure 2.8 (a) and (b) that guiding centre drift occurs *only in the direction orthogonal to the direction of modulation of the dominant Fourier component in the potential.* There is no net drift in any other direction. According to the studies of 1D LSSLs, strong COs are observed for transport in the direction orthogonal to the guiding centre drift direction. Thus in experiments with asymmetric 2D LSSLs (with square lattice), *strong COs* should be observed for transport *in the direction of modulation of the dominant Fourier component only* and there should be *no COs at all* for transport *in the direction of modulation of weaker Fourier components,* in the limit

$\omega_c \tau >> 1$. This means that different Fourier components cannot independently contribute to COs.

Contours of
$$\cos(2\pi X / a) + \cos(2\pi Y / a)$$
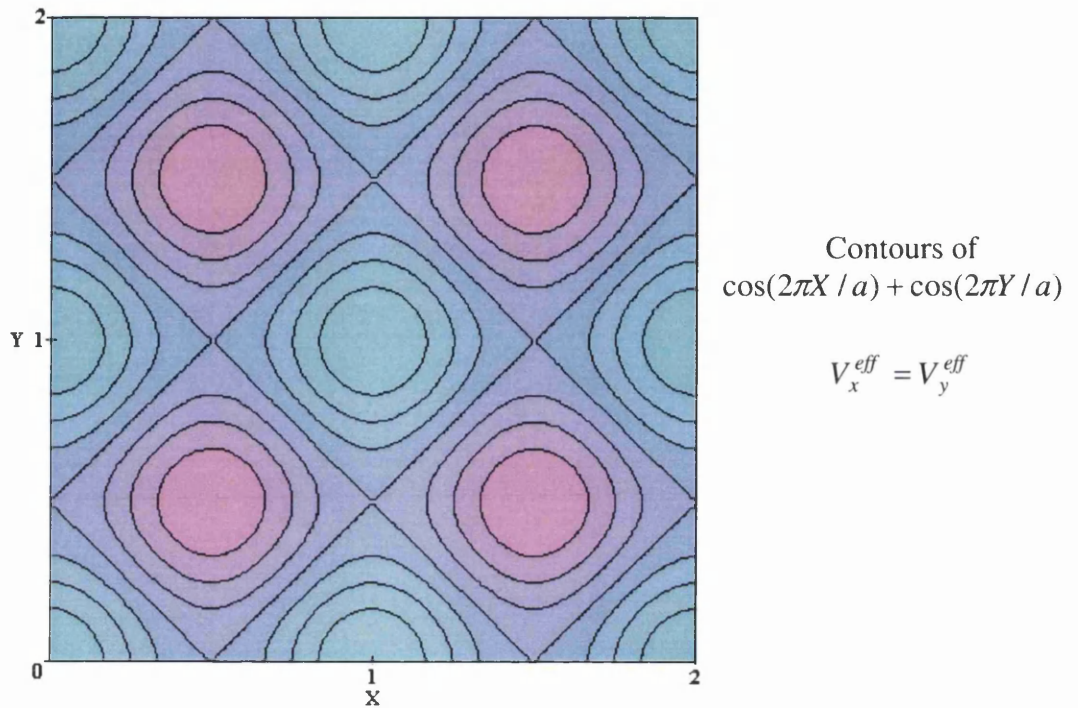
$$V_x^{eff} = V_y^{eff}$$

Figure 2.7
Contours of a *symmetric* 2D periodic effective potential:
$$V^{eff}(X,Y) = V_x^{eff} \cos(2\pi X / a) + V_y^{eff} \cos(2\pi Y / a)$$
$$+ V_{11}^{eff} \cos[2\pi(X + Y)/a] + V_{1-1}^{eff} \cos[2\pi(X - Y)/a]$$
with $V_x^{eff} = V_y^{eff}$, and $V_{11}^{eff} = V_{1-1}^{eff} = 0$ shown over 4 unit cells (2 by 2) of the lattice. The scales along both the axes are in unit of a.
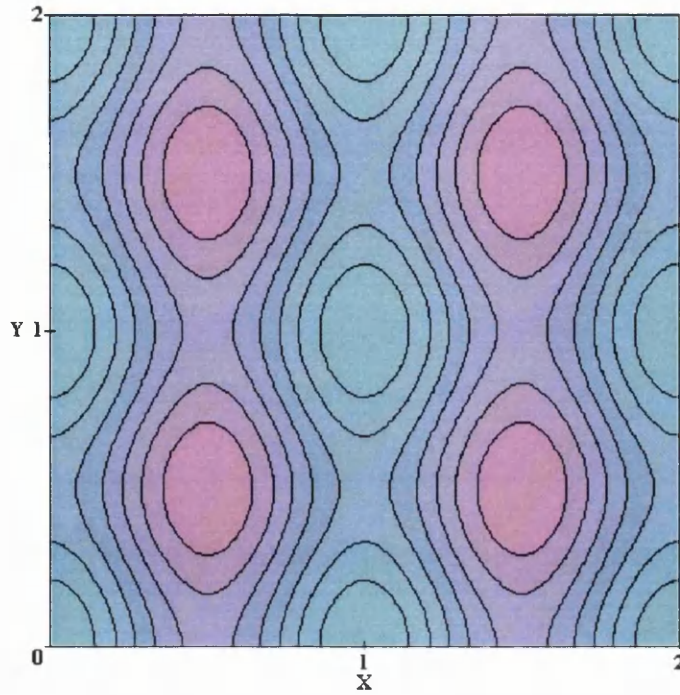
(a)
Contours of
$\cos(2\pi X / a) + 0.5\cos(2\pi Y / a)$

$V_x^{eff} > V_y^{eff}$
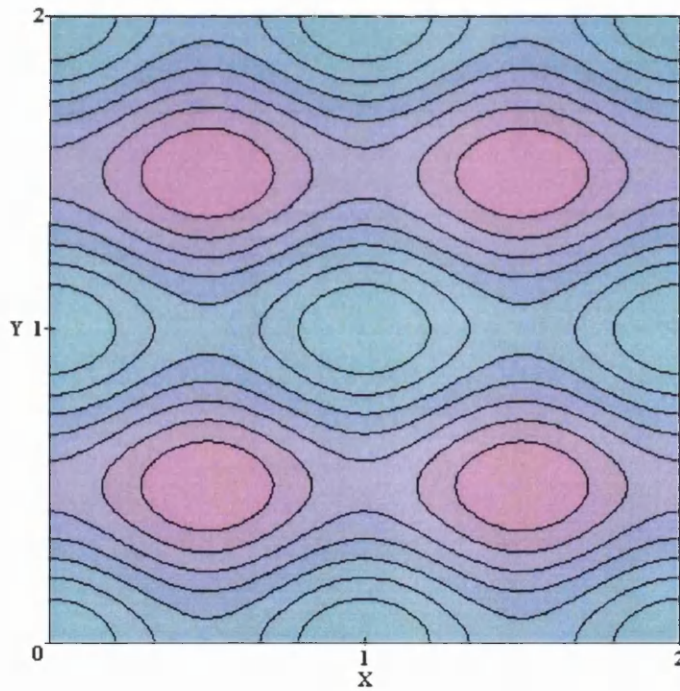
(b)
Contours of
$0.5\cos(2\pi X / a) + \cos(2\pi Y / a)$

$V_x^{eff} < V_y^{eff}$

Figure 2.8
Contours of an asymmetric 2D periodic effective potential:
$$V^{eff}(X,Y) = V_x^{eff}\cos(2\pi X / a) + V_y^{eff}\cos(2\pi Y / a)$$
$$+ V_{11}^{eff}\cos[2\pi(X + Y)/a] + V_{1-1}^{eff}\cos[2\pi(X - Y)/a]$$
with (a) $V_x^{eff} = 2V_y^{eff}$, and $V_{11}^{eff} = V_{1-1}^{eff} = 0$, (b) $2V_x^{eff} = V_y^{eff}$, and
$V_{11}^{eff} = V_{1-1}^{eff} = 0$ shown over 4 unit cells (2 by 2) of the lattice. The scales
along both the axes are in unit of a.

Figure 2.9 below shows the contours of effective potential when one of the diagonal Fourier components is dominant. The open trajectories are found to be along the direction orthogonal to the direction of modulation of the dominant diagonal Fourier component. Figure 2.9 (a) and (b) show emphatically that non-dominant Fourier components, although present, cannot introduce any open trajectories orthogonal to their directions of modulation along which guiding centre could drift. Thus guiding centre drift direction is determined by the dominant Fourier component *only* and hence different Fourier components *cannot* independently contribute to COs. Figure 2.9 also shows that when there is a dominant diagonal Fourier component in a superlattice of square symmetry, the open bands of trajectories of guiding centre run at an angle of 45° to both the axial directions. As the angle is equal with both X and Y axis, the drift contributes equally to ρ_{xx} and ρ_{yy}. The magnetoresistance characteristics should therefore be identical for transport along X and Y directions. In such a case, the period of COs in both ρ_{xx} and ρ_{yy} should be the period of the diagonal Fourier component which is $a/\sqrt{2}$ for a square lattice of period a.

If the diagonal Fourier component ceases to be dominant, the open trajectories of guiding centre no longer run along diagonal directions, as Figure 2.10 below shows. The drift turns to one of the axial directions instead. This is a remarkable phenomenon, which we call "switching" of the direction of guiding centre drift between diagonal and axial directions. This should be observed in experiments by changing gate bias or magnetic field. Switching can occur depending on gate bias if the change in gate bias changes the relative dominance between the diagonal and axial Fourier components. If, however, different Fourier components are nearly equal to each other in amplitude, then a change in magnetic field can change the dominance between the effective potentials associated with the diagonal and axial Fourier components. This is because the dependence of the effective potentials of the axial and diagonal Fourier components on magnetic field are different as discussed before.

One last example showing that different Fourier components in a 2D periodic potential cannot give rise to open guiding centre trajectories simultaneously is shown in Figure 2.11 below. As Figure 2.11 shows, open trajectories develop only in the direction orthogonal to the direction of modulation of the dominant Fourier component in the potential, V_{11}^{eff} in the case shown. The rest of the Fourier components although present are *dummy* in giving rise to guiding centre drift and hence COs according to the semi-classical model.

(a)
Contours of
$\cos(2\pi X / a) + 0.5\cos(2\pi Y / a)$
$+ 1.25\cos[2\pi(X + Y)/a]$
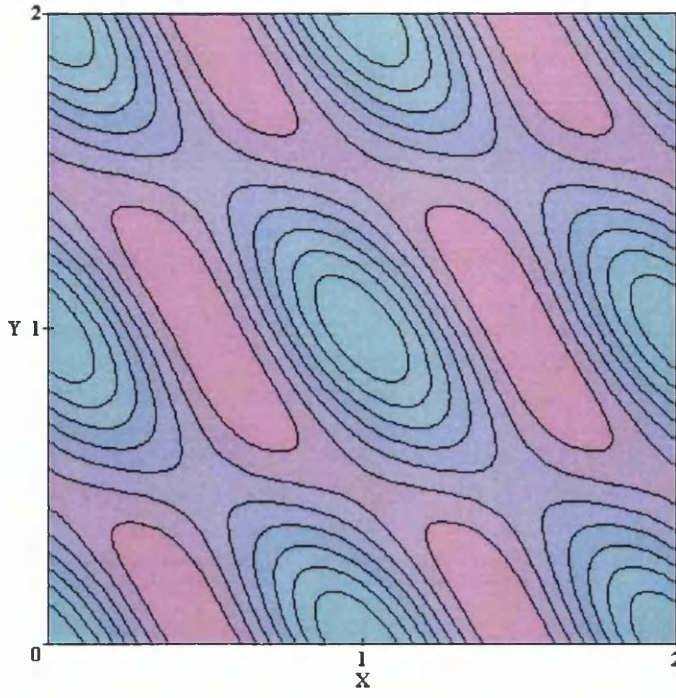
V_{11}^{eff} is dominant

(b)
Contours of
$\cos(2\pi X / a) + 0.5\cos(2\pi Y / a)$
$+ 1.25\cos[2\pi(X - Y)/a]$
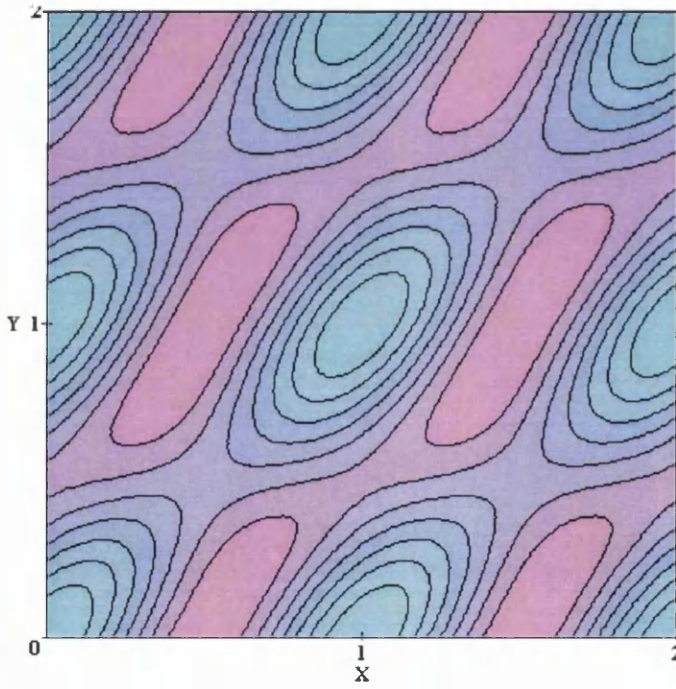
V_{1-1}^{eff} is dominant

Figure 2.9
Contours of an asymmetric 2D periodic effective potential:
$$V^{eff}(X,Y) = V_x^{eff}\cos(2\pi X / a) + V_y^{eff}\cos(2\pi Y / a)$$
$$+ V_{11}^{eff}\cos[2\pi(X + Y)/a] + V_{1-1}^{eff}\cos[2\pi(X - Y)/a]$$
with (a) $V_x^{eff} = 2V_y^{eff}$, $V_{11}^{eff} = 1.25V_x$ and $V_{1-1} = 0$, (b) $V_x^{eff} = 2V_y^{eff}$,
$V_{11}^{eff} = 0$ and $V_{1-1} = 1.25V_x$ shown over 4 unit cells (2 by 2) of the lattice.
The scales along both the axes are in unit of a.

(a)
Contours of
$\cos(2\pi X / a) + 0.5\cos(2\pi Y / a)$
$+ 0.25\cos[2\pi(X + Y)/a]$
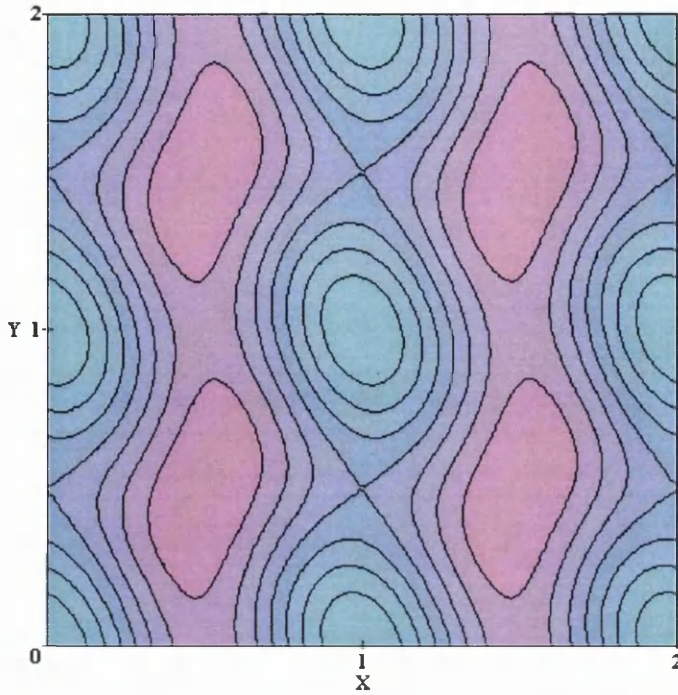
V_{11}^{eff} is NOT dominant
V_x^{eff} is dominant

(b)
Contours of
$\cos(2\pi X / a) + 0.5\cos(2\pi Y / a)$
$+ 0.25\cos[2\pi(X - Y)/a]$
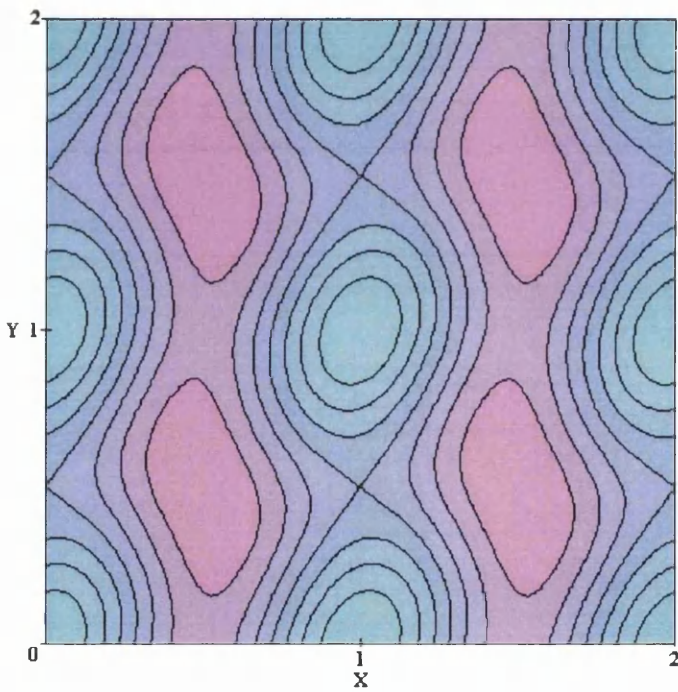
V_{1-1}^{eff} is NOT dominant
V_x^{eff} is dominant

Figure 2.10
Contours of an asymmetric 2D periodic effective potential:
$V^{eff}(X,Y) = V_x^{eff}\cos(2\pi X / a) + V_y^{eff}\cos(2\pi Y / a)$
$+ V_{11}^{eff}\cos[2\pi(X + Y)/a] + V_{1-1}^{eff}\cos[2\pi(X - Y)/a]$
with (a) $V_x^{eff} = 2V_y^{eff}$, $V_{11}^{eff} = 0.25V_x$ and $V_{1-1} = 0$, (b) $V_x^{eff} = 2V_y^{eff}$,
$V_{11}^{eff} = 0$ and $V_{1-1} = 0.25V_x$ shown over 4 unit cells (2 by 2) of the lattice.
The scales along both the axes are in unit of a.

Contours of
$0.3\cos(2\pi X / a) + 0.3\cos(2\pi Y / a)$
$+ 0.8\cos[2\pi(X + Y)/a]$
$+ 0.4\cos[2\pi(X - Y)/a]$

V_{11}^{eff} is dominant
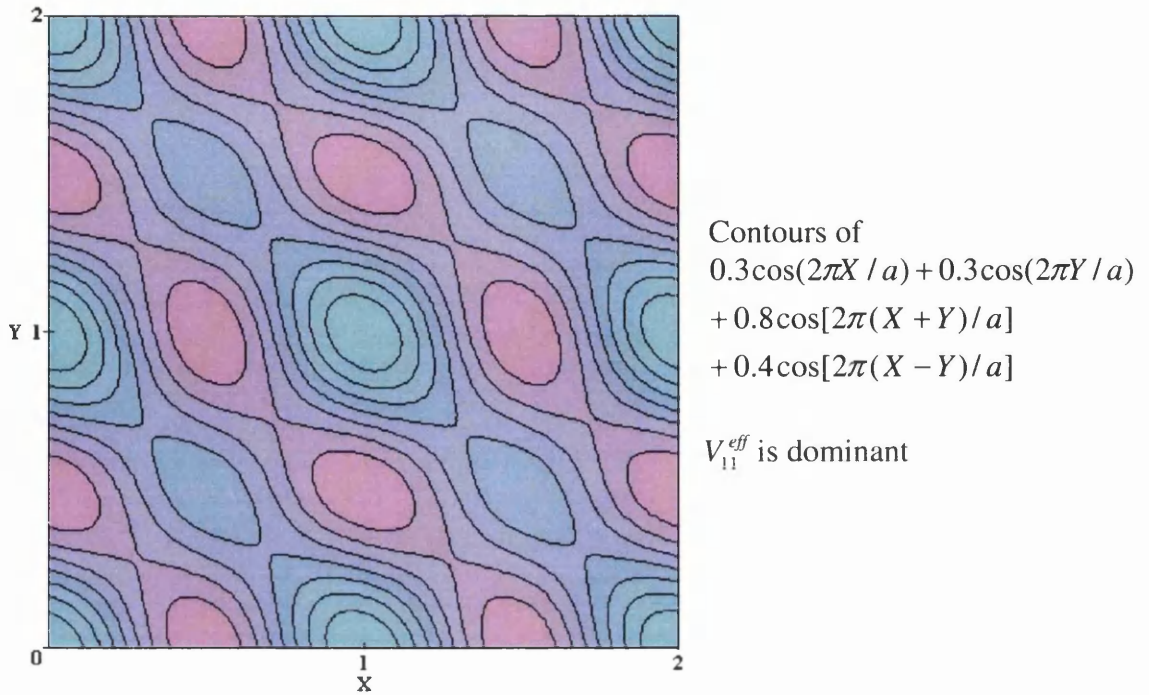
Figure 2.11
Contours of an asymmetric 2D periodic effective potential:
$$V^{eff}(X,Y) = V_x^{eff} \cos(2\pi X / a) + V_y^{eff} \cos(2\pi Y / a)$$
$$+ V_{11}^{eff} \cos[2\pi(X + Y)/a] + V_{1-1}^{eff} \cos[2\pi(X - Y)/a]$$
with $V_x^{eff} = V_y^{eff}$ and $V_{11}^{eff} = 2V_{1-1}^{eff} = (8/3)V_x^{eff}$, shown over 4 unit cells
(2 by 2) of the lattice. The scales along both the axes are in unit of a.

All the examples demonstrate the most important premises of the guiding centre drift model [71] that:

- In asymmetric 2D LSSLs, there can be only one direction of drift of the guiding centre for a given condition determined by the dominant Fourier component in the effective potential and the drift occurs along the direction orthogonal to the direction of modulation of the dominant Fourier component.

- The Fourier components in 2D LSSLs do *not* independently contribute to resistivity.

As noted before, the predictions of the guiding centre drift model [71] are in sharp contrast with those of a previous semi-classical model [70] and a quantum mechanical calculation [65].

2.4 Evaluation of the literature on 2D LSSLs

The survey of literature shows the following notable features.

- There is a range of theories and predictions for magnetotransport features in 2D LSSLs depending on the modulation amplitude relative to the Fermi energy [60, 65, 66, 67, 70, 71].

- The experimental position regarding magnetotransport in weakly modulated 2D LSSLs is less certain compared with that of 1D LSSLs. COs of various phases were observed, particularly in the early days of investigations [28, 30, 31, 32, 33].

- An outstanding question that remained is why COs of 2D LSSLs are generally about an order of magnitude smaller in amplitude than that of the COs in the ρ_{xx} data of 1D LSSLs or suppressed [28]. This has been attributed to resolution of minibands although there is no conclusive experimental evidence that minigaps in Landau levels could ever be resolved above dilution refrigerator temperature or above mK temperature. The magnetotransport data of an experiment on 2D LSSLs that contain features that have been attributed to miniband effects produced one of the largest COs ever observed in 2D LSSLs [36].

- One important puzzle is that COs frequently decrease in amplitude with more negative gate bias [34, 35], which has never been the case in 1D LSSLs.

- There have been assertions that internal structure of Landau levels has been resolved as there have been observations of splitting of peaks of SdH oscillations. Although a few of such splitting could be related to Hofstadter's butterfly, there are splitting which could not be accounted for [40].

- Many observations on weakly modulated 2D LSSLs have been attributed to quantum mechanical effects, namely resolution of minibands, suppression of band conductivity, change of relative dominance between band conductivity and scattering conductivity and so on [28, 34, 36, 38, 39, 40, 41, 42, 63].

- There are two semi-classical models [70, 71] for weakly modulated 2D LSSLs, which have very conflicting predictions. There is a band conductivity calculation [65] the predictions of which are formally the same as those of a semi-classical model [70].

2.5 What remained to be done when the project was started

The above summary of the notable features of the literature makes it clear that the following studies on weakly modulated 2D LSSLs remained to be done.

- To study the transport of electrons in weakly modulated 2D LSSLs with a view to understanding the conduction mechanism involved.

- To settle the conflict in the predictions between the two semi-classical models [70, 71].

- To see how much of the observations can be accounted for in terms of semi-classical model(s) and what remains to be attributed to quantum mechanical effects.

- To understand why COs of 2D LSSLs are generally an order of magnitude smaller in amplitude than that of the COs in the ρ_{xx} data of 1D LSSLs or suppressed.

- To understand why COs of 2D LSSLs decrease in amplitude with more negative gate bias.

- To see if magnetotransport features can be obtained in accord with the predictions of Hofstadter's butterfly.

- To see if any novel phenomenon can be discovered.

2.6 References of Chapter II

[1] For an introduction see for example, D. Weiss, M. L. Roukes, A. Menschig, P. Grambow, K. v. Klitzing and G. Weimann;
Physical Review Letters **66** (1991) 2790

[2] D. Weiss, K. v. Klitzing, K. Ploog, G. Weimann; Europhysics Letters **8** (1989) 179

[3] R. R. Gerhardts, D. weiss and K. v. Klitzing;
Physical Review Letters **62** (1989) 1173

[4] R. W. Winkler, J. P. Kotthaus and K. Ploog;
Physical Review Letters **62** (1989) 1177

[5] C. W. J. Beenakker; Physical Review Letters **62** (1989) 2020

[6] P. Vasilopoulos and F. M. Peeters; Physical Review Letters **63** (1989) 2120

[7] C. Zhang, R. R. Gerhardts; Physical Review B **41** (1990) 12850

[8] R. R. Gerhardts and C. Zhang; Surface Science **229** (1990) 92

[9] P. Vasilopoulos and F. M. Peeters; Surface Science **229** (1990) 96

[10] R. Menne and R. R. Gerhardts; Physical Review B **57** (1998) 1707

[11] P. Streda and A. H. MacDonald; Physical Review B **41** (1990) 11892

[12] P. H. Beton, E. S. Alves, P. C. Main, L. Eaves, M. W. Dellow, M. Henini, O. H. Hughes, S. P. Beaumont and C. D. W. Wilkinson;
Physical Review B **42** (1990) R9229

[13] P. H. Beton, M. W. Dellow, P. C. Main, E. S. Alves, L. Eaves, S. P. Beaumont and C. D. W. Wilkinson; Physical Review B **43** (1991) R9980

[14] P. H. Beton, P. C. Main, M. Davison, M. Dellow, R. P. Taylor, E. S. Alves, L. Eaves, S. P. Beaumont and C. D. W. Wilkinson;
Physical Review B **42** (1990) 9689

[15] R. Cuscó, M. C. Holland, J. H. Davies, I. A. Larkin, E. Skuras, A. R. Long and S. P. Beaumont; Surface Science **305** (1994) 643

[16] R. Cuscó, E. Skuras, S. Vallis, M. C. Holland, A. R. Long, S. P. Beaumont, I. A. Larkin and J. H. Davies; Superlattices and Microstructures **16** (1994) 283

[17] M. Kato, A. Endo and Y. Iye;
Journal of the Physical Society of Japan **66** (1997) 3178

[18] P. D. Ye, D. Weiss, R. R. Gerhardts, K. von Klitzing, K. Eberl, H. Nickel and C. T. Foxon; Semiconductor Science and Technology **10** (1995) 715

[19] E. Skuras, A. R. Long, I. A. Larkin, J. H. Davies and M. C. Holland;
Applied Physics Letters **70** (1997) 871

[20] R. J. Luyken, A. Lorke, A. M. Song, M. Streibl, J. P. Kotthaus, C. Kadow, J. H. English and A. C. Gossard; Applied Physics Letters **73** (1998) 1110

[21] C. J. Emeleus, B. Milton, A. R. Long, J. H. Davies, D. E. Petticrew and M.C. Holland; Applied Physics Letters **73** (1998) 1412

[22] C. J. Emeleus, B. Milton, A. R. Long, J. H. Davies, D. E. Petticrew and M.C. Holland; Superlattices and Microstructures **25** (1999) 39

[23] B. Milton, C. J. Emeleus, K. Lister, J. H. Davies and A. R. Long;
Physica E **6** (2000) 555

[24] Y. Paltiel, D. Mahalu, H. Shtrikman, G. Bunin and U. Meirav;
Semiconductor Science and Technology **12** (1997) 987

[25] J. H. Davies and I. A. Larkin; Physical Review B **49** (1994) 4800

[26] I. A. Larkin, J. H. Davies, A. R. Long and R. Cuscó;
Physical Review B **56** (1997) 15242

[27] A. R. Long, E. Skuras, S. Vallis, R. Cuscó, I. A. Larkin, J. H. Davies and M. C. Holland; Physical Review B **60** (1999) 1964

[28] R. R. Gerhardts, D. Weiss and U. Wulf; Physical Review B **43** (1991) 5192

[29] D. Weiss, K. v. Klitzing, K. Ploog and G. Weimann;
Surface Science **229** (1990) 88

[30] E. S. Alves, P. H. Beton, M. Henini, L. Eaves, P. C. Main, O. H. Hughes, G. A. Toombs, S. P. Beaumont and C. D. W. Wilkinson;
Journal of Physics; Condensed Matter **1** (1989) 8257

[31] H. Fang and P. J. Stiles; Physical Review B **41** (1990) 10171

[32] A. Lorke, J. P. Kotthaus and K. Ploog; Physical Review B **44** (1991) 3447

[33] C. T. Liu, D. C. Tsui, M. Shayegan, K. Ismail, D. A. Antoniadis and H. I. Smith;
Applied Physics Letters **58** (1991) 2945

[34] O. Steffens, T. Schlösser, P. Rotter, K. Ensslin, M. Suhrke, J. P. Kotthaus, U.
Rössler and M. Holland; Journal of Physics: Condensed Matter **10** (1998) 3859

[35] T. Schlösser, K. Ensslin, J. P. Kotthaus and M. Holland;
Semiconductor Science and Technology **11** (1996) 1582

[36] C. Albrecht, J. H. Smet, D. Weiss, K. von Klitzing, R. Hennig, M. Langenbuch,
M. Suhrke, U. Rössler, V. Umansky, H. Schweizer;
Physical Review Letters **83** (1999) 2234

[37] C. Albrecht, J. H. Smet, D. Weiss, K. von Klitzing, V. Umansky, H. Schweizer;
Physica B **249-251** (1998) 914

[38] D. Weiss, A. Menschig, K. von Klitzing and G. Weimann;
Surface Science **263** (1992) 314

[39] T. Schlösser, K. Ensslin, J. P. Kotthaus and M. Holland;
Surface Science **361/362** (1996) 847

[40] T. Schlösser, K. Ensslin, J. P. Kotthaus and M. Holland;
Europhysics Letters **33** (1996) 683

[41] K. Ensslin and T. Schlösser; Physica Scripta **T66** (1996) 135

[42] C. Albrecht, J. H. Smet, K. von Klitzing, D. Weiss, V. Umansky and
H. Schweizer; Physical Review Letters **86** (2001) 147

[43] A. Soibel, U. Meirav, D. Mahalu and H. Shtrikman;
Semiconductor Science and Technology **11** (1996) 1756

[44] E. Paris, J. Ma, A. M. Kriman, D. K. Ferry and E. Barbier;
Journal of Physics; Condensed Matter **3** (1991) 6605

[45] K. Y. Lee, D. P. Kern, K. Ismail, R. J. Haug, T. P. Smith III, W. T. Masselink and
J. M. Hong; Journal of Vacuum Science and Technology B **8** (1990) 1366

[46] C. G. Smith, W. Chen, M. Pepper, H. Ahmed, D. Hasko, D. A. Ritchie, J. E. F.
Frost and G. A. C. Jones;
Journal of Vacuum Science and Technology B **10** (1992) 2904

[47] F. H. Claro and G. H. Wannier; Physical Review B **19** (1979) 6068

[48] R. Schuster, K. Ensslin, J. P. Kotthaus, G. Böhm and W. Klein;
Physical Review B **55** (1997) 2237

[49] D. R. Hofstadter; Physical Review B **14** (1976) 2239

[50] A. H. MacDonald; Physical Review B **28** (1983) 6713

[51] M. A. Andrade Neto and P. A. Schulz; Physical Review B **52** (1995) 14093

[52] H. Silberbauer; Journal of Physics: Condensed Matter **4** (1992) 7355

[53] V. Gudmundsson and R. R. Gerhardts; Physical Review B **52** (1995) 16744

[54] V. Gudmundsson and R. R. Gerhardts; Surface Science **362** (1996) 505

[55] O. Kühn, P. E. Selbmann, V. Fessatidis and H. L. Cui;

Journal of Physics: Condensed Matter **5** (1993) 8225

[56] D. Springsguth, R. Ketzmerick and T. Geisel; Physical Review B **56** (1997) 2036

[57] T. Geisel, R. Ketzmerick and G. Petschel; Physical Review Letters **67** (1991) 3635

[58] R. Fleischmann, T. Geisel, R. Ketzmerick and G. Petschel;

Semiconductor Science and Technology **9** (1994) 1902

[59] R. R. Gerhardts and D. Pfannkuche; Surface Science **263** (1992) 324

[60] D. Pfannkuche and R. R. Gerhardts; Physical Review B **46** (1992) 12606

[61] G. Petschel and T. Geisel; Physical Review Letters **71** (1993) 239

[62] R. R. Gerhardts; Physica Scripta **T39** (1991) 155

[63] Y. Tan; Physical Review B **49** (1994) 1827

[64] A. V. Vagov; Physical Review B **51** (1995) 5065

[65] F. M. Peeters and P. Vasilopoulos; In the Proceedings of the 20th International

Conference on the Physics of Semiconductors (ICPS-20), edited by E. M.

Anastassakis and J. D. Joannopoulos,

(World Scientific, Singapore, 1990); p.1589

[66] P. Rotter, M. Suhrke and U. Rössler; Physical Review B **54** (1996) 4452

[67] R. B. S. Oakeshott and A. MacKinnon;

Journal of Physics; Condensed Matter **6** (1994) 1519

[68] J. H. Davies, D. E. Petticrew and A. R. Long; Physical Review B **58** (1998) 10789

[69] D. E. Petticrew, J. H. Davies, A. R. Long and I. A. Larkin;

Physica B **249-251** (1998) 900

[70] R. R. Gerhardts; Physical Review B **45** (1992) 3449

[71] D. E. Grant, A. R. Long and J. H. Davies; Physical Review B **61** (2000) 13127

[72] R. Ketzmerick, K. Kruse, D. Springsguth and T. Geisel;

Physical Review Letters **84** (2000) 2929

[73] Götz J. O. Schmidt; Physical Review B **47** (1993) R13007

Chapter III: Design of experiments, fabrication of devices and experimental procedure

3.1 Design of the experiments

In view of conflicting predictions of two semi-classical models [1, 2] regarding the magnetoresistance characteristics of weakly modulated 2D LSSLs (in which the potential modulation amplitude is a few percent of the Fermi energy), primary interest turned to setting up of experiments suitable to test these predictions and the design and realisation of appropriate devices.

It was obvious that this requires the following.

- A way to fabricate *asymmetric* 2D LSSLs in which the amplitudes of the Fourier components in orthogonal directions (in the plane of the 2DEG) are unequal.

- Comparison of the magnetoresistances of asymmetric 2D LSSLs with those of *symmetric* 2D LSSLs in which the amplitudes of the modulations in any two orthogonal directions in the plane of the 2DEG are equal.

Although the 2D LSSL with a rectangular pattern stands as a candidate for asymmetric devices, it does not possess a symmetric counterpart. Periodic stress modulation was used [3] to realise different modulation amplitudes in different directions on a substrate in the case of 1D LSSLs, as the stress modulates the 2DEG by the anisotropic piezoelectric effect [4, 3]. Although the effect was first discovered in metal gated 1D LSSLs [4], a patterned strained layer of pseudomorphic $In_{0.2}Ga_{0.8}As$ close to the surface proved very useful in providing strong (potential amplitude about 10% of Fermi energy) and strongly anisotropic modulation in different directions in short period 1D LSSLs [3]. So it became apparent that if the strained layer is introduced close to the surface of heterostructures [3] and patterned with a two-dimensional pattern (even of square symmetry) to realise 2D LSSLs, there will be cases that the Fourier components in orthogonal directions (in the plane of the 2DEG) have different amplitudes. Devices with symmetric modulation can be obtained if the surface of a heterostructure that does not contain the strained layer is patterned with a 2D pattern of square symmetry. This is because there is no distinction between different directions in the plane of the heterojunction of orthodox GaAs-AlGaAs heterostructures (apart from any intrinsic, small mobility anisotropy). But a small amount of stress is introduced in these otherwise unstressed devices when these are gated, resulting in a small asymmetry in the potential landscape.

Two different types of semiconductor heterostructures containing high mobility two-dimensional electron gases (2DEG) and grown by molecular beam epitaxy (MBE) were used. One was an orthodox GaAs-$Al_{0.3}Ga_{0.7}As$ heterostructure and the other was identical except for a pseudomorphic strained 6 nm thick layer of $In_{0.2}Ga_{0.8}As$ introduced from 10 nm below the surface. The GaAs cap in the strained heterostructures was reduced in thickness by 6 nm to make the depth of the 2DEG identical in both the stressed and the unstressed heterostructures.

10 nm GaAs cap

6 nm $In_{0.2}Ga_{0.8}As$ stressor

2 nm GaAs

3 nm $Al_{0.3}Ga_{0.7}As$

2 nm GaAs

10 nm $Al_{0.3}Ga_{0.7}As$

Si delta doping

20 nm $Al_{0.3}Ga_{0.7}As$ spacer

two-dimensional electron gas (2DEG)

GaAs substrate
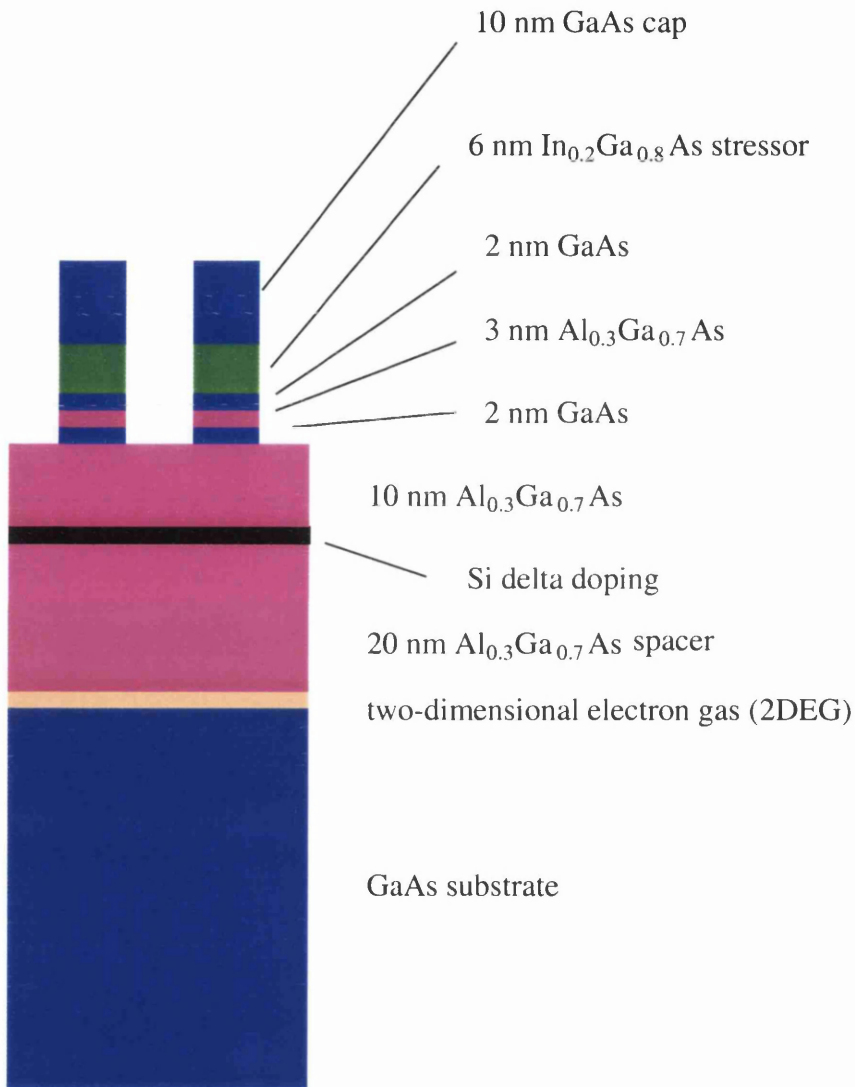
Figure 3.1
A schematic diagram of the layer structure of the *stressed* heterostructure grown by MBE. There is a 6 nm thick, strained layer of $In_{0.2}Ga_{0.8}As$ near the surface. The etch depth used to realise the surface pattern is indicated. After patterning the strained layer, periodic stress modulation is produced at the 2DEG. We call the devices fabricated using this heterostructure *stressed* devices.
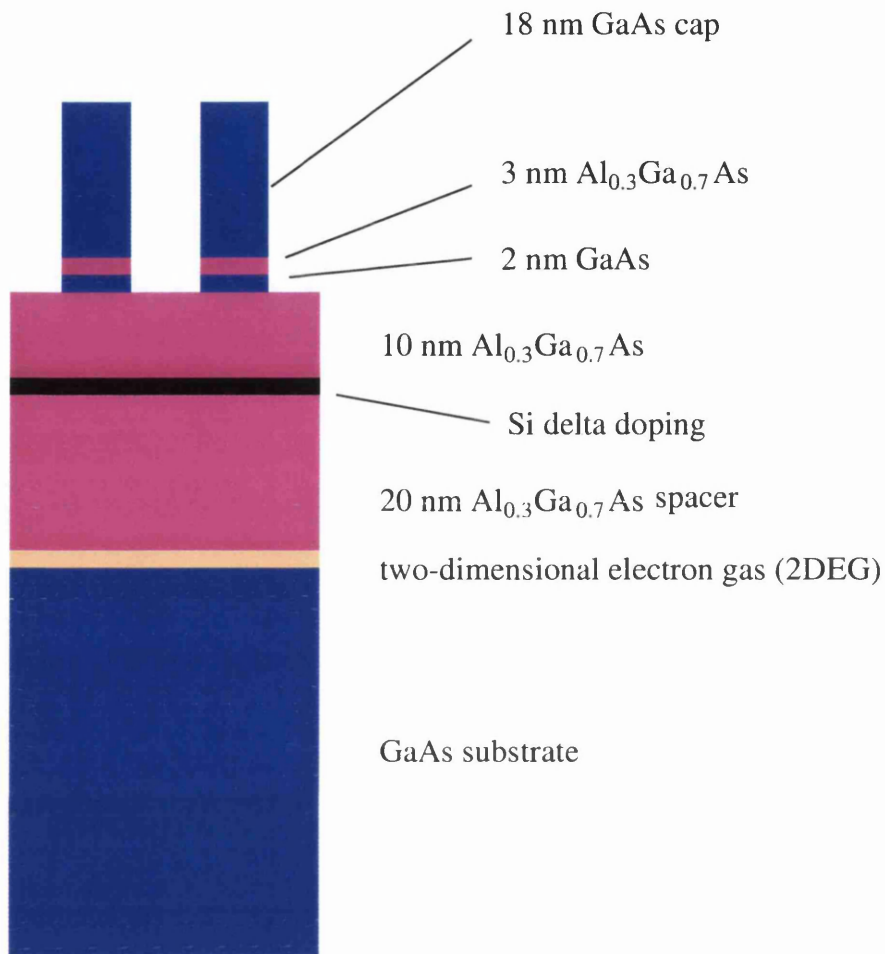
Figure 3.2
A schematic diagram of the layer structure of the *unstressed*
heterostructure grown by MBE. There is GaAs in place of InGaAs near
the surface. The etch depth used to realise surface pattern is indicated.
Essentially symmetric modulation at the 2DEG is realised if the surface
is patterned with square symmetry. We call the devices realised using
this heterostructure *unstressed* devices.

Figure 3.1 and Figure 3.2 above show schematic diagrams of the layer
structures of both types of heterostructures. In each case, the spacer is 20 nm thick and
the heterojunction containing the 2DEG is 53 nm below the unpatterned surface. The
heterostructures were grown on (100) GaAs wafers. The layer of $In_{0.2}Ga_{0.8}As$ is
strained in that its lattice constant differs by 7.2% from that of the underlying GaAs or

AlGaAs. As the substrate is very thick, the laminar layer of $In_{0.2}Ga_{0.8}As$ adjusts its lattice constant to fit with the substrate and hence elastic energy builds up in the direction of growth and the layer puts stress on the underlying material. The layer being very thin, the elastic energy remains smaller than what is required to generate dislocations and subsequent degradation of the quality of the heterostructure as discussed in section 1.1.

After patterning the heterostructure surface, there arise two sources of modulation at the 2DEG:

- surface effect

- piezoelectric effect.

Periodic removal of material from the surface brings the surface states closer to the 2DEG, and brings about periodic modulation at the 2DEG. This is the only source of modulation in the case of patterned unstressed heterostructures. This is called "surface effect" [3]. In the patterned stressed heterostructures, besides the surface effect, there is periodic stress modulation [3] along [011] and [01$\bar{1}$] directions due to the piezoelectric effect, while there is no such modulations along [010] and [001]. The stress modulations along [011] and [01$\bar{1}$] are equal in magnitude but opposite in sign [4]. The surface effect has the same sign in all directions and for a square lattice, it is equal in magnitude in any two given orthogonal directions in the plane of the 2DEG, which makes the potential landscape of the unstressed heterostructures patterned with square symmetry *symmetric*. In patterned stressed heterostructures, of [011] and [01$\bar{1}$], the two contributions to modulation add to each other in one direction and partially cancel each other in the other. Thus the two orthogonal Fourier components along [011] and [01$\bar{1}$] become unequal in amplitude and the potential landscape becomes *asymmetric*. There is however no asymmetry between the modulations in [010] and [001] directions, as the modulations in these two directions are due to surface effects only and these are orthogonal directions. Change in the gate bias changes only the surface component of the potential but leaves the stress component almost unchanged (apart from any change in screening effect) as it is due to bound charge density. As such the degree of asymmetry between the modulations in the [011] and [01$\bar{1}$] directions can be changed by changing the gate bias. If the lattice constants of a square lattice are aligned along [010] and [001], then the two diagonal Fourier components are aligned along the piezoelectric directions [011] and [01$\bar{1}$]. As such the stress contributions to the two diagonal Fourier components are equal in magnitude but opposite in sign. As the

surface contribution adds in, the two diagonal Fourier components become unequal in amplitude. As such the potential landscape becomes asymmetric. Change in gate bias can again be used to change the degree of asymmetry between the two diagonal Fourier components. There is, however, no asymmetry between the two axial directions [010] and [001] in this case.

Thus we can say that if square lattices are realised on stressed heterostructures keeping the lattice constant aligned along [010], [011], [001] and [01$\bar{1}$] directions in four different instances, then

- in the case of [011] and [01$\bar{1}$], the asymmetry will be between the two axial Fourier components i.e. those along the principal lattice directions,

- in the case of [010] and [001] the asymmetry will be between the two diagonal Fourier components,

- gate voltage can be used to change the degree of asymmetry in each case.

Unstressed heterostructures patterned in the same way provide symmetric potential landscape in each case.

Thus this design of experiments is ideal to test the predictions of the two semi-classical models [1, 2]. Both stressed and unstressed 2D LSSLs with rectangular patterns provide asymmetric potential landscapes as well, as will be discussed in the next two chapters.

3.2 Fabrication of devices

The fabrication of working devices involves a number of steps. These are described in the following sections. The main steps are

- fabrication of Hall bars,

- realisation of the resist pattern for superlattices on the surface of the Hall bars,

- pattern transfer by reproducible shallow etching,

- removal of the resist,

- evaporating metal to realise gates.

3.2.1 Fabrication of Hall bars

The first few stages of fabrication are aimed at producing Hall bars from the heterostructure materials containing a 2DEG. The process of realising Hall bars of the heterostructures involves, both in principle and in practice, physical removal of the heterostructure material from the so-called isolation areas (see Figure 3.3 and Figure 3.4 below) that are outside the Hall bar shaped areas at the surface of the

heterostructures. The removal must be up to little greater a depth than that of the 2DEG. This leaves 2DEG in areas of Hall bar shape for conduction to take place. This is done as follows.

- The isolation areas are exposed in a bi-layer of resist coating heterostructure surface by electron beam lithography to be left with Hall bar shaped areas covered by the bi-layer of resist on the surface of the heterostructures (see Figure 3.3 and Figure 3.4).

- The removal of the material from the isolation areas is done by etching using ammonium hydroxide, hydrogen peroxide and water mixture in the volume ratio 1:0.7:100 with 1% wetting agent (details below) added to the mixture. The wetting agent helps in diminishing the surface tension of the solution. The etchant thereby becomes able to smoothly reach the fine edges of the Hall bar shaped resist pattern. Thus Hall bars with very sharp or distinct edges are realised.

- The etching also electrically isolates different Hall bars and the two ohmic pads to be used for application of gate bias from each Hall bar (see Figure 3.3 and Figure 3.4). These are achieved as the Hall bar shaped areas are designed to accompany the required exposed areas round each Hall bar (see Figure 3.3 and Figure 3.4). The isolation etching removes material from these exposed areas as well thereby electrically isolating each Hall bar and the ohmics used for applying gate bias.

- After etching, the resist is removed in acetone and Hall bars of the heterostructures are realised.

One other crucial thing is that ohmic contacts with the 2DEG at the end of each arm of the Hall bars are established for passing current through the Hall bars and measuring voltage across the desired pair of arms. This is often done before realising the Hall bars. The procedure is to expose the required areas (see Figure 3.3 and Figure 3.4), at the end of the arms of each (would be) Hall bar, in a bi-layer of resist coating the surface of heterostructures by electron beam lithography and evaporate suitable layers of metals followed by lift-off. The metal is then diffused through the semiconductor to contact the 2DEG. Rapid thermal annealing is necessary to do this because there is GaAs at the heterostructure surface. GaAs contains a high density of surface states and hence the Fermi level at the surface of the heterostructure is pinned in the middle of the energy gap which is 0.7 meV below the conduction band edge at the surface. This potential acts as a Schottky barrier. This is why annealing of the metal is essential to establish ohmic contact with the 2DEG. As the isolation areas do not cover the areas on the ohmics, the isolation etching cannot remove the heterostructure

material under the ohmic pads. Hence 2DEG remains under ohmic pads, in continuous contact with the 2DEG in the Hall bar.

100 μm

For isolation

For ohmics

For gate

The two ohmics that are connected to the gate
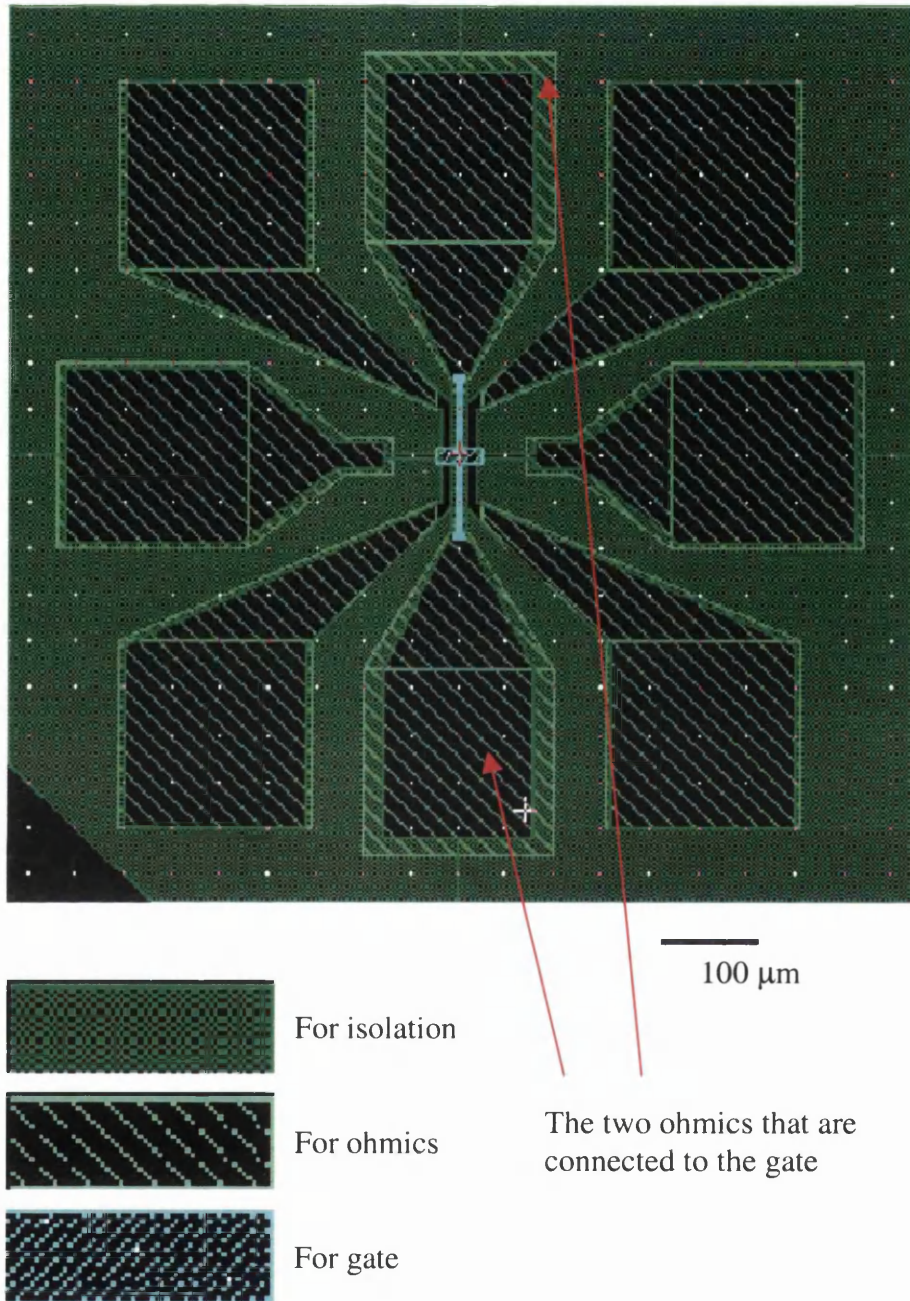
Figure 3.3
The design used in electron beam lithography for realising a Hall bar showing the areas of exposure in resist coating the surface of heterostructure material for isolation etching, evaporating metal to get ohmics and gate. The isolation area surrounds the Hall bar and the ohmics; thus isolation etching isolates each Hall bar from the rest of the Hall bars and leaves 2DEG under the Hall bars and ohmics only. The two ohmics indicated by arrows are isolated from the Hall bar and connected to the gate. These two ohmics are used for application of gate bias.

50 μm
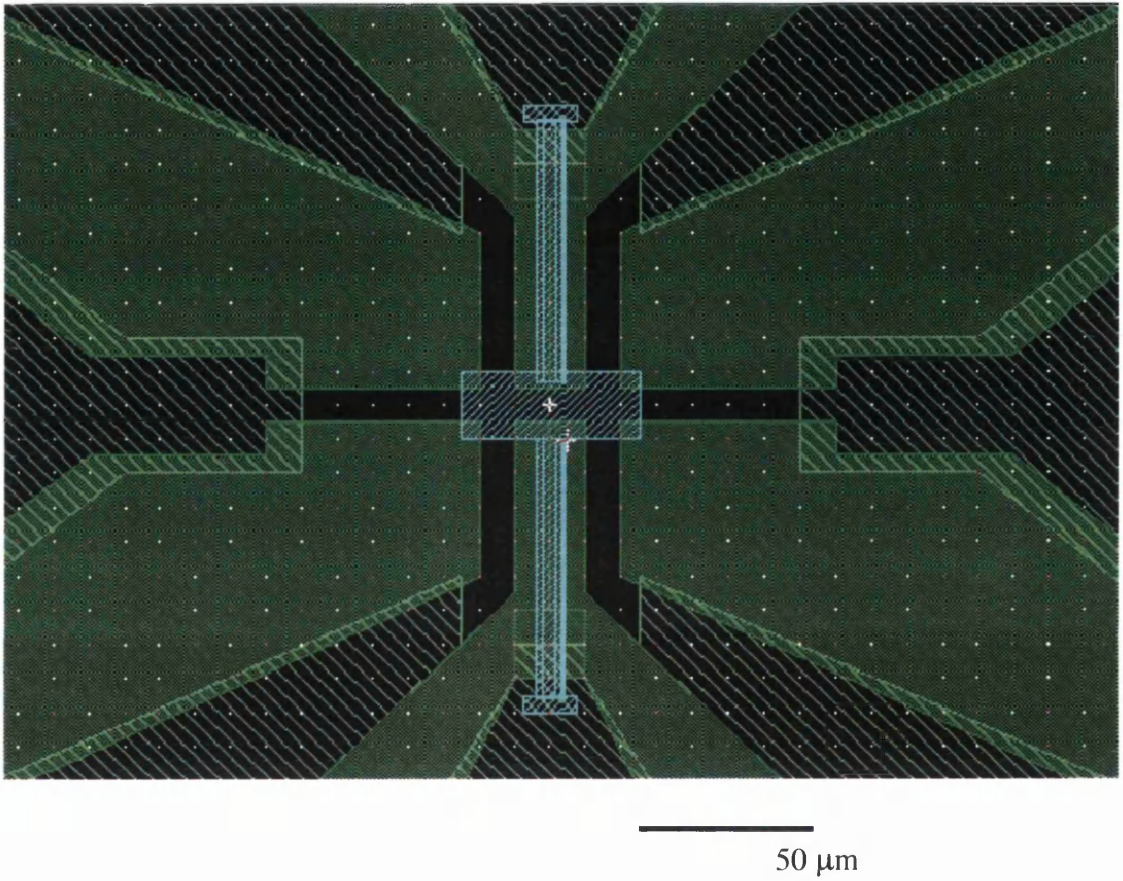
Figure 3.4
A zoomed in view of the preceding design of the Hall bar. The specifications are the same as in Figure 3.3.

Hall bars of dimension 10 μm wide with the voltage contacts 30 μm apart were fabricated as shown in Figure 3.5 below. Therefore the geometric length / width factor of the Hall bars is 3.
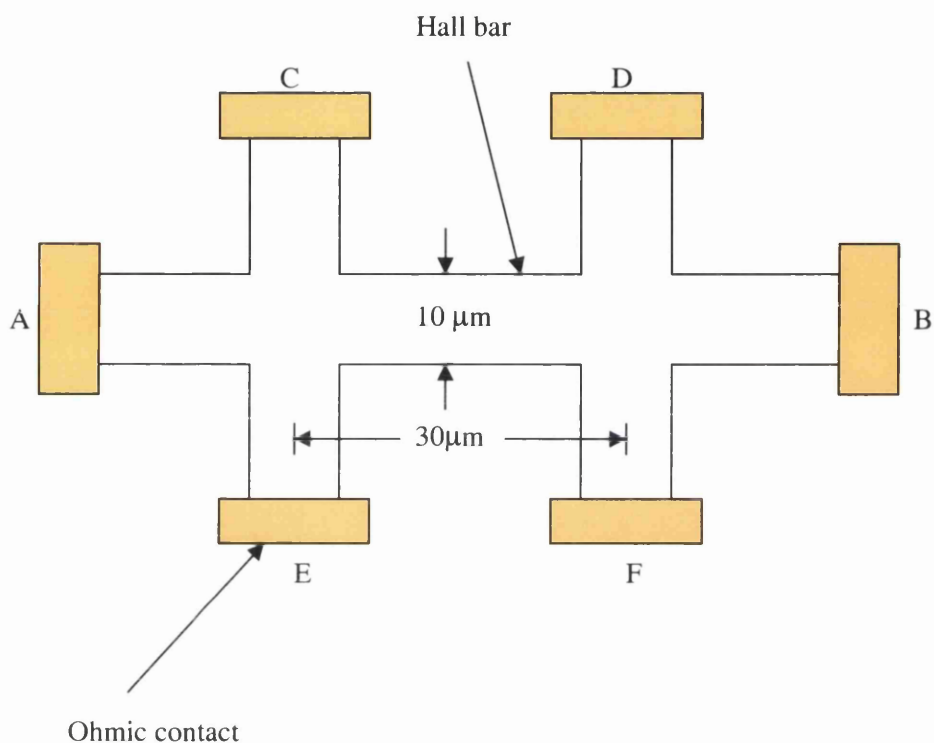
Figure 3.5
Schematic diagram of a Hall bar showing the critical dimensions and ohmic contacts. A and B are source and drain contacts for passing current while C, D, E, F are the voltage contacts. Voltages measured across C and D or E and F give longitudinal voltages while those measured across C and E or D and F give Hall voltages. The longitudinal and Hall voltages divided by the said current give longitudinal and Hall resistances respectively. Resistances divided by the geometric factor of 3 give resistivities.
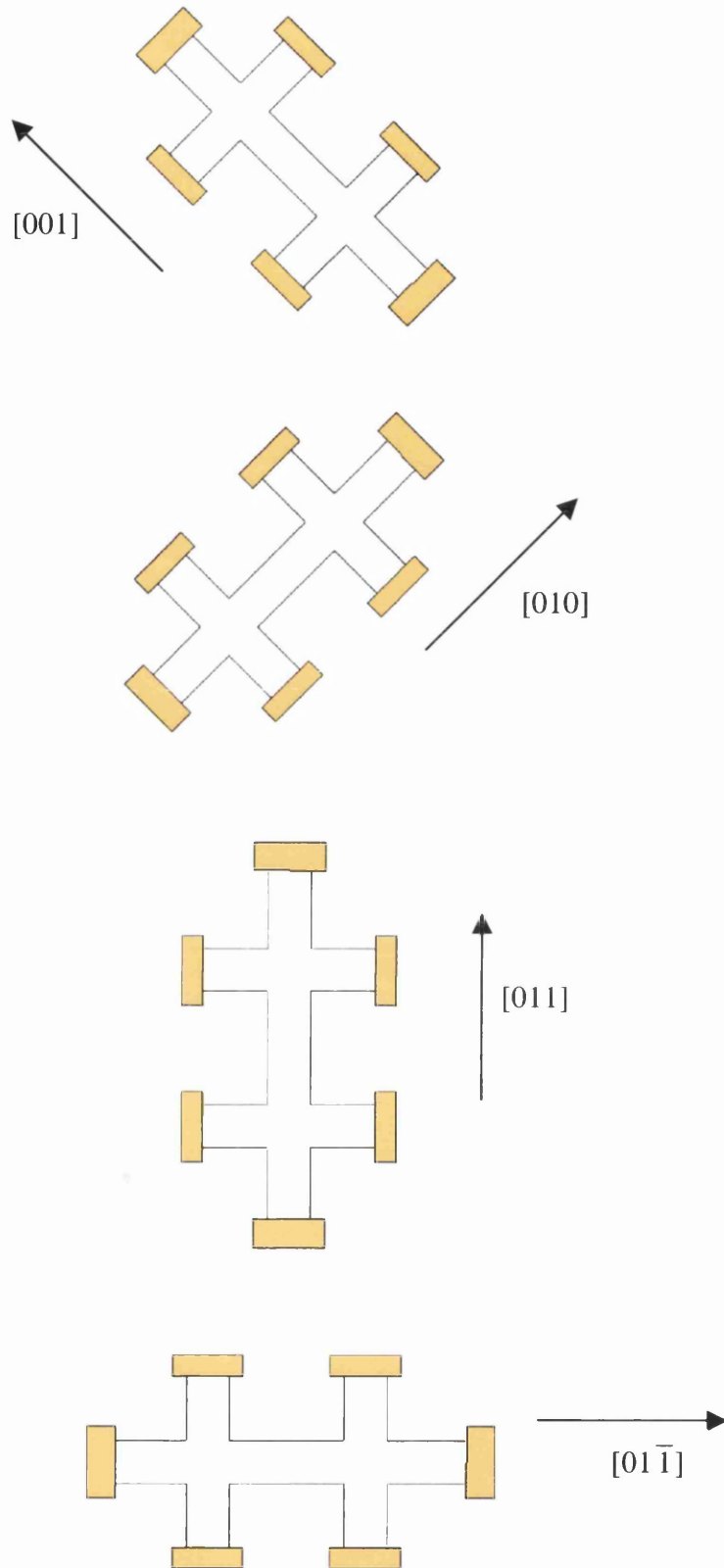
Figure 3.6
Schematic diagram of the arrangement of a group of four Hall bars oriented in different directions (as indicated) on the (100) GaAs substrate.

As transport is intended to be studied in different directions in which the amplitudes of potential modulation to be realised are different, Hall bars were fabricated in groups of four, the length of which were oriented along different directions on the (100) substrate, namely, [010], [011], [001] and [01$\bar{1}$]. Figure 3.6 shows the arrangement of a group of four Hall bars. As can be seen in Figure 3.6, the Hall bars oriented along orthogonal directions are designed to be nearest neighbours of each other so that cleaving can be done to get such a pair of Hall bars on a given chip. This is because the number of contacts on the standard chip carrier is limited to 18 and hence at best two Hall bars can be accommodated in a given experiment. As will be understood from the description of data in later chapters, transport in a given set of orthogonal directions needs to be compared. Hence the pairs of Hall bars aligned along [01$\bar{1}$] and [011] or [010], [001] are placed next to each other.

3.2.2 Realisation of resist pattern for 2D LSSLs

The next stage of fabrication is the production of the superlattices. This involves defining a regular 2D pattern at the surface of the Hall bars by shallow etching. As already mentioned, the strained layer of InGaAs has to be patterned to get stressed devices. Hence etching is necessary. Unstressed devices were required for comparison with the stressed ones, and hence etching had to be used for realising unstressed devices as well.

To define an etched pattern at the surface of the Hall bars, a resist pattern as etch mask must be defined at the surface of the Hall bars first. This is done by high resolution electron beam lithography. A resist coating is spun at the surface of the Hall bars first. After baking the coated resist for about three hours at 180°C, a 2D pattern is written by exposure to electron beam. The latent image thereby obtained is developed by selectively removing the resist from the exposed areas. This is done by using a standard chemical, the developer, for a set time at 23°C. The developer brings out the latent pattern based on the solubility difference created by the exposure between the exposed and unexposed areas of the resist coating. As the appearance, quality and the aspect ratio of the developed pattern depends on the dose of electron beam used, a dose test is performed before writing the pattern on Hall bars. The dose test involves producing on a plain heterostructure surface, the resist pattern of the same area as on Hall bars for a range of doses. Then the pattern is inspected using a scanning electron microscope (SEM) to determine a dose in the middle of the dose range that resulted in the best quality pattern. The choice of the dose to lie in the middle of the dose range

that gives good pattern guarantees the most efficient utilization of the available process latitude. The pattern is written on the Hall bars using the said dose and developed under exactly the same conditions as used in developing the dose test pattern.

As it is of great interest to observe quantum mechanical effects, very short period (around 100 nm) patterns were necessary for the superlattices. The resist patterns realised on the Hall bars in this project were:

- 50 nm diameter pillars in a square grid of 100 nm period,
- 50 nm diameter holes in a square grid of 100 nm period,
- 50 nm diameter holes in a rectangular grid of 100 nm by 130 nm period,
- 50 nm diameter holes in a rectangular grid of 100 nm by 170 nm period,
- 40 nm diameter holes in a square grid of 80 nm period.

The figures below show representative SEM images of the resist patterns obtained on Hall bars for different types of lattices. Note that the scale marker refers only to the horizontal direction. Because of the way the line scan in the images is printed, the vertical axis can be distorted even if the pattern is viewed vertically from the top.

300 nm
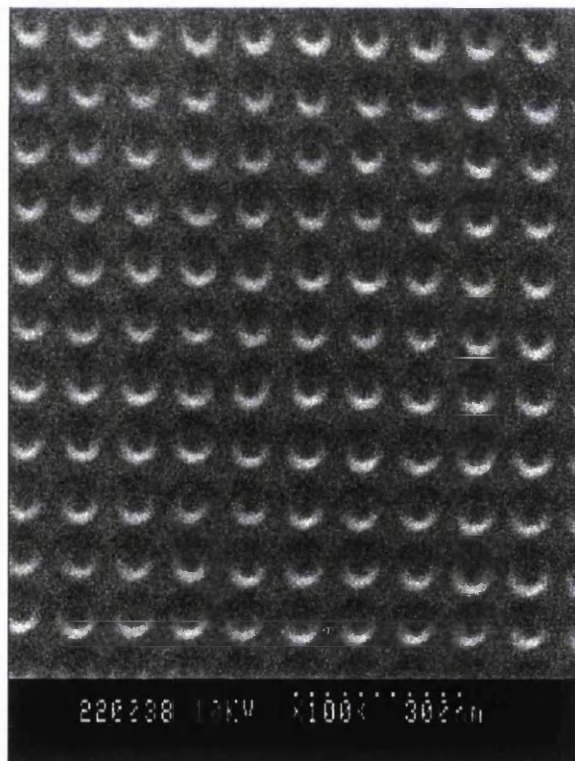
Figure 3.7
SEM image of 50 nm diameter pillars of resist arranged on 100 nm period square grid realised on the surface of Hall bars. The pattern was viewed at an angle to get the impression of pillars.
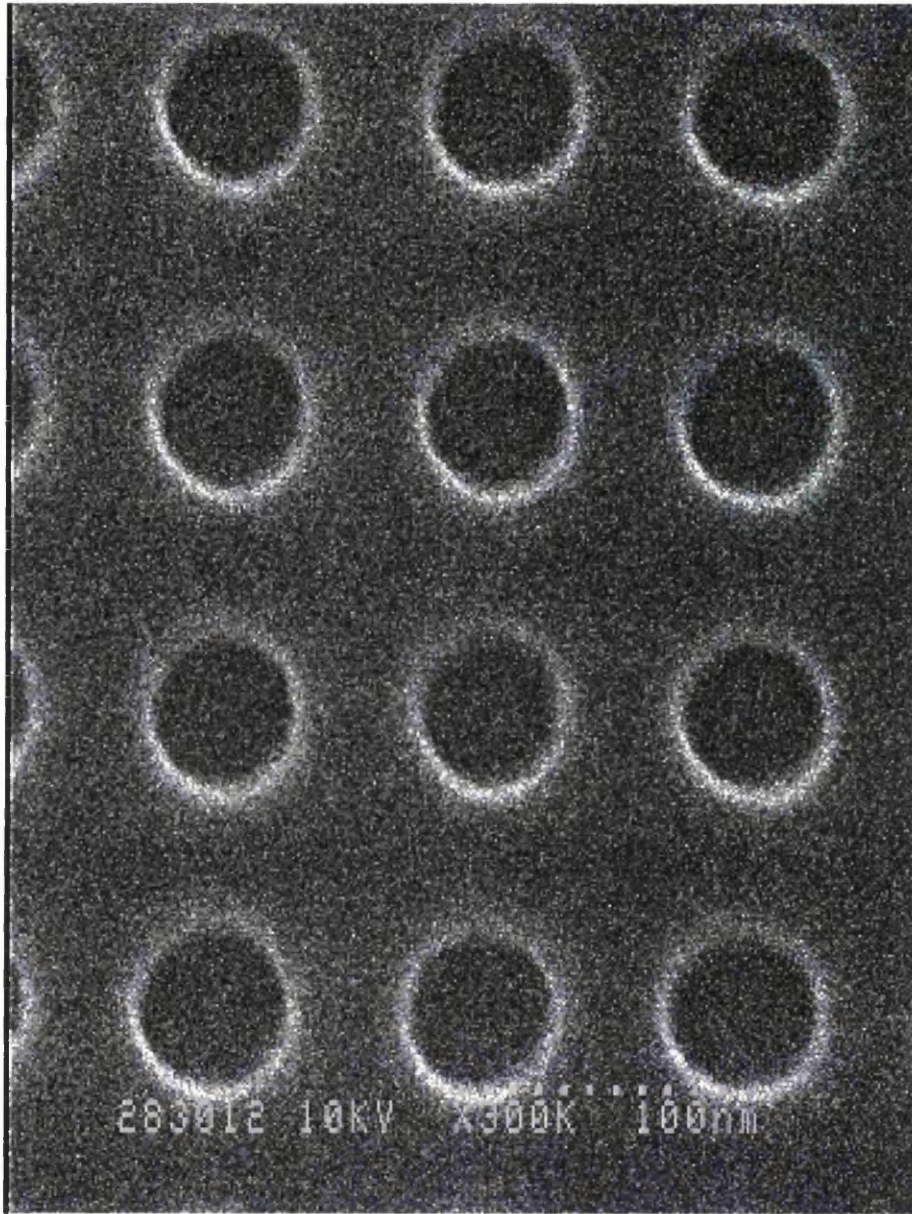
100 nm

Figure 3.8
Representative SEM image of a pattern of 50 nm diameter holes arranged on 100 nm period square grid realised in a resist layer coating the surface of Hall bars.

1 μm
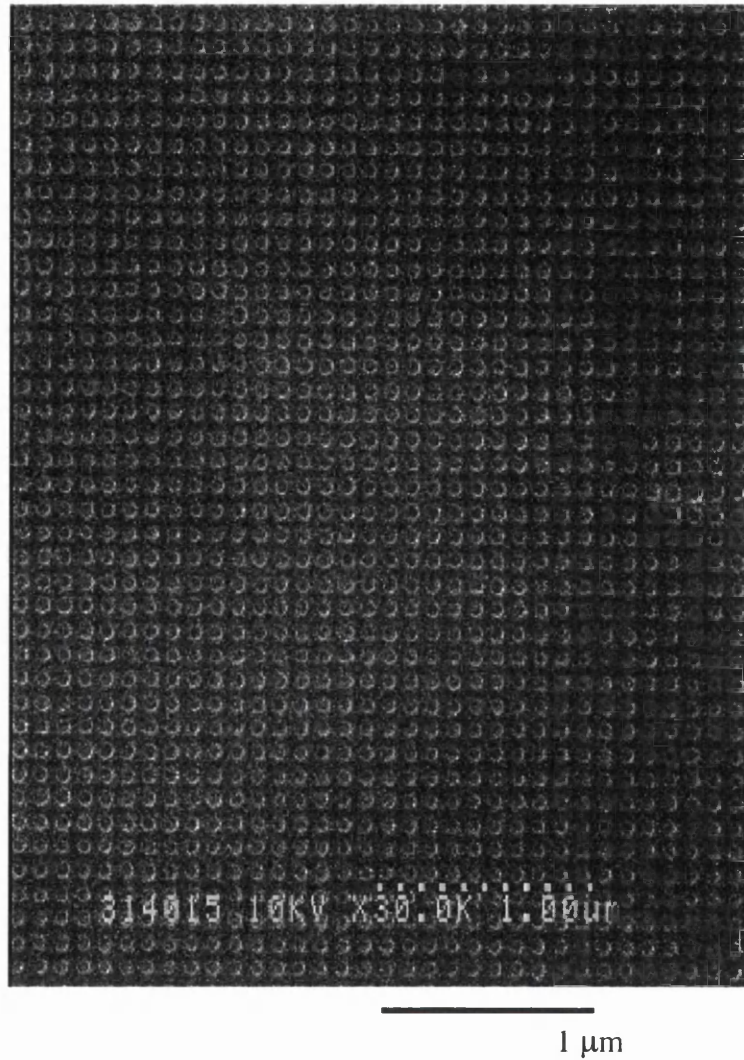
Figure 3.9
Representative SEM image of 50 nm diameter holes arranged on 100 nm period square grid realised in a resist layer coating the surface of Hall bars, shown over about 3.5 μm × 4.5 μm area on Hall bar showing the uniformity of the pattern over such a large area.
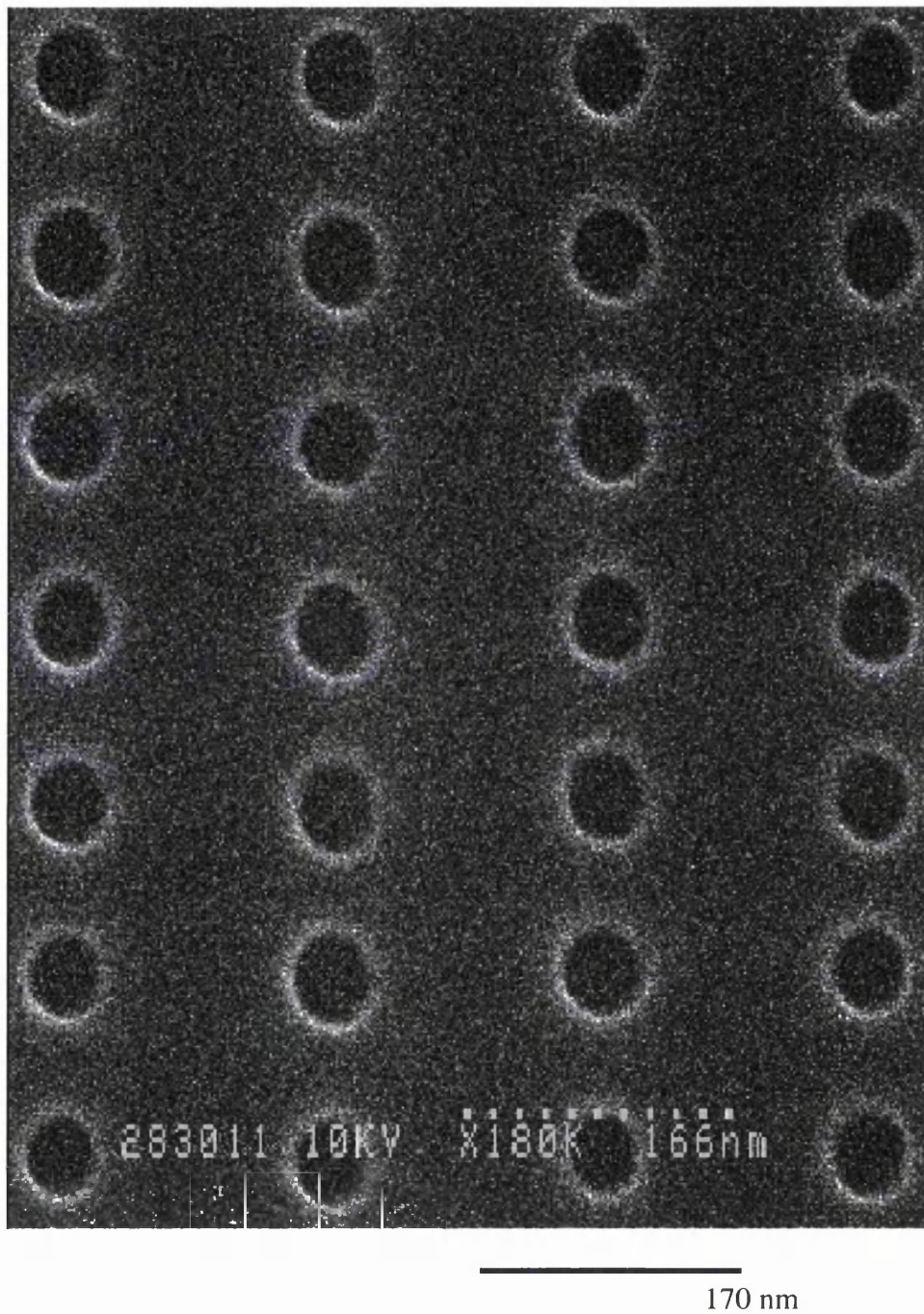
170 nm

Figure 3.10
Representative SEM image of a pattern of 50 nm diameter holes
arranged on 170 nm by 100 nm period rectangular grid realised in a
resist layer coating the surface of Hall bars.
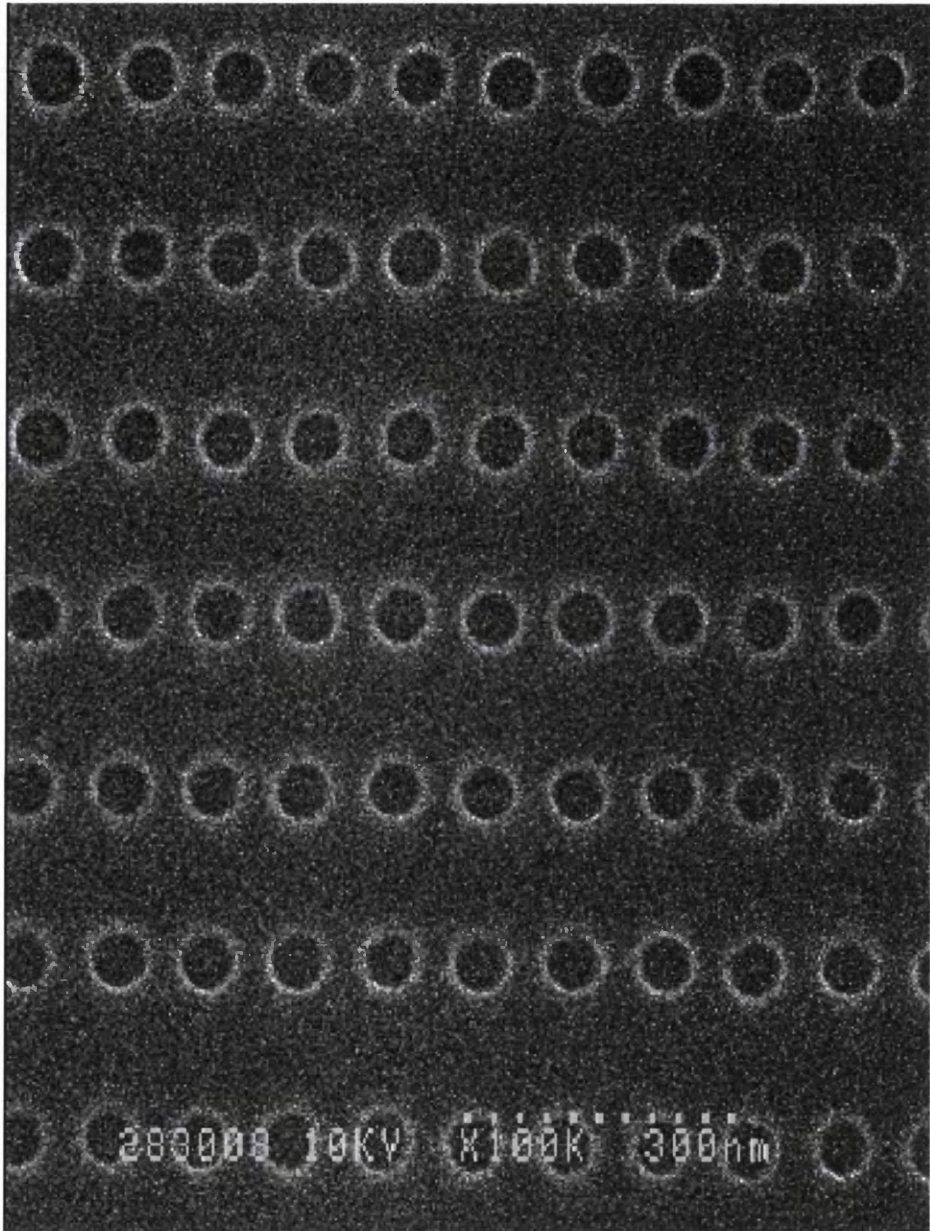
300 nm

Figure 3.11
Representative SEM image of 50 nm diameter holes arranged on 100 nm by 170 nm period rectangular grid realised in a resist layer coating the surface of Hall bars.
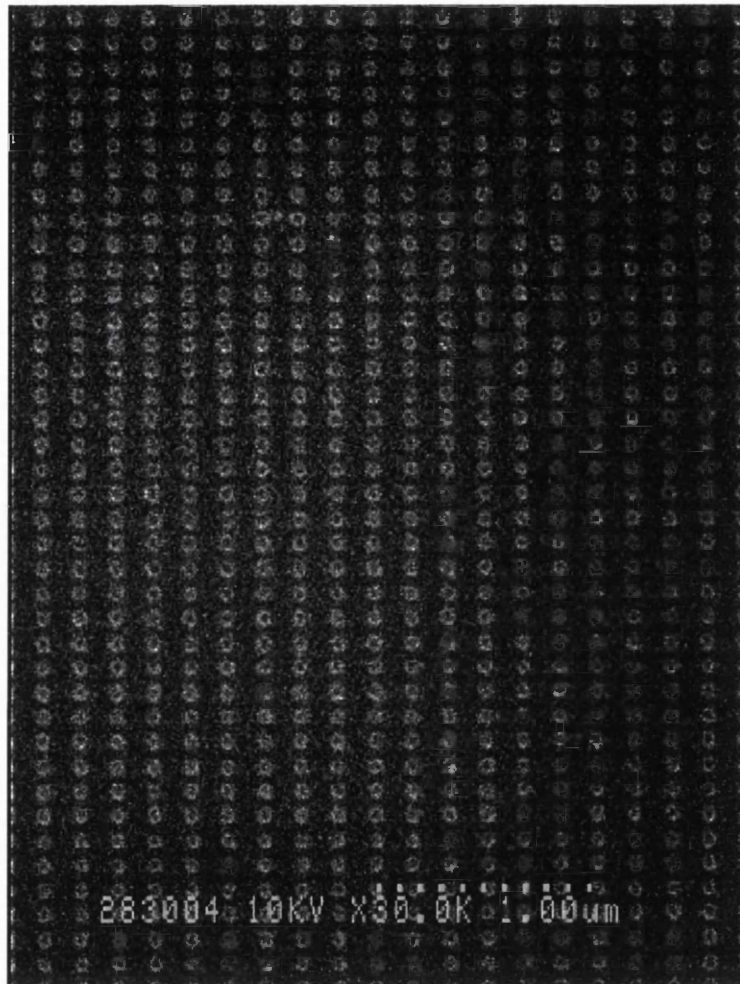
1 µm

Figure 3.12
Representative SEM image of 50 nm diameter holes arranged on 170 nm
by 100 nm period rectangular grid realised in a resist layer coating the
surface of Hall bars, shown over about 3.5 µm × 4.5 µm area on Hall bar
showing the uniformity of the pattern over such a large area.
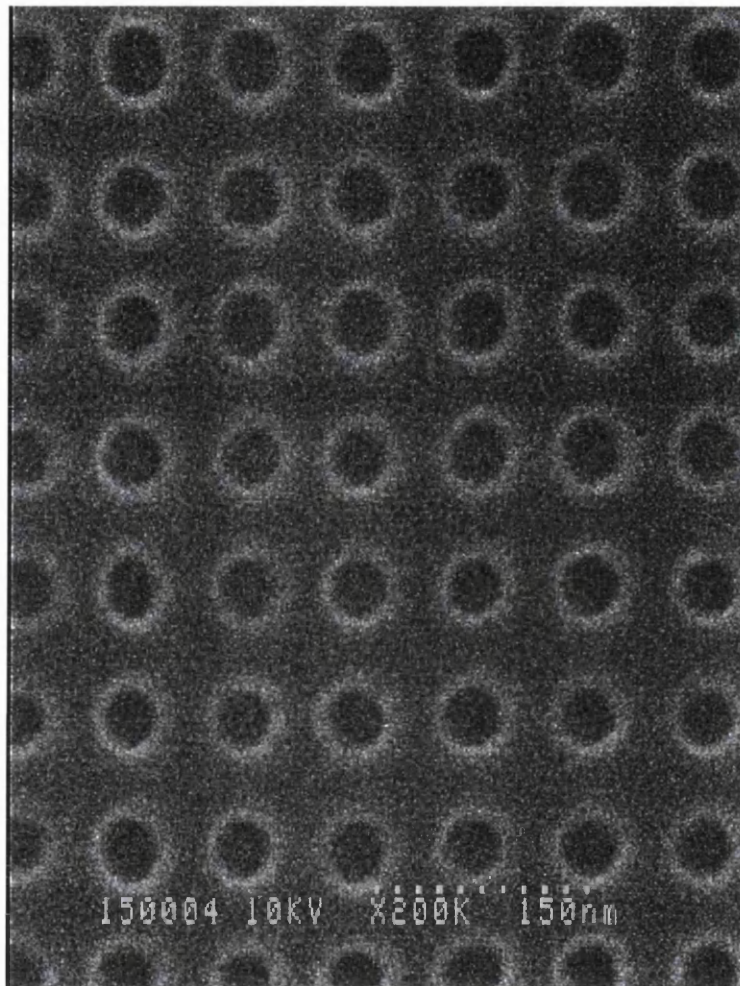
160 nm

Figure 3.13
Representative SEM image of a lattice of 40 nm diameter holes arranged
on 80 nm period square grid realised in a resist layer coating Hall bars.

670 nm
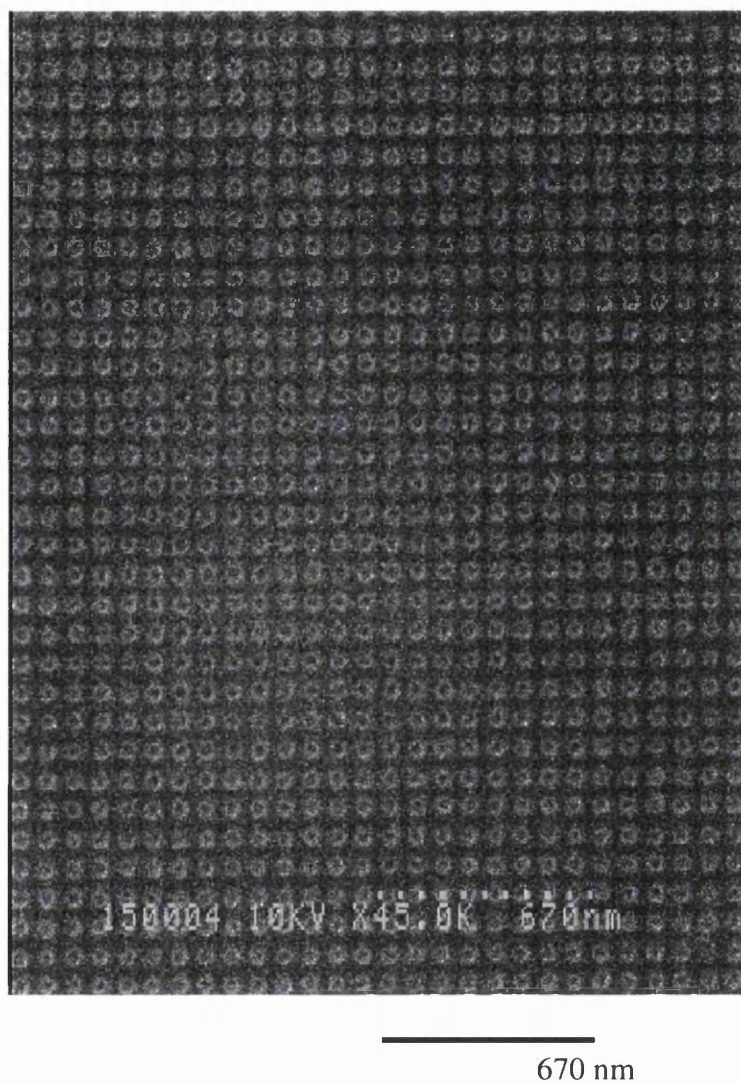
Figure 3.14
Representative SEM image of about 40 nm diameter holes arranged on
80 nm period square grids realised in a resist layer coating Hall bars,
displayed on a much larger scale showing uniformity of the pattern over
a larger area. It is difficult to resolve the pattern on a scale larger than
this.
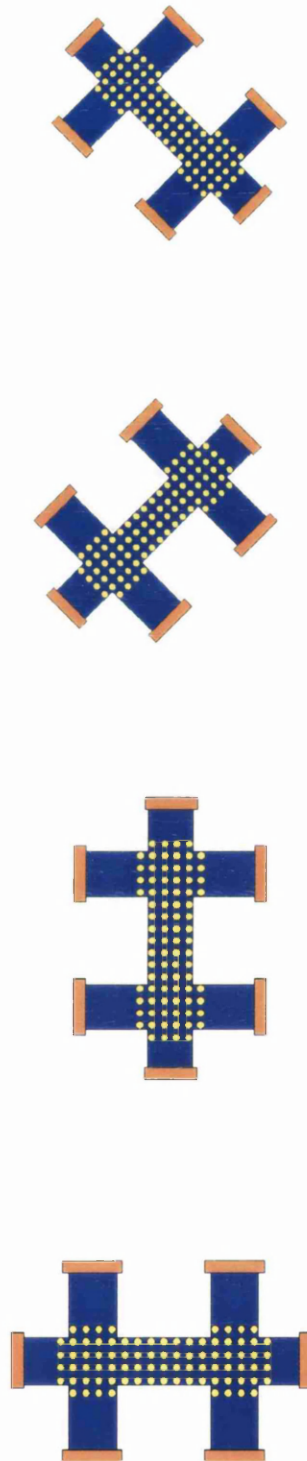
Figure 3.15
Schematic diagram showing that the principal axes of the pattern are kept along and across Hall bars of all four orientations studied.

20 μm
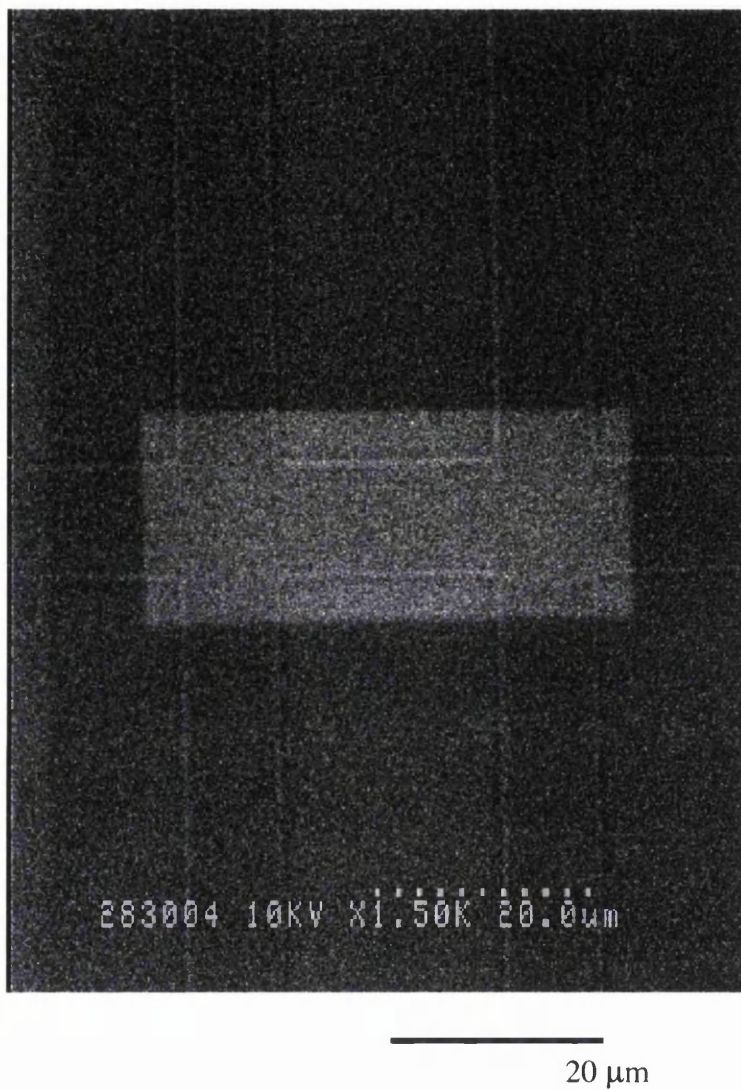
Figure 3.16
SEM image of a Hall bar containing patterned resist showing the extent
of the pattern relative to the Hall bar.

The principal axes of the pattern (i.e. the lattice constants) were kept along and orthogonal to the length of each Hall bar as indicated in Figure 3.15. The extent of the pattern was 46 μm by 16 μm to cover the entire region between the voltage contacts and extend an extra 3 μm in all directions as shown in Figure 3.16. This extent is a compromise between the minimum area to be covered and larger area the pattern of which is affected by the proximity affect. Due to the build up of dose, the aspect ratio of the pattern becomes different in the middle compared with that around the edges if the area of the pattern is larger. Extensive scanning electron microscopy confirmed that in a patterned area as large as 46 μm by 16 μm that we used, the aspect ratio of the pattern remains perfectly uniform throughout the pattern.

In obtaining a short period resist pattern, adhesion of resist to the semiconductor surface is important. As the resist pattern has to be transferred by etching, an important point is to make sure the resist pattern does not degrade in the etching process. This is achieved by enhancing the adhesion of the patterned resist with the underlying semiconductor. To this end, a thin layer (known to be as thin as a mono-layer) of an adhesive agent known as "primer" was spun to coat the surface of the Hall bars and the coated layer was baked at 75°C for 30 minutes before coating the Hall bars with the resist layer to be patterned with nano-scale periodicity.

3.2.3 Wet etch process development

After realising the resist pattern, the crucial step is to transfer the pattern by a reproducible shallow etching. The available reactive ion etching process proved irreproducible. Hence a suitable, reproducible wet etching process was developed that can be routinely used to transfer a nano-scale pattern. The first stage was an extensive survey of literature on suitable and simple wet etching processes that can be performed routinely to etch GaAs and InGaAs and stop on $Al_{0.3}Ga_{0.7}As$. The survey revealed that the citric acid based etching process is simple and promising. The relevant information obtained from the few papers that appeared helpful is summarised below.

M. Tong et al. [5] presented a selective wet etching process on samples grown by MBE on (100) GaAs substrates. They used mixtures of citric acid solution and hydrogen peroxide in various volume ratios at 20°C and found that for 3.5:1 ratio etch rate of GaAs is 6 nm /sec while that of $Al_{0.3}Ga_{0.7}As$ is 0.04 nm/sec corresponding to a selectivity of 150. The selectivity turned out to be different for different volume ratios of the acid solution and the peroxide and also for different Al mole fractions in AlGaAs. Here selectivity means the etch rate of GaAs divided by the etch rate of

AlGaAs. They prepared the citric acid solution by adding equal weight of citric acid monohydrate and deionized water. They used 30% hydrogen peroxide. They found that the etch rate of GaAs is constant for line widths from as high as 2 μm to as low as 300 nm. The etchant is found not to be corrosive of PMMA resist. They also compared results of wet and dry etching.

Moon et al. [6] presented a reproducible and selective etching process involving citric acid and hydrogen peroxide. They prepared the citric acid solution by dissolving 1:1 weight ratio of citric acid monohydrate with deionized water and stirring for two hours. They freshly mixed the citric acid solution with hydrogen peroxide in different volume ratios from 0.7:1 to 3:1 and etched the sample with stirring at room temperature. They stopped the etching by rinsing in deionized water and measured etch depths after removing the patterned photoresist. They found that the ratio 1.5:1 provided the best selectivity. For Al mole fraction of 0.3 in AlGaAs, the selectivity was 159 and was different for different mole fractions. AFM studies showed that for 0.3 Al mole fraction in AlGaAs, the surface etched by the solution of ratio 1.5:1 is smooth and much better than those etched by H_3PO_4 solution (H_3PO_4:H_2O_2:H_2O = 4:1:180). They attributed this to the fact that slow etchant leaves the etched surface smooth. Their study attributes the selectivity to the formation of relatively insoluble Al_2O_3 on the surface of AlGaAs, which suppresses further dissolution of AlGaAs.

Jong-Hee Kim et al. [7] presented a selective wet etching process using citric acid and hydrogen peroxide. They prepared the acid solution by mixing citric acid monohydrate in 1:1 weight ratio with deionized water. The citric acid and hydrogen peroxide mixtures were prepared by adding the acid solution to 30% hydrogen peroxide in the desired volume ratio just before etching. They have put great emphasis on oxide etching (for ~15 seconds) just before the etching process. They performed the etching at room temperature of 22°C. For volume ratio of 3:1 of citric acid to hydrogen peroxide, they obtained selectivity as high as 100 for GaAs over $Al_{0.32}Ga_{0.68}As$.

C. Juang et al. [8] found 10:1 volume ratio of 50% by weight of citric acid solution to 30% hydrogen peroxide to be a better etchant of GaAs-$Al_{0.3}Ga_{0.7}As$ heterostructures than ammonium hydroxide-hydrogen peroxide solutions in terms of selectivity of the etch rate, smoothness of the etched surface and abruptness of the etch defined edge. Moreover, they found that the citric acid-hydrogen peroxide mixture does not attack the photoresist they used. They noted that the etching process is simple and reproducible.

T. Kitano et al. [9] presented a selective wet etching process involving citric acid, hydrogen peroxide and ammonium hydroxide. They found the selectivity of GaAs over $Al_{0.15}Ga_{0.85}As$ as 80 and that over $Al_{0.3}Ga_{0.7}As$ as 120 by adjusting the pH and the acid to peroxide ratio. Their investigations suggested that etch stop mechanism was due to the formation of insoluble Al_2O_3 on the surface of AlGaAs. The etching was done at room temperature. Anhydrous citric acid crystals were dissolved in water. The pH of the citric acid solution was adjusted by the addition of ammonium hydroxide and the pH was controlled within a range of ±0.05. This mixture was added to hydrogen peroxide at the desired volume ratio. They etched without stirring and stopped etching by rinsing in water for about 1 minute. Their ratio of acid to peroxide is awkwardly large.

G. C. DeSalvo et al. [10] investigated selective etching of materials in various III-V semiconductor heterostructures by mixtures of citric acid and hydrogen peroxide at different volume ratios from 0.2:1 to 20:1. They performed the etching at room temperature. Anhydrous citric acid crystals were dissolved in deionized water at the ratio of 1 g acid crystal to 1 ml water. They noted that as the reaction is endothermic, quick dissolution is hindered and hence they prepared the acid solution one day in advance of etching to ensure complete dissolution and room temperature stability. They prepared the mixture of acid solution and 30% hydrogen peroxide at desired volume ratios 15 minutes before etching to allow the etchant to return to room temperature if any temperature change occurs due to the mixing. They noted that citric acid and hydrogen peroxide mixture at any volume ratio does not erode the photoresist pattern used. Etching was stopped by rinsing in flowing deionized water for at least 1 minute.

Tong et al. [11] studied selectivity of etching InGaAs on InP, InAlAs on InP and InGaAs on InAlAs by a mixture of citric acid and hydrogen peroxide. They found selectivities as high as 500 and 187 for etching InGaAs on InP and InAlAs on InP respectively. The selectivity for etching of InGaAs on InAlAs was found to vary from 25 to 2.5 depending on the acid to peroxide ratio of 1 and 10 respectively. They also reported etched profiles.

G. C. DeSalvo et al. [12] found that citric acid and hydrogen peroxide mixtures at volume ratios from 0.5:1 to 50:1 provides good selective etching of various III-V semiconductor materials grown by MBE. They found that depending on the volume ratio of the acid and peroxide, the etchant turns non-selective from selective. They obtained selectivities as high as 116 for GaAs over $Al_{0.3}Ga_{0.7}As$ while 120 for $In_{0.2}Ga_{0.8}As$ over $Al_{0.3}Ga_{0.7}As$. They noted that the citric acid and hydrogen peroxide

mixture does not erode the photoresist used as etch mask. They also studied etching selectivities for heterostructures involving InGaAs, InAlAs and InP.

X. Hue et al. [13] studied etching of GaAs and $Al_{0.22}Ga_{0.78}As$ in citric acid, hydrogen peroxide and ammonium hydroxide mixture. They prepared the acid solution by dissolving citric acid monohydrate with deionized water at the ratio 1.5 g:100 ml. After adjusting the pH of the acid solution by the addition of 30% ammonium hydroxide, they mixed 30% hydrogen peroxide to prepare the etchant. With a pre-oxide etch, they performed the etching without stirring and stopped etching in deionized water. By optimising the pH and the acid to peroxide ratio, they realised the selectivity of GaAs over $Al_{0.22}Ga_{0.78}As$ as high as 200 at 20°C.

M. Tong et al. [14] reported uniform etching of InGaAs with a selectivity of 25 over InAlAs using 1:1 citric acid : hydrogen peroxide solution.

B. Y. Mao et al. [15] investigated etching characteristics of GaAs and $Al_{0.28}Ga_{0.72}As$ in citric acid and hydrogen peroxide mixtures and measured etch rate and selectivity over a wide concentration range. They found that by changing the concentration of the solution, the selectivity (etch rate of GaAs : $Al_{0.28}Ga_{0.72}As$) could be changed from 80:1 to reverse selectivity of 1:1.4 and the etch rate of GaAs could also be varied from 400 nm /minute to less than 15 nm /minute. They chose a non-selective low etch rate process for gate recess etch, since the selective etch as they noted shows high GaAs etch rate and causes excessive undercut in the cap layer. They observed that low etch rate etching by citric acid and hydrogen peroxide mixture provides very uniform etching which is the best result using non-selective wet etch and compares very well with published results using dry etch.

H. J. Lee et al. [16] studied selective etching characteristics of GaAs-$Al_xGa_{1-x}As$ heterostructures in citric acid and hydrogen peroxide mixture for x = 0.15, 0.2 and 0.3. They found 4:1 ratio of citric acid (50% by weight): hydrogen peroxide mixture to be a better selective etchant than ammonia-hydrogen peroxide solutions. For x = 0.3, they obtained selectivity more than 110.

The points regarding etching by citric acid and hydrogen peroxide mixtures that are notable in the above papers are listed below.

1) Citric acid and hydrogen peroxide mixture etches GaAs and InGaAs.

2) The selectivity of the etchant for GaAs over AlGaAs depends on the volume ratio of citric acid and hydrogen peroxide and the etchant may turn non-selective for some ratios.

3) Etching can be performed at room temperature.

4) 30% hydrogen peroxide can be used.

5) Deionized water is necessary for the preparation of citric acid solution.

6) Citric acid in the form of either citric acid monohydrate or anhydrous citric acid crystals is to be used in preparing the acid solution.

7) The pattern of 300 nm period grating could be transferred using citric acid and hydrogen peroxide mixture.

8) The citric acid and hydrogen peroxide mixture is not corrosive of PMMA or photoresist used as etch mask.

9) The etchant should be reproducible.

10) In preparing the citric acid solution, stirring for a long time is required as the reaction is endothermic which impedes the dissolution.

11) Etchant has to be freshly prepared just before etching.

12) Etching can be done with or without stirring.

13) Etching can be stopped in deionized water.

14) The etchant leaves the etched surface smooth.

15) The citric acid and hydrogen peroxide mixture is a better etchant than $H_3PO_4:H_2O_2:H_2O$.

16) Oxide etching (for ~15 seconds) just before etching in citric acid and hydrogen peroxide mixture is very important.

17) Citric acid and hydrogen peroxide mixture is a better etchant than NH_4OH and H_2O_2 mixture regarding selectivity, smoothness of the etched surface and abruptness of etch defined edge.

18) Etching by a citric acid and hydrogen peroxide mixture is simple for routine use.

19) Etching involving citric acid, ammonium hydroxide and hydrogen peroxide involves accurate pH adjustment.

20) Citric acid and hydrogen peroxide mixture etches InGaAs uniformly.

21) Change of the volume ratio of citric acid and hydrogen peroxide changes not only the selectivity but also the etch rate of GaAs.

22) In selective etching, etch rate of GaAs is high and hence it etches GaAs cap layer too fast producing excessive undercut. For example, despite having a selectivity of 150, the recipe of Tong et al. [5] etches GaAs cap at a rate of 6 nm /second which is quite high.

23) Certain volume ratios turn the citric acid and hydrogen peroxide mixture into a non-selective but very slow etchant. Etching with such a slow etchant provides very uniform etching with best results [15].

In view of the above list of features, it seemed very promising that citric acid and hydrogen peroxide mixture could be used in this project following the above as a

guide. The major challenge that appeared was to implement the etching process within the laboratory conditions for transferring nano-scale pattern. Questions that posed were: if the etchant will etch through 50 nm diameter holes in resist or material around 50 nm diameter pillars of resist arranged on typically 100 nm period grid as the resist pattern for LSSLs; if the resist we use will survive the etching.

The heterostructures on which etching is to be performed for pattern transfer consist of the following layers from the surface:

10 nm GaAs

6 nm $In_{0.2}Ga_{0.8}As$

2 nm GaAs

3 nm $Al_{0.3}Ga_{0.7}As$

2 nm GaAs

10 nm $Al_{0.3}Ga_{0.7}As$

Si delta doping

20 nm $Al_{0.3}Ga_{0.7}As$ spacer

2DEG

and GaAs substrate.

At first the etching was tried at room temperature by a mixture of citric acid and 30% hydrogen peroxide in the volume ratio 3.5:1 as per Tong et al. [5]. The acid solution was prepared by mixing 15 g of citric acid monohydrate with 15 g of deionized water and stirring for an hour by a magnetic stirrer. But it turned out that the etchant failed to transfer nano-scale pattern of 50 nm diameter dots of resist arranged on 100 nm period grid. The etchant did not etch at all.

If a wetting agent is mixed with an etchant, it is known in our fabrication laboratory to make it possible for the etchant to reach narrow slots of a pattern. The agent is known as "FC93" and it contains, according to manufacturer, iso-propyl alcohol (IPA) and ammonium perfluoroalkyl sulphonates and it is available in our laboratory as a mixture called "FC93 solution" consisting of 20 ml FC93, 60 ml water and 20 ml IPA. It was thus expected that if an amount of FC93 solution is added to the citric acid and hydrogen peroxide mixture, the etchant should be able to transfer nano-scale pattern. However, as we had no knowledge about the effect of FC93 solution on citric acid and hydrogen peroxide mixture, it became necessary to characterise the etching by citric acid and hydrogen peroxide mixture after adding FC93. We needed to know if the etchant still etches, if the etch rate slows down or speeds up with the addition of FC93, if it erodes the resist mask or not and so on. To this end, structural rather than electrical characterisation of a micron scale pattern became necessary at

first. Then depending on success, it was to be made amenable to nano-scale pattern transfer. This was done as follows.

1) 50 μm period grating of resist consisting of trenches of width 20 μm was realised on the heterostructure materials (that are used in this project) using the same resist prepared in the same manner as is done for realising resist pattern for superlattices. The substrate containing the micron scale resist pattern was cleaved into quite a few pieces.

2) The citric acid solution was prepared by dissolving 15 g citric acid monohydrate into 15 g deionized water by stirring the mixture by a magnetic stirrer for one hour.

3) Immediately before etching, an oxide etchant was prepared by mixing 10 ml of concentrated hydrochloric acid with 40 ml deionized water and adding 0.5 ml FC93 solution. The beaker containing the oxide etchant was labelled as beaker no. 1.

4) 50 ml iso-propyl alcohol was taken in a beaker labelled as no. 2.

5) The citric acid solution was added to 10 g 30% hydrogen peroxide and 1 ml FC93 solution was added. The beaker was labelled as no. 3.

6) 1 ml FC93 solution was added to 100 ml deionized water in a beaker labelled as no. 4.

7) 100 ml deionized water was taken in a beaker labelled as no. 5.

A small piece of substrate containing the micron scale resist pattern was first oxide etched for 15 seconds in beaker no. 1 holding it in the oxide etchant by a tweezer and then transferred to beaker no. 2 for 60 seconds for stopping the oxide etching. Then the substrate was blown dry by nitrogen gas very gently not to harm the etch mask in any way. Then the substrate was held in the etchant in beaker no. 3 for the desired length of time. Then the substrate was transferred to beaker no. 4 and held for 30 seconds to get rid of the etchant from narrow slots and then transferred to beaker no. 5 and held for 60 seconds to get rid of the etchant completely. In every beaker, the substrate was held by a tweezer and was moved continuously without agitation so that the entire piece of substrate is treated uniformly.

Ten pieces of small substrates were etched for 20, 30, 40, 50, 60, 70, 80, 90, 100 and 110 seconds respectively and the resist was then removed in acetone and blown dry. The etch depths in the micron scale trenches were measured using a surface profiler called "Dektak" and turned out to be as noted in Table 3.1. It turned out that the etchant is very strong and etched GaAs, InGaAs, AlGaAs and is non-selective. The resist used as etch mask remained unaffected by the etchant. The next course of action was to change the ratio of citric acid solution and hydrogen peroxide in the etchant to

try to turn it into a selective or at least slow etchant to get reproducible timed etching. Different volume ratios were tried and the results obtained are as noted in Table 3.2.

Table 3.1
Etch depths in 50 µm period trenches for various etch time obtained by the mixture of citric acid solution and hydrogen peroxide in 3:1 weight ratio. Details are in the text above.

Etch time (seconds)	Etch depth (nm)
20	40
30	120
40	230
50	360
60	470
70	560
80	630
90	700
100	850
110	900

Table 3.2
Etch depths obtained for various volume ratios for two set etch times.

Volume ratio of citric acid solution and hydrogen peroxide	Etch depth (nm) for 20 second etch	Etch depth (nm) for 40 second etch
10:1	90	160
3:1	40	230
3:2	35	40
1:1	25	30
1:2	(not obtained)	16
1:3	(not obtained)	12

It turned out that for increasing hydrogen peroxide content, the etchant turned slower and slower and 1:3 ratio appeared very attractive. Etch depths for a few longer etch times were obtained for this ratio and were found to be

- 25 nm for 80 seconds

- 30 nm for 120 seconds.

It should be remarked that in the literature, a volume ratio of 3:1 instead has been noted to give selective etching [7]. This may be attributed to a change in the chemistry of the etching process due to the addition of FC93 in the citric acid and hydrogen peroxide mixture.

The 1:3 volume ratio of citric acid solution and hydrogen peroxide was applied directly to pattern transfer of 100 nm period 2D LSSLs and working devices were obtained readily. The volume ratio and the FC93 content were adjusted from time to time to conform with change of reagent bottles to keep the etching under control. Even a 1:4 ratio was used on some occasions and FC93 content in the etchant had to be reduced to as low as 0.2 ml. AFM images of the superlattices confirmed that the etchant could transfer the pattern of even 40 nm diameter holes on 80 nm period grid absolutely perfectly. The etchant could be used routinely to fabricate high quality superlattices with high reproducibility. This is unlike the fact that due to the surface tension of the etchant, etched profile becomes non-uniform [17]. The FC93 diminishes the surface tension and hence the etched profiles obtained are perfectly uniform, as confirmed by AFM.

The notable features of the etching process are as follows.

- It is suitable for transferring nano-scale pattern. I etched through 40 nm diameter holes successfully and transferred the pattern perfectly to the material.

- It is an extremely slow etchant. An etch depth of about 20 nm through the nano-holes could be obtained in typically 100 seconds and hence it provides high reproducibility.

- It etches $In_{0.2}Ga_{0.8}As$ besides GaAs.

It should be pointed out that it remains arguable if the success of the etchant is due to any selectivity between GaAs and AlGaAs or due to the fact that the etch rate itself is very low in both GaAs and AlGaAs for the volume ratio used or due to a combination of the two properties. That the etchant could be turned slow enough to etch for a long time, typically 100 seconds, to get the desired etch depths made it unnecessary to investigate the selectivity (if any) of the etchant.

3.2.4 Breakthrough in fabrication

A resist pattern of pillars with positive resist was attempted first. But due to narrow process latitude, this process proved very unrealistic with the laboratory conditions. This agrees with an early observation of K. Y. Lee et al. [18] that in realising resist pattern for superlattices, exposing dots rather than a grid of the same period yields, because of a smaller exposure area, a reduction in the exposure time and proximity effect. This enhances process latitude, pattern fidelity and resolution. Nevertheless, repeated attempts eventually made it possible to realise some devices [19] by the method of exposing grids and hence getting a pattern of pillars of resist before discovering a way to increase the process latitude. Several other processing steps were checked if these were responsible for the lack of success of the pillar method and the short process latitude was finally identified to be the reason.

As to the fabrication process, it has been a major discovery for me that the process latitude of the pattern of holes is an order of magnitude larger than that of pillars. Because of this, a large range of devices of very high quality could be fabricated in a short period to meet the requirements of the project.

3.2.5 After pattern transfer

After the pattern transfer, the resist mask was removed completely. If is not removed, the patterned resist layer will generate periodic stress [20] and will make it impossible to get unstressed devices. Resist was removed from both stressed and unstressed devices for comparison. Fabrication was completed by covering the patterned area by ~200 nm thick continuous Ti-Au Schottky gate by evaporation. The process of realising gate is to expose the required areas (see Figure 3.3 and Figure 3.4) in a bi-layer of resist coating Hall bars and evaporate metal followed by lift off. The extent of the gate relative to that of the superlattices and Hall bars is shown in Figure 3.17 below. As the metal is evaporated on the patterned area, it is expected to penetrate the etched regions, notably the etched holes or areas round pillars on the surface. This is demonstrated by experiment in that the surface component of the potential modulation at the 2DEG could be changed by application of an electrostatic bias to the gate as discussed in the following chapters. Figure 3.18 below shows a magnified optical image of a gated device.

30 μm

 Isolation area

 Superlattice area

 Gate area
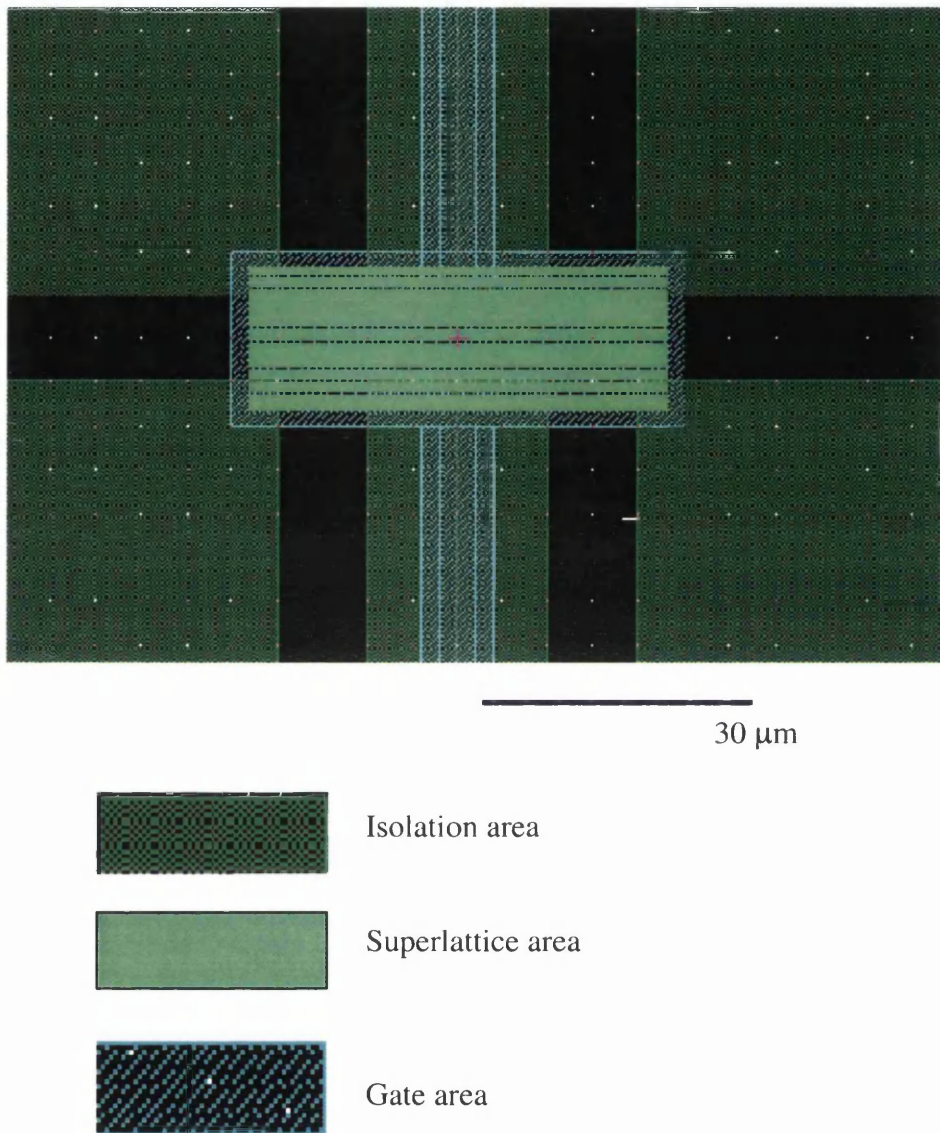
Figure 3.17
The design used in electron beam lithography showing the extents of the
superlattices and gate relative to the Hall bar.

200 μm
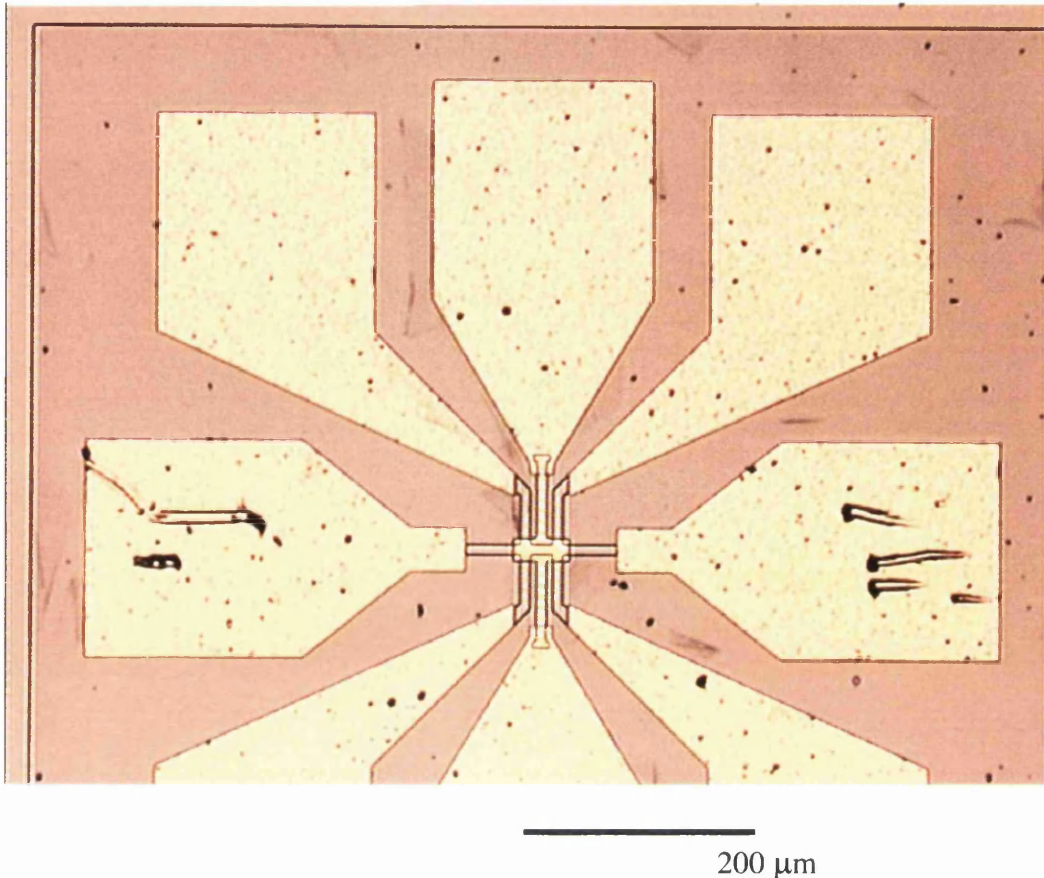
Figure 3.18
Magnified optical image of a gated device. The large golden pads are
ohmic contacts to the arms of the Hall bar in the middle. The small
golden rectangular pad in the middle is the continuous gate overlying the
etched lattice realised at the surface of the Hall bar. Two golden wires
are seen to connect the gate to two isolated (discussed in Figure 3.3)
ohmic pads to apply the gate bias.

3.2.6 Representative SEM images of etched pattern

Working devices without gates were realised and the magnetotransport of these
were studied in almost all cases and the etched patterns were examined by SEM in
detail after measurements to make sure that correct patterns were in action. This is to
confirm the main features of the data with first hand knowledge of the etched pattern.
Moreover, before evaporating metal to realise gates on every set of devices, a few
devices were removed by cleaving and kept without a gate. The patterns of these
ungated devices were also extensively examined by SEM to make sure that gated
devices had the correct pattern. This assumes that the pattern of the gated devices is as
good as that of the ungated devices, which is plausible as these were together in all
fabrication steps. SEM images of various superlattices are shown below.

300 nm
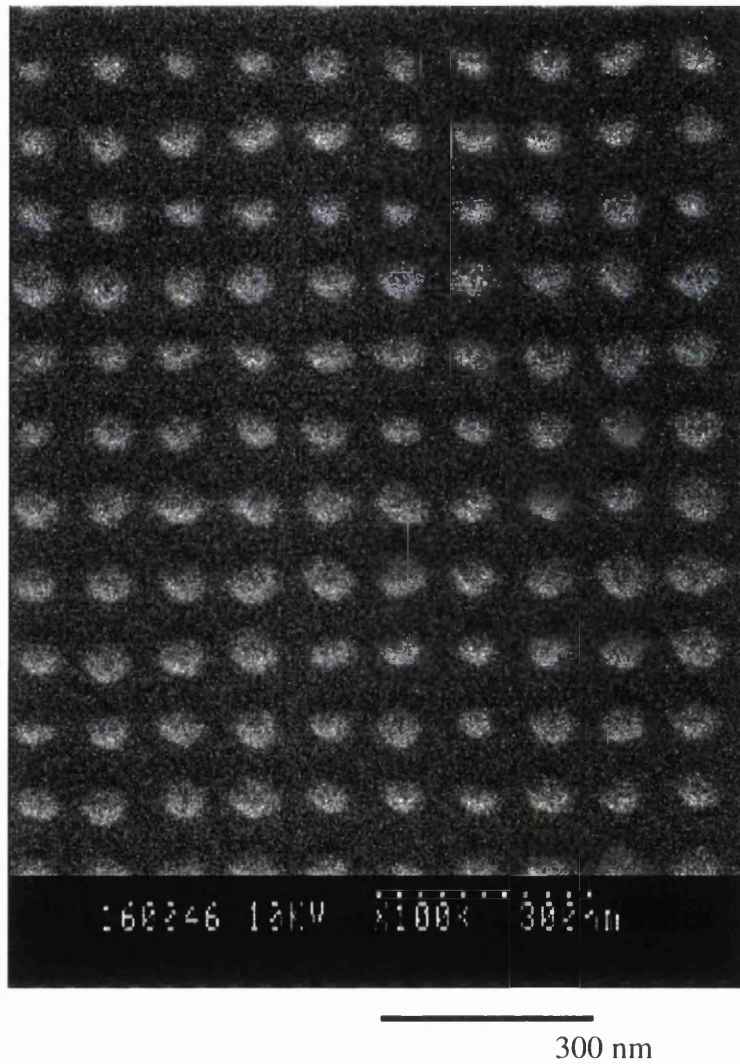
Figure 3.19
SEM image of an etched pattern of 50 nm diameter pillars arranged on 100 nm period square grid realised at the surface of Hall bars. The image was taken from a device without a gate but after removal of the resist.

600 nm
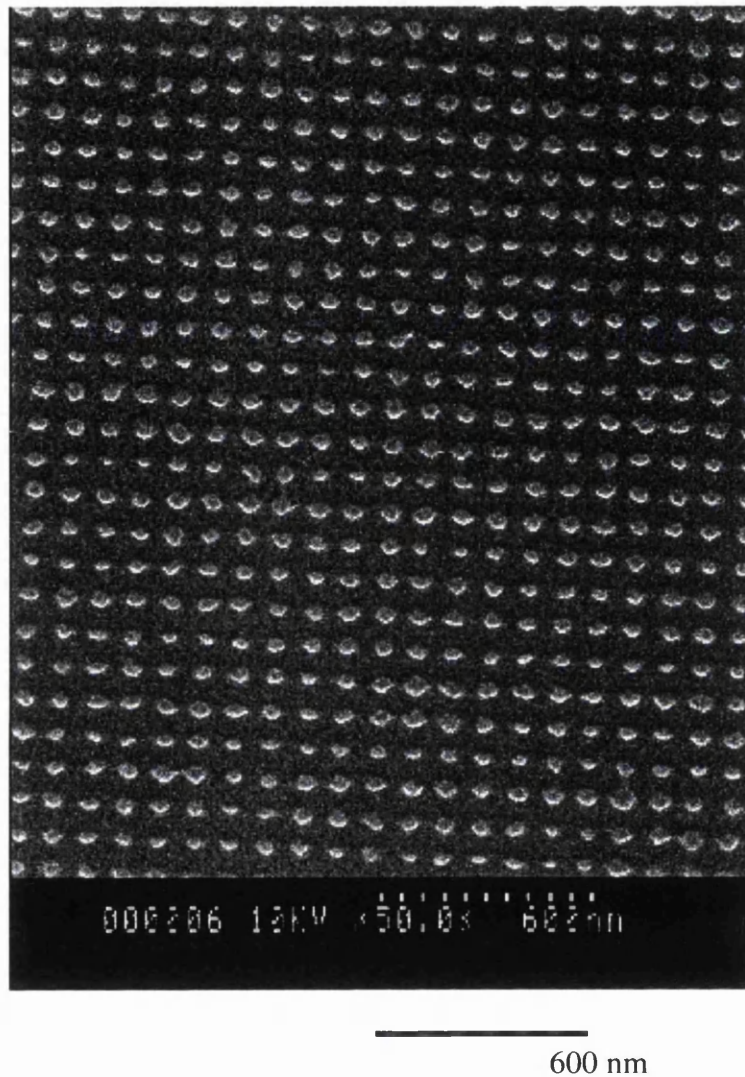
Figure 3.20
SEM image of an etched pattern of 50 nm diameter pillars arranged on
100 nm period square grid realised at the surface of Hall bars. The image
was taken from a device without a gate but after removal of the resist
and shown on a larger scale showing a larger area. There are some
imperfections, as the process latitude of the pattern of pillars is narrow
as already discussed.
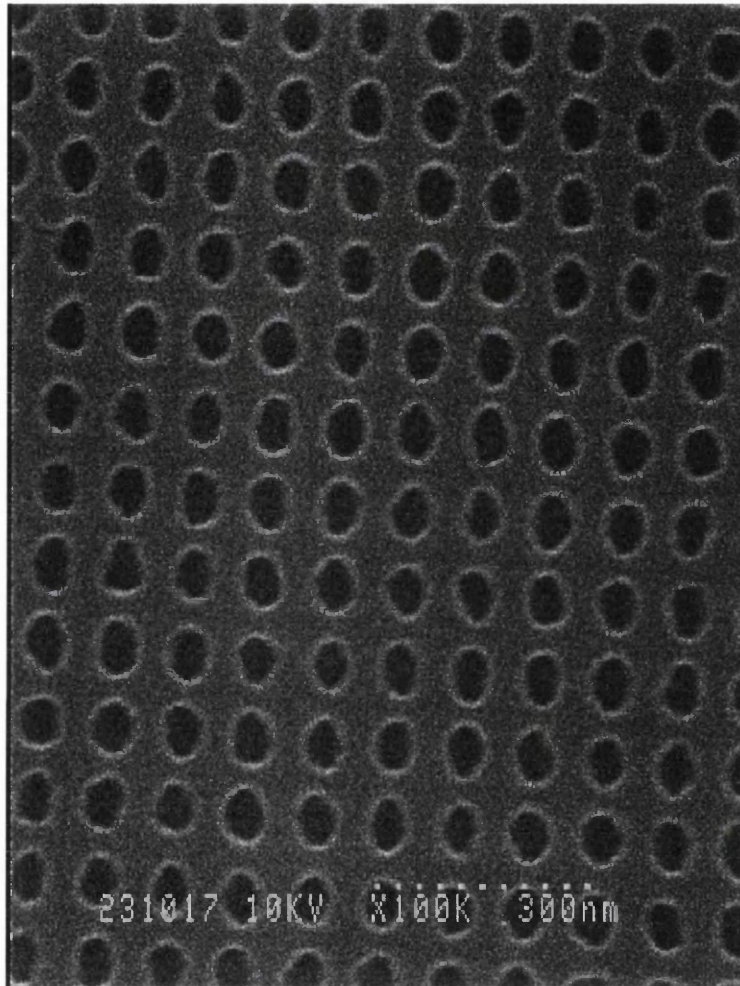
300 nm

Figure 3.21
Representative SEM image of a pattern of shallow etched 50 nm
diameter holes arranged on 100 nm period square grid realised at the
surface of Hall bars. The image was taken from a device without a gate
but after removal of the resist.
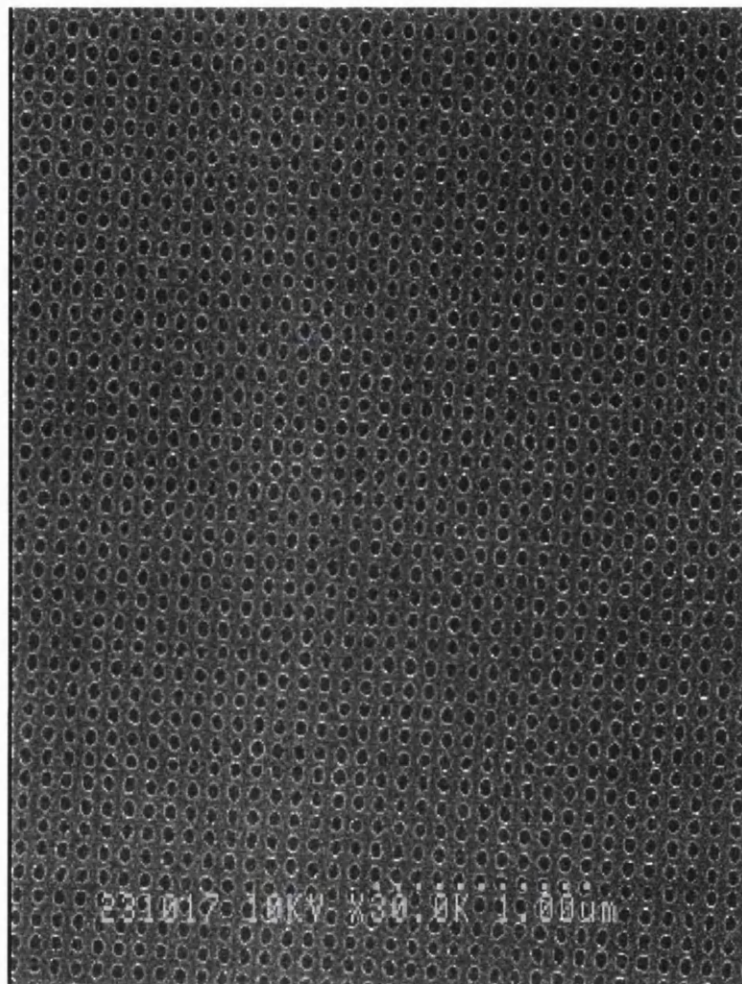
1 µm

Figure 3.22
Representative SEM image of 50 nm diameter shallow etched holes arranged on 100 nm period square grid realised at the surface of Hall bars. The image was taken from a device without a gate but after removal of the resist. The etched pattern is shown over about 3.5 µm × 4.5 µm area on Hall bar demonstrating the uniformity of the pattern over such a large area.
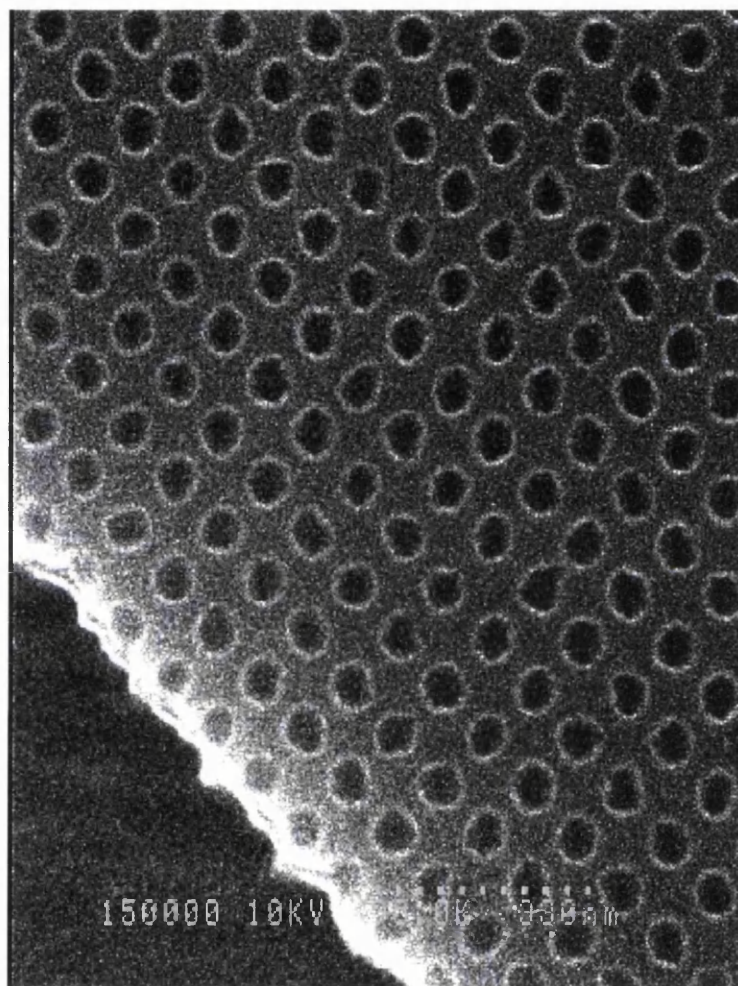
300 nm

Figure 3.23
Representative SEM image of a pattern of shallow etched 50 nm diameter holes arranged on 100 nm period square grid seen at the edge of a Hall bar. The image was taken from a device without a gate but after removal of the resist. This image shows that the aspect ratio of the etched pattern was found to remain the same up to the isolation edges of the Hall bars.

1 μm
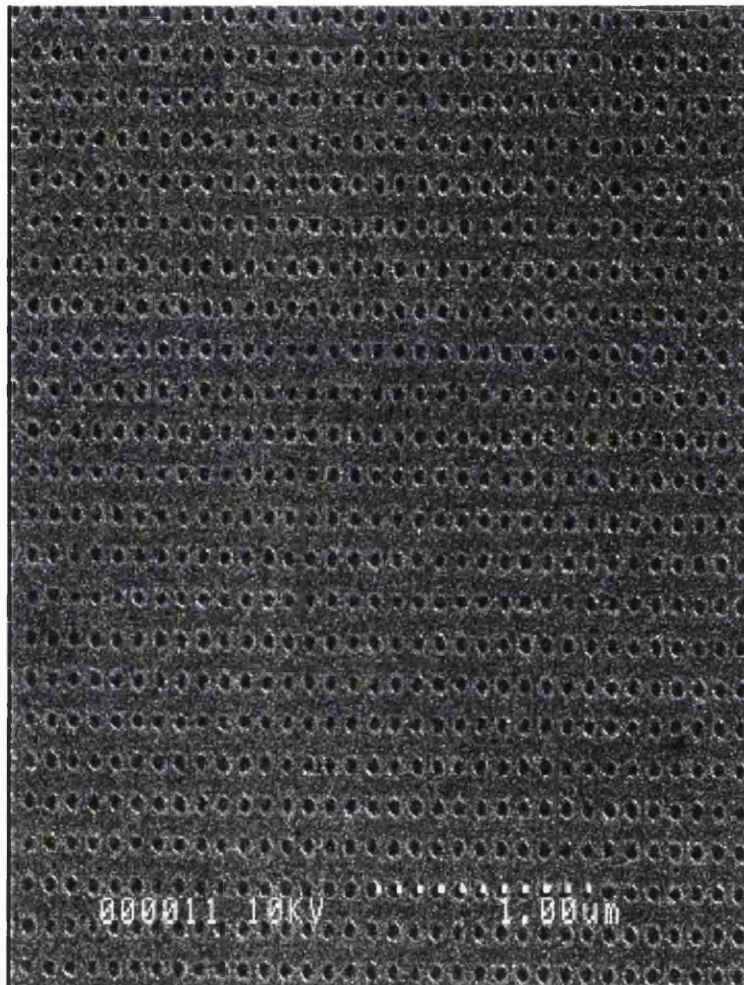
Figure 3.24
Representative SEM image of a pattern of shallow etched 50 nm diameter holes arranged on 100 nm by 170 nm period rectangular grid realised at the surface of Hall bars. The image was taken from a device without a gate but after removal of the resist. The etched pattern is shown over about 3.5 μm × 4.5 μm area on Hall bar demonstrating the uniformity of the pattern over such a large area.

3.2.7 Representative AFM images of etched pattern

Atomic Force Microscope (AFM) was used to obtain images of ungated superlattices of each set of devices to reveal the quality of the etched pattern. Figure 3.25 to Figure 3.33 are some representative images.
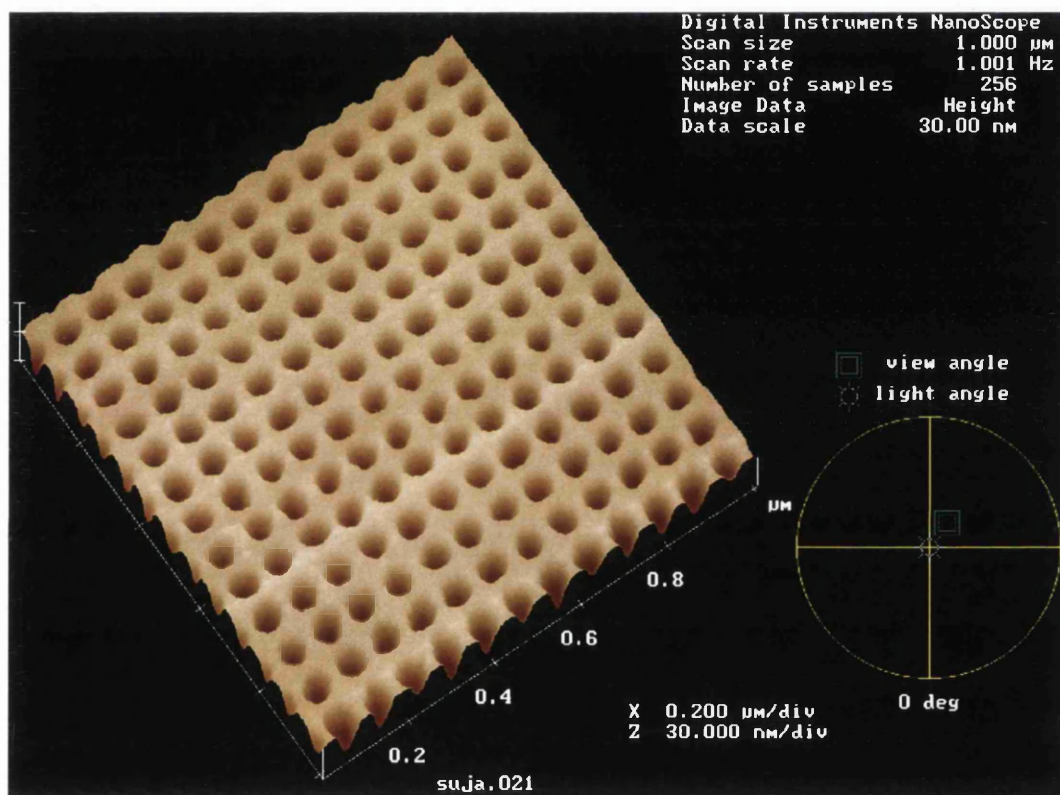
Figure 3.25
Representative AFM image of 80 nm period 2D LSSL of about 40 nm diameter etched holes. The image was taken from a device without a gate but after removal of the resist.
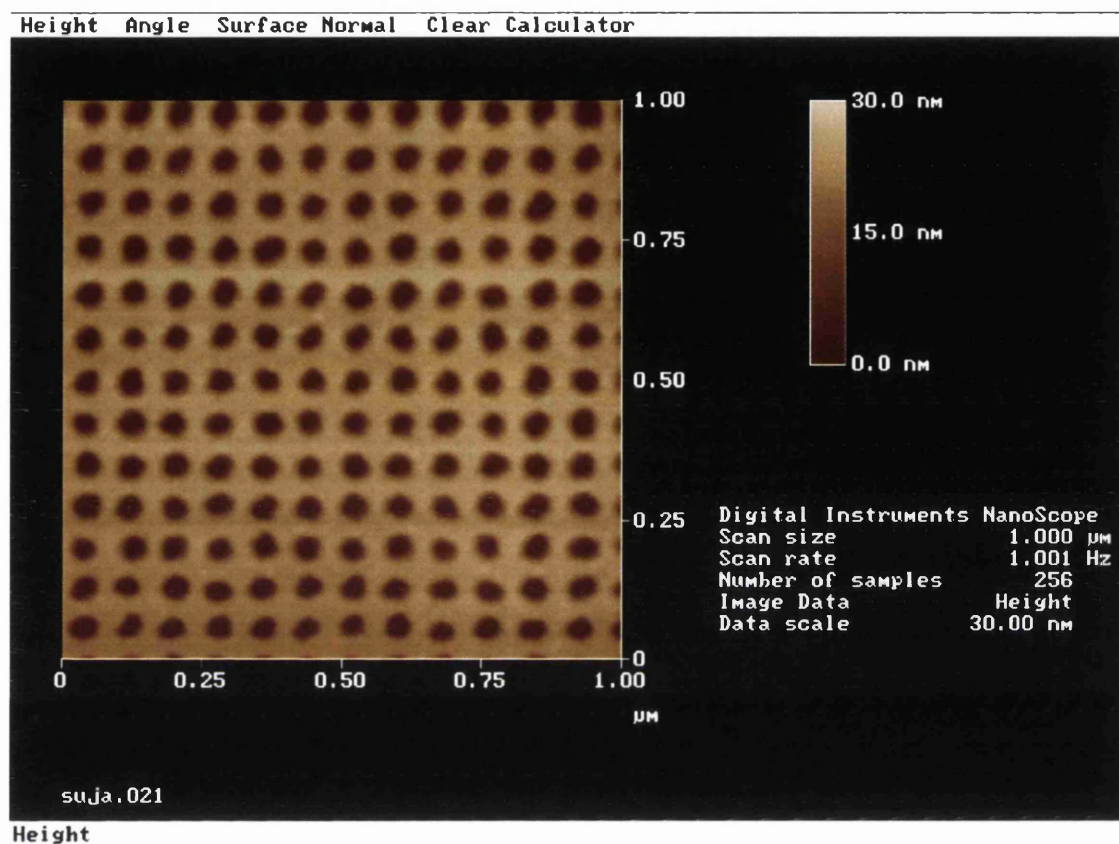
Figure 3.26
Top view of the AFM image of Figure 3.25. The height contrast colour
scale reveals that a) the etching has been uniform and b) the etch depth
is about 20 nm.
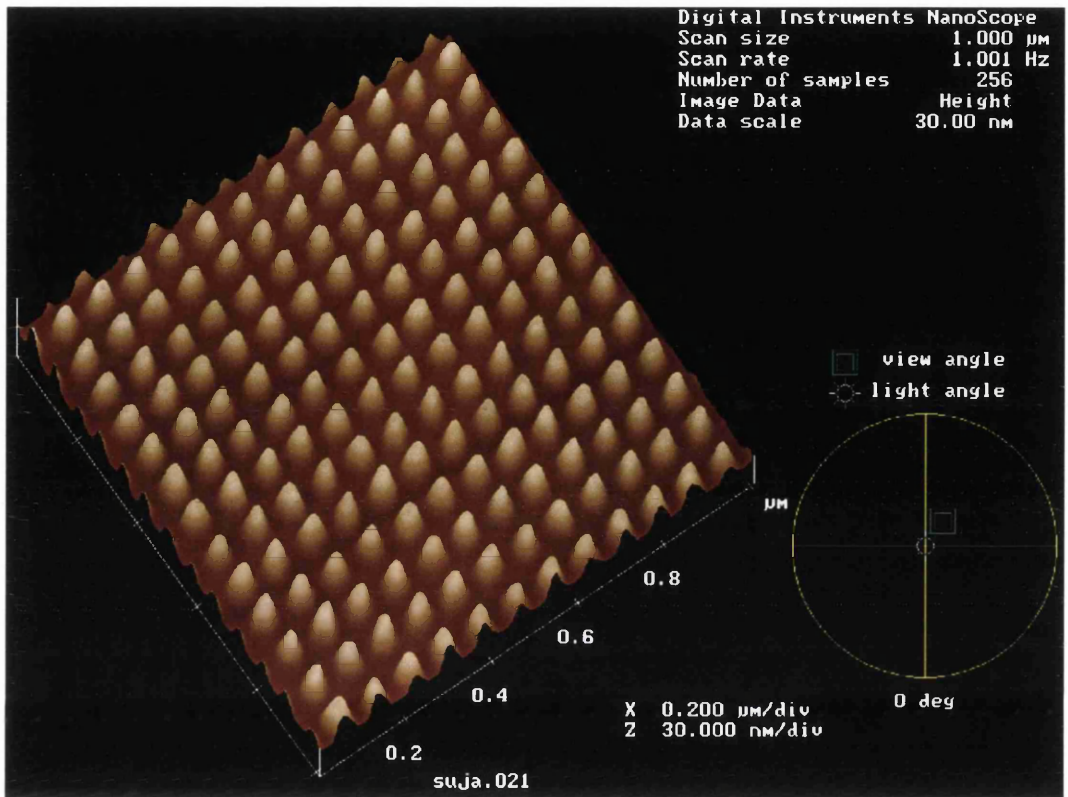
Figure 3.27
Inverted view of the AFM image of Figure 3.25 showing the depth and uniformity of the etched holes.
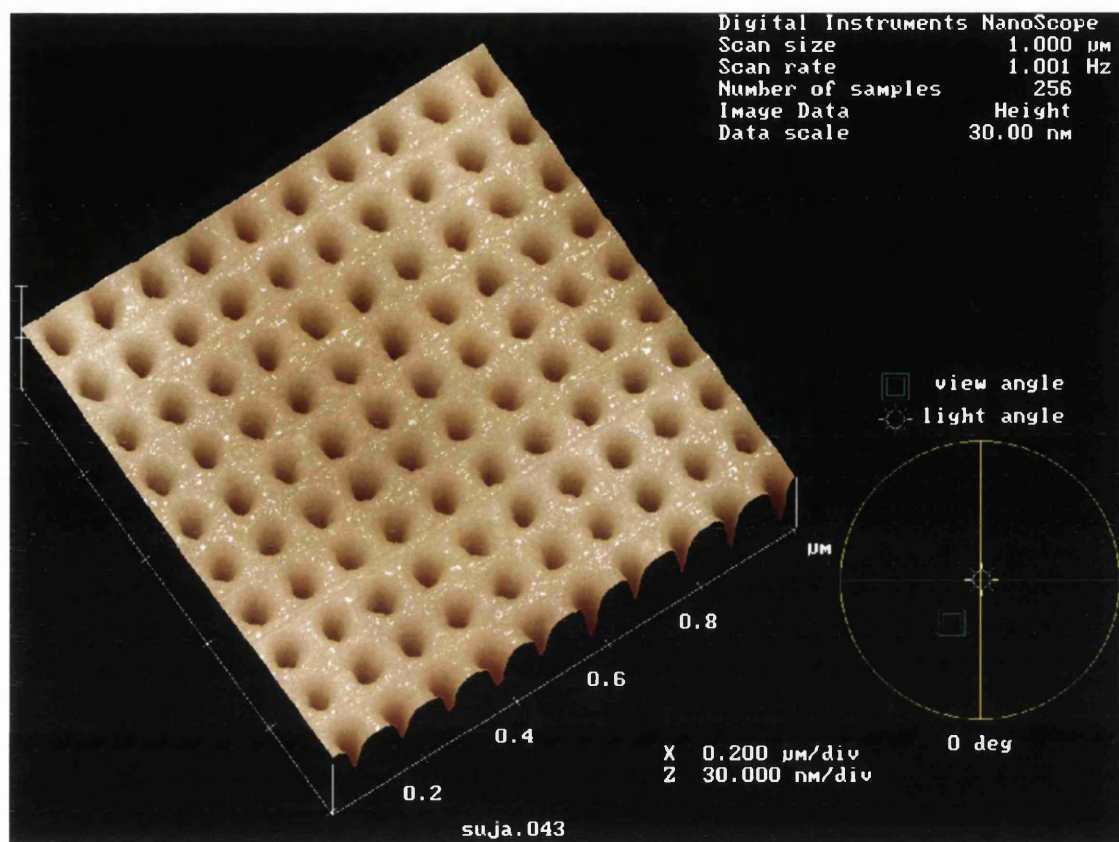
Figure 3.28
Representative AFM image of 100 nm period 2D LSSL of about 50 nm diameter etched holes. The image was taken from a device without a gate but after removal of the resist.
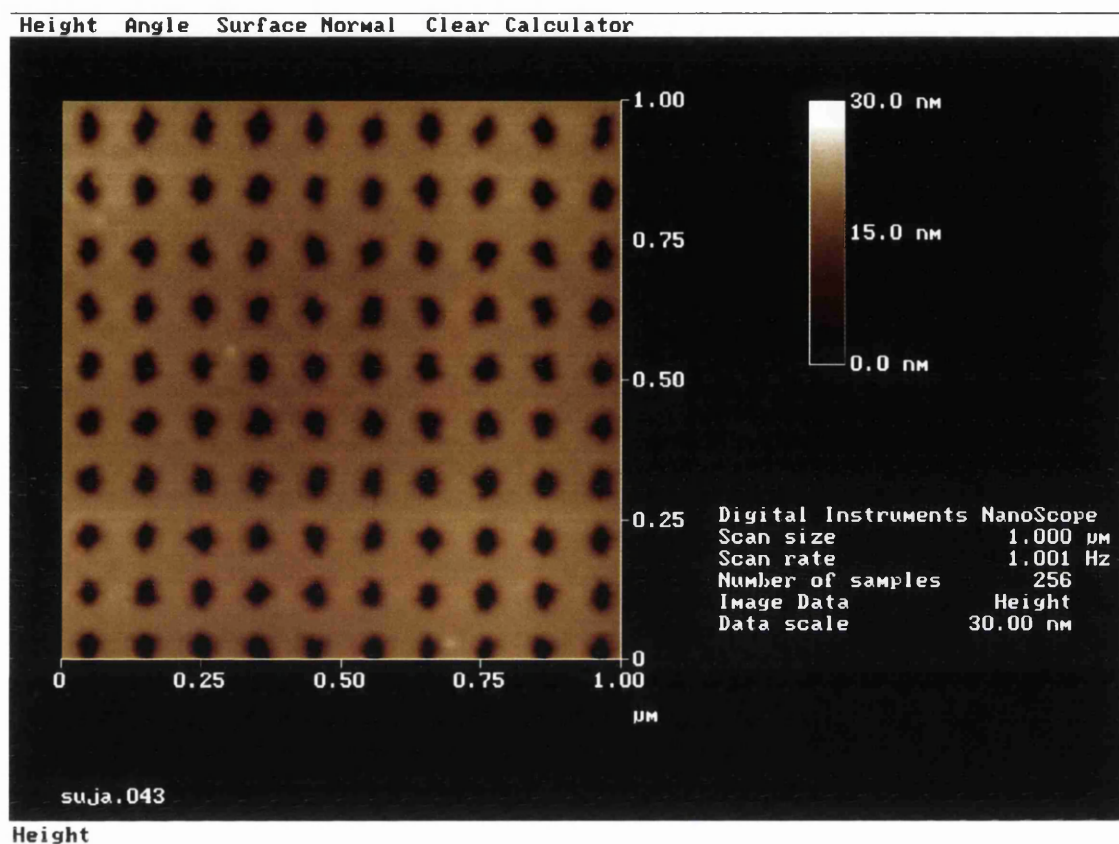
Figure 3.29
Top view of the AFM image of Figure 3.28. The height contrast colour
scale reveals that a) the etching has been uniform and b) the etch depth
is about 20 nm.
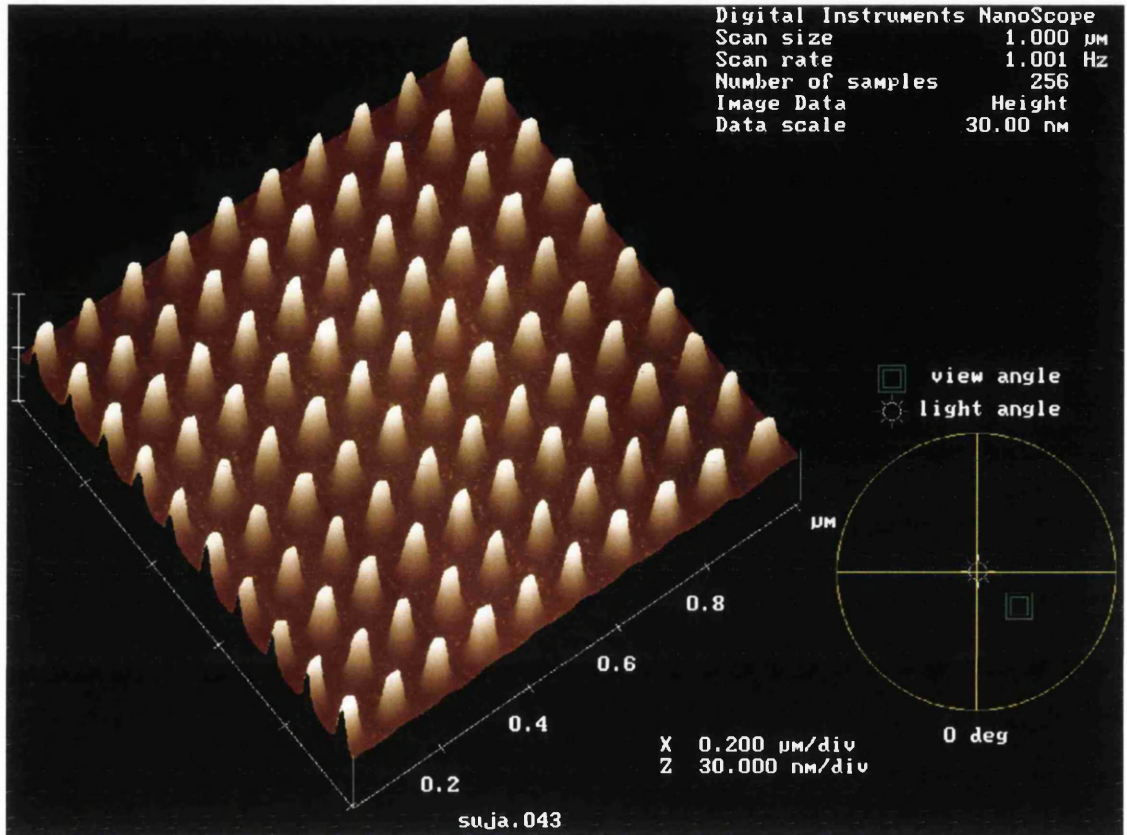
Figure 3.30
The inverted view of the AFM image of Figure 3.28 showing the depth
and uniformity of the etched holes.
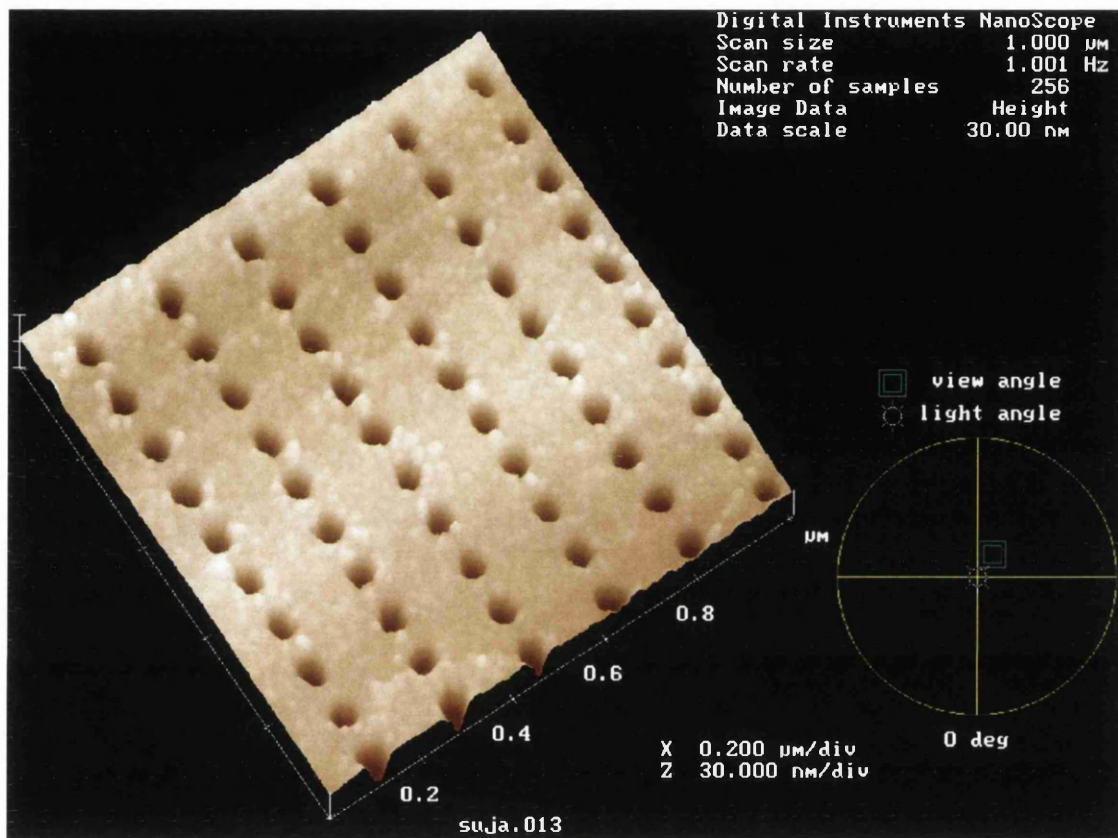
Figure 3.31
Representative AFM image of shallow etched 50 nm diameter holes arranged on 170 nm by 100 nm period rectangular grid. The image was taken from a device without a gate but after removal of the resist.
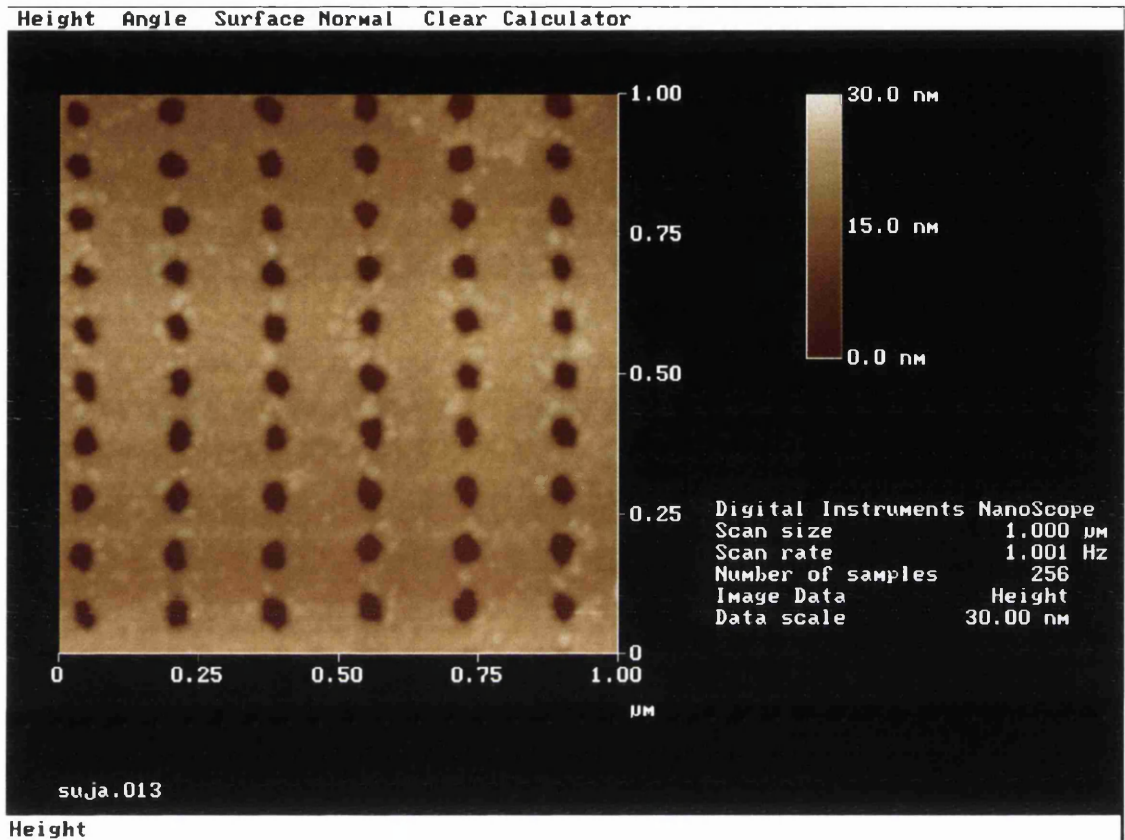
Figure 3.32
Top view of the AFM image of Figure 3.31. The height contrast colour
scale reveals that a) the etching has been uniform and b) the etch depth
is about 20 nm.
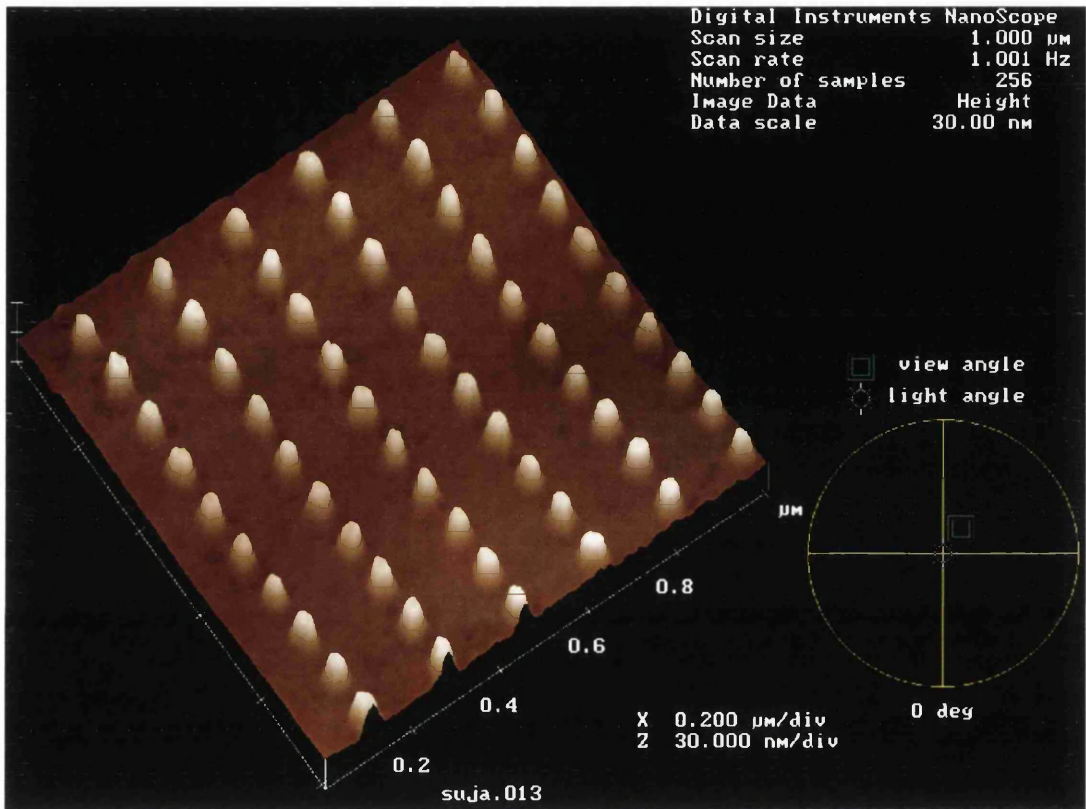
Figure 3.33
The inverted view of the AFM image of Figure 3.31 showing the depth
and uniformity of the etched holes.

The above AFM images show that the etched pattern is quite uniform over
about 1 μm^2 area. The inverted views reveal that the holes have been etched to a
uniform depth and have uniform bores. That the depths of etched holes is about 20 nm
confirms that in the case of stressed devices the holes have completely passed through
the strained layer of InGaAs.

3.3 Experimental procedure

A small piece of substrate material containing a couple of devices is at first glued to a package containing 18 contacts ("pins"). The ohmic pads are then bonded to these pins by wire bonder using 25 μm diameter gold wire, which is a tricky but indispensable job and needs a great deal of skill. The bonding involves a direct interaction with the micron-sized world using an optical microscope as the interface. The package is then put at the end of an insert rod, which provides electrical contact to every pin of the package from the other end of the rod. The rod containing the devices is inserted in the sample space of a cryostat in which liquid Helium is continuously evaporated under pressure reduced by a rotary pump. As such, the boiling point of liquid Helium is reduced from 4.2 K to about 1.6 K. An automatic temperature controller allows one to settle the temperature of the sample space to any desired value between 1.6 K to 300 K. A thermometer in contact with the device end of the insert rod allows the accurate measurement of the temperature of the device. As the COs appear superimposed on SdH oscillations, the temperature of the devices is adjusted to 4 K to suppress the low field SdH oscillations and to reveal the COs more clearly. As the SdH oscillations are more temperature sensitive than the COs, the low field SdH oscillations are suppressed without affecting the COs any appreciably.

The measurement process is schematically described in Figure 3.34. A potential divider circuit is used to pass typically 100 nA current through the device while measuring the resistances. A magnetic field perpendicular to the plane of the 2DEG (contained in the devices) can be continuously swept between 0 and about 10 T. About 3 T is enough for superlattices of around 100 nm period as the cyclotron radius becomes smaller than the lattice constant for higher fields and the cyclotron orbits no longer interact with the periodic potential. Phase sensitive detectors aided by pre-amplification of signals by differential amplifiers are used to measure the current flowing through the Hall bar and the voltage drop across the desired pair of contacts of the sample. Voltage drop across two side contacts is used to get the longitudinal magnetoresistance while to get Hall resistance two opposite contacts of a Hall bar are used as voltage contacts. A computer program accumulates the data and instantly displays the resistance of the sample as a function of the magnetic field. The program also stores the data in a file in a designated folder at the end of each magnetic field sweep.

The isolated ohmic pads mentioned in Figure 3.3 and Figure 3.18 are wire-bonded to some of the pins of the 18 pin package and dc voltage is applied from an

external source from the other end of the insert. This dc voltage acts as gate bias as the said isolated pads are connected to the gate as shown in Figure 3.3, Figure 3.4 and Figure 3.18. Magnetoresistances are measured for various gate biases as well.
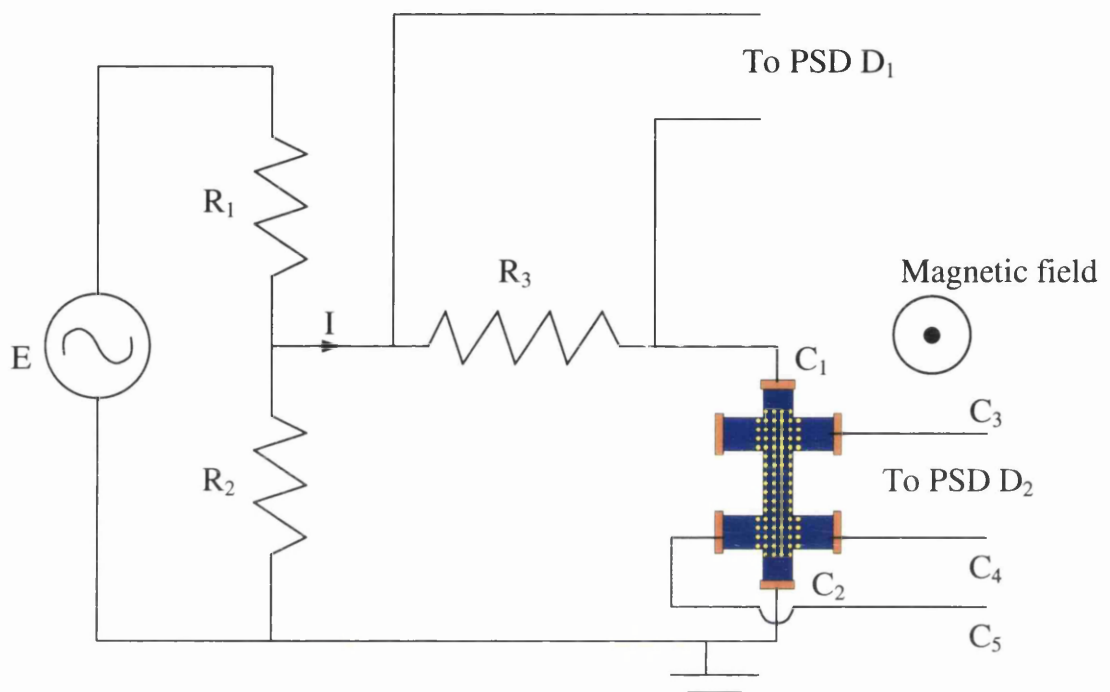
Figure 3.34
A schematic diagram of the measurement of magnetoresistances. E represents the a.c. excitation voltage (18 Hz, different from that of the main electricity), usually 1 V (r.m.s.), applied from an external source. R_1, R_2 and R_3 are resistors of 100 kΩ, 100 Ω and 10 kΩ respectively forming a potential divider circuit allowing only about 100 nA current through the sample. C_1 and C_2 are the source and the drain contacts. I is the current passing through the sample obtained as the voltage measured by the phase sensitive detector (PSD) D_1 divided by R_3. Voltage drop measured across the contacts C_3 and C_4 gives longitudinal voltage while that across C_4 and C_5 gives Hall voltage, measured by another PSD D_2. The output signals are amplified by a factor of 1000 using differential amplifiers before being fed into the PSD's. The sample is placed in a cryostat at liquid Helium temperature. A magnetic field perpendicular to the sample plane is swept between desired values as the current through and the voltage drop across the sample are measured by the PSD's.

One other aspect of the investigations involves cooling down the samples to milli-Kelvin (mK) temperatures. This is sometimes important for investigating quantum mechanical effects. A dilution refrigerator is used to reach device temperature of about 30 mK. Extremely slow magnetic field sweeps are used to extract the details of the magnetoresistance features. Details of the measurement process in this extreme condition including the electronics involved can be found in reference [21].

3.4 References of Chapter III

[1] R. R. Gerhardts; Physical Review B **45** (1992) 3449

[2] D. E. Grant, A. R. Long and J. H. Davies; Physical Review B **61** (2000) 13127

[3] C. J. Emeleus, B. Milton, A. R. Long, J. H. Davies, D. E. Petticrew and M.C.
   Holland; Applied Physics Letters **73** (1998) 1412

[4] E. Skuras, A. R. Long, I. A. Larkin, J. H. Davies and M. C. Holland;
   Applied Physics Letters **70** (1997) 871

[5] M. Tong, D. G. Ballegeer, A. Ketterson, E. J. Roan, K. Y. Cheng and I. Adesida;
   Journal of Electronic materials **21** (1992) 9

[6] Eun-A Moon, Jong-Lam Lee, H. M. Yoo;
   Journal of Applied Physics **84** (1998) 3933

[7] Jong-Hee Kim, D. H. Lim and G. M. Yang;
   Journal of Vacuum Science and Technology B **16** (1998) 558

[8] C. Juang, K. J. Kuhn and R. B. Darling;
   Journal of Vacuum Science and Technology B **8** (1990) 1122

[9] T. Kitano, S. Izumi, H. Minami, T. Ishikawa, K. Sato, T. Sonoda and M. Otsubu;
   Journal of Vacuum Science and Technology B **15** (1997) 167

[10] G. C. DeSalvo, R. Kaspi and C. A. Bozada;
   Journal of Electrochemical Society **141** (1994) 3526

[11] M. Tong, K. Nummila, A. A. Ketterson, I. Adesida, L. Aina, M. Mattingly;
   Journal of Electrochemical Society **139** (1992) L91

[12] G. C. DeSalvo, W. F. Tseng and J. Comas;
   Journal of Electrochemical Society **139** (1992) 831

[13] X. Hue, B. Boudart and Y. Crosnier;
   Journal of Vacuum Science and Technology B **16** (1998) 2675

[14] M. Tong, K. Nummila, A. Ketterson, I. Adesida, C. Caneau and R. Bhat;
   IEEE Electron Device Letters **13** (1992) 525

[15] B. Y. Mao, J. A. Nielsen, R. A. Friedman and G. Y. Lee;

Journal of Electrochemical Society **141** (1994) 1082

[16] H. J. Lee, M. S. Tse, K. Radhakrishnan, K. Prasad, J. Weng, S. F. Yoon, X. Zhou,

H. S. Tan, S. K. Ting and Y. C. Leong; Materials Science and Engineering B-Solid

State Materials For Advanced Technology **35** (1995) 230

[17] J. Smoliner, V. Rosskopf, G. Berthold, E. Gornik, G. Böhm and G. Weimann;

Physical Review B **45** (1992) 1915

[18] K. Y. Lee, D. P. Kern, K. Ismail, R. J. Haug, T. P. Smith III, W. T. Masselink and

J. M. Hong; Journal of Vacuum Science and Technology B **8** (1990) 1366

[19] S. Chowdhury, C. J. Emeleus, B. Milton, E. Skuras, A. R. Long, J. H. Davies,

G. Pennelli and C. R. Stanley; Physical Review B **62** (2000) R4821

[20] C. Albrecht, J. H. Smet, D. Weiss, K. von Klitzing, R. Hennig, M. Langenbuch,

M. Suhrke, U. Rössler, V. Umansky, H. Schweizer;

Physical Review Letters **83** (1999) 2234

[21] "A measurement system for and the measurement of single particle energies in

quantum dots" : Ph.D. thesis by Kevin Lister, University of Glasgow, Glasgow

G12 8QQ, U.K.

Chapter IV: Transport in stressed square and unstressed rectangular lattices: commensurability oscillations of two-dimensional lateral surface superlattices are defined by asymmetry

A wide range of asymmetric and symmetric 2D LSSLs were fabricated, some containing a strained layer close to the surface. The magnetoresistances were measured with a view to understanding the mechanism of electron transport in 2D LSSLs. It was found that the data obtained from asymmetric 2D LSSLs fit very well with a semi-classical model [1], while to understand those of symmetric 2D LSSLs, an interplay between the semi-classical [1] and quantum mechanical [2] aspects of physics is necessary. The data of asymmetric 2D LSSLs were found to agree with two major aspects of the semi-classical theory [1]. Those of stressed square and unstressed rectangular 2D LSSLs confirm that the commensurability oscillations of 2D LSSLs are defined by the asymmetry in the potential landscape. Those of stressed rectangular 2D LSSLs provide a striking confirmation of the concept of *switching* of the guiding centre drift direction in asymmetric 2D LSSLs. Thus naturally, the discussion of the data has been divided into three chapters. Chapter IV contains the discussion on the magnetoresistances of stressed square and unstressed rectangular 2D LSSLs which demonstrates that the commensurability oscillations of 2D LSSLs are defined by the asymmetry in the potential landscape as envisaged by the guiding centre drift model of Grant, Long and Davies [1]. Chapter V contains the discussion on the magnetoresistances of stressed rectangular 2D LSSLs which provides a striking experimental confirmation of *switching* of guiding centre drift direction in asymmetric 2D LSSLs, a phenomenon predicted by the guiding centre drift model of Grant, Long and Davies [1]. Finally, magnetoresistance data of symmetric 2D LSSLs are discussed in Chapter VI which demonstrate that an interplay between semi-classical dynamical effects [1] and quantum mechanical effects [2] is necessary to account for the data in detail. Moreover, as also discussed in Chapter VI, symmetric, stressed, short period and high mobility 2D LSSLs show a characteristic amplitude modulation of COs involving inverse flux quantum periodicity.

4.1 Stressed devices with square lattices

Although the rectangular superlattice on an unstressed Hall bar is an asymmetric 2D LSSL, it does not posses a direct symmetric counterpart. Hence the

square superlattice with periodic stress modulation was realised first to compare the magnetoresistance characteristics of the asymmetric 2D LSSL with those of its symmetric counterpart, namely the unstressed device of square symmetry discussed in section 6.2. As discussed in section 3.1, in stressed devices, addition of periodic stress modulation to the surface effect turns the potential landscape of square lattices asymmetric. Both ungated and gated stressed devices containing square lattices were realised and the data are discussed in the following two sub-sections.

4.1.1 Ungated stressed devices with square lattices

Two pairs of ungated devices were fabricated and measured after removal of resist. The two pairs were etched for two different set times. Scanning electron microscopy following the measurements confirmed that correct pattern had been obtained. Data are discussed below.

The pair of traces in Figure 4.1 below was obtained in the same cooling cycle as the two devices were on the same chip. The data have some very striking features.

- There are very large COs, as large as for the ρ_{xx} data of 1D LSSLs, for transport in $[01\bar{1}]$ direction [on a (100) GaAs wafer] while there are no COs for transport along the orthogonal direction [011]. (The quality of the lattices on both the Hall bars was, however, found to be identical in every respect in the extensive microscopy carried out after the measurement over the entire extent of etched patterns.)

- Associated with the large COs is a large PMR at low magnetic field, which saturated at 0.36 T, a remarkably high value. There is a broad PMR like feature in the [011] data at low field that saturated at about 0.45 T.

The magnetic field values of the CO minima calculated for $[01\bar{1}]$ using the mean carrier density obtained from several high field SdH oscillations and taking the period to be 100 nm are indicated in Figure 4.1 by red vertical bars. The correct location of the k = 1 minimum has been obscured by the very strong SdH oscillations at the high magnetic fields. The agreement of these calculated locations of CO minima with the experimental data demonstrates that the phase factor φ in the commensurability condition $2R_c = (k - \varphi)a$ is very close to 1/4, unlike in many of the results reported in the literature.

One other point that should be noted is that the carrier density and specially the mobility of both the devices decreased appreciably during pattern transfer, as is apparent in Table 4.1 below. The mobility μ was calculated using the mean carrier density n_{2D} (obtained from several SdH oscillations at high fields) and the zero field

resistivity ρ_0 for each curve using $\mu = 1/(en_{2D}\rho_0)$. The mobility reduced to below 10 $m^2V^{-1}s^{-1}$ which is nowhere near the high mobility used in searches for quantum mechanical effects [3].
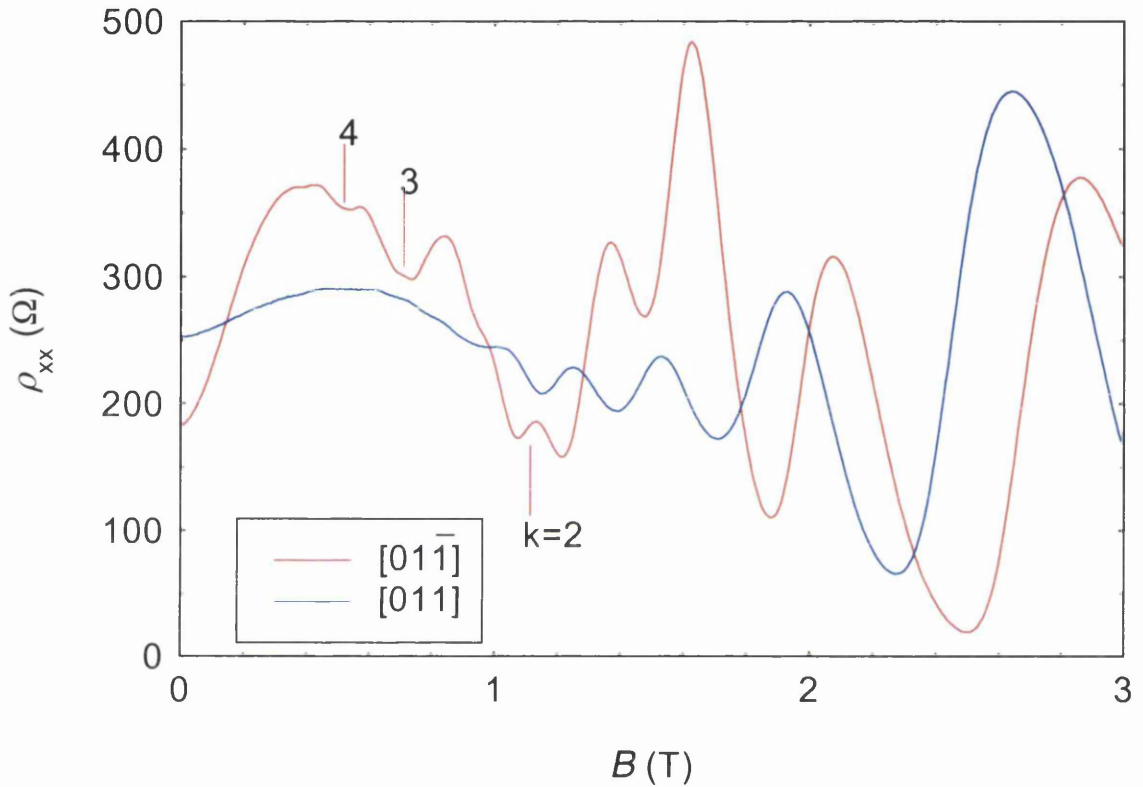
Figure 4.1
Magnetoresistivities of *ungated* stressed devices measured at 4 K after removal of resist. Transport is along the [011] and [01$\bar{1}$] directions in 100 nm period square superlattices of 50 nm diameter shallow etched holes at the surface of the Hall bars. The 100 nm period was aligned along both [011] and [01$\bar{1}$] directions. The red vertical bars indicate the locations of predicted minima of COs in [01$\bar{1}$] for 100 nm period for the carrier density in question, obtained from the SdH oscillations at higher magnetic field. There are no COs in [011]; oscillations above about 1 T are SdH oscillations.

Table 4.1
Comparison of the carrier density and mobility of the devices of Figure
4.1 with those of unpatterned Hall bars under similar conditions.

	Carrier density (m^{-2})	Mobility ($m^2V^{-1}s^{-1}$)
Unpatterned Hall bar	Typically 4.3×10^{15}	Around 90
$[01\overline{1}]$ device of Figure 4.1	3.5×10^{15}	9.8
$[011]$ device of Figure 4.1	3.4×10^{15}	7.2

Before giving a theoretical account of the data, it is both relevant and important to describe the potential landscape defined at the 2DEG by the stressed lattices of square symmetry. AFM studies confirmed that the shallow etched holes have passed through the strained layer of InGaAs. As such, periodic stress modulation has been realised which couples to the 2DEG by the anisotropic piezoelectric effect [4]. There is no stress modulation along [010] and [001] directions, while there are significant stress modulations along [011] and $[01\overline{1}]$ on a (100) GaAs wafer. The stress modulations along [011] and $[01\overline{1}]$ are equal in magnitude but opposite in sign. Besides stress modulation, periodic removal of material from the heterostructure surface brings the surface states periodically closer to the 2DEG and thereby brings about periodic modulation at the 2DEG. This is called the "surface effect" [4]. The surface effect has same sign in all directions. In particular for a square superlattice, the surface effects along the pair of orthogonal directions (axial or diagonal) in the plane of the 2DEG are equal. Thus of $[01\overline{1}]$ and [011], the two sources of modulation add to each other along one direction and cancel each other in the other. This cancellation is partial or complete depending on whether the modulations along [011] due to the two mechanisms are unequal or equal respectively. For 100 nm period, $[01\overline{1}]$ is the direction of reinforcement [5]. So the potential landscape is asymmetric. The modulation along $[01\overline{1}]$ is dominant, i.e. larger than those along [011], [010] and [001]. An important point to note is that diagonal Fourier components along both [010] and [001] are present in the potential landscape, but are weak and there is no asymmetry between them. These are because the period associated ($100/\sqrt{2}$ nm) is shorter and modulations along [010] and [001] directions are due to surface effect only. The modulation amplitude associated with a short period is small [6]. The relative amplitudes of the four Fourier components in the periodic potential are illustrated in a reciprocal lattice diagram in Figure 4.2 below.
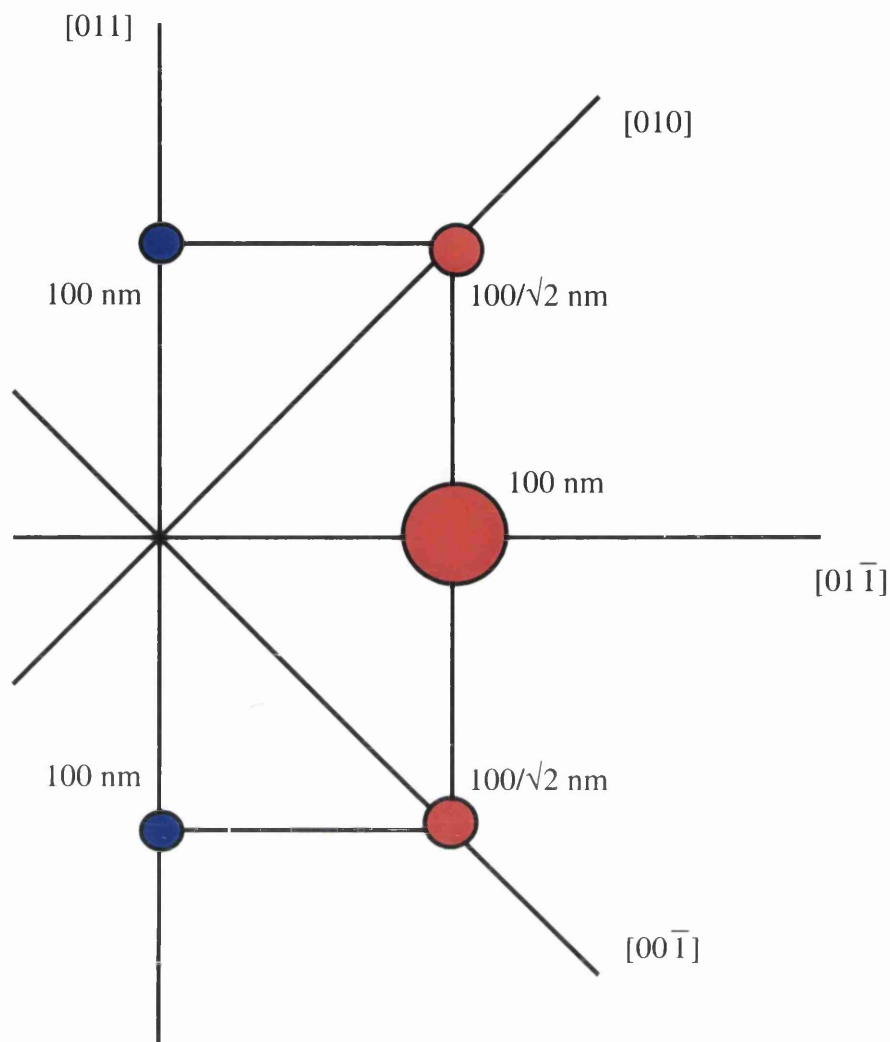
Figure 4.2
Reciprocal lattice points (shown over half of reciprocal space) of a 100 nm period stressed square lattice, with the 100 nm period aligned along [01$\overline{1}$] and [011] directions. The relative sizes of the circles at the reciprocal lattice points indicate schematically the relative amplitudes of the Fourier components, while the two colours of circles, red and blue, indicate opposite sign of potential. (It is assumed that the surface component is smaller than the stress component, which is appropriate for short period superlattices.)

(a) Transport along [011]

[001]

[011] is the direction
of guiding centre drift

[010]

(b) Transport along [01 $\bar{1}$]

[01 $\bar{1}$] is the direction of
modulation of the dominant
Fourier component
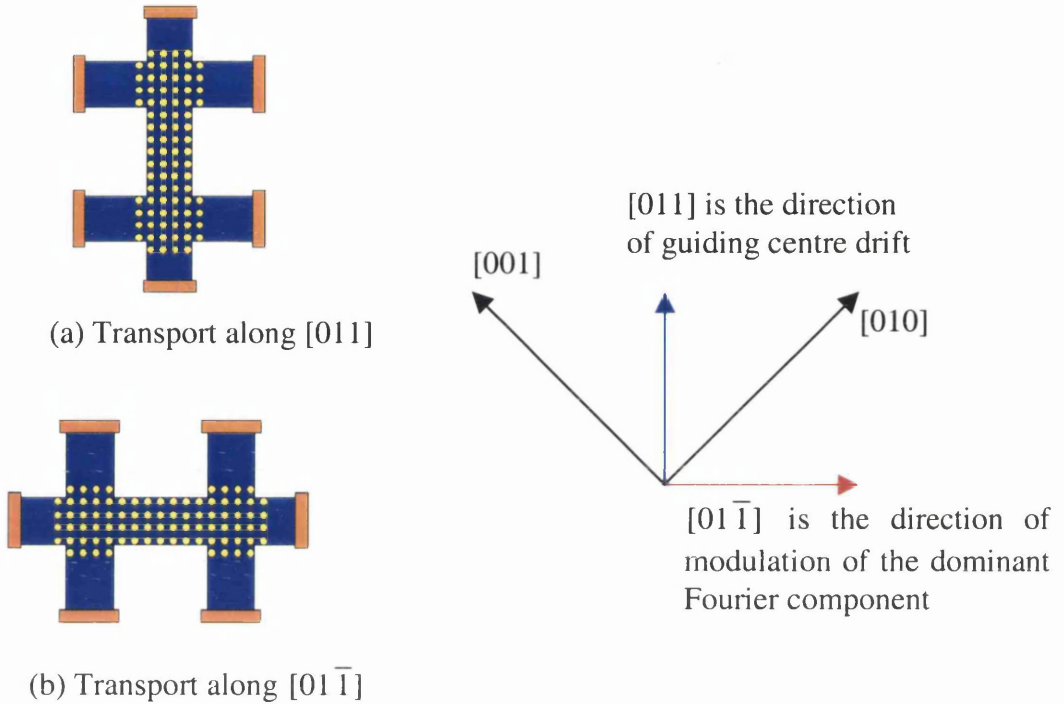
Figure 4.3
A schematic diagram showing the direction of modulation of the
dominant Fourier component and guiding centre drift direction relative
to the two Hall bars in question. In (a) transport is along [011], across
the direction of modulation of the dominant Fourier component and
guiding centre drifts along the Hall bar. In (b) transport is along [01 $\bar{1}$],
the direction of modulation of the dominant Fourier component and
guiding centre drifts across the Hall bar.

As discussed in Chapter II, according to the guiding centre drift model [1], in
asymmetric 2D LSSLs guiding centre drifts *only* in the direction orthogonal to the
direction of modulation of the dominant Fourier component. This situation is depicted
in Figure 4.3. For transport along [011] (see Figure 4.3(a)), orthogonal to the direction
of modulation of the dominant Fourier component, guiding centre drifts along the Hall
bar. As there is no component of this drift across the Hall bar, no COs should be picked
up in the magnetoresistances *exactly* as is observed (see Figure 4.1). Again, for
transport along [01 $\bar{1}$] (see Figure 4.3(b)), along the direction of modulation of the
dominant Fourier component, guiding centre drifts across the Hall bar. In analogy with

1D LSSLs, there should be large COs in the magnetoresistances *exactly* as is observed (see Figure 4.1). There can be *only* one direction of guiding centre drift determined by the dominant Fourier component as predicted by the guiding centre drift model [1] in agreement with experiment.

If the cancellation of the two sources of modulation in [011] is partial (not complete), significant stress modulation is expected to be present in [011] (assuming that the modulation due to the surface effect is weaker than the stress modulation, which is the case in short period superlattices, as already mentioned) that did not give rise to COs for transport in [011] (see Figure 4.1). This contradicts the early semi-classical model [7] and a corresponding quantum mechanical calculation [2] according to which every Fourier component in a 2D LSSL independently contributes to the magnetoresistivity. This point is further addressed in section 4.1.2. Moreover, as already noted, diagonal Fourier components are present in the potential landscape, but there is no sign of these in the data (see Figure 4.1). Admittedly, it can be argued that the diagonal Fourier components, being of short period ($100/\sqrt{2}$ nm) and due to surface effect only, are too weak to be present in the COs. The modulation amplitude associated with a short period is small [6], as already mentioned.

The observation of large PMR in [01$\bar{1}$] (see Figure 4.1) suggests that large PMR is associated with large asymmetry in the potential landscape. This is discussed in section 4.1.3 in more detail with reference to gated devices in which the degree of asymmetry could be changed by biasing the overlying gate.

We now discuss the data of the other pair of ungated devices. These two devices were etched for a shorter time than that of the devices of Figure 4.1. The directions of transport this time are [010] and [001], with the 100 nm period along these two directions. Data are shown in Figure 4.4 below, and were obtained in the same cooling cycle as the two devices were on the same chip. There are several remarkable features in the data as follows.

- The period of the COs of both devices is *not* 100 nm but $100/\sqrt{2}$ nm.

- The magnetoresistance characteristics of both the devices are almost identical.

- The COs are weak in amplitude.

- There is an interference like feature at low magnetic field indicated by the arrow.

The minima of the COs agree remarkably well with the calculated locations for $100/\sqrt{2}$ nm period as indicated by vertical bars in Figure 4.4. This demonstrates that the period is $100/\sqrt{2}$ nm and that the phase factor φ in the commensurability condition $2R_c = (k - \varphi)a$ is very close to 1/4 for $a = 100/\sqrt{2}$ nm.
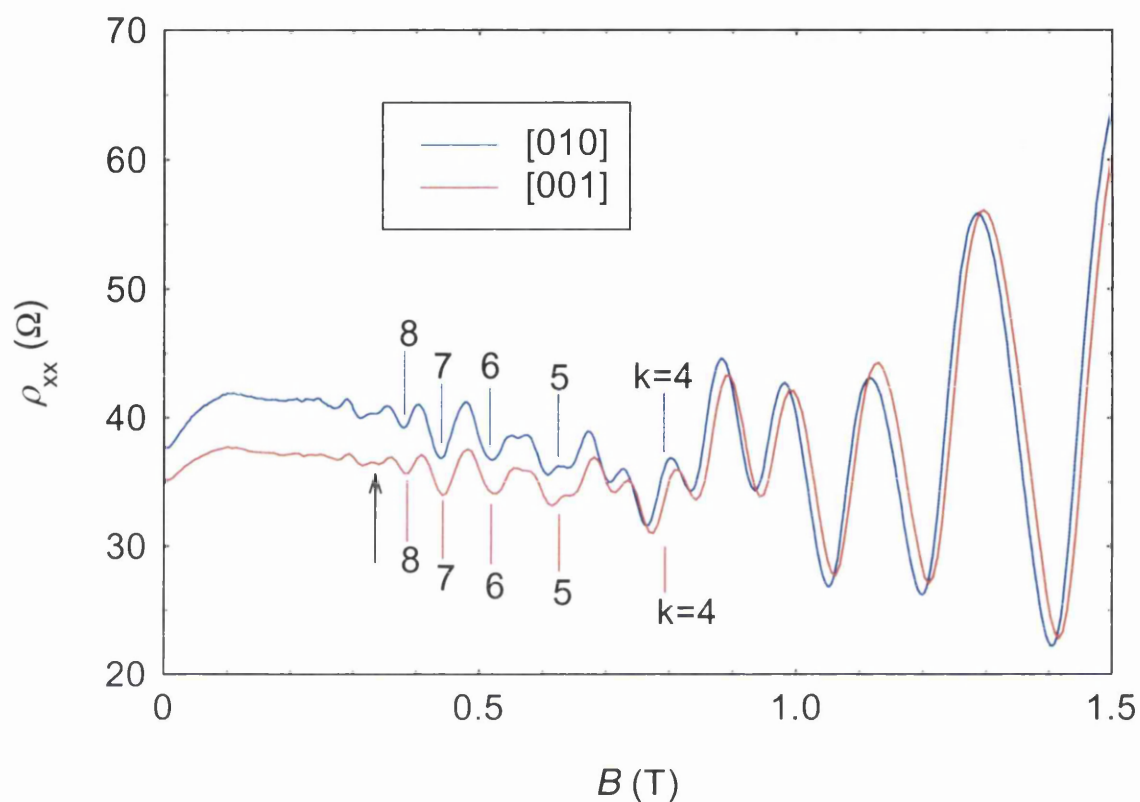
Figure 4.4

Magnetoresistivities of *ungated* stressed devices measured at 4 K after removal of resist. Transport is along the [010] and [001] directions in 100 nm period square superlattices of 50 nm diameter shallow etched holes at the surface of the Hall bars. The 100 nm period was aligned along the [010] and [001] directions. The vertical bars, red ones for the red trace and blue ones for the blue trace, indicate the predicted locations of minima of the COs for $100/\sqrt{2}$ nm period for the carrier densities obtained from respective SdH oscillations at higher magnetic field.

It is important to describe the potential landscape before giving a theoretical account of the data. As already noted, the Fourier components along [010] and [001] are due to surface effects only and being the orthogonal principal directions in the square lattice, there is no asymmetry between these two directions. However, there are stress modulations along both the diagonal Fourier components of the two devices in question, as the diagonal Fourier components in question are along the [011] and [01$\bar{1}$] directions this time. The stress modulations along [011] and [01$\bar{1}$] are equal in magnitude but opposite in sign. The surface effect has the same sign in all directions in the plane of the 2DEG. The surface effects associated with the diagonal Fourier components are small, because the period 100/$\sqrt{2}$ nm is short. As already mentioned, the modulation amplitude associated with a short period is small [6]. The surface effect adds to the stress modulation along one of the diagonal Fourier components and the two modulations partially cancel each other along the other diagonal Fourier component. For periods around 100 nm, theory predicts [6, 8] that [01$\bar{1}$] is the direction of reinforcement. Hence, the diagonal Fourier component along [01$\bar{1}$] is dominant, i.e. larger than those along [011], [010] and [001]. The axial Fourier components, although larger in period, cannot dominate because (a) these are due to the surface effect only and (b) the devices were etched for a shorter time introducing a smaller surface effect. The asymmetry is small, as the surface effect is small. The relative amplitudes of the four Fourier components in the periodic potential are illustrated in a reciprocal lattice diagram in Figure 4.5 below.

As discussed in Chapter II, according to the guiding centre drift model [1], in asymmetric 2D LSSLs, guiding centre drifts *only* in the direction orthogonal to the direction of modulation of the dominant Fourier component. The situation is depicted in Figure 4.6 below. [011] is the direction of guiding centre drift. As shown in Figure 4.6, the directions of transport [001] and [010] in the two Hall bars are both at an angle of 45° with the direction of guiding centre drift. Hence the drift has components across both the Hall bars and these components are equal. Hence the magnetoresistance characteristics of both the Hall bars should be identical and the period of the COs in both should be that of the diagonal Fourier components of the square lattice which is 100/$\sqrt{2}$ nm as observed (see Figure 4.4 above). The COs are weak, as the asymmetry is small, as already discussed. This is because in a potential landscape in which the asymmetry is small, a large fraction of guiding centre trajectories are closed and do not contribute to COs according to the guiding centre drift model [1].

The interference-like feature in the data is discussed later in section 4.1.2 along

with the question if the previous models [2, 7] can account for the data.
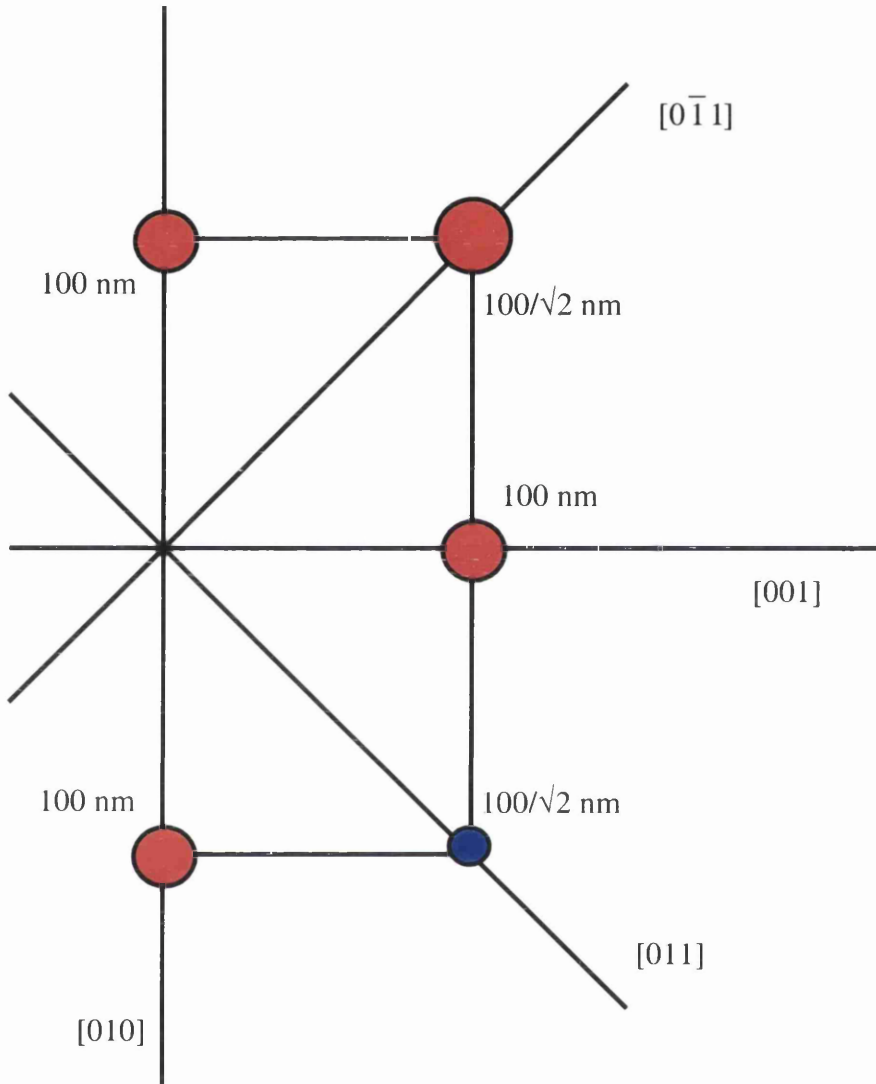
Figure 4.5
Reciprocal lattice points (shown over half of reciprocal space) of a 100 nm period stressed square lattice, with the 100 nm period aligned along the [010] and [001] directions. The relative sizes of the circles at the reciprocal lattice points indicate the relative amplitudes of the Fourier components, while the two colours of the circles, red and blue, indicate opposite sign of potential.

(a) Transport along [001]

[011] is the direction of guiding centre drift

[001]

[010]

[01 $\bar{1}$] is the direction of modulation of the dominant Fourier component

(b) Transport along [010]
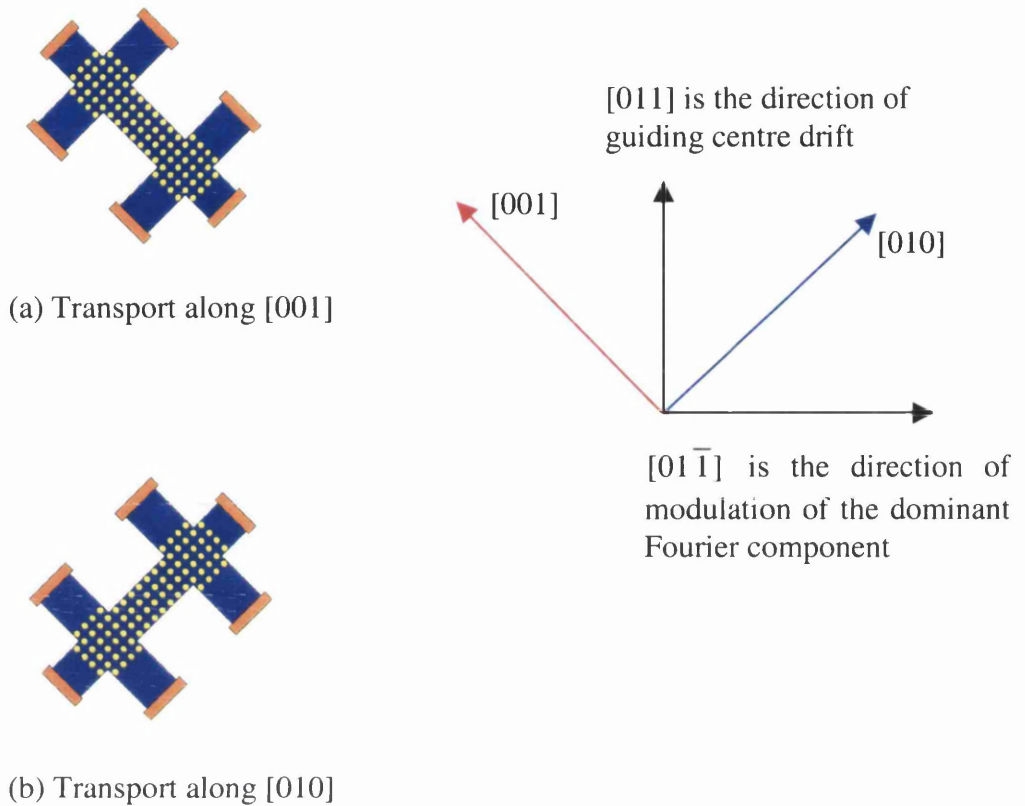
Figure 4.6

Schematic diagram showing the direction of modulation of the dominant Fourier component and guiding centre drift direction relative to the two Hall bars in question. In (a) transport is along [001], at an angle of 45° with the guiding centre drift direction. In (b) transport is along [010], also at an angle of 45° with the guiding centre drift direction.

4.1.2 Gated stressed devices with square lattices

Referring to the devices of Figure 4.1, if the two sources of modulation have not cancelled each other exactly in the [011] direction, there are potential modulations along both [01 $\bar{1}$] and [011], that along [01 $\bar{1}$] being larger in amplitude than that along [011]. But as there is no standard way to determine the potential amplitudes from the magnetoresistance data of 2D LSSLs, it can be argued that the observation of no COs in the [011] direction (see Figure 4.1) may well have been due to an exact cancellation of the two sources of modulation along [011]. To address this issue, gated devices were fabricated in which the change in gate bias changes the surface effect appreciably while

leaving the stress modulation unchanged (apart from any small change in screening). Hence there cannot be an exact cancellation of the two types of modulations in [011] direction for all gate biases.

Data obtained from ungated devices were discussed above, before discussing below those of the gated devices. This is because they show the main features of the data, for samples where the quality of the etched pattern could then be confirmed.

Having obtained (ungated) working devices discussed above, the resist pattern of several sets of four Hall bars was transferred by shallow etching for a duration intermediate between those of the ungated devices discussed above. Then the resist pattern was removed and subsequent lithographic steps and evaporation were performed to realise thick continuous gate overlying the etched area of the Hall bars. A group of four devices was removed by cleaving just before the evaporation. Extensive SEM studies of this revealed that the etched pattern is correct on Hall bars of all four orientations. The pattern of these ungated devices should be representative of that of the gated devices. Magnetotransport was studied on two sets of four gated devices. Data are discussed below. Figure 4.7 shows the data for Hall bars in the cleavage directions without gate bias.

The magnetic field values of the CO minima calculated as before for $[01\bar{1}]$ for 100 nm period are indicated in Figure 4.7 by red vertical bars. The agreement with data demonstrates that the phase factor φ in $2R_c = (k - \varphi)a$ is very close to 1/4.

The two devices of each orientation were 2.5 mm apart on the substrate. The two orthogonal Hall bars were close to each other on each chip and were measured in the same cooling cycle. As Figure 4.7 demonstrates, the data have been reproduced quite closely from two devices of each kind. This indicates that etching has been uniform over an area on the millimetre scale.

The mobility of the devices has been lowered appreciably during pattern transfer, to around 15 $m^2V^{-1}s^{-1}$. The data of Figure 4.7 are consistent with those of the ungated devices already discussed in section 4.1.1. There are large COs in $[01\bar{1}]$ and no COs in [011]. There is large PMR associated with large COs. The same explanations illustrated in picture as in Figure 4.2 and Figure 4.3 hold and hence the data agree with the guiding centre drift model [1]. Data for several other gate biases are shown below to clarify if the absence of COs in [011] direction is due to an exact cancellation of the two types of modulations along [011]. As this is a subtle point, data obtained from two sets of devices are shown for each gate bias.
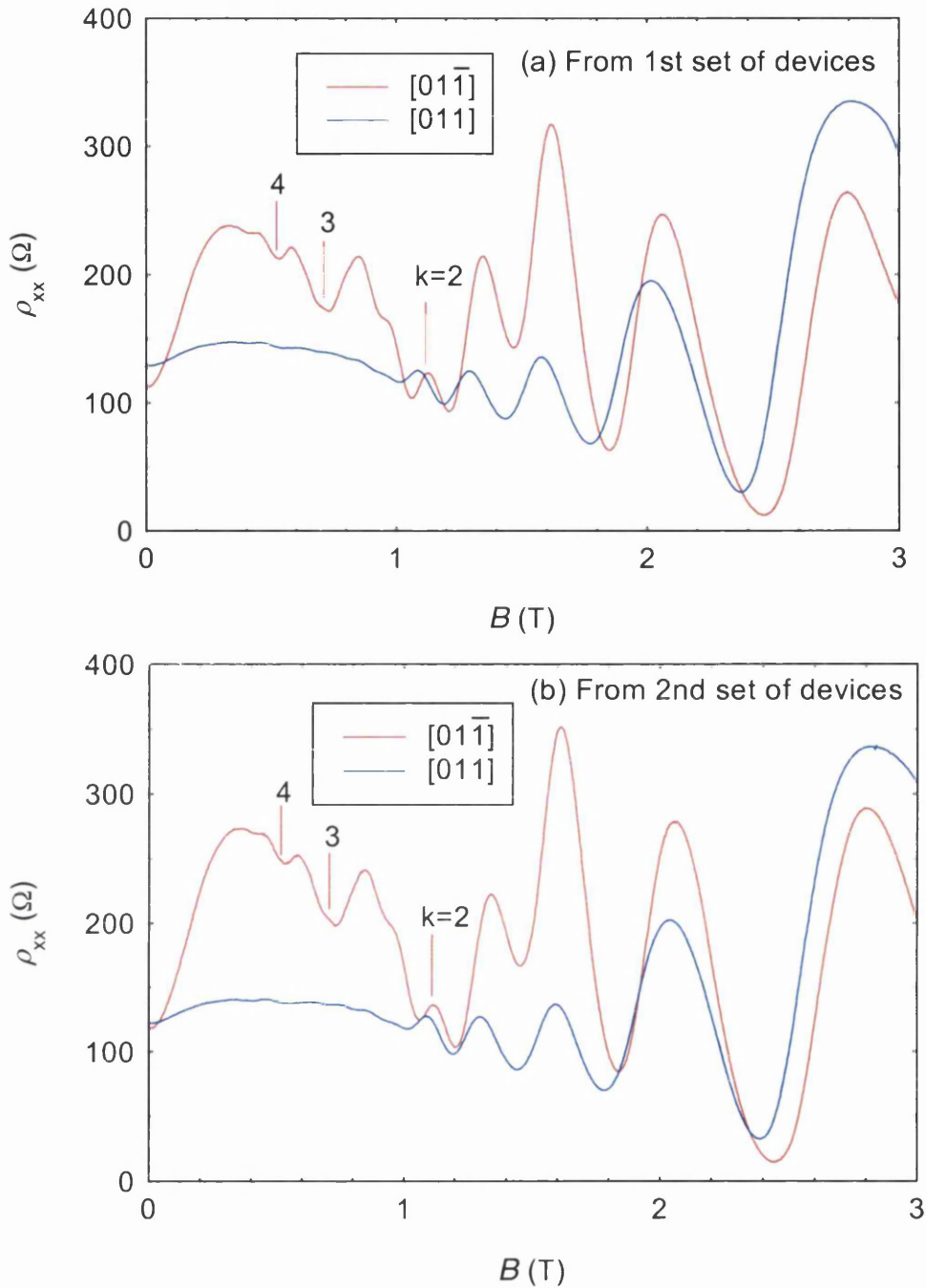
Figure 4.7

Magnetoresistivities of *gated* stressed devices of (a) 1st set, (b) 2nd set measured at 4 K without any gate bias. Transport is along the [011] and [01$\bar{1}$] directions in 100 nm period square lattice with 50 nm diameter shallow etched holes at the surface of Hall bars. The 100 nm period was aligned along both [011] and [01$\bar{1}$] directions. The red vertical bars indicate the locations of predicted minima of COs in [01$\bar{1}$] for 100 nm period and for the appropriate carrier densities obtained from the SdH oscillations at higher magnetic field. There are *no* COs at all in [011]; the oscillations above about 1 T are SdH oscillations.
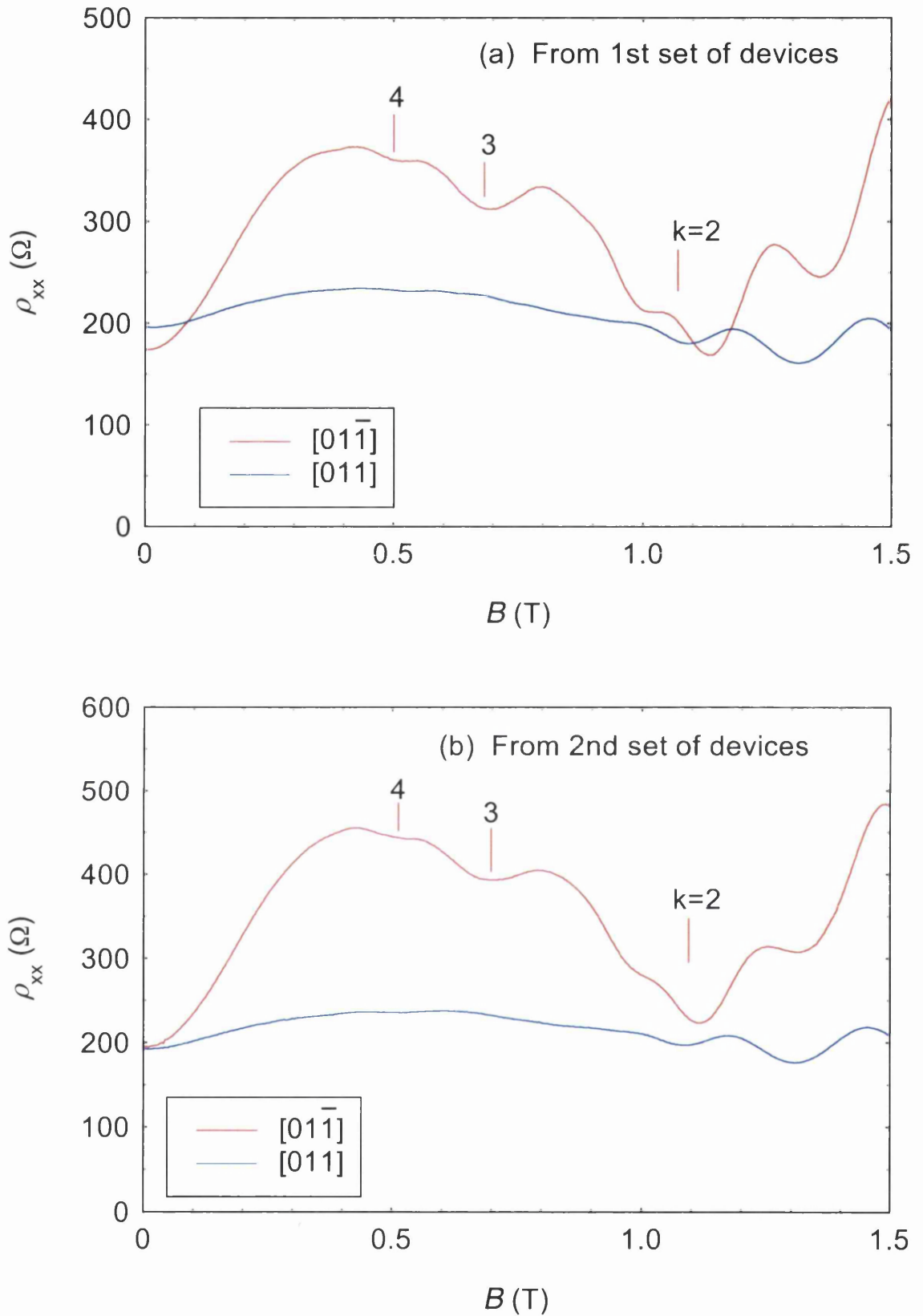
Figure 4.8
Data at -0.05 V gate bias from (a) 1st and (b) 2nd set of devices. Other
specifications are as in Figure 4.7 above.
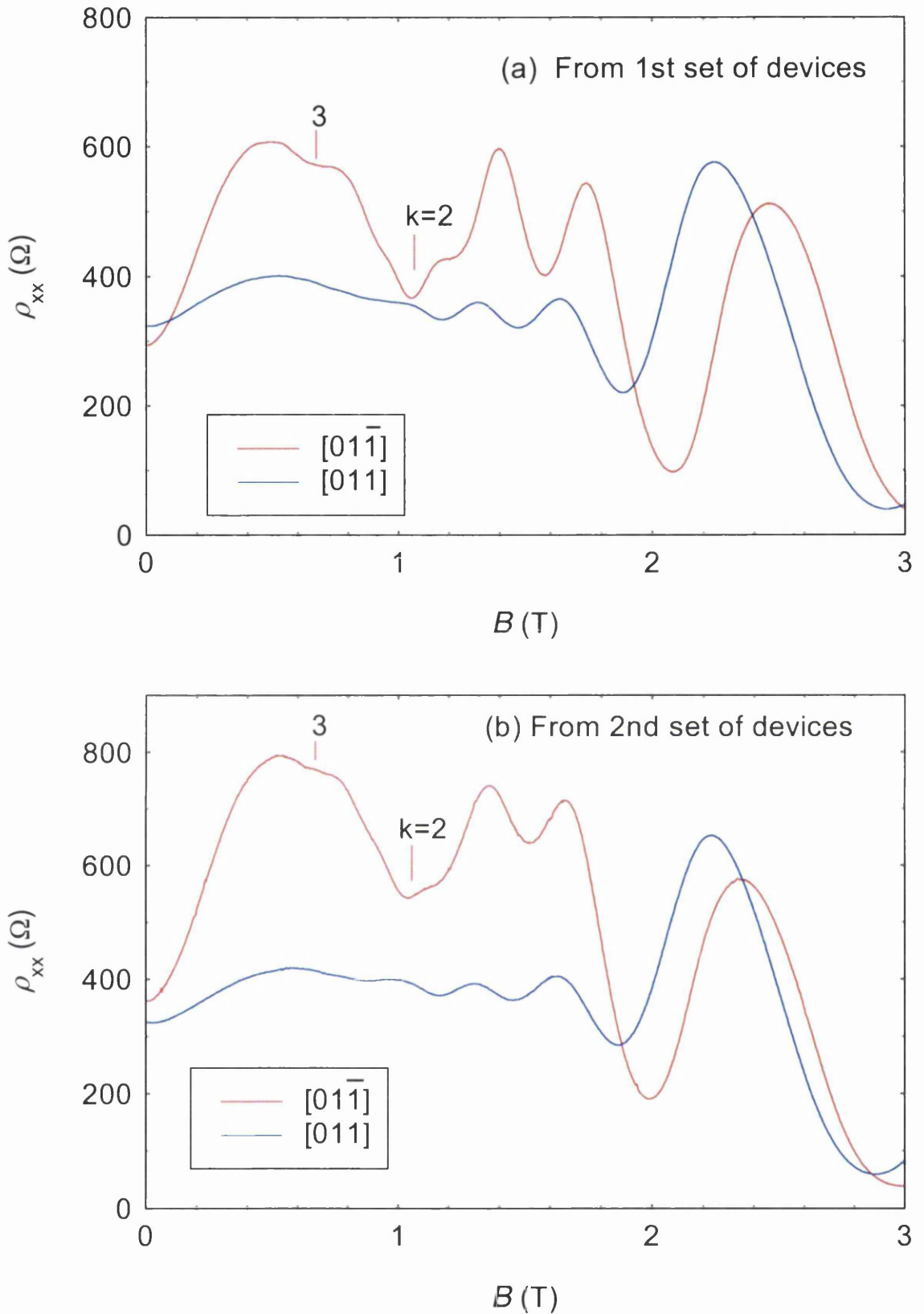
Figure 4.9
Data at -0.1 V gate bias from (a) 1st and (b) 2nd set of devices. Other specifications are as in Figure 4.7 above.
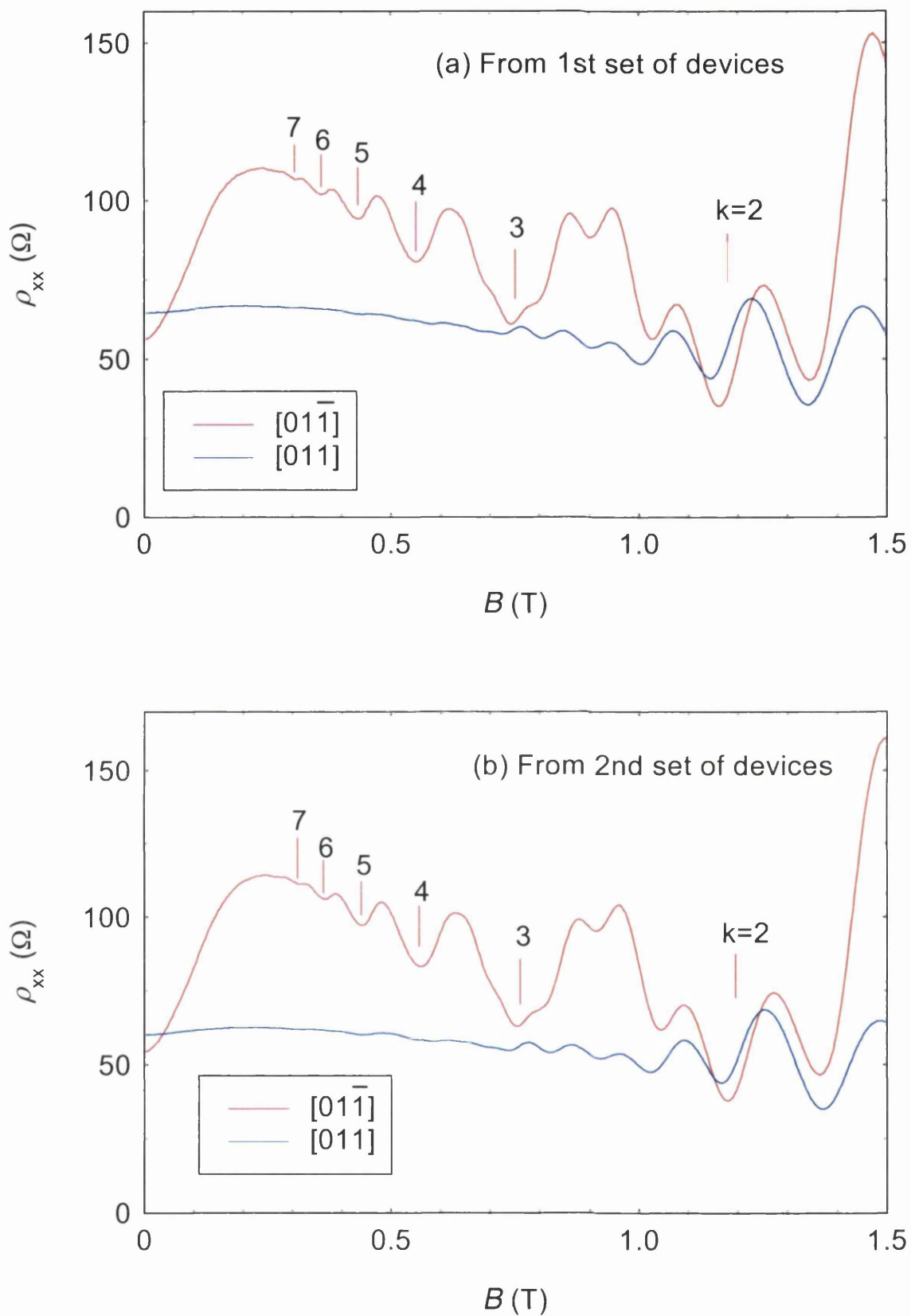
Figure 4.10
Data at +0.1 V gate bias from (a) 1st and (b) 2nd set of devices. Other
specifications are as in Figure 4.7 above.
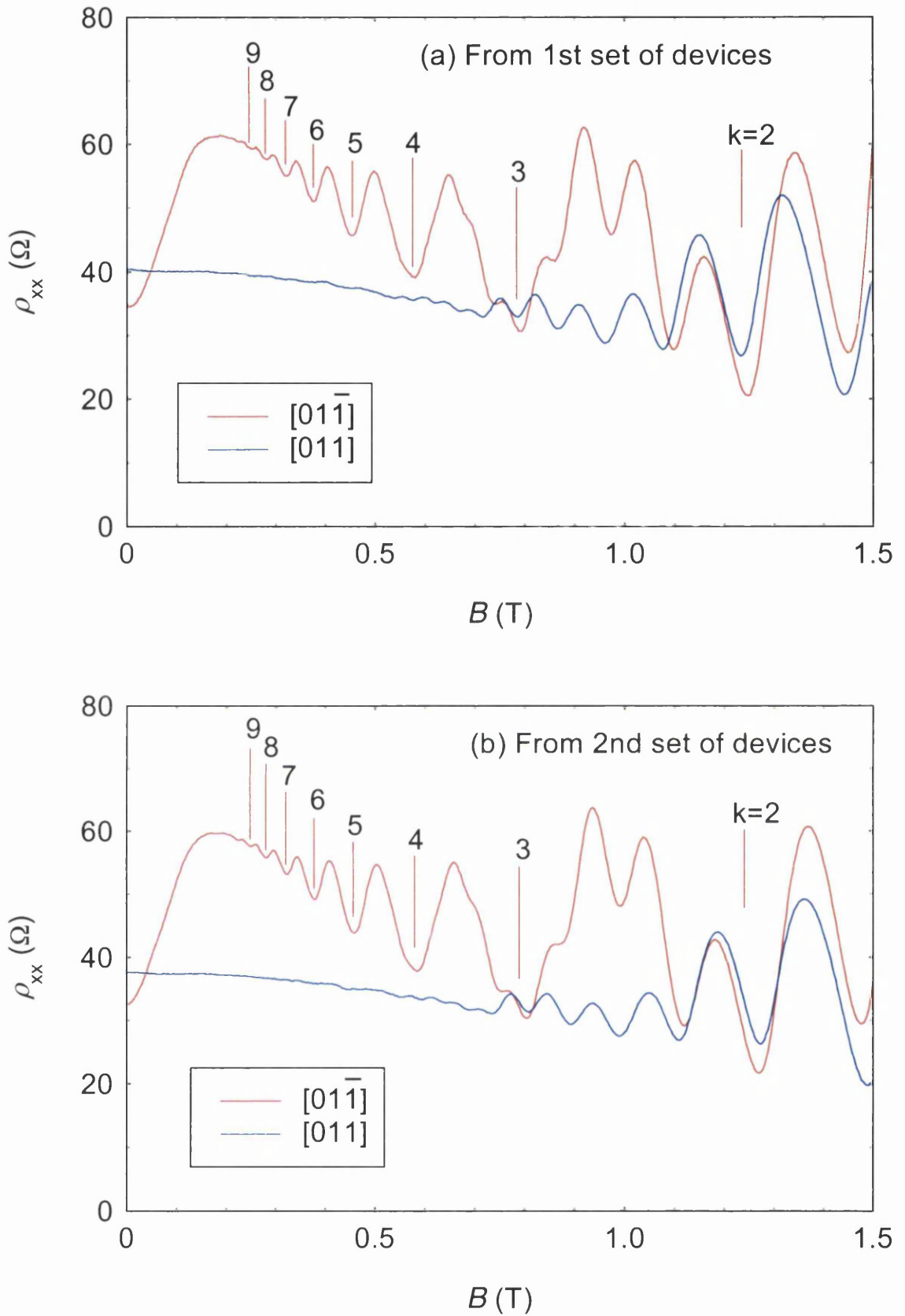
Figure 4.11
Data at +0.2 V gate bias from (a) 1st and (b) 2nd set of devices. Other
specifications are as in Figure 4.7 above.
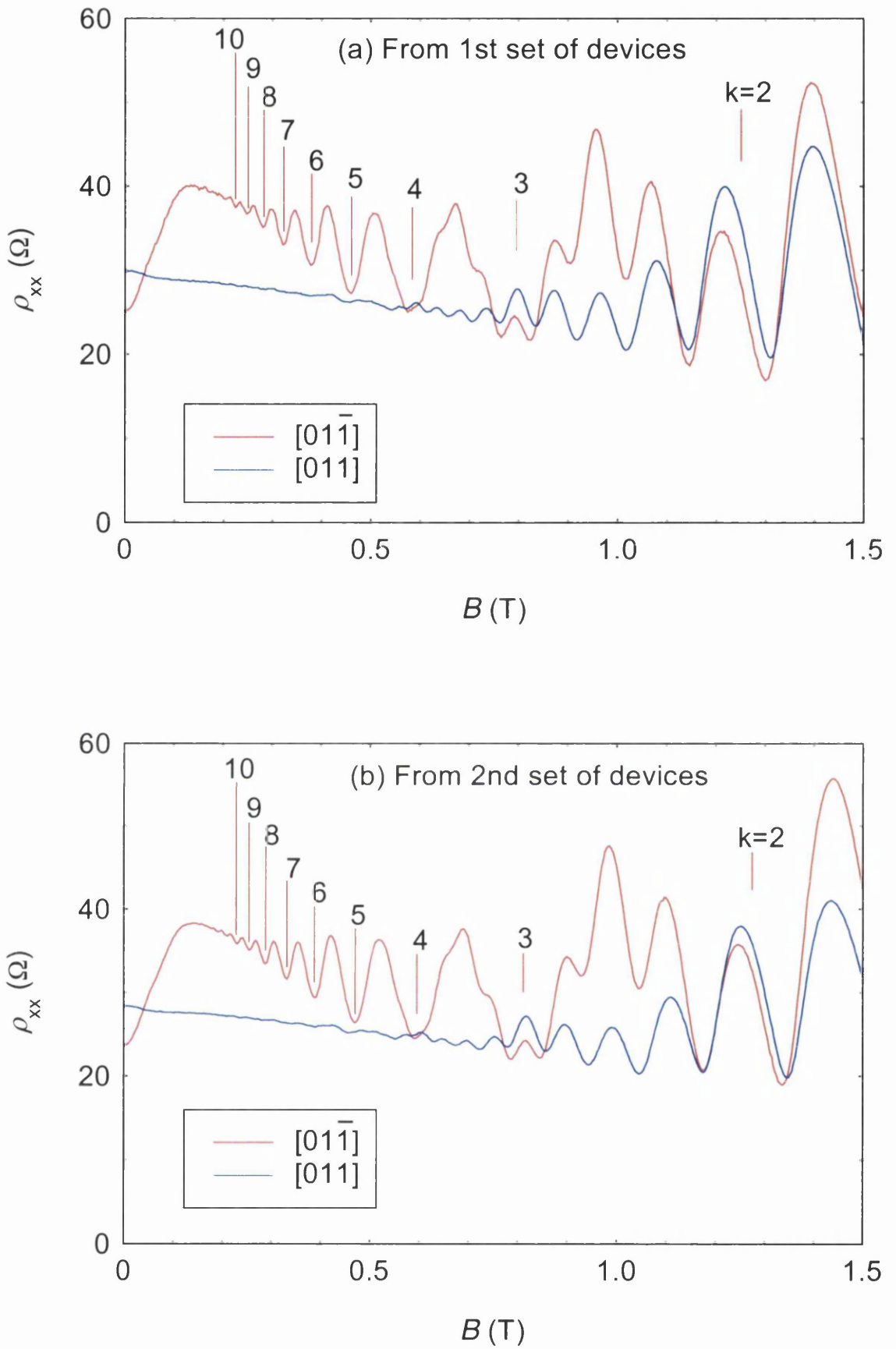
Figure 4.12
Data at +0.3 V gate bias from (a) 1st and (b) 2nd set of devices. Other
specifications are as in Figure 4.7 above.

It is clear from the above figures (Figure 4.7 to Figure 4.12) that there are *no* COs for transport in [011] direction at *any* gate bias. As already mentioned, there cannot be an exact cancellation of modulations due to surface effect and stress modulation in the [011] direction at more than one gate bias. Moreover, for large positive gate bias (e.g. as for Figure 4.12), the surface effect is reduced appreciably (leading to a lower cancellation of the two sources of modulation along [011]) leading to a larger modulation in [011] direction (due to stress modulation) comparable with that along [01$\bar{1}$]. Hence there is significant (stress) modulation along [011] direction for some gate biases that did not give rise to COs for transport along [011]. This provides a *striking* confirmation of the guiding centre drift model [1] and contradicts sharply with the previous semi-classical model [7] and the equivalent quantum mechanical calculation [2]. Thus the previous semi-classical model [7] and the equivalent quantum mechanical calculation [2] are both unable to account for the data. Moreover, the independence of the contributions of different Fourier components to the COs as stipulated in these two formulations [2, 7] calls for simultaneous presence of COs of the periods of both axial and diagonal Fourier components in the data for transport along both [011] and [01$\bar{1}$], which is not observed. Admittedly, it can be argued that the diagonal Fourier components are too weak to be observed in COs, as already discussed.

As before, the magnetic field values of the CO minima calculated for [01$\bar{1}$] for 100 nm period are shown in the figures (Figure 4.8 to Figure 4.12) by red vertical bars. The agreement with data demonstrates that the phase factor $\varphi = 1/4$ in $2R_c = (k - \varphi)a$ for all gate biases.

Some weak oscillations may be discerned in [011] data for +0.2 V and +0.3 V gate biases in Figure 4.11 and Figure 4.12 respectively. Those of +0.3 V gate bias are shown on an exaggerated scale in Figure 4.13. Assuming (arguably) that these oscillations are COs, a gradual transition from in-phase COs at low field to anti-phase COs at high field is observed (see Figure 4.13). This magnetoresistance feature may be compared with the observations of D. Weiss et al. [9] who found magnetic field dependent transition from in-phase COs at lower magnetic field to anti-phase COs at higher fields and ascribed it to suppression of band conductivity. D. Pfannkuche and R. R. Gerhardts [10] attributed the magnetoresistance feature of Weiss et al. [9] to a transition between dominant band conductivity and dominant scattering conductivity. Y. Tan [11] also discussed the said experimental observation of Weiss et al. [9] in terms of relative role of band conductivity and scattering conductivity. As discussed in

section 6.4, the said suppression may be attributed to the asymmetry in the potential landscape.
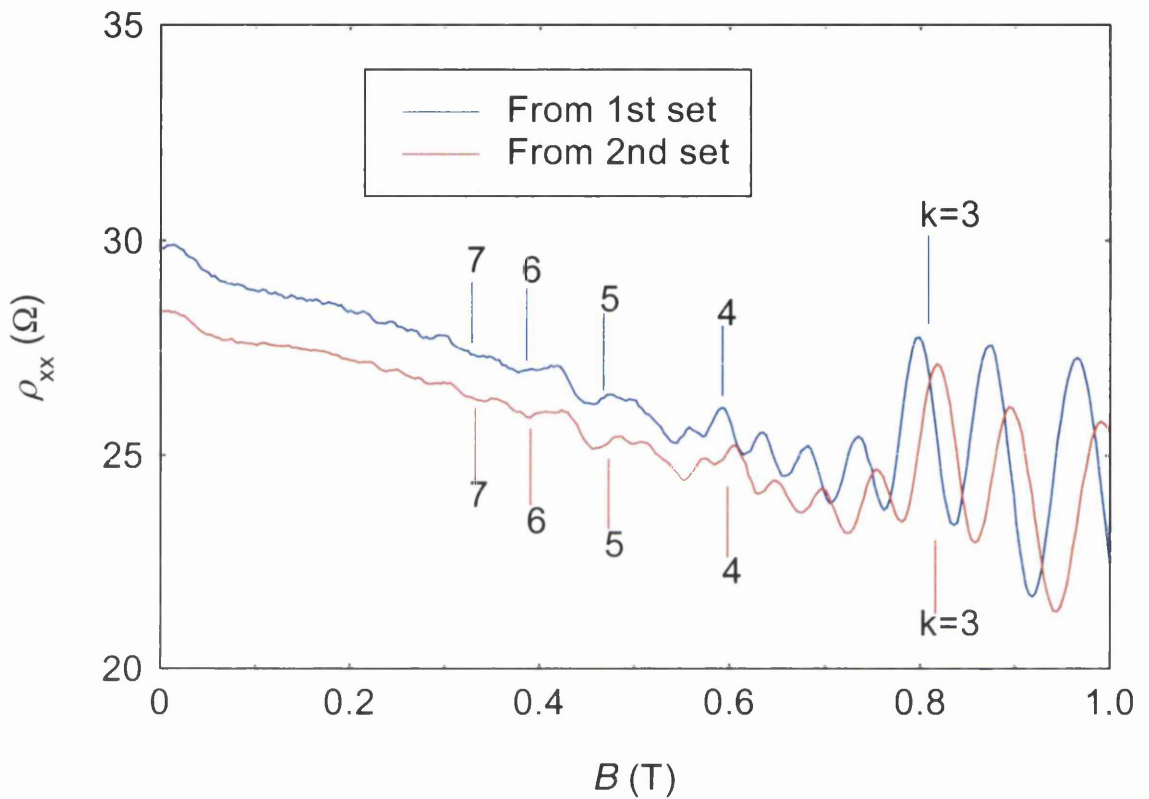
Figure 4.13
Magnetoresistivities of the two [011] devices of Figure 4.12 on a more sensitive scale. Vertical bars (red for the red trace and blue for the blue trace) indicate the magnetic field values of CO minima for 100 nm period calculated for each trace with the carrier densities obtained from respective SdH oscillations.

Data for transport along [010] and [001] directions in gated devices are shown in Figure 4.14 below for forward gate bias. There are some remarkable features in the data as follows.

- The period of the COs in both [010] and [001] is *only* $100/\sqrt{2}$ nm; there is no presence of the 100 nm period.
- The characteristics of the data in the two directions are almost identical.
- The COs are weak as are the PMR.
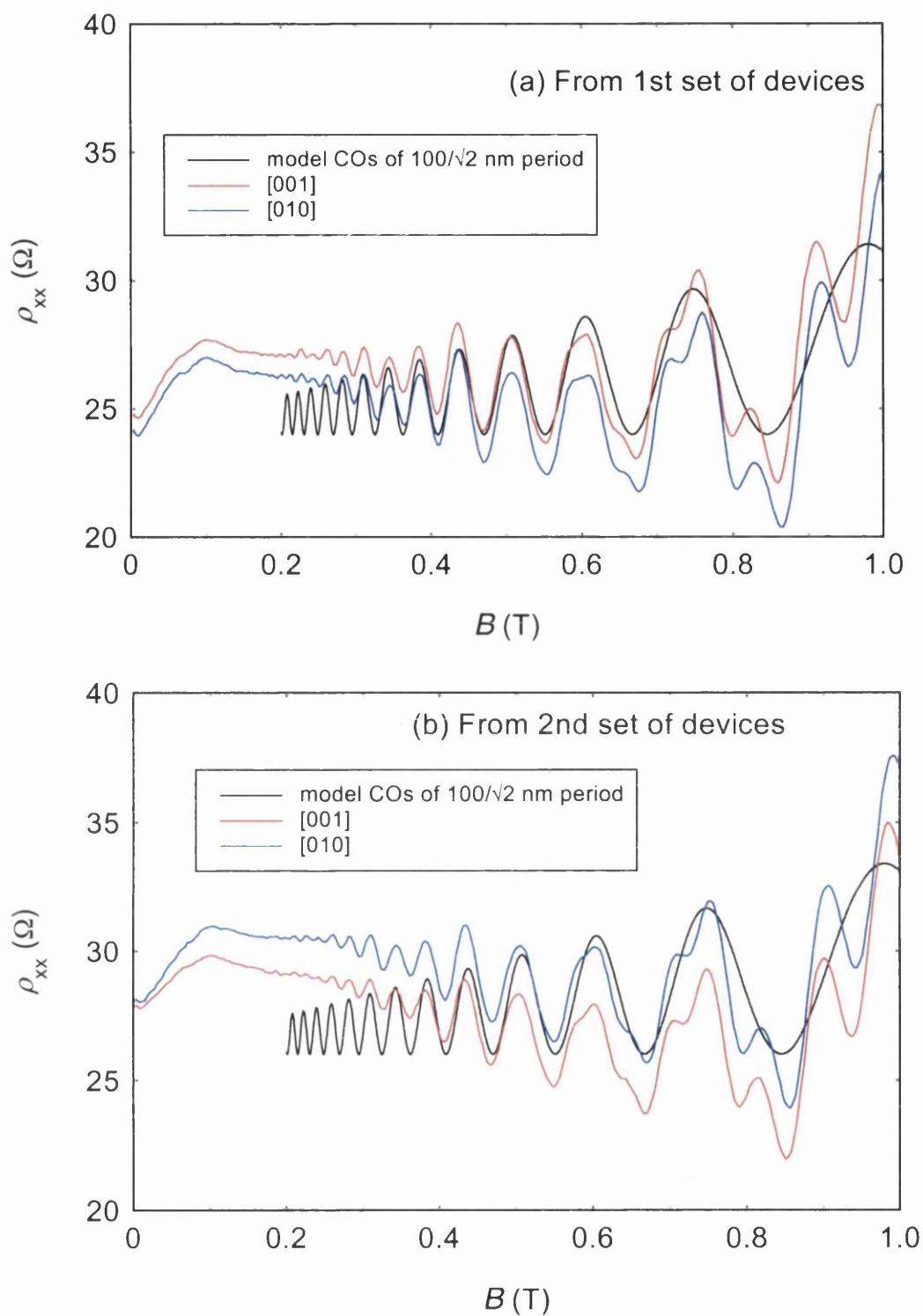
Figure 4.14

Magnetoresistivities of *gated* stressed devices measured at 4 K with +0.3 V gate bias. Transport is along [010] and [001] directions in a 100 nm period square lattice of 50 nm diameter shallow etched holes on the surface of Hall bars. The 100 nm period was aligned along both the [010] and [001] directions. Agreement with model COs shows that the period of the COs in both [010] and [001] is 100/√2 nm.

The agreement of the model COs of $100/\sqrt{2}$ nm period with the data (see Figure 4.14) shows that the phase factor φ in $2R_c = (k - \varphi)a$ is again very close to 1/4. The model COs were calculated using 1D formulation [12] and adjusting the amplitude of oscillations to match that of the data. (But they do not match the data everywhere.)

The data are consistent with those of the ungated devices discussed in section 4.1.1. This is because the ungated [010] and [001] devices were etched for a shorter time and hence the surface effect was small. The data can be accounted for using the guiding centre drift model [1]. At appreciably positive gate bias (+0.3 V in Figure 4.14), the surface effect is reduced to small values. Hence the axial Fourier components along [010] and [001] which are due to surface effect only are turned small in amplitude. The stress modulations along [01$\overline{1}$] and [011] are equal and opposite and remains almost unaltered by the gate bias apart from any change in screening effect. The residual surface effect adds to the stress modulation along [01$\overline{1}$] and partially cancels that along [011]. Thus the diagonal Fourier component along [01$\overline{1}$] becomes dominant and guiding centre drifts along [011]. Thus the picture depicted in Figure 4.5 and Figure 4.6 holds. Consequently, the magnetoresistance characteristics in both [010] and [001] directions should be identical and COs in both should have the period $100/\sqrt{2}$ nm *exactly* as observed (see Figure 4.14). The COs are weak, as the asymmetry is small, for the surface effect is small due to forward gate bias.

The data of Figure 4.14 contradict the semi-classical model [7] and the equivalent quantum mechanical calculation [2]. The independence of the contributions of different Fourier components to COs as stipulated in these two formulations [2, 7] calls for simultaneous presence of COs of the periods of both axial and diagonal Fourier components in the data (resembling Figure 2.5) for transport along both [010] and [001], unlike observations (see Figure 4.14, Figure 4.15 and Figure 4.16). The axial Fourier components have surface effect only but are larger in period, while the dominant diagonal Fourier component has both the surface modulation and stress modulation but is shorter in period. Moreover, the data of Figure 4.12 reveal that there is non-trivial amount of surface effect associated with the axial Fourier components of 100 nm period for +0.3 V gate bias. Since the devices of Figure 4.12 and Figure 4.14 were etched at the same time and the etching is uniform over large area, significant surface effect along the axial Fourier components of 100 nm period is expected in the case of Figure 4.14. Thus the potential amplitude associated with 100 nm period in the devices of Figure 4.14 is comparable with, although smaller than that of the dominant diagonal Fourier component. Thus it cannot be argued that the axial Fourier component

is too weak to be present in the COs of Figure 4.14. Thus the previous semi-classical model [7] and the equivalent quantum mechanical calculation [2] both are unable to account for the data. Only the dominant Fourier component contributes to COs in *striking* agreement with the guiding centre drift model [1].
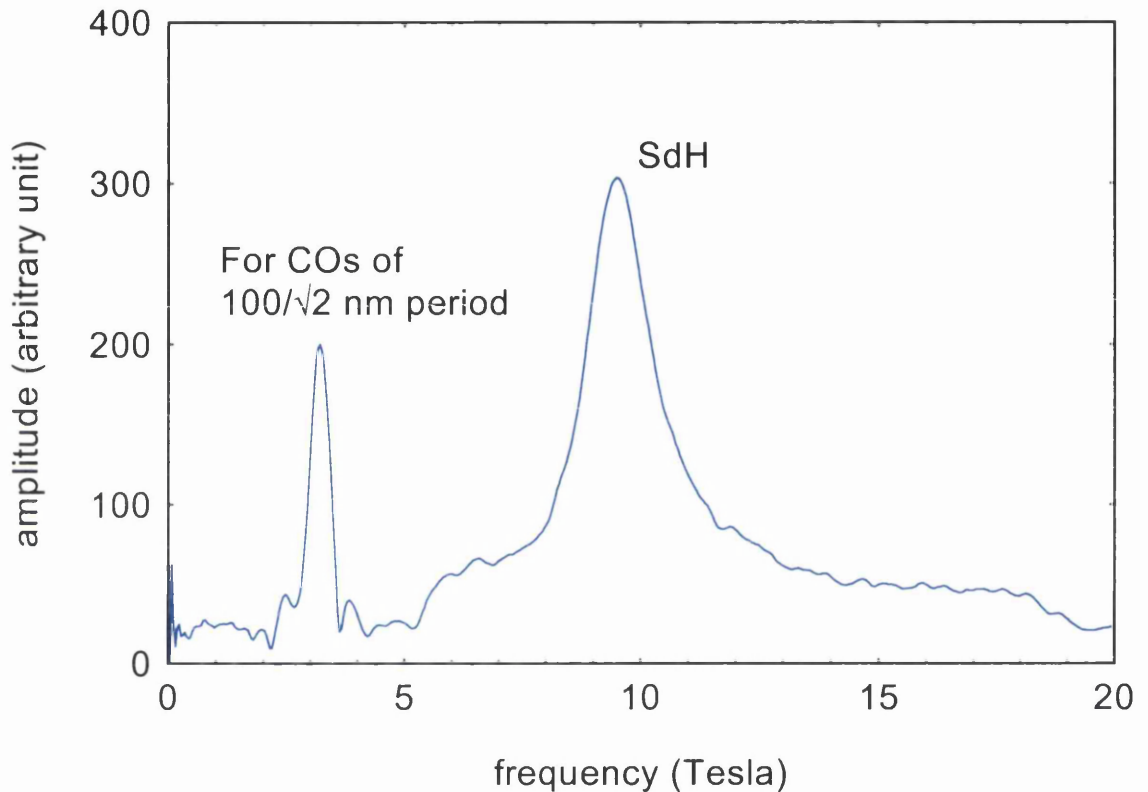
Figure 4.15
Fast Fourier transform of the [001] data of Figure 4.14(b) for the magnetic field range 0 to 1.48 T showing that there is no peak for 100 nm period COs. The peak at about 3.2 T is for the COs of 100/√2 nm period and that at about 9.6 T is for SdH oscillations. The peak for 100 nm period was expected at about 3.2/√2 ≈ 2.26 T.

One other point should be noted about the data of Figure 4.14. Although there is only one frequency in the COs corresponding to 100/√2 nm period, not 100 nm (see Figure 4.15), there is a degree of amplitude modulation present (see Figure 4.14). The peaks around about 0.43 T and 0.31 T are particularly prominent. It is possible to discern this in Figure 4.4 as well. There can be several reasons for this. Firstly, these fields are close to the magnetic fields (0.41 and 0.276 T respectively) when one flux quantum h/e passes through 2 and 3 square unit cells respectively of side 100/√2 nm

defined by the two diagonal Fourier components. We discuss this type of behaviour in section 6.3, where data obtained from symmetric 2D LSSLs are discussed. The small disagreements between 0.43 and 0.41 T and also between 0.31 and 0.276 T may be attributed to the fact that the potential landscape is not perfectly symmetric. Secondly, as shown in Figure 4.16, the amplitude modulation fits roughly with COs of 241 nm period which corresponds to the difference of the frequencies in inverse magnetic field corresponding to 100 nm and $100/\sqrt{2}$ nm periods, as $\dfrac{1}{100} \sim \dfrac{1}{100/\sqrt{2}} \approx \dfrac{1}{241}$. The period corresponding to the amplitude modulation is not 100 nm anyway.
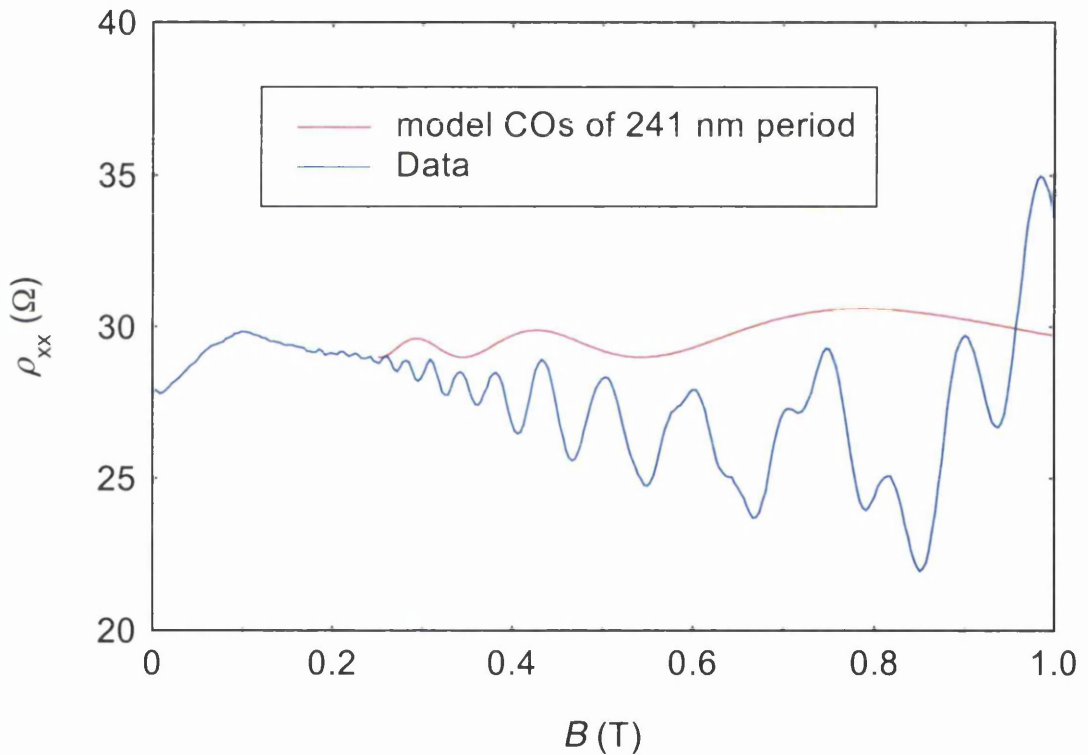
Figure 4.16
[001] data of Figure 4.14(b) shown with model COs of 241 nm period showing that the amplitude modulation in the COs of the data agrees with COs of 241 nm period corresponding to the difference frequency in inverse magnetic field for 100 nm and $100/\sqrt{2}$ nm periods.

The magnetoresistances at less positive gate bias are extremely interesting. The data at +0.1 V gate bias are shown in Figure 4.17. As shown in Figure 4.17, the data agree well with the model curves obtained as suitable superposition of COs of both 100

nm and $100/\sqrt{2}$ nm periods. Such a superposition is an important prediction of the perturbation models [2, 7] and is in apparent disagreement with the guiding centre drift model [1].

According to the guiding centre drift model [1], there can be only one direction of drift for a given set of conditions. Superposition, on the other hand, implies the simultaneous presence of more than one direction of drift of the guiding centre of a given electron for a given set of conditions, according to the model. However, there is a way to understand the data within the guiding centre drift model [1] as follows.

For less positive gate bias (+0.1 V), the surface effect is only weakly suppressed by the gate bias. Hence the axial Fourier components are appreciable in amplitude and are expected to be more comparable in amplitude with the dominant diagonal Fourier component. As the axial Fourier components and the dominant diagonal Fourier component are nearly equal to each other, the period of COs can change between 100 nm and $100/\sqrt{2}$ nm with changing magnetic field. As discussed in section 2.3.2, the effective potential has Bessel functions in each Fourier component. These Bessel functions are magnetic field dependent via the cyclotron radius in their arguments. Moreover, the arguments of the Bessel functions of the axial and diagonal Fourier components are different. Thus the Bessel functions of the axial and diagonal Fourier components have different magnetic field dependence. Hence change in magnetic field can change the dominant Fourier component in the effective potential from being axial to diagonal or vice-versa (see Figure 4.18). This can change the period of the COs accordingly. As soon as the diagonal Fourier component is dominant, the COs turn to $100/\sqrt{2}$ nm period. Again, as soon as the dominance returns to the axial Fourier components, the COs turn to 100 nm period. In view of the complicated fashion in which the magnetic field dependent switching of dominance occurs (see Figure 4.18), the resulting magnetoresistance curve will be difficult to distinguish from the simple superposition used to fit the data in Figure 4.17.

One further question with regard to this argument needs to be considered. There is no asymmetry between the two axial Fourier components, as these being along [010] and [001], are orthogonal to each other and are due to the surface effect only. How then can there be 100 nm period COs when the dominance is with axial Fourier components? A possible answer is that the situation is reminiscent of the unstressed devices of square symmetry discussed in section 6.2, where weak COs are in fact observed. We postpone the discussion to this chapter.
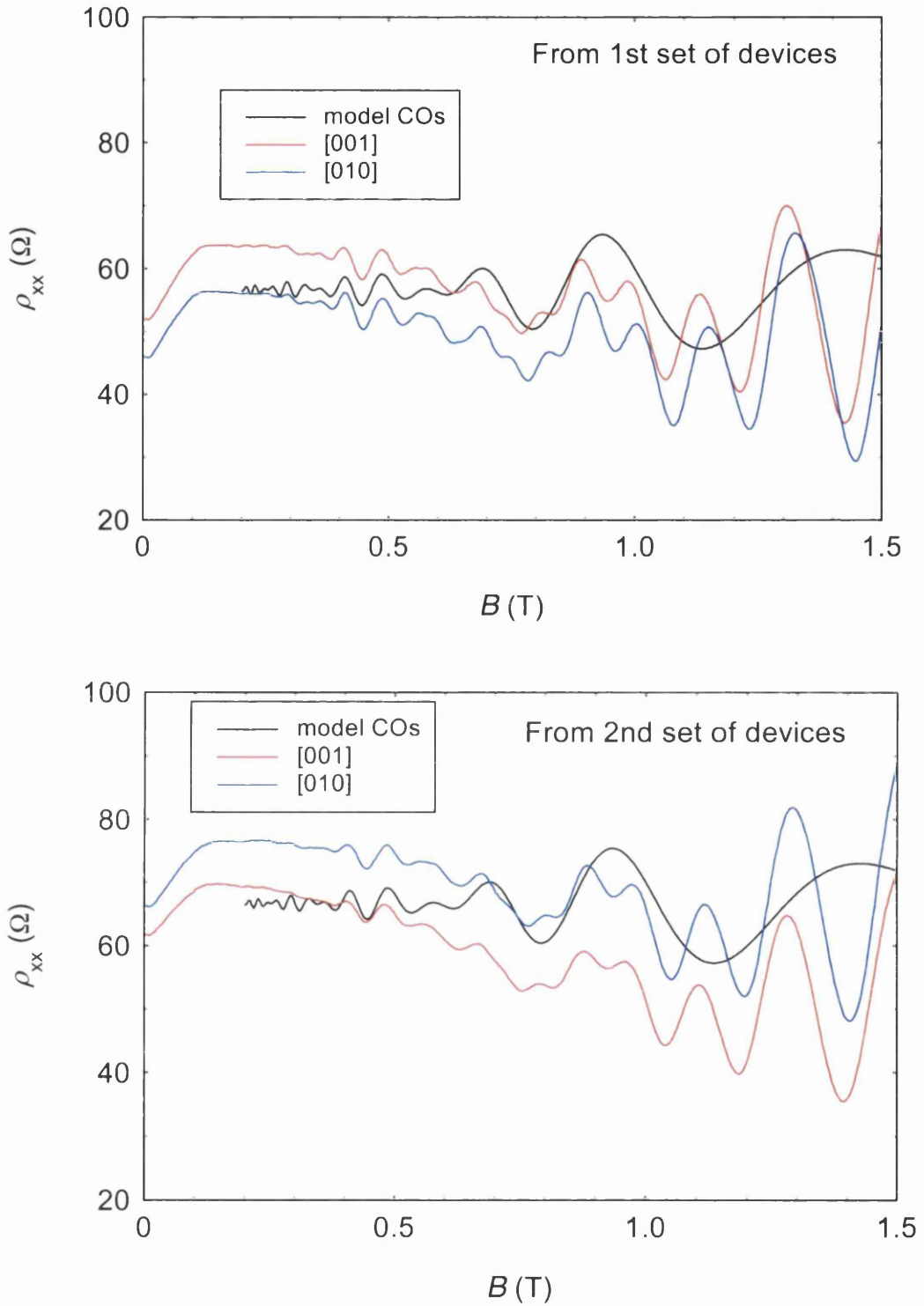
Figure 4.17

Magnetoresistivities of *gated* stressed devices measured at 4 K with +0.1 V gate bias. Transport is along [010] and [001] directions in a 100 nm period square lattice of 50 nm diameter shallow etched holes at the surface of Hall bars. 100 nm period was aligned along both [010] and [001] directions. The black traces show model COs obtained by suitable superposition of COs of 100 nm and 100/√2 nm periods.
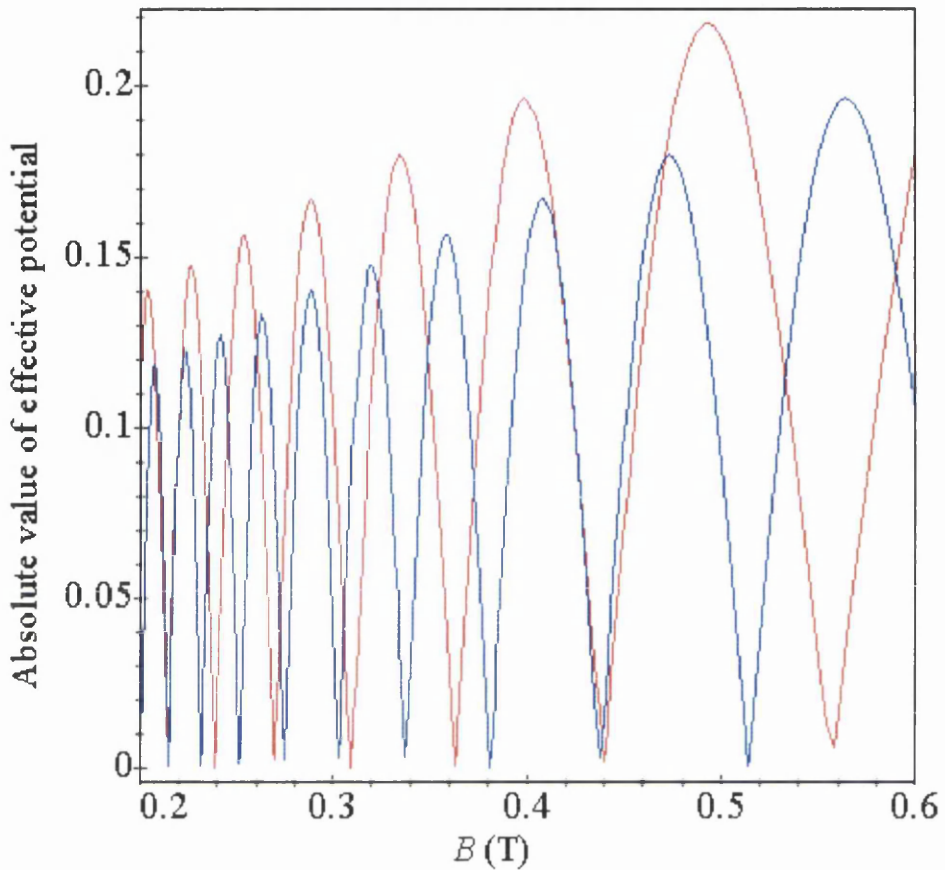
Figure 4.18

The absolute values of effective potentials $V_x J_0(2\pi R_c / a)$ (the red curve) for axial and $V_d J_0(2\pi R_c /(a/\sqrt{2})$ (the blue curve) for diagonal Fourier component of a square superlattice of period a plotted against magnetic field. The parameters used are $V_x = V_d = 1$, carrier density 4×10^{15} m^{-2}, $a = 100$ nm. The complicated set of cross over between the two traces shows that the magnetic field dependent switching of dominance between axial and diagonal Fourier components occurred in a complicated fashion.

The ungated devices of Figure 4.4, although etched for short time, have an appreciable surface effect. Hence magnetic field dependent switching of guiding centre drift between axial and diagonal direction is possible for some magnetic field. This is a possible way to understand the interference-like feature indicated by the arrow in Figure 4.4.

Although the data of Figure 4.17 could be interpreted in terms of a magnetic field dependent switching of the guiding centre drift direction, this explanation may not seem entirely convincing. The observation and conclusion reached in Chapter VI that the quantum mechanical model [2] works in symmetric potential landscape leaves room for an interpretation of the data of Figure 4.17 in terms of this quantum mechanical model. The axial and the dominant diagonal Fourier components are comparable in amplitude in the case of Figure 4.17. Moreover, the two axial Fourier components are equal in amplitude. Hence the potential landscape is not too far from symmetric. COs of the period of both the axial and diagonal Fourier components were observed in the data of Figure 4.17, in agreement with the expectations of the quantum mechanical model [2]. That the COs are not as large as in the ρ_{xx} data of 1D LSSLs may be accounted for by the simultaneous presence of the semi-classical effect involving closed trajectories of guiding centre motion [1], as discussed in Chapter VI. Admittedly, the potential amplitudes are not expected to be very large either.

4.1.3 The systematic behaviour of the low field positive magnetoresistance (PMR)

It can be gathered from the data presented in this chapter that significant PMR has been observed for transport along the direction of modulation of the dominant axial Fourier component only. This contradicts the simulations [1] in a 2D periodic potential, which show that every Fourier component leads to significant PMR and that PMR is present in both directions and also in the symmetric 2D periodic potential. In the absence of any working theoretical formulation of PMR in the case of 2D LSSLs, it is important to present the experimental data in this regard. Figure 4.19 below shows experimental data that reveal that as the gate bias is made more positive, the amplitude and the saturation magnetic field of PMR decrease along with the asymmetry in the potential landscape. Table 4.2 along with Figure 4.20 and Figure 4.21 below summarise the experimental systematic of amplitude and saturation magnetic field of PMR obtained using the data of Figure 4.19.

As the above data of this chapter reveal, PMR is significant in the $[01\bar{1}]$ direction while there is no significant PMR in the [011], [010] or [001] directions. This contradiction with the results of the simulations may be due to some effects present in the devices that were not considered in the simulations. For example, remote ionized impurities may cause random fluctuations in the potential that may disturb the streaming orbits of electrons [13] responsible for the PMR. There can be effects due to small angle scattering as well.
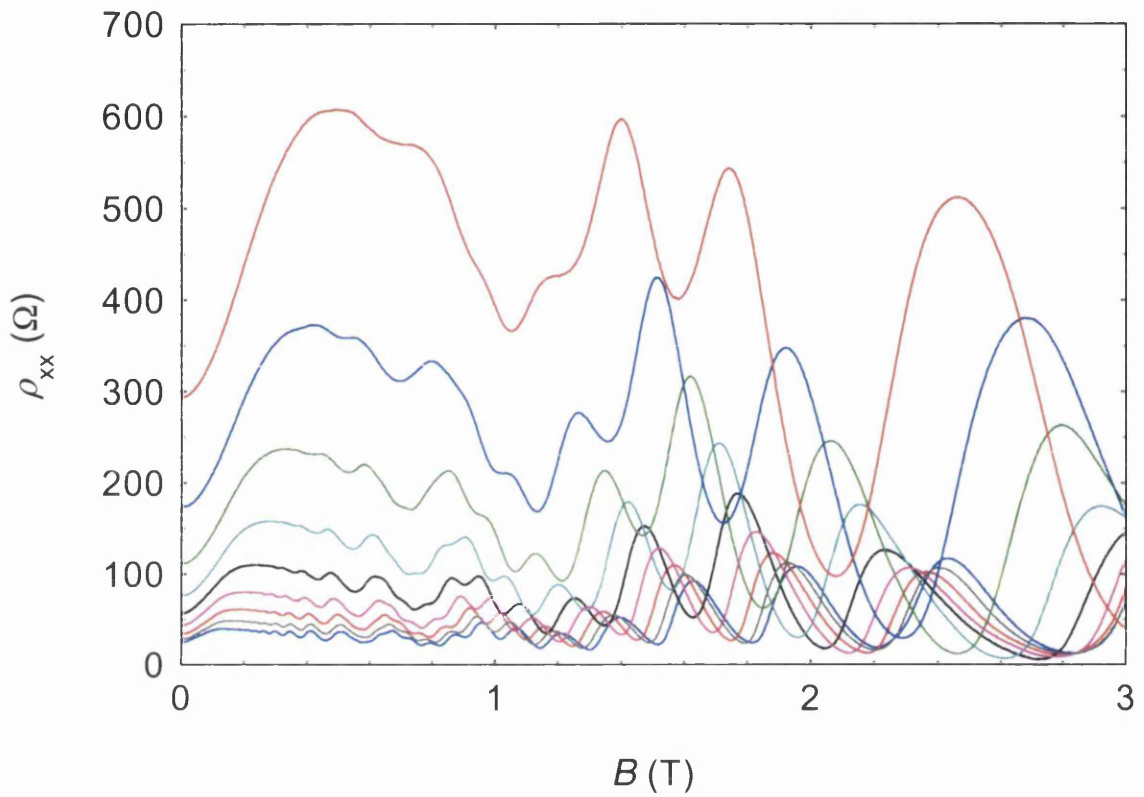
Figure 4.19
Magnetoresistivities of the stressed devices of the 1st set measured at 4 K with different gate biases. Transport is along the [01 $\bar{1}$] direction in a 100 nm period square lattice of 50 nm diameter shallow etched holes at the surface of Hall bars. 100 nm period was aligned with [01 $\bar{1}$]. Gate voltages applied are –0.1 V (for top red trace) to +0.3 V (for bottom blue trace) in step of 0.05 V.

Table 4.2
Zero field resistivity ρ_0, amplitude $\Delta\rho$ and saturation magnetic field B_s of PMR along with $\Delta\rho/\rho_0$ for various gate biases obtained from the magnetoresistivity data of Figure 4.19.

Gate voltage (V)	Zero field resistivity ρ_0 (Ω)	Amplitude[*] of PMR $\Delta\rho$ in magnetoresistivity data (Ω)	Saturation field, B_s of PMR (T)	$\Delta\rho/\rho_0$
-0.1	294	313	0.49	1.06
-0.05	174.5	198	0.4	1.13
0	112.2	126	0.33	1.12
+0.05	77	81	0.27	1.05
+0.1	56.1	54	0.23	0.96
+0.15	43	37	0.19	0.86
+0.2	34.6	27	0.17	0.78
+0.25	29	20	0.15	0.69
+0.3	25	15	0.13	0.6

[*]The amplitude of PMR was obtained as the difference in magnetoresistivities between saturation magnetic field and zero magnetic field.
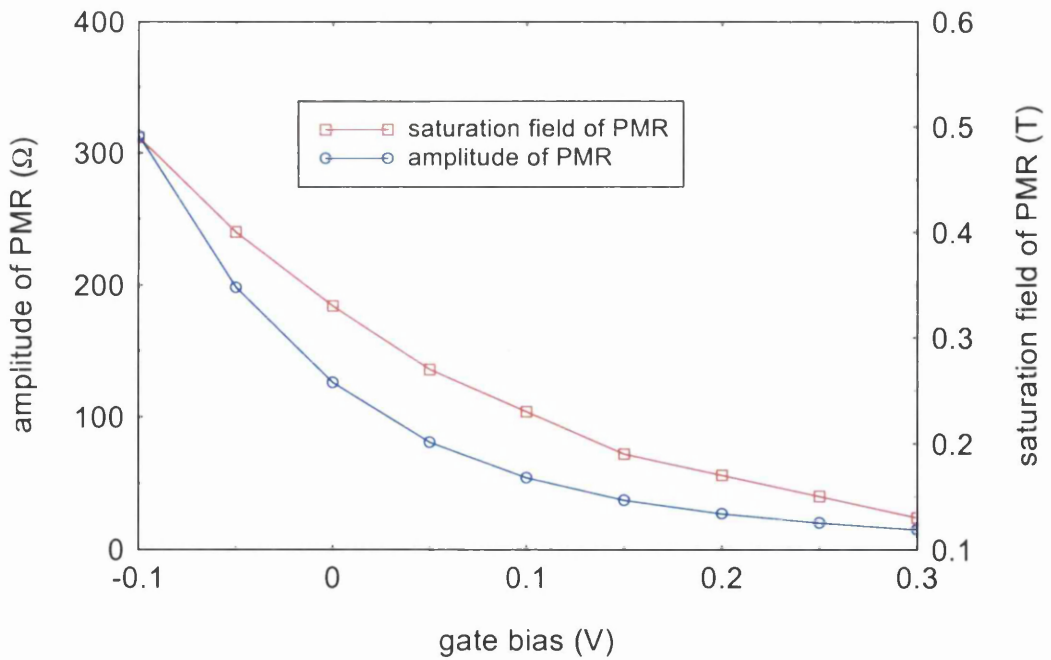
Figure 4.20
Saturation magnetic field and amplitude of PMR as a function of gate bias plotted using Table 4.2.
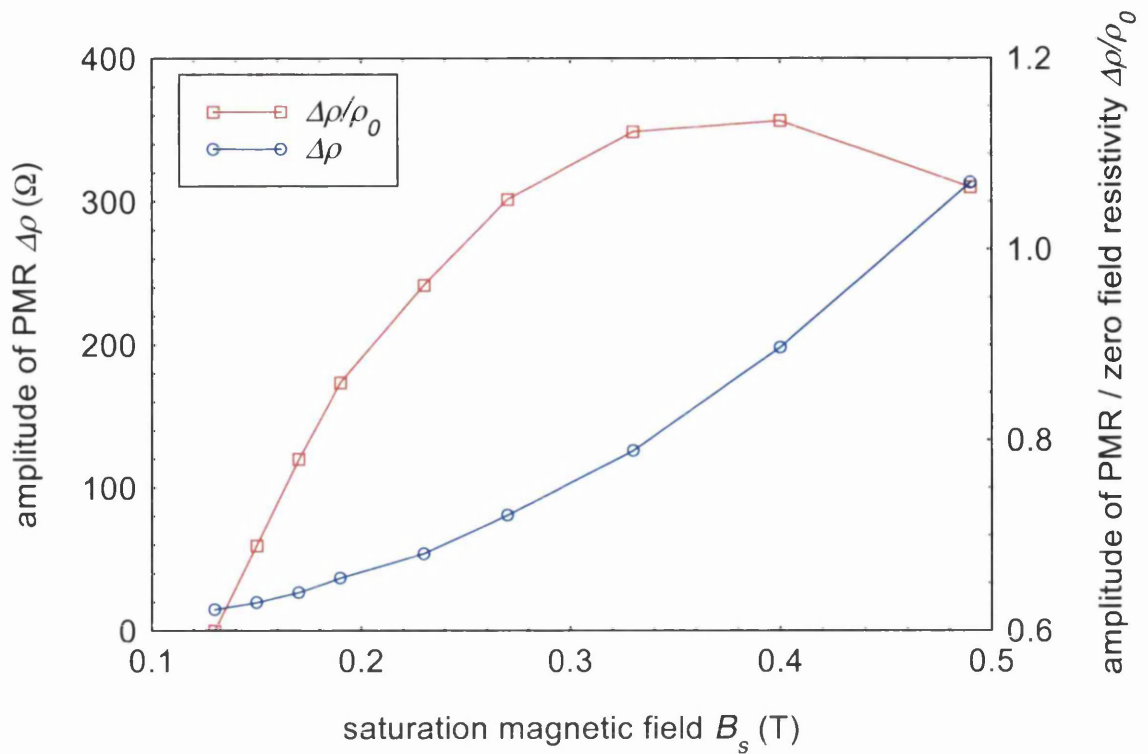
Figure 4.21
Amplitude of PMR $\Delta\rho$ and $\Delta\rho/\rho_0$ plotted against saturation magnetic field B_s using Table 4.2. Here ρ_0 is the zero field resistivity.

4.1.4 Interpretation of some relevant data in the literature

Before concluding the discussion on asymmetric 2D LSSLs of square lattices, it is interesting to try to gather some interpretation of some of the relevant data in the literature.

C. Albrecht et al. [3] in their studies realised 120 nm period lattice of holes in a PMMA resist layer coating Hall bar and then evaporated metal thicker than the resist layer followed by no lift off to realise a patterned Schottky gate. They observed large COs in magnetoresistances even in absence of any gate bias. As the sample was cooled down, the patterned resist is likely to introduce periodic stress modulation at the 2DEG. Patterned resist and metal may cause periodic modulation at the surface potential. As the surface modulation adds to the stress modulation, the symmetry of the potential landscape may break resulting in large COs as observed. Private communication with D. Weiss [14] revealed that the transport in this study was along one of the cleavage directions, but which one was not identified.

C. T. Liu et al. [15] fabricated 200 nm period 2D square grid of LSSLs by X-ray nanolithography and lift off. Magnetotransport at zero gate bias showed no COs at all. At positive bias the COs were just visible, while large COs were observed at negative gate bias. The gate may introduce periodic stress modulations which are equal in magnitude but opposite in sign in the cleavage directions. Such anti-symmetric periodic potential gives rise to symmetric potential landscape. There should be no COs for transport in such symmetric potential landscape as expected from the guiding centre drift model [1]. For negative gate biases, a strong and isotropic electrostatic potential is added to the anti-symmetric stress modulations giving rise to asymmetric potential landscape in which there can be significant drift of guiding centre [1] producing the strong COs observed. At forward bias, the effect of gate bias is less (due to screening effect). In this early study the phase factor φ in the commensurability condition $2R_c = (k - \varphi)a$ of the COs agrees well with 1/4 (as do ours).

4.2 Unstressed devices with rectangular lattices

One of the reasons why superlattices of rectangular symmetry are interesting is that these provide an asymmetric potential landscape even in absence of stress. The asymmetry arises because of the inequality of the lattice constants. The modulation associated with the shorter period is more attenuated than that with the larger period before it reaches the 2DEG [6]. Hence the amplitude of the Fourier component associated with the shorter period is smaller than that with the larger period. Both ungated and gated devices were realised and the data are discussed below.

4.2.1 Ungated unstressed devices with rectangular lattices

Resist patterns of 50 nm diameter holes arranged on 170 nm by 100 nm period rectangular grids on a resist layer coating several groups of four Hall bars on a piece of unstressed heterostructure material were transferred by shallow wet etching. The 170 nm period was aligned along the length of every Hall bar. Two pairs of ungated devices were obtained first, etched for two different set times. The magnetoresistances of these ungated devices, measured after removal of resist, are discussed first. Data are shown in Figure 4.22.

The most notable points regarding the data of Figure 4.22 below are as follows.

- The COs correspond to a period of only 170 nm.

- The magnetoresistance characteristics for transport in different directions are almost identical.
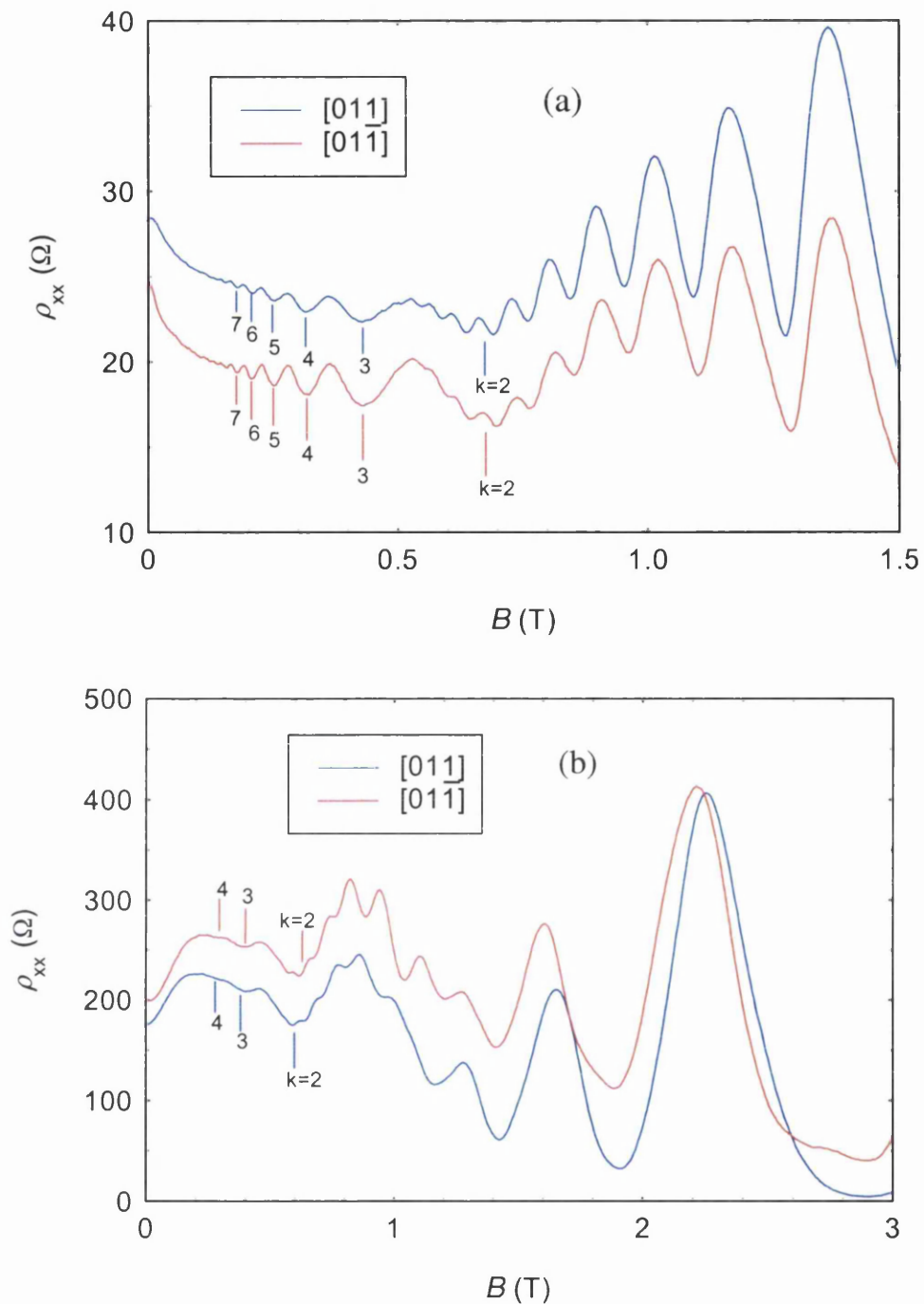
Figure 4.22

Magnetoresistivities of *ungated* unstressed devices etched for (a) shorter time and (b) longer time measured at 4 K after removal of resist. Transport is along the [011] and [01 $\bar{1}$] directions in a 170 nm by 100 nm period rectangular lattice of 50 nm diameter shallow etched holes at the surface of Hall bars. The 170 nm period is aligned along the length of each Hall bar. The vertical bars, red ones for the red traces and blue ones for the blue traces, indicate the locations of predicted minima of COs of 170 nm period for the carrier densities in question obtained from the respective SdH oscillations at higher magnetic field.

The minima of the COs of all the four ungated devices agree remarkably well with the calculated locations for 170 nm period shown in Figure 4.22. Hence the phase factor φ in $2R_c = (k - \varphi)a$ is very close to 1/4 for $a = 170$ nm.

Before giving a theoretical account of the data, it is important to note that the devices are ungated and the resist pattern was also removed after etching and before measurement. As such there should not be any reason for the presence of any stress at all. As such the four devices in question are as close to examples of entirely unstressed rectangular LSSLs one can get. Thus there will be no stress-induced asymmetry in the potential landscape.

Despite being unstressed devices, the symmetry of the potential landscape is broken due to the inequality of the lattice constants along and across the Hall bars. As already mentioned, modulation of the shorter period is more significantly attenuated than that of the longer period [6] before it reaches the 2DEG. As such the amplitude of the Fourier component associated with 170 nm period is larger than that with 100 nm period. Moreover, the two diagonal Fourier components being $170\times100/\sqrt{(170^2+100^2)}$ = 86 nm in period (see Figure 4.23 below) are weaker in amplitude as well. As 170 nm is the longest among the periods present, the Fourier component of 170 nm period is the dominant Fourier component in the potential landscape. The relative amplitudes of different Fourier components in the potential landscape are represented in Figure 4.24 below.

As 170 nm period is along every Hall bar, the dominant Fourier component is along the length of every Hall bar. According to the guiding centre drift model [1], the guiding centre drifts *only* in the direction orthogonal to the direction of modulation of the dominant Fourier component. Thus guiding centre drifts across every Hall bar. The situation is depicted in Figure 4.25 below. In analogy with 1D LSSLs, there should be large COs of *only* 170 nm period in the magnetoresistances as observed (see Figure 4.22 above).

There is no distinction between different directions of transport in unstressed heterostructures, apart from any intrinsic mobility anisotropy. This accounts for the observation that the magnetoresistances for transport along different directions with the same period (170 nm) along the direction of transport are almost identical (see Figure 4.22 above).

A very important point to note is that as represented in Figure 4.24 all the four Fourier components are non-zero in amplitude, although *only* that of 170 nm period is present in the data (see Figure 4.22). If every Fourier component in 2D LSSLs

independently contributes to the magnetoresistivities as stipulated in the previous models [2, 7], the magnetoresistances of similar devices but with 100 nm period along the direction of transport is expected to show COs of 100 nm period which is *not* observed (see the following section, in particular Figure 4.27). Thus the previous semi-classical model [7] and the corresponding quantum mechanical calculation [2] are both unable to account for the data.
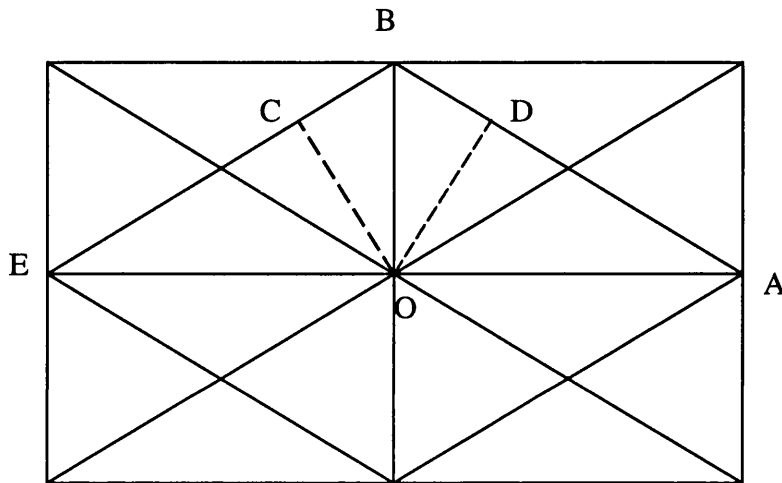
Figure 4.23
The spacing in every set of parallel lines gives the periodicity of one of the four Fourier components of a rectangular lattice. $OA = a$ and $OB = b$ are the periods of the two axial Fourier components, while $OC = OD$ is that of the two diagonal Fourier components. Here $OC \perp BE$ and $OD \perp$ AB. Since OAD and ODB are similar triangles, $OD/OB = AD/OA$. Hence $OD = (b/a) \sqrt{(a^2 - OD^2)}$ which leads to $OD = ab / \sqrt{(a^2 + b^2)}$. Thus for $a = 170$ nm and $b = 100$ nm, $OC = OD = 170 \times 100/\sqrt{(170^2 + 100^2)} \approx$ 86 nm.
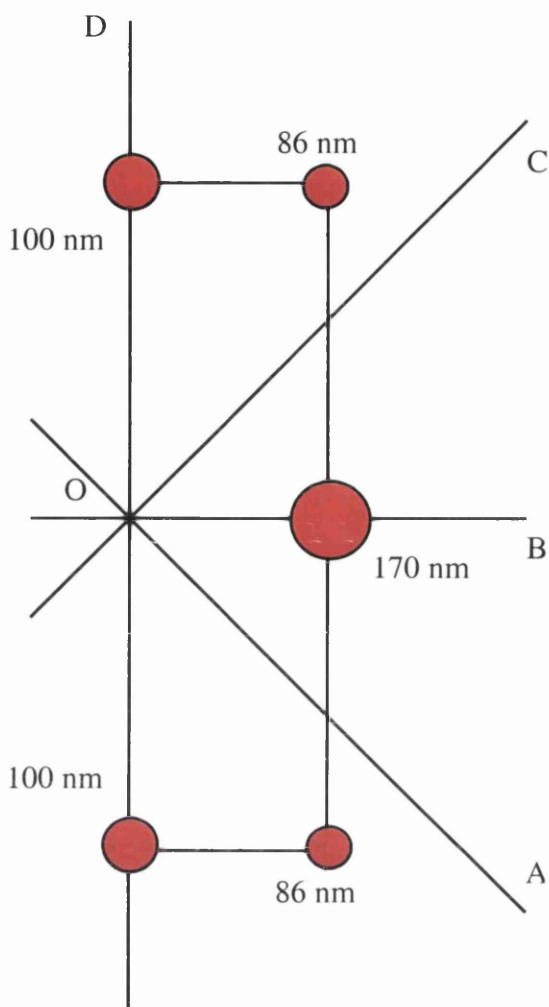
Figure 4.24
Reciprocal lattice points (shown over half of reciprocal space) of 170 nm by 100 nm period unstressed rectangular lattice. The relative sizes of the circles at the reciprocal lattice points indicate the relative amplitudes of the Fourier components. The same colour of the circles indicates the same sign of potential. The devices being unstressed, the picture holds whether OA, OC are cube axes and OB, OD are cleavage directions or OA, OC are cleavage directions and OB, OD are cube axes.

Direction of guiding centre drift

Direction of transport.
Direction of longest period and hence direction of modulation of the dominant Fourier component.
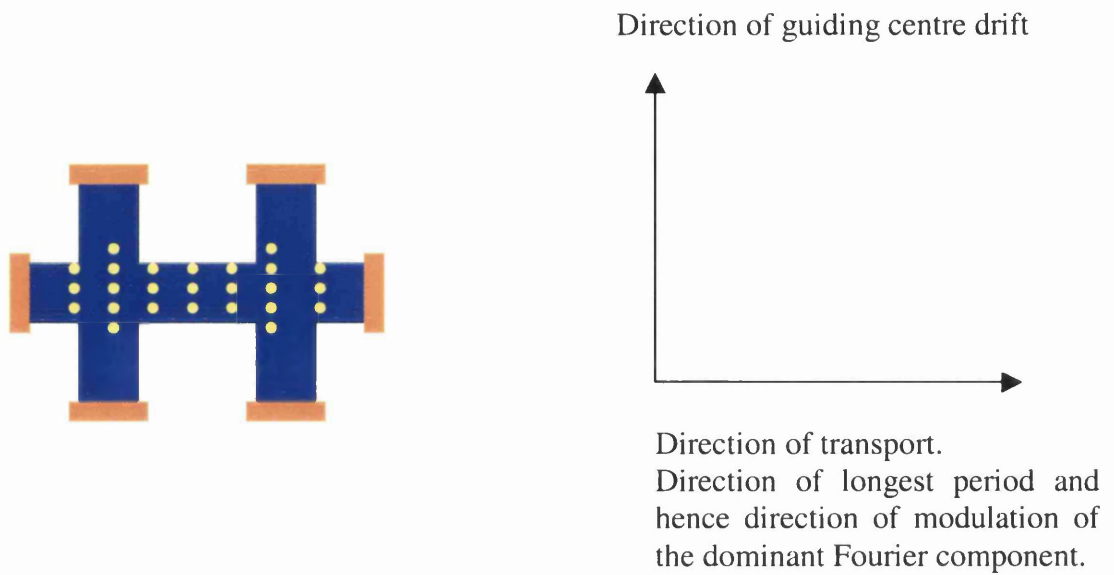
Figure 4.25
Schematic diagram showing the direction of modulation of the dominant Fourier component and guiding centre drift direction relative to the Hall bars of Figure 4.22.

4.2.2 Gated unstressed devices with rectangular lattices

Gated devices were realised as well by transferring the resist pattern with an etch duration intermediate between those of the two pairs of ungated devices discussed above. The 170 nm period was aligned along the length of every Hall bar. The resist pattern was removed before evaporating the metal to realise the gate. Magnetoresistances of the gated devices were measured at 4 K. COs corresponding to *only* 170 nm period were observed for all Hall bars irrespective of their orientation, [010], [011], [001] or [01$\bar{1}$]. A representative magnetoresistance trace is shown in Figure 4.26 below.

The data of the gated devices are consistent with those of the ungated devices already discussed. The observation can be accounted for in that any small asymmetry in the potential landscape introduced by the stress of the gate could not dominate the fairly strong asymmetry introduced by the inequality of the lattice constants. Hence the asymmetry defined by the inequality of the lattice constants prevails. Hence the experimental situation depicted in Figure 4.24 and Figure 4.25 above holds. As shown in Figure 4.26, the phase factor φ of the COs is 1/4 in $2R_c = (k - \varphi)a$ in the gated device as well.
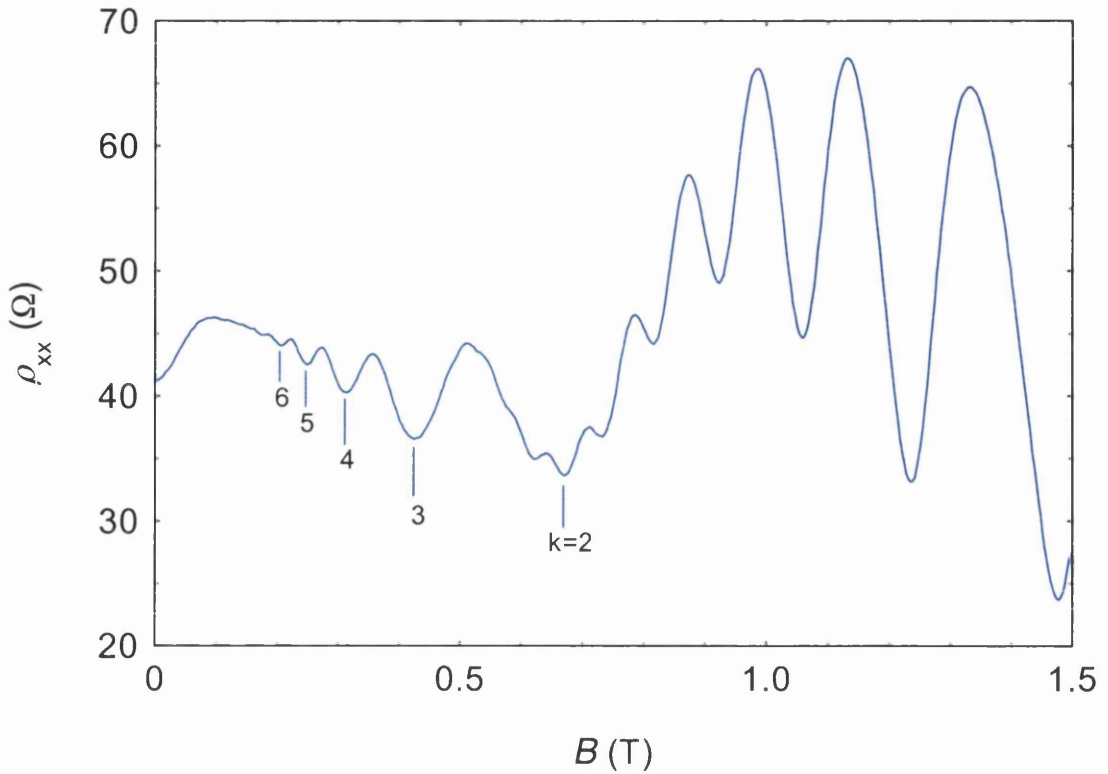
Figure 4.26
Magnetoresistivities of *gated* unstressed device measured at 4 K without any gate bias. Transport is along the [011] direction in 170 nm by 100 nm period rectangular lattice of 50 nm diameter shallow etched holes at the surface of the Hall bar. The 170 nm period was aligned along the length of the Hall bar. The blue vertical bars indicate the locations of predicted minima of COs of 170 nm period for the carrier density in question obtained from the SdH oscillations at higher magnetic field.

It is tempting to compare the data with those of unstressed square lattices. The COs observed in unstressed rectangular lattices are much larger than those of the unstressed square lattices discussed in section 6.2 asserting the role of asymmetry in defining and observing larger COs in 2D LSSLs.

R. Schuster et al. [16] studied magnetotransport in strongly modulated 2D LSSLs (anti-dots) of rectangular symmetry in which the potential modulation amplitude is larger than the Fermi energy. For transport along the longer lattice constant, they observed oscillations commensurate with the shorter lattice constant orthogonal to the direction of transport. These are due to different pinned electron trajectories round a certain number of anti-dots. Ours are shallow etched superlattices and hence are weakly modulated instead. Our oscillations are commensurate with larger lattice constant instead.

Gated devices with 100 nm period along the direction of transport were studied as well. Some data are shown in Figure 4.27 below. As Figure 4.27 shows, the magnetoresistances contain complex structures and the COs do *not* correspond to any certain period. The discussion of the data is postponed to section 6.5, as further concepts developed in Chapter V and Chapter VI are necessary.
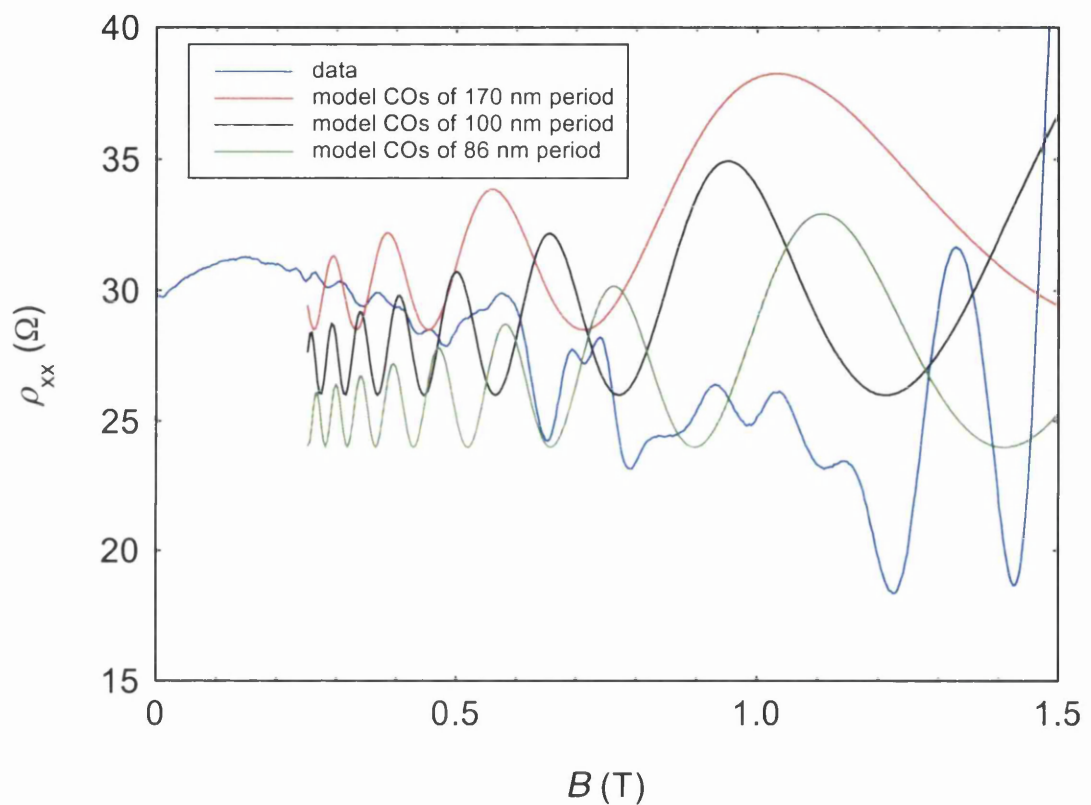
Figure 4.27
Magnetoresistivities of *gated* unstressed device measured at 4 K without any gate bias. Transport is along the [011] direction in 100 nm by 170 nm period rectangular lattice of 50 nm diameter shallow etched holes at the surface of the Hall bar. The 100 nm period was aligned along the length of the Hall bar. Model COs of 170, 100 and 86 nm periods are also shown, manifesting that the COs do not correspond to any certain period.

4.3 Calculation of the phase factor and effect of hysteresis of magnet

In most of the above figures, the calculated magnetic field values of the CO minima have been shown by vertical bars. These were calculated using $2R_c = (k - \varphi)a$ with $\varphi = 0.25$. Agreement of these bars with the experimentally observed CO minima qualitatively demonstrates that the phase factor φ is fairly close to 0.25. In this section, the phase factor has been calculated explicitly for one of the data traces ($[01\bar{1}]$ data of Figure 4.11(a)) to reveal quantitative agreement. The reason for choosing this particular trace is that it has several COs with distinct turning points that reduces the error in determining the magnetic field values of the CO minima.
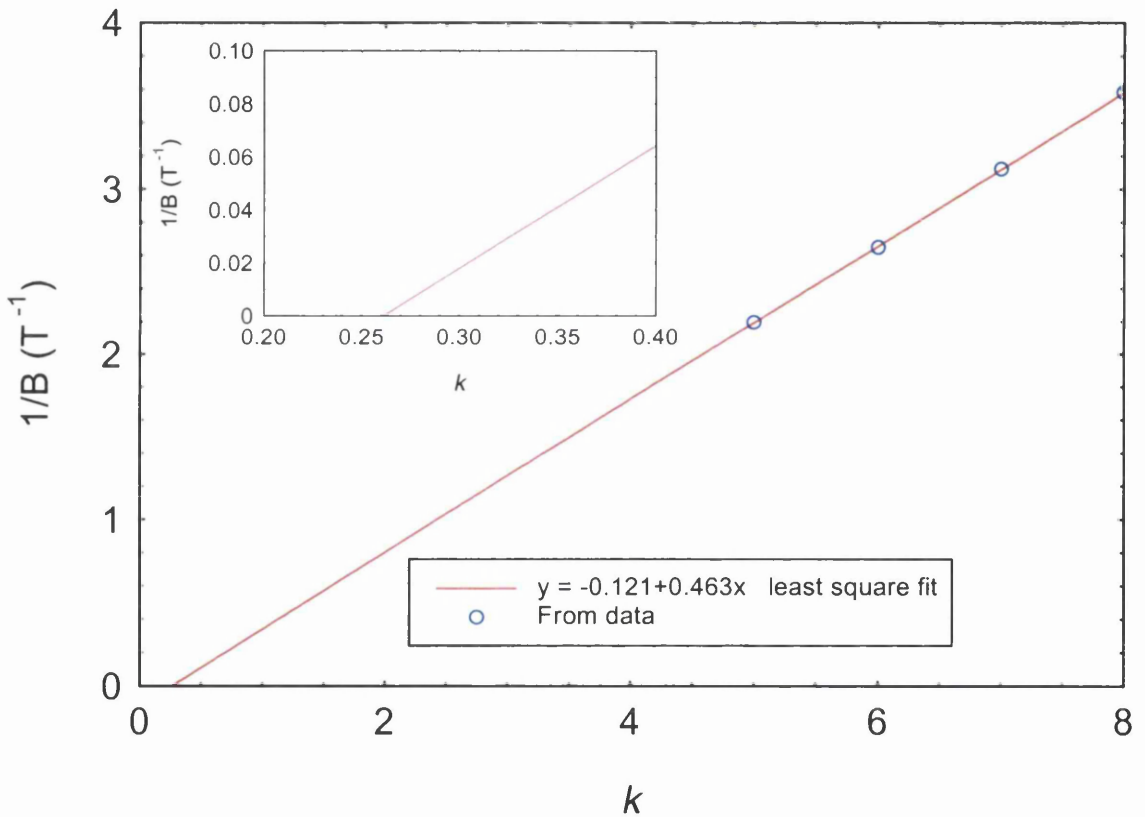
Figure 4.28

$1/B$ values of the CO minima for $k = 5, 6, 7$ and 8 for the $[01\bar{1}]$ device of Figure 4.11 (a) shown with the least square fit. As discussed in the main text of this section, the intercept of the fitted line on the k axis gives the phase factor. Inset shows a zoomed in view of the fitted line revealing that the phase factor is about 0.26, in close agreement with the expected value 0.25.

The equation $2R_c = (k - \varphi)a$ can be recast as $(2\hbar\sqrt{2\pi n_{2D}} / ea)(1/B) = k - \varphi$ which resembles a linear equation of the form $y = a + bx$ where y stands for $1/B$ and x stands for k. From the $[01\bar{1}]$ data of Figure 4.11 (a), one can get $1/B$ values of 2.197, 2.652, 3.125 and 3.584 for the CO minima corresponding to $k = 5, 6, 7$ and 8 respectively. Thus we have $x_i = 5, 6, 7$ and 8 and corresponding $y_i = 2.197, 2.652, 3.125$ and 3.584 respectively. A least square statistical fit of the equation $y = a + bx$ to the data demands that

$$a = \bar{y} - b\bar{x}$$

(4.1)

and

$$b = \frac{n\sum_i (x_i y_i) - (\sum_i x_i)(\sum_i y_i)}{n\sum_i x_i^2 - (\sum_i x_i)^2}$$

(4.2)

with $n = 4$. We can also calculate statistical error in a and b. Use of the above-mentioned values in Equation (4.1), (4.2) leads to the fit $y = -(0.123 \pm 0.016) + (0.463 \pm 0.0024)x$. This is shown in Figure 4.28. It can be gathered from $(2\hbar\sqrt{2\pi n_{2D}} / ea)(1/B) = k - \varphi$ that φ is given by the zero of $1/B$. Thus φ is given by $y = -0.123 + 0.463x = 0$. Hence $\varphi = 0.123/0.463 = 0.26 \pm 0.03$. The value is consistent with the expected $\varphi = 0.25$.

The magnetic field used in the experiments was obtained using a superconducting magnet. The magnet consists of a large coil through which current is passed. Magnetoresistance measurements involved sweeping the magnetic field from zero to the desired value for some data traces and sweeping the field down to zero for some others. As the magnetic field of the coil is varied, an induced emf is introduced the polarity of which is different between magnetic field sweep up and down. This emf introduces an extra current in the coil that can pass through the heater H (see Figure 4.29). This extra current adds to or subtracts from the measuring current I_0 (see Figure 4.29). Thus the net current in the coil becomes different from the measuring current. This introduces an error in the magnetic field and hence in the determination of the phase factor.

Figure 4.30 shows that the hysteresis of the magnetoresistances introduces an error of 0.6 mT out of 0.316 T in the calculation of the phase factor. The relation between the phase factor and the magnetic field as $(2\hbar\sqrt{2\pi n_{2D}} / ea)(1/B) = k - \varphi$ enables one to get an estimate in the resulting error in calculating the phase factor.

Evidently, $\Delta\varphi \sim (2\hbar\sqrt{2\pi m_{2D}}\,/ea)\Delta B/B^2$. Using $n_{2D} = 4.3\times10^{15}$ m^{-2}, a = 80 nm, ΔB =

0.6 mT and B = 0.316 T one can find $\Delta\varphi \approx$ +0.016. The sign is appropriate for the

direction of magnetic field sweep in this case. This error is smaller than statistical error

associated with deducing φ from the data of Figure 4.28. We therefore do not include

explicitly the error due to magnetic field sweep in discussing the phase of the COs.
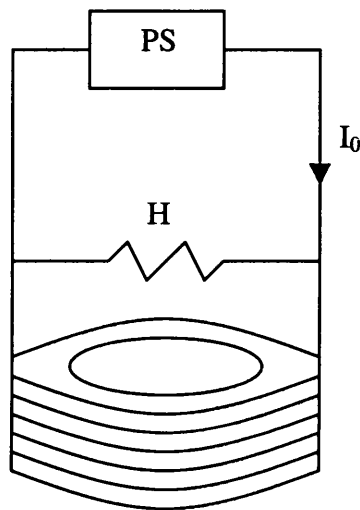
Figure 4.29

A coil of a superconducting magnet shown with the heater H. I_0 is the
current (from the power supply PS) passed through the coil. I_0 is used to
measure the magnetic field. As the magnetic field is swept, an induced
emf is introduced that can pass a current through H thereby making the
current in the coil different from I_0. For sweep up and sweep down of
the magnetic field, the polarities of the induced emf are opposite. Thus
the net current in the coil is larger or smaller than I_0 depending on the
polarity of the induced emf. H is kept on for passing current from PS
through the coil while it can be turned off to get the magnet in a
persistent mode.
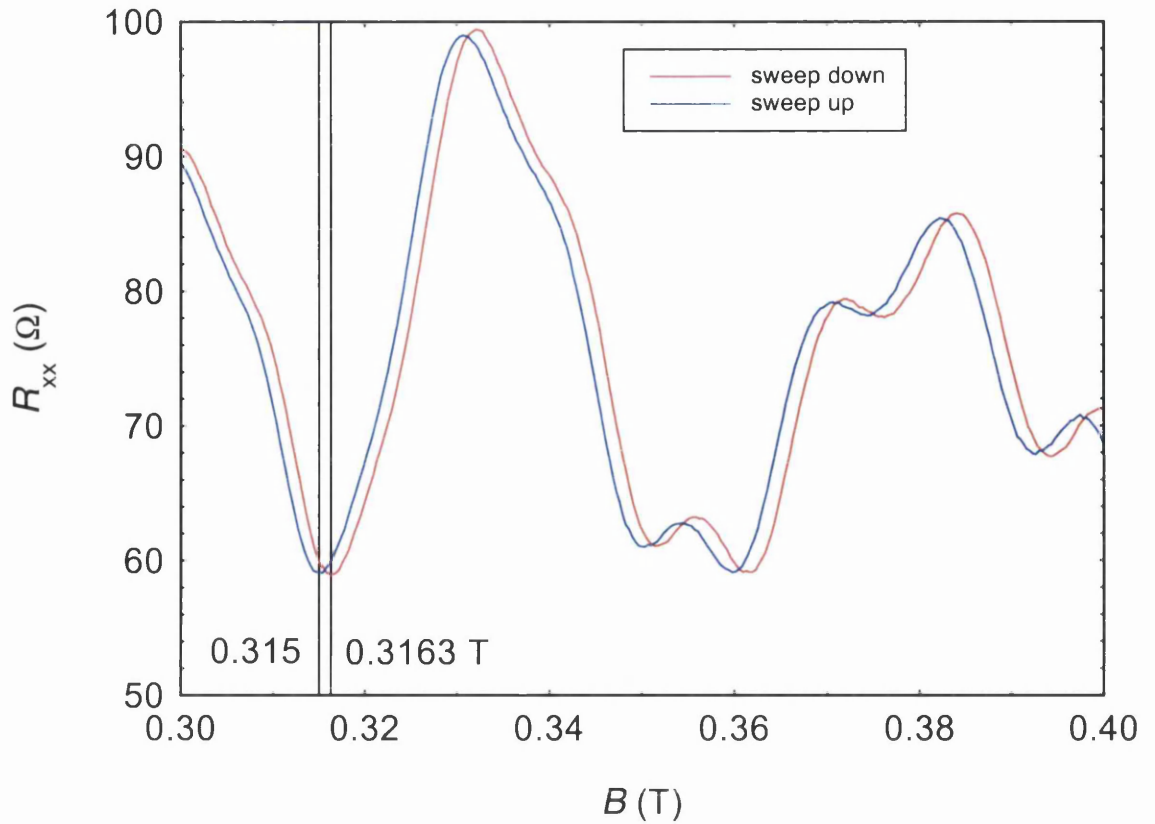
Figure 4.30
The hysteretic behaviour of the magnetoresistances between magnetic field sweep up and down. A CO minimum is found at 0.315 and 0.3163 T respectively for magnetic field sweep up and down. Thus the actual field for the minimum is (0.3150+0.3163)/2 T = 0.3156 T. Thus in a given magnetic field sweep, the hysteresis introduces an error of (0.3163 ~ 0.3156) T = ±0.6 mT in the calculation of the phase factor.

4.4 Concluding remarks

Our studies of weakly modulated asymmetric 2D LSSLs confirm the role of asymmetry in defining the observed magnetoresistance characteristics. The characteristics of the COs are found to be in striking agreement with the guiding centre drift model of D. E. Grant, A. R. Long and J. H. Davies [1]. The previous semi-classical model [7] and an equivalent quantum mechanical calculation [2] were both found to be unable to account for the data. Experimentally strong low field PMR is always associated with the dominant axial Fourier component when it is in the direction of transport and absent or weak for transport in the direction of weaker potential or when the COs are weak. The experimentally observed systematic behaviour of the low field PMR has been summarised, which is expected to be a guide in developing a realistic working model in this regard. The work has been published [17, 18].

4.5 References of Chapter IV

[1] D. E. Grant, A. R. Long and J. H. Davies; Physical Review B **61** (2000) 13127

[2] F. M. Peeters and P. Vasilopoulos; In the Proceedings of the 20th International
Conference on the Physics of Semiconductors (ICPS-20), edited by E. M.
Anastassakis and J. D. Joannopoulos, (World Scientific, Singapore, 1990); p.1589

[3] C. Albrecht, J. H. Smet, D. Weiss, K. von Klitzing, R. Hennig, M. Langenbuch, M.
Suhrke, U. Rössler, V. Umansky, H. Schweizer;
Physical Review Letters **83** (1999) 2234

[4] C. J. Emeleus, B. Milton, A. R. Long, J. H. Davies, D. E. Petticrew and M.C.
Holland; Applied Physics Letters **73** (1998) 1412

[5] B. Milton, C. J. Emeleus, K. Lister, J. H. Davies and A. R. Long;
Physica E **6** (2000) 555

[6] J. H. Davies, D. E. Petticrew and A. R. Long; Physical Review B **58** (1998) 10789

[7] R. R. Gerhardts; Physical Review B **45** (1992) 3449

[8] I. A. Larkin, J. H. Davies, A. R. Long and R. Cuscó;
Physical Review B **56** (1997) 15242

[9] D. Weiss, A. Menschig, K. von Klitzing and G. Weimann;
Surface Science **263** (1992) 314

[10] D. Pfannkuche and R. R. Gerhardts Physical Review B **46** (1992) 12606

[11] Y. Tan; Physical Review B **49** (1994) 1827

[12] C. W. J. Beenakker; Physical Review Letters **62** (1989) 2020

[13] P. H. Beton, E. S. Alves, P. C. Main, L. Eaves, M. W. Dellow, M. Henini, O. H.
Hughes, S. P. Beaumont and C. D. W. Wilkinson;
Physical Review B **42** (1990) R9229

[14] D. Weiss; (private communication)

[15] C. T. Liu, D. C. Tsui, M. Shayegan, K. Ismail, D. A. Antoniadis and H. I. Smith;
Applied Physics Letters **58** (1991) 2945

[16] R. Schuster, K. Ensslin, J. P. Kotthaus, G. Böhm and W. Klein;
Physical Review B **55** (1997) 2237

[17] S. Chowdhury, A. R. Long, J. H. Davies, D. E. Grant, E. Skuras and C. J.
Emeleus; In the proceedings of the 25th International Conference on the Physics of
Semiconductors 2000 (ICPS25), Osaka, Japan, edited by Noboru Miura and
Tsuneya Ando, (Springer-Verlag Berlin Heidelberg, 2001); Part I, p.757.

[18] S. Chowdhury, A. R. Long, E. Skuras, C. J. Emeleus and J. H. Davies; Journal of
the Korean Physical Society, (to be published).

Chapter V: Transport in stressed rectangular superlattices: manifestations of switching of guiding centre drift direction in asymmetric two-dimensional lateral surface superlattices

5.1 Introduction

Studies of 100 nm period stressed devices with square superlattices were discussed in section 4.1. For appreciably positive gate bias, magnetoresistance data for transport along [010] and [001] with a 100 nm period along these directions showed COs of the period of the diagonal Fourier components. This is because one of the diagonal Fourier components became dominant. However, when the positive gate bias was reduced, the dominance did not go to axial Fourier components. Rather, a magnetic field dependent transition of dominance between diagonal and axial Fourier components took place, as indicated by the presence of COs of both $100/\sqrt{2}$ nm and 100 nm periods in the data. This suggests that greater asymmetry is required in the potential landscape to achieve transfer of dominance from a diagonal to an axial Fourier component.

For this reason, stressed devices with rectangular superlattices were fabricated, and the magnetoresistances of these devices are discussed in this chapter. Rectangular lattices with (principal) periods 100 nm by 130 nm and 100 nm by 170 nm were realised on Hall bars aligned along the [010] and [001] directions. Both stress-induced asymmetry (discussed in section 4.1.1) and the asymmetry due to inequality of the lattice constants (discussed in section 4.2.1) are present in the potential landscape of these stressed rectangular superlattices. As discussed in this chapter, the former dominates at appreciably positive gate bias while the latter dominates at less positive gate bias. This enables the transfer of dominance from one of the diagonal to one of the axial Fourier components as the positive gate bias is reduced. Consequently, the guiding centre drift direction *switches* from a diagonal to an axial direction of the superlattice and the period of the COs was observed to change accordingly. Such phenomenon of *switching* of guiding centre drift direction is completely in accord with the guiding centre drift model of D. E. Grant, A. R. Long and J. H. Davies [1].

For intermediate gate biases, the dominant diagonal and axial Fourier components are nearly equal to each other and the change in magnetic field changes the dominant Fourier component in the effective potential as discussed in section 4.1.2. Consequently, a *magnetic field dependent switching* of guiding centre drift direction

between diagonal and axial directions takes place and accordingly magnetoresistivity structures are observed indicating magnetic field dependent change of period of the COs. This phenomenon of magnetic field dependent *switching* of guiding centre drift direction is also completely in accord with the guiding centre drift model of D. E. Grant, A. R. Long and J. H. Davies [1].

5.2 Rectangular stressed superlattices with 100 nm by 130 nm period

A resist pattern of approximately 50 nm diameter holes arranged on 100 nm by 130 nm period rectangular grids on Hall bars was transferred to the semiconductor by shallow etching. The 100 nm period was along the length of the Hall bars aligned with [001] while 130 nm period was along the length of the Hall bars aligned with [010]. The resist pattern was then removed and thick continuous Schottky gates were obtained covering the etched areas. The magnetoresistivities of one pair of such devices measured in the same cooling cycle are shown in Figure 5.1 and Figure 5.2 below for different gate biases.

It is important to note that the two devices in question were etched at the same time. Hence we expect the modulation strengths to be similar in the two devices. Thus transport in the two devices is equivalent to transport in two orthogonal directions in the same superlattice.

It is immediately noticeable in Figure 5.1 and Figure 5.2 that for large positive gate bias (+0.4 V), the period of the COs observed is *neither* 100 nm *nor* 130 nm but 79 nm, as shown by the agreement with model COs of 79 nm period.

As the positive gate bias was reduced, remarkable phenomena occurred.

- For transport along 130 nm period, the CO peaks indicated by arrows (see Figure 5.1) gradually died away as the period of the COs changed to 130 nm. At +0.1 V gate bias, the transition of CO period to 130 nm is complete, manifested by the agreement of the COs of the data trace with the model COs of 130 nm period.

- For transport in the orthogonal direction, i.e. along 100 nm period, all the COs except for the ones indicated by arrows (see Figure 5.2) died away as the gate bias was reduced to +0.1 V.

- Magnetoresistivity structures are present in the data of both the devices for some gate biases indicating magnetic field dependent transition of CO period between 130 nm and 79 nm (elucidated later in this section).

A very important point to note is that COs of 100 nm period are *not* present in the data of both the devices at any gate bias.
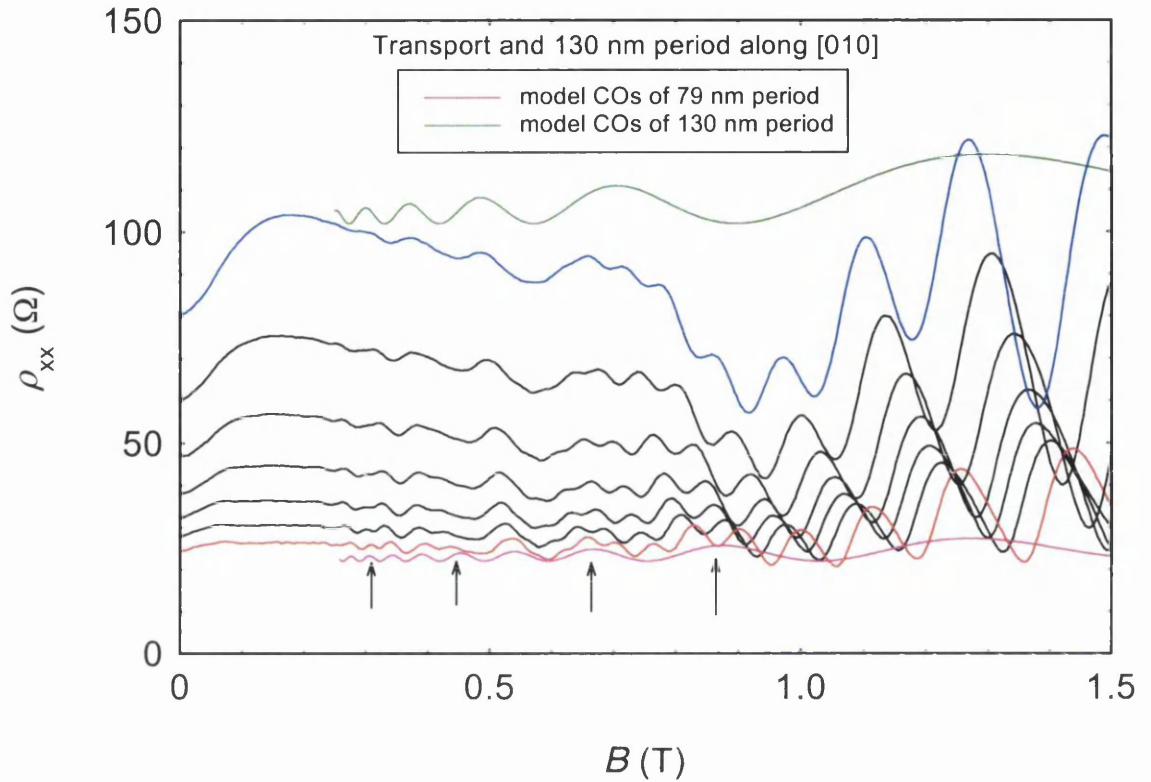
Figure 5.1

Magnetoresistivities of gated stressed device measured at 4 K for different gate biases. The biases are from +0.4 V (for the red trace) to +0.1 V (for the deep blue trace) in steps of -0.05 V. Transport is along the [010] direction in a 130 nm by 100 nm period rectangular lattice of 50 nm diameter shallow etched holes in the surface of a Hall bar. The 130 nm period was aligned along the [010] direction. Model COs of 130 nm and 79 nm periods are also shown in the figure. The model COs were calculated for the traces at +0.1 V and +0.4 V gate biases respectively, using 1D theory [2] adjusting the amplitudes of COs to match those of the data and carrier densities obtained from respective SdH oscillations at higher magnetic field. As the gate bias is turned less positive, the peaks in the red trace indicated by the arrows die away, while the rest of the peaks survive. Oscillations above about 0.6 T are dominated by SdH oscillations.
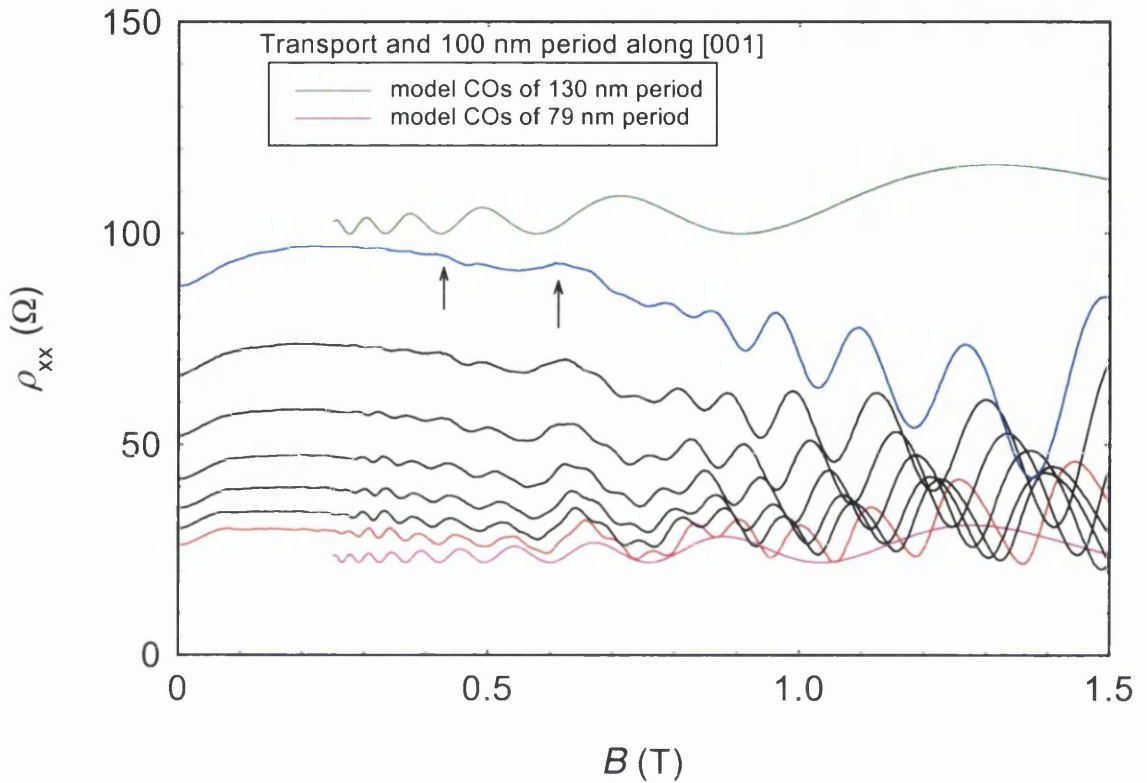
Figure 5.2
Magnetoresistivities of gated stressed device measured at 4 K for different gate biases. The biases are from +0.4 V (for the red trace) to +0.1 V (for the deep blue trace) in steps of -0.05 V. Transport is along the [001] direction in a 100 nm by 130 nm period rectangular lattice of 50 nm diameter shallow etched holes in the surface of a Hall bar. The 100 nm period was aligned along the [001] direction. Model COs of 130 nm and 79 nm periods are also shown in the figure. The model COs were calculated for the traces at +0.1 V and +0.4 V gate biases respectively using 1D theory [2] adjusting the amplitudes of COs to match those of the data and the carrier densities obtained from respective SdH oscillations at higher magnetic field. As the gate bias is turned less positive, all the peaks gradually die away except for the ones indicated by the arrows.

Before presenting theoretical explanations of the data, it is important to describe the potential landscape in the two devices in question. The reciprocal lattice points of the rectangular lattice are shown in Figure 5.3 below. It was shown in section 4.2.1 that for rectangular lattices of (principal) periods a and b, the periods of the two diagonal Fourier components are equal and given by $ab/\sqrt{(a^2 + b^2)}$. Hence for 100 nm by 130 nm period lattices, the period of the diagonal Fourier components is $100\times130/\sqrt{(100^2+130^2)}$ nm = 79 nm as indicated in Figure 5.3. An important point to note in Figure 5.3 is that the diagonal Fourier components, although not exactly along the [011] and [01$\bar{1}$] directions, are close to these directions. This has important consequences, as described below.
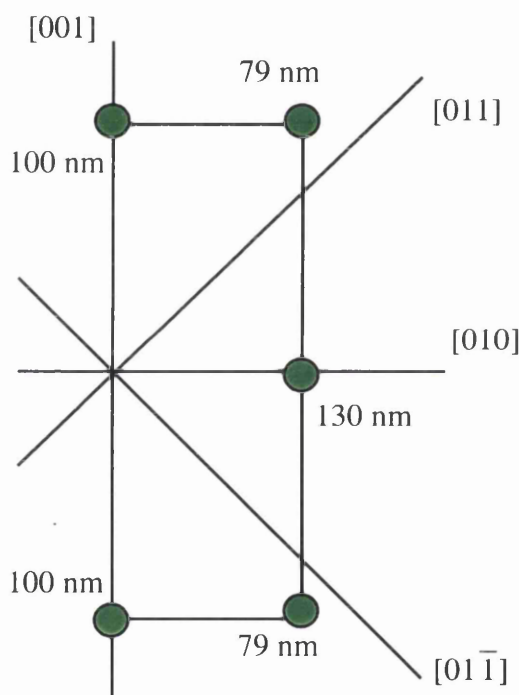
Figure 5.3
Reciprocal lattice points of 100 nm by 130 nm period rectangular lattices (shown over half of reciprocal space) for the 130 nm period along [010]. The periods of the Fourier components in question are indicated near the appropriate reciprocal lattice points. The diagonal Fourier components are seen to be close to the [011] and [01$\bar{1}$] directions. (The relative amplitudes and signs of the Fourier components are *not* addressed in the figure).
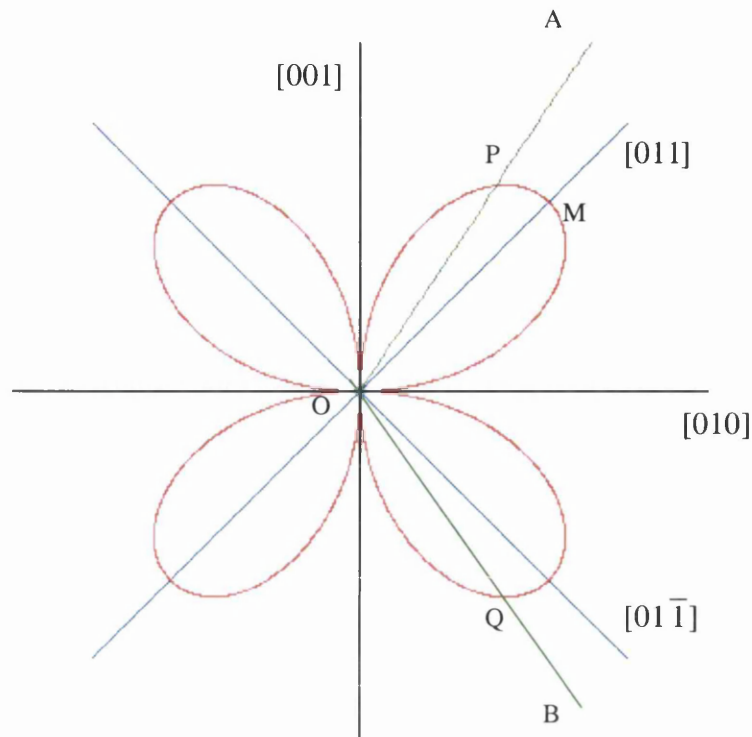
Figure 5.4
The red curve is a polar diagram of the variation of stress modulation with direction as *sin2θ*, where *θ* is the angle measured anti-clockwise with respect to [010]. Along the blue lines, stress modulations have maximum absolute values (OM). There is no stress modulation along the [010] and [001] directions, while directions like OA and OB although different from [011] and [01 1̄] have stress modulations as much as OP and OQ respectively.

As depicted in Figure 5.4, stress modulation is anisotropic and varies as *sin2θ*, where *θ* is the angle between [010] and the direction of interest (measured anti-clockwise) on a (100) GaAs wafer [3]. As shown in Figure 5.4, there are (non-zero) stress modulations along the directions close to [011] and [01 1̄]. Thus the diagonal Fourier components of the rectangular lattices in question have stress modulations associated with them. The axial Fourier components being along [010] and [001] in the two devices in question have no stress modulations associated with them (see Figure 5.4). Hence modulations associated with the axial Fourier components are due to the surface effect only [4].

The stress modulations along [011] and [01$\bar{1}$] are equal but opposite in sign [3]. The surface effect has the same sign in all directions [4]. Hence of [011] and [01$\bar{1}$], the two types of modulations add to each other in one direction, while they cancel each other in the other. For periods close to 100 nm, theory predicts that [01$\bar{1}$] is the direction of reinforcement [5, 6]. Hence the two types of modulations add to each other along [01$\bar{1}$] and cancel each other along [011]. Thus the diagonal Fourier component close to the [01$\bar{1}$] direction is larger in amplitude than that close to [011].

For large positive gate bias, the surface potentials associated with all the Fourier components are reduced to small values. The stress modulations, however, remain almost unchanged, apart from any small change due to change in screening effect. Thus [01$\bar{1}$], along which stress modulation adds to the small surface effect, becomes the direction of dominant potential. Since [01$\bar{1}$] is close to a diagonal Fourier component, one of the diagonal Fourier components becomes dominant. However, because the surface effect is small, the asymmetry of the potential landscape is small. According to the guiding centre drift model [1], guiding centre drifts *only* in the direction orthogonal to the direction of modulation of the dominant Fourier component. Thus the direction of guiding centre drift is close to [011] direction as shown schematically in Figure 5.5 below. It is clear from Figure 5.5 that the drift has components across both the Hall bars in question. Thus COs for transport in both the devices should pick up the period (79 nm) of the diagonal Fourier component *exactly* as observed (see the data in Figure 5.1 and Figure 5.2 at +0.4 V and compare with the model COs of 79 nm period). As already noted, the asymmetry is small and hence the COs are weak in amplitude.

It is important to note that as indicated in Figure 5.5, both the axial and diagonal Fourier components have non-zero amplitudes, although COs picked up only the period of the diagonal Fourier components (see data of Figure 5.1 and Figure 5.2 at +0.4 V gate bias). According to the observations, *only* the dominant Fourier component contributes to COs, in *striking* agreement with the guiding centre drift model [1]; different Fourier components do *not* independently contribute to COs unlike what is expected from a previous semi-classical model [7] and an equivalent quantum mechanical calculation [8]. Thus these two models [7, 8] are unable to account for the data.

One point which is worth mentioning is that each Fourier component like $\cos(2\pi x/a)$, can be expanded as $\frac{1}{2}(e^{i2\pi x/a} + e^{-i2\pi x/a})$; but the two parts are

conjugate of each other and hence Fourier components at only four reciprocal lattice points are important.

(a)

(b) 130 nm period along [010]   (c) 100 nm period along [001]
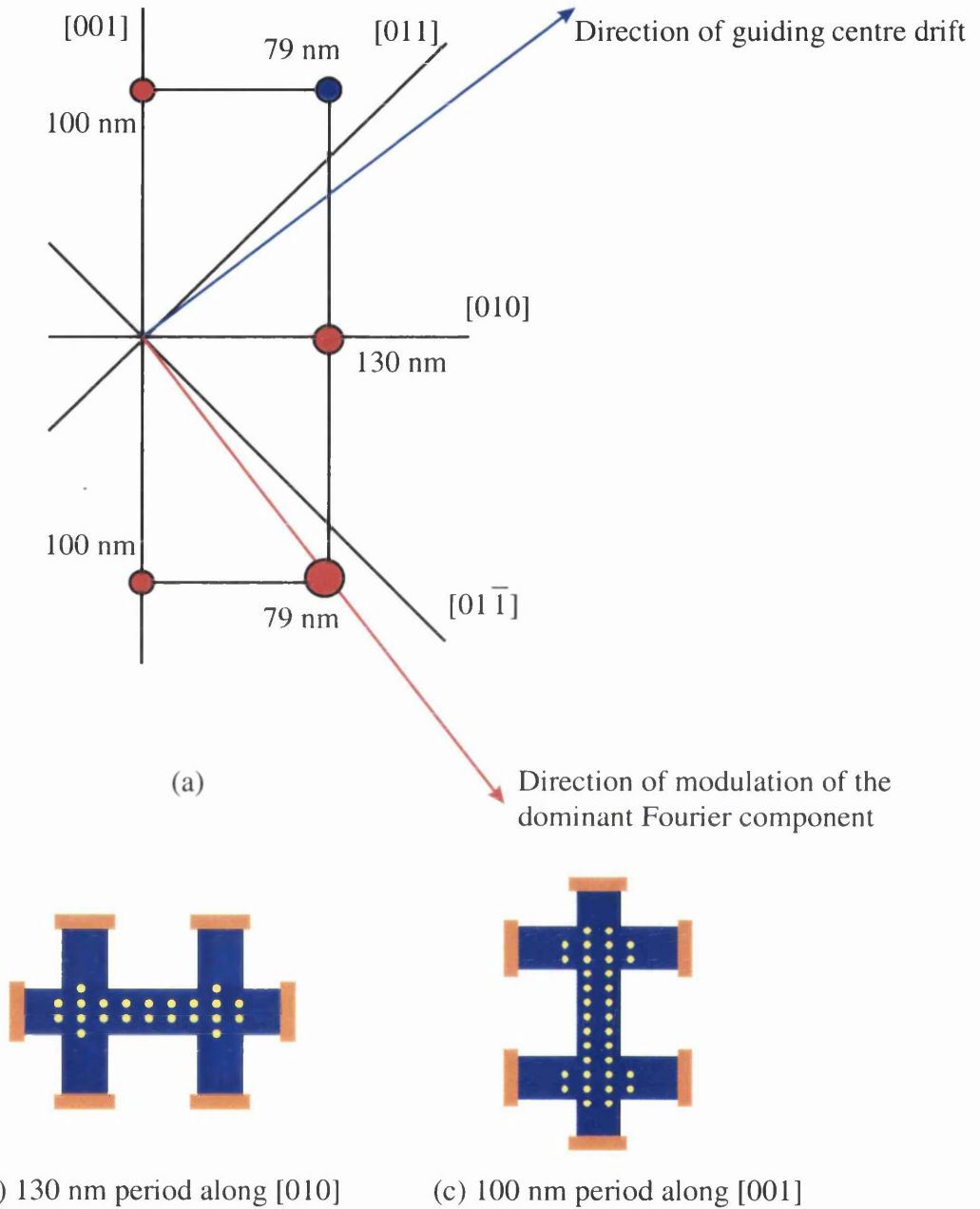
Figure 5.5
(a) Reciprocal lattice diagram showing the direction of modulation of the dominant Fourier component and guiding centre drift direction in stressed 130 nm by 100 nm period rectangular lattices for the 130 nm period along [010] and *large positive gate bias*. The sizes of the circles at the reciprocal lattice points represent relative amplitudes of the Fourier components while the two colours of circles indicate opposite sign of potential. The guiding centre drift direction is close to [011], along the direction of the blue arrow orthogonal to that of the red arrow, at an angle with both [010] and [001]. In (b) transport is along [010] and the 130 nm period while in (c) transport is along [001] and 100 nm period, both at an angle with the guiding centre drift direction.

(a)
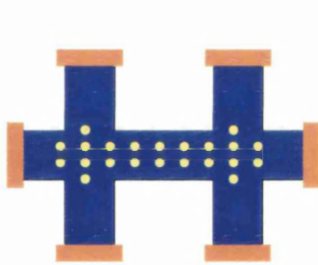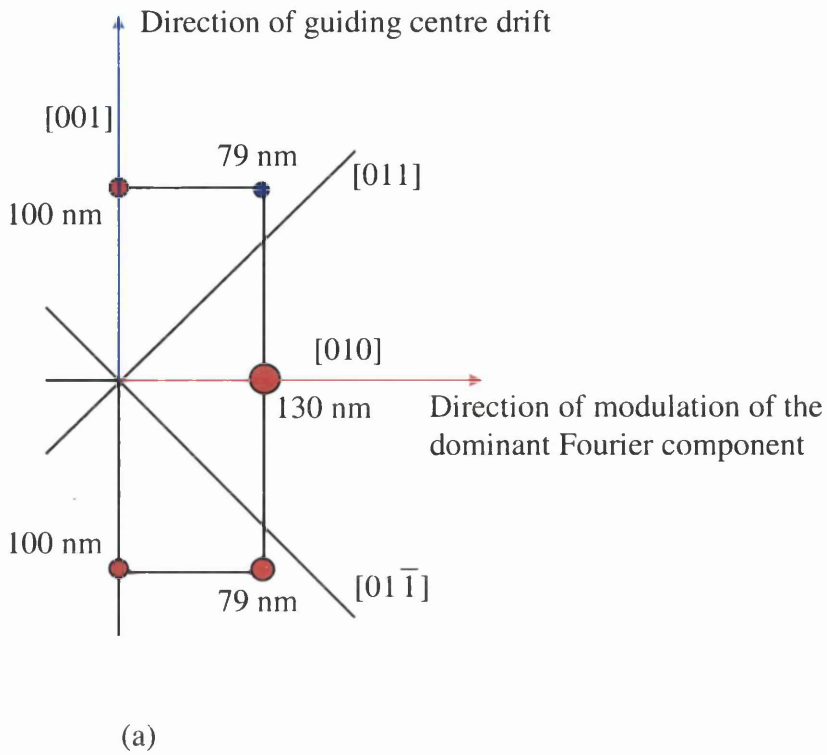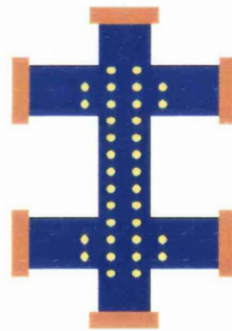
(b) 130 nm period along [010]   (c) 100 nm period along [001]

Figure 5.6
(a) Reciprocal lattice diagram showing the direction of modulation of the dominant Fourier component and guiding centre drift direction in stressed 130 nm by 100 nm period rectangular lattices for the 130 nm period along [010] and *appreciably small positive gate bias*. The sizes of the circles at the reciprocal lattice points represent the relative amplitudes of the Fourier components while the two colours of circles indicate opposite sign of potential. The guiding centre drift direction is [001], along the direction of the blue arrow orthogonal to that of the red arrow. In (b) transport is along [010] and the 130 nm period while in (c) transport is along [001] and the 100 nm period. Guiding centre drift is across the Hall bar of (b) and along the Hall bar of (c).

Besides the asymmetry induced by stress, the difference in lattice constants in the rectangular lattices also introduces asymmetry in the potential landscape as discussed in detail in section 4.2.1. This is because the modulation associated with the shorter period is more attenuated than that with the larger period before it reaches the 2DEG [5].

As the positive gate bias is reduced, the surface effect becomes larger. The 130 nm period being longer than both 100 nm and 79 nm periods, the modulation due to the surface effect associated with 130 nm period is larger than those due to the surface effects associated with the 100 nm and 79 nm periods. Moreover, the stress modulations, being associated with shorter period (79 nm), can be surpassed by the surface effect associated with the longest period (130 nm) if the positive gate bias is reduced appreciably. Hence for small positive gate bias, the Fourier component associated with the 130 nm period becomes dominant in the potential landscape.

According to the guiding centre drift model [1], guiding centre drifts *only* in the direction orthogonal to the direction of modulation of the dominant Fourier component. Thus the direction of guiding centre drift is [001] as shown schematically in Figure 5.6 above. As is evident from Figure 5.6, the guiding centre drift direction is across the Hall bar oriented along [010] and along the Hall bar oriented along [001]. Hence for +0.1 V gate bias, there are COs of 130 nm period in Figure 5.1, while there is no COs of 130 nm period in Figure 5.2.

Thus the change of the period of the COs from 79 nm to 130 nm as the gate bias is changed from +0.4 V to +0.1 V is accounted for in that guiding centre drift direction has *switched* from close to [011] direction (at +0.4 V bias) to [001] direction (at +0.1 V bias).

Again, as indicated in the reciprocal lattice diagram of Figure 5.6, both the axial and diagonal Fourier components have non-zero amplitudes, but COs picked up only the period (130 nm) of the dominant axial Fourier component (see data of Figure 5.1 at +0.1 V gate bias). According to the observations, *only* the dominant Fourier component contributes to COs, in *striking* agreement with the guiding centre drift model [1]. It is observed that different Fourier components do *not* independently contribute to COs. In particular, there are no COs of 100 nm period for transport along the 100 nm period (see Figure 5.2). Thus the previous semi-classical model [7] and an equivalent quantum mechanical calculation [8] are both unable to account for the data.

Now let us turn to intermediate gate biases for the device of Figure 5.1. The data for the +0.2 V gate bias are shown again in Figure 5.7 below. Comparison with model COs of 130 nm and 79 nm periods (shown in Figure 5.7) reveals that all the CO

peaks in the data agree with 130 nm period except for the ones between the two CO minima indicated by M_1 and M_2. There are two CO peaks under the SdH oscillations in the data (indicated by the red trace) between the two CO minima M_1 and M_2. One corresponds to the 130 nm period CO peak marked as P_1, while the other one corresponds to 79 nm period CO peak marked as P_2. In fact, the 79 nm period peak in question appeared as a shoulder on the 130 nm period peak in question. The magnetoresistance feature in question is discernible in the data of Figure 5.1 for +0.15 V and +0.25 V gate biases as well. As discussed below, this magnetoresistance feature can be accounted for as a magnetic field dependent transition of CO period between 79 nm and 130 nm.
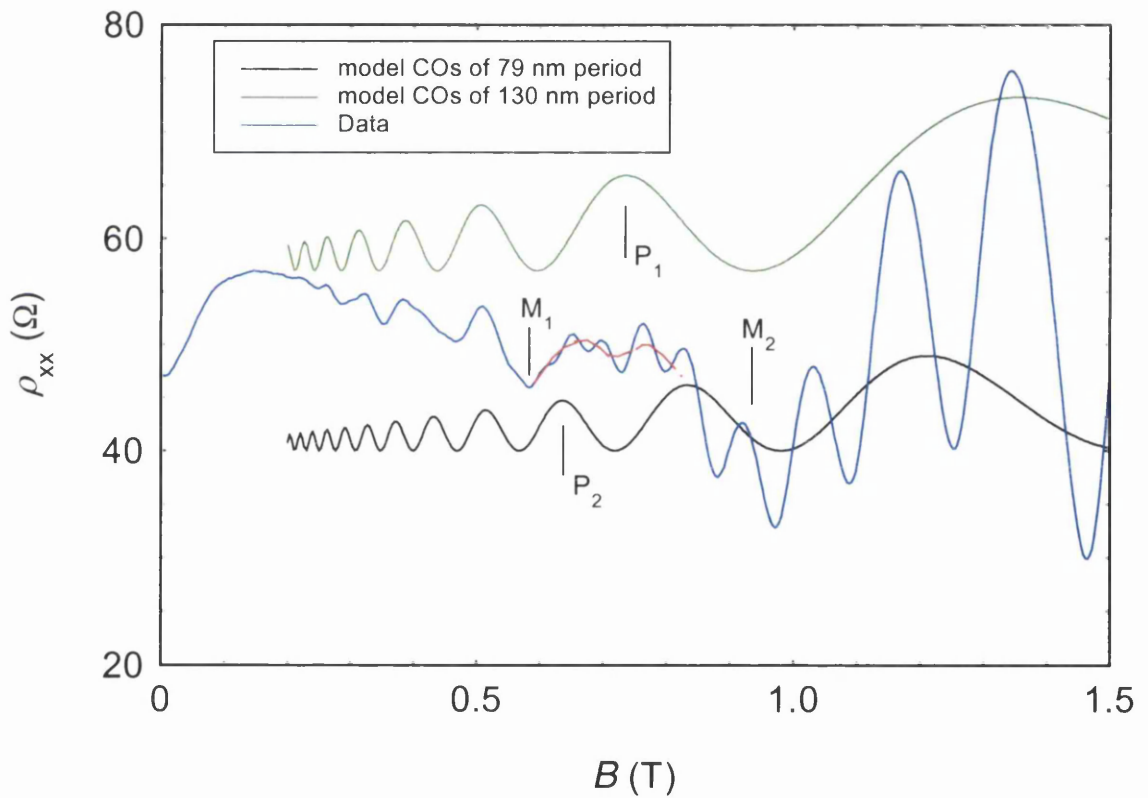
Figure 5.7
Magnetoresistivities of the gated stressed device of Figure 5.1 measured at 4 K with +0.2 V gate bias. Between the two CO minima M_1 and M_2, there are two CO peaks in the data trace under the SdH oscillations, as indicated by the red trace. One corresponds to the 130 nm period CO peak P_1, while the other one corresponds to 79 nm period CO peak P_2. The rest of the peaks in the data trace correspond to 130 nm period (although the shapes are irregular).

For intermediate gate biases like +0.2 V, the dominant axial and diagonal Fourier components are expected to be nearly equal to each other in amplitude. The magnetic field dependence of the effective potentials of the two Fourier components are different as discussed in detail in section 4.1.2 (regarding the stressed square lattices for transport along [010] and [001] at less positive gate bias). Thus change in magnetic field can change the dominant Fourier component of the effective potential for some magnetic field ranges leading to change of guiding centre drift direction and consequent change in CO period. Thus the presence of COs of two different periods in the data as observed can be accounted for as due to a magnetic field dependent *switching* of guiding centre drift direction in accord with guiding centre drift model [1]. The observation cannot be accounted for by a superposition of COs of 130 nm and 79 nm periods as stipulated by the earlier models [7, 8], because in that case both the periods should have been present for all other CO peaks unlike observation.
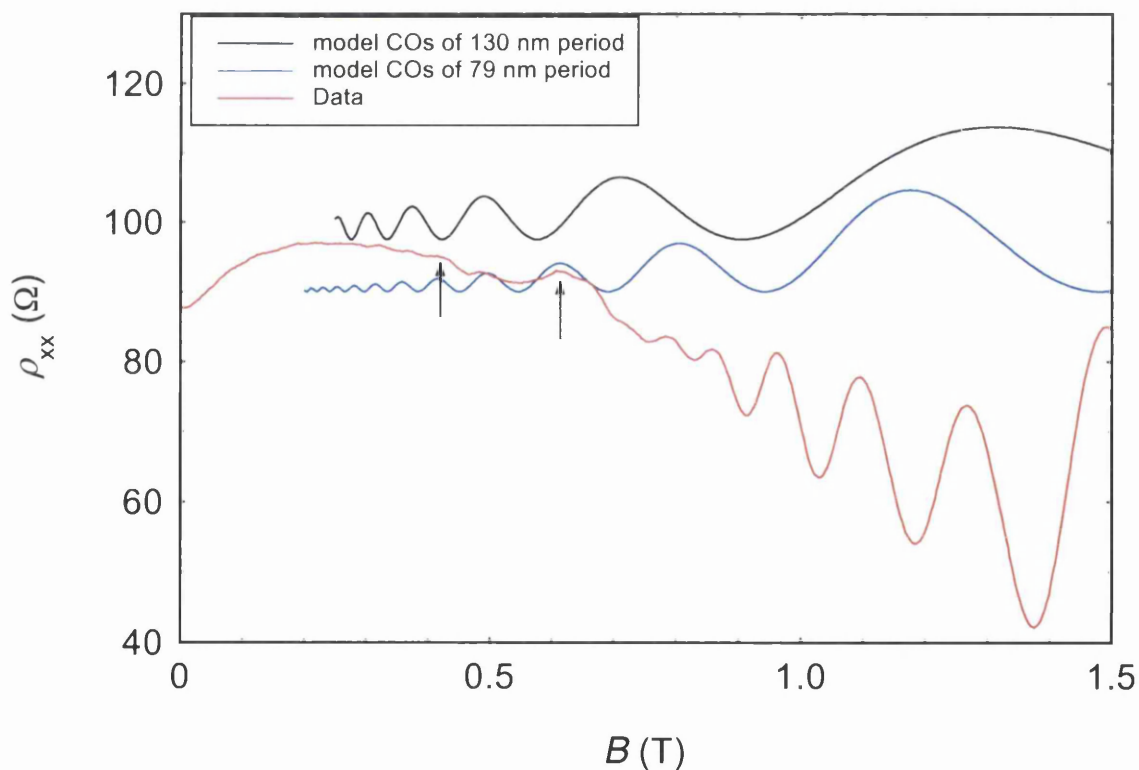
Figure 5.8
Magnetoresistivities of the gated stressed device of Figure 5.2 measured at 4 K with +0.1 V gate bias. The two peaks in the data indicated by the arrows agree with those of a trace containing model COs of 79 nm period.

The magnetic field dependent switching of guiding centre drift direction also occurred in the device of Figure 5.2. At +0.1 V gate bias, the direction of modulation of the dominant Fourier component (of 130 nm period) [010] is across the Hall bar and hence guiding centre drift is along [001], i.e. along the length of the Hall bar, as already discussed. As this drift has no component across the Hall bar, the COs (of 130 nm period) are suppressed (absent). Data are shown again in Figure 5.8 along with model COs of both 130 nm and 79 nm periods. At the magnetic field values indicated by arrows in Figure 5.8, the effective potential associated with the dominant axial Fourier component of 130 nm period is minimal, as can be seen in the trace containing 130 nm period model COs. Thus a diagonal Fourier component turned dominant at these magnetic fields producing the two peaks (indicated by arrows). That the two peaks are indeed due to *switching* of guiding centre drift to diagonal direction is ascertained in Figure 5.8. It is clear from Figure 5.8 that indeed the two peaks agree with those of the trace containing model COs of 79 nm period. It is noteworthy that the CO peak at about 0.5 T, intermediate between the two indicated by the arrows, is suppressed (absent) because the axial Fourier component of 130 nm period is dominant at this field (as can be seen in the trace containing model COs of 130 nm period) and the drift is along the Hall bar. The observations cannot be accounted for by the earlier models [7, 8] according to which COs of 100 nm period were expected in the data of Figure 5.8 (unlike observations), as transport is along the 100 nm period in the superlattice.

Before leaving the discussion on the 130 nm by 100 nm period stressed superlattices, one very subtle point should be addressed. As the gate bias was gradually reduced from +0.4 V to +0.1 V, the effect of *switching* became more marked in the data of Figure 5.1 than in those of Figure 5.2. A contributory factor may well be that according to Figure 5.5, the direction of guiding centre drift is at a smaller angle to [010] and hence the component of drift across the Hall bar of Figure 5.2 is larger.

All the effects discussed so far in this chapter were also observed in the magnetoresistance data of 100 nm by 170 nm period stressed superlattices as well, as discussed in the following section.

5.3 Rectangular stressed superlattices with 100 nm by 170 nm period

A resist pattern of approximately 50 nm diameter holes arranged on 100 nm by 170 nm period rectangular grids on Hall bars was transferred to the semiconductor by shallow etching. Hall bars used were oriented along the [010] and [001] directions. Two sets of devices were fabricated. In one set, the 170 nm period was aligned along

Hall bars of both the orientations, while in the other set the 100 nm period was aligned along Hall bars of both the orientations. The resist pattern was then removed and thick continuous Schottky gates were realised covering the etched areas. Magnetoresistivities of one device of each set are shown in Figure 5.9 and Figure 5.10 for different gate biases.
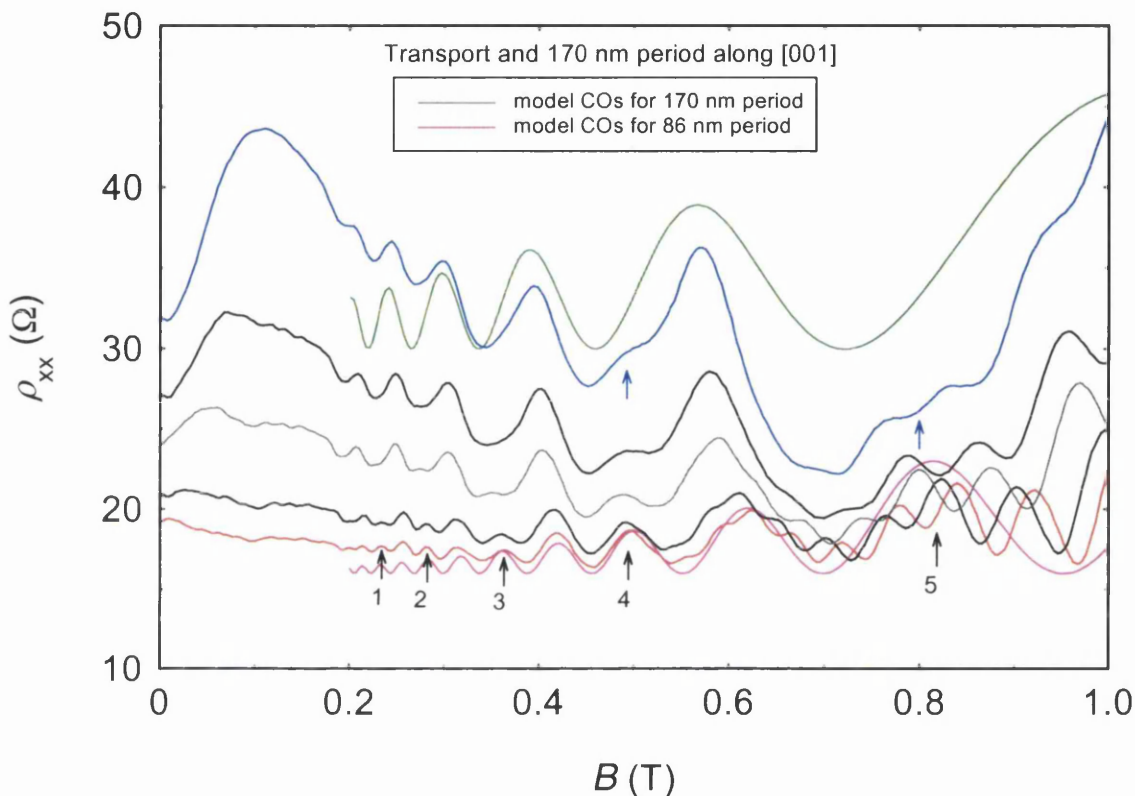
Figure 5.9

Magnetoresistivities of a gated stressed device measured at 4 K with different gate biases: 0.3, 0.2, 0.1, 0.05 and 0 V from bottom (red trace) to top (deep blue trace). The transport was along the [001] direction in a 170 nm by 100 nm period rectangular lattice of 50 nm diameter shallow etched holes at the surface of a Hall bar. The 170 nm period was aligned along [001] direction. Model COs of 170 nm and 86 nm periods are shown in the figure. The model COs were calculated for the traces at 0 V and +0.3 V gate biases respectively using 1D theory [2] with the amplitudes adjusted to match those of the data and the carrier densities obtained from respective SdH oscillations at higher magnetic field. As gate bias is made less positive, the alternate peaks in the red trace indicated by the black arrows gradually die away (while some remnant remains at 0.5 T and 0.8 T indicated by blue arrows), while the rest of the peaks survive (and grow larger).
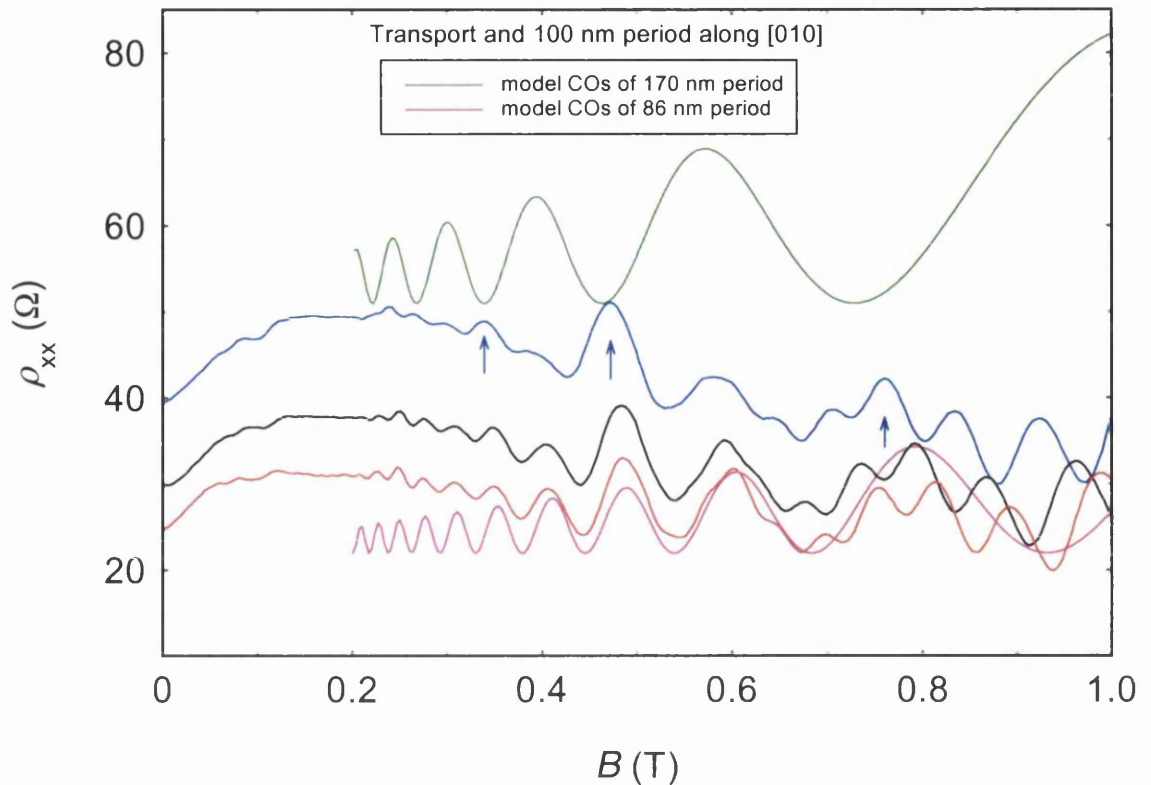
Figure 5.10

Magnetoresistivities of a gated stressed device measured at 4 K with different gate biases: 0.4, 0.3 and 0.2 V from bottom (red trace) to top (deep blue trace). The transport was along the [010] direction in a 100 nm by 170 nm period rectangular lattice of 50 nm diameter shallow etched holes at the surface of a Hall bar. The 100 nm period was aligned along [010] direction. Model COs of 170 nm and 86 nm periods are also shown in the figure. The model COs were calculated for the traces at +0.2 V and +0.4 V gate biases respectively using 1D theory [2] with the amplitudes adjusted to match those of the data and the carrier densities obtained from respective SdH oscillations at higher magnetic field. As the gate bias is turned less positive, alternate CO peaks gradually die away leaving the ones indicated by the arrows.

It should be mentioned that similar data were obtained for 170 nm period along [010] and 100 nm period along [001] direction. It should also be noted that the two devices of Figure 5.9 and Figure 5.10 are from two sets of devices *not* etched at the same time. Hence potential modulation strengths are not expected to be the same in the two devices for a given gate bias. The modulation strengths are, however, expected to be adjustable by gate bias.

It can be noticed in the above two figures that for large positive gate bias (0.3 V in Figure 5.9 and 0.4 V in Figure 5.10) the period of the COs is *neither* 100 nm *nor* 170 nm but 86 nm. This is clear in the above two figures from the agreement of the data with model COs of 86 nm period.

As the positive gate bias was reduced, remarkable phenomena occurred.

- For transport along the 170 nm period, alternate CO peaks indicated by the black arrows (see Figure 5.9) gradually died away as the period of the COs changed to 170 nm. At 0 V gate bias, the transition of CO period to 170 nm is almost complete, as is clear from the agreement of the data with model COs of 170 nm period.

- For transport in the orthogonal direction, i.e. along the 100 nm period, alternate COs (except for the ones indicated by arrows (see Figure 5.10)) gradually died away as the positive gate bias was reduced. Note that the COs that did not die away, although corresponding to the 170 nm period, are in anti-phase to the 1D prediction.

- Magnetoresistivity structures are present in the data of both the devices for some gate biases, which correspond to the magnetic field dependent transition of CO period between 170 nm and 86 nm (elucidated later in this section).

As in the case of stressed 100 nm by 130 nm period superlattices, there are no COs of 100 nm period in the data of both the devices at any gate bias.

The potential landscapes in the two devices in question are similar to those of 100 nm by 130 nm lattices. The differences are:

(a) The period of the diagonal Fourier components of 100 nm by 170 nm period lattices is $100 \times 170/\sqrt{(100^2 + 170^2)}$ nm = 86 nm. This is almost exactly half of the 170 nm period.

(b) As the difference between the two lattice constants (100 nm and 170 nm) is greater this time compared with that of 100 nm by 130 nm lattices, the symmetry is broken more strongly at less positive gate bias.

As before, for large positive gate bias, one of the diagonal Fourier components (that close to $[01\bar{1}]$) becomes dominant and guiding centre drift occurs close to [011] direction. The drift has components across both the Hall bars in question and COs in both the devices should pick up only the period of the diagonal Fourier component exactly as observed (see data at 0.3 V in Figure 5.9 and 0.4 V in Figure 5.10). This is in accord with the guiding centre drift model [1]. As before, for large forward gate bias, the asymmetry in the potential landscape is small and hence COs are weak in amplitude. It should be noted that as the device of Figure 5.10 was more strongly etched, the asymmetry in the potential landscape in this device is larger even at +0.4 V

gate bias leading to COs of larger amplitude than those in Figure 5.9 for large forward gate bias.

As before, as the positive gate bias was reduced to small values, the axial Fourier component of longer period (170 nm) turned dominant and guiding centre drift *switched* to the direction orthogonal to the direction of modulation of the dominant Fourier component. Thus the direction of drift *switched* from close to [011] to the [010] direction. Since the drift is across the Hall bar of Figure 5.9, fairly large COs of 170 nm period were observed (see 0 V data of Figure 5.9 and compare with the neighbouring model COs of 170 nm period). As 86 nm is almost exactly half of 170 nm, the transition of CO period from 86 nm to 170 nm involved suppression of alternate CO peaks as can be seen in Figure 5.9. As the drift is along [010], it has no component across the Hall bar of Figure 5.10; hence no regular COs of 170 nm period were observed (see 0.2 V data of Figure 5.10 and compare with the neighbouring model COs of 170 nm period). Some of the CO peaks observed are in anti-phase to those of 170 nm period COs predicted by 1D model [2] and are discussed later in this section.

Thus change of period of COs from 86 nm to 170 nm as gate bias is changed from large positive to less positive can be accounted for in that guiding centre drift direction has *switched* from close to [011] to [010] direction, in accord with guiding centre drift model [1]. An important point in the discussion here (and also in that of 100 nm by 130 nm superlattices discussed in the previous section) is that the 100 nm period COs are completely absent from the data, while it was expected to be present for transport along 100 nm period. This is one of the most important observations in favour of the guiding centre drift model [1]. As in the case of 100 nm by 130 nm lattices, the experimental observations suggest that *only* the dominant Fourier component contributes to COs in *striking* agreement with the guiding centre drift model [1]. Different Fourier components do *not* independently contribute to COs in contradiction to a previous semi-classical model [7] and the equivalent quantum mechanical calculations [8]. These formulations [7, 8] are therefore unable to account for the data.

Now let us turn to the data of the device of Figure 5.9 for intermediate gate biases. Data for 0.1 V gate bias are shown again in Figure 5.11. Comparison with model COs of 170 nm and 86 nm periods (also shown in Figure 5.11) reveals that all the COs in the data agree with 170 nm period except for the peaks indicated by arrows. Comparison with model COs of 86 nm period shows that the peaks identified by arrows in fact agree with those of 86 nm period. As before, the magnetoresistance feature in question can be accounted for as a result of magnetic field dependent *switching* of

guiding centre drift direction between the axial and diagonal directions and consequent transition of CO period between 170 nm and 86 nm.

The magnetoresistance features in question are discernible in the data of Figure 5.9 for 0.2, 0.05 and even 0 V gate biases as well. The two blue arrows in Figure 5.9 identify two CO peaks that are remains of 86 nm period CO peaks marked by black arrow number 4 and 5. The two peaks marked by blue arrows produced shoulders on the main 170 nm period CO peaks. The supplementary peaks are spectacular and are particularly easy to see in this data because of the coincidence that 86 nm is almost exactly half of 170 nm.
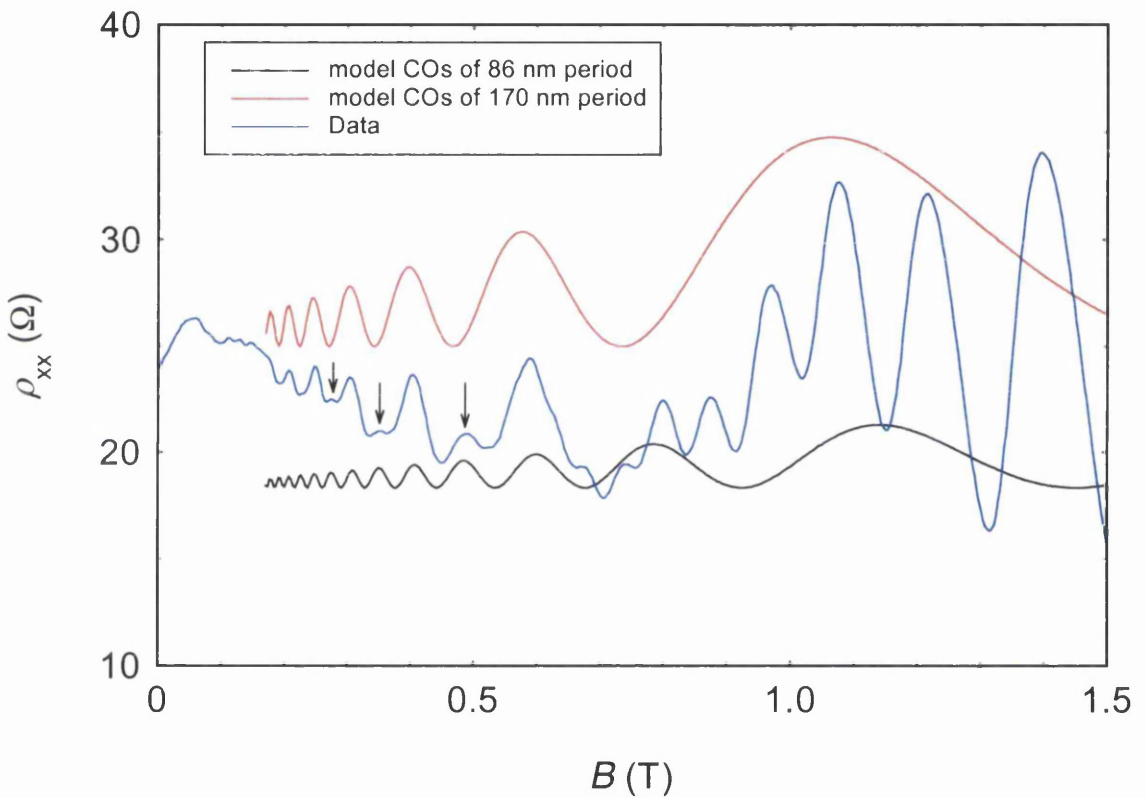
Figure 5.11
Magnetoresistivities of the gated stressed device of Figure 5.9 measured at 4 K with +0.1 V gate bias. All the COs agree with 170 nm period except for the CO peaks indicated by the arrows. The peaks identified by the arrows agree with 86 nm period COs. The data trace as a whole corresponds to a magnetic field dependent *switching* of CO period between 170 nm and 86 nm.

The magnetic field dependent *switching* of guiding centre drift direction also occurred in the device of Figure 5.10. At +0.2 V gate bias, the direction of modulation of the dominant (axial) Fourier component is across the Hall bar and hence guiding

centre drift is along [010], i.e. along the length of the Hall bar. As this drift has no component across the Hall bar, the CO peaks (of 170 nm period) are suppressed. Data are again shown in Figure 5.12. At the magnetic field values indicated by arrows in Figure 5.12, the effective potential associated with the dominant axial Fourier component of 170 nm period is minimal, as can be seen in the trace containing 170 nm period model COs. Thus one of the diagonal Fourier components turned dominant at these magnetic fields producing the peaks indicated by the arrows. Comparison with model COs of 170 nm period in Figure 5.12 reveals that these peaks appeared in *anti-phase* with conventional COs of 170 nm period and hence can *only* be explained in terms of magnetic field dependent *switching* of dominant Fourier component between axial and diagonal directions. That the peaks are indeed due to *switching* of guiding centre drift to the diagonal direction is confirmed in Figure 5.12 below. It is clear from Figure 5.12 that indeed the peaks in question agree with those of the trace containing model COs of 86 nm period.
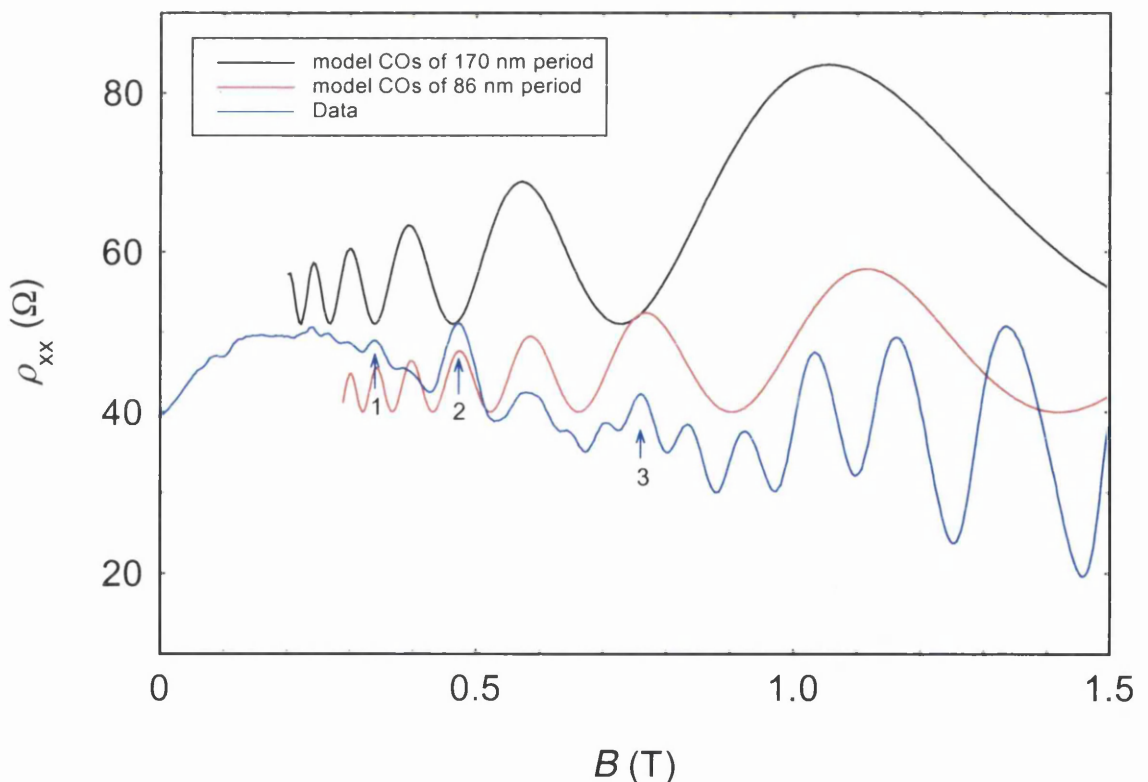
Figure 5.12
Magnetoresistivities of the gated stressed device of Figure 5.10 measured at 4 K with +0.2 V gate bias. The peaks in the data indicated by the arrows agree with those of a trace containing model COs of 86 nm period. The peaks identified by arrow number 3 is not as significant relative to the background as the other two, possibly because it is under SdH oscillations.

5.4 Magnetic fields of switching in terms of effective potential

As to the magnetic field dependent switching of the CO period between axial and diagonal Fourier components, the magnetic fields at which switching occurs is not always clear (see for example Figure 4.17). However, in cases where it is clearer (see for example Figure 5.11), the relevant effective potentials can be plotted together to explicitly relate the cross over of dominance between them with the fields at which switching occurs. An example is given in Figure 5.13. The black and red lines are Fourier amplitudes (Bessel functions) in the effective potential. The dominant amplitude determines the periodicity of the COs. The switchover points are where black and red lines intersect and the green arrows in Figure 5.13 shows that these positions correspond to minima in the experimental trace as expected. Agreement between experiment and theory is excellent.
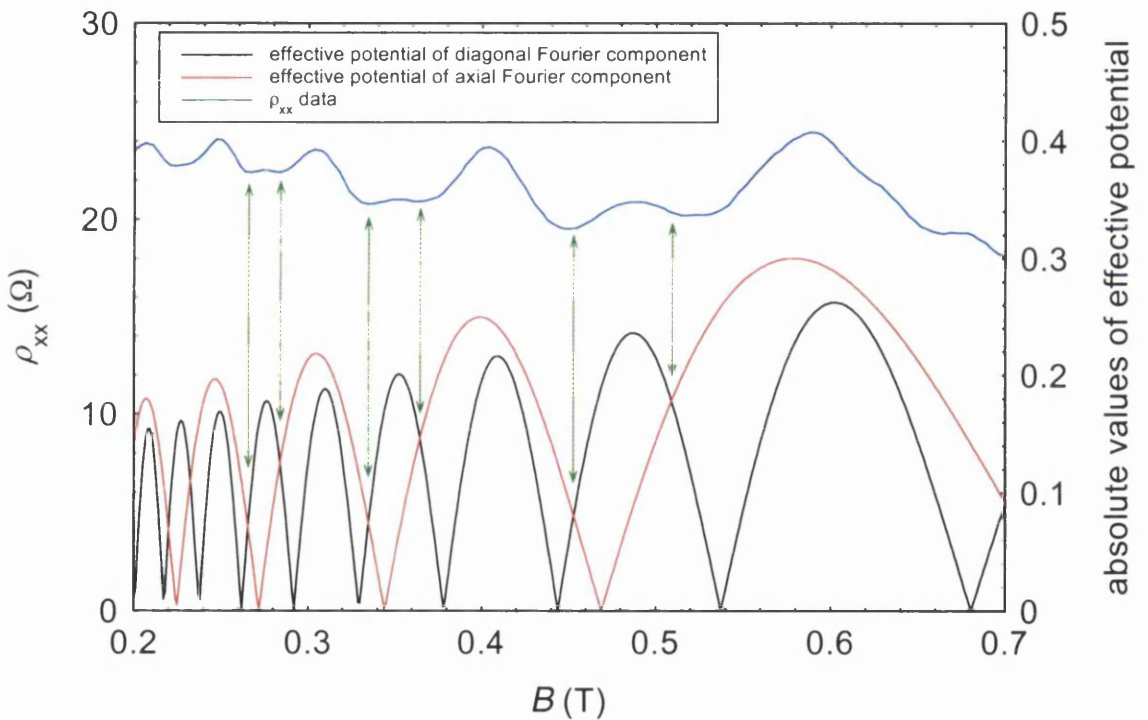
Figure 5.13
The data of Figure 5.11 plotted with the magnetic field dependence of the absolute values of the effective potentials associated with the axial and diagonal Fourier components i.e. $V_x J_0(2\pi R / a_x)$ and $V_d J_0(2\pi R / a_d)$ respectively. The parameters used are carrier density 4.42×10^{15} m^{-2} (obtained from SdH oscillations), $a_x = 170$ nm, $a_d = 86$ nm, $V_x = 1$, $V_d = 1.2 V_x$. Arrows indicate the magnetic fields at which the effective potentials change dominance. The switching of the CO period in the data also occurred near these magnetic fields. The discrepancy for the switching above 0.5 T is possibly because of the SdH oscillations.

5.5 The experimental systematic of positive magnetoresistance (PMR)

The experimental systematic of PMR in the case of stressed square lattices was discussed in section 4.1.3. It is important to note the similar pattern in the data from the rectangular superlattices of this chapter as well.

As before, PMR is primarily associated with larger asymmetry in the potential landscape and with the dominant axial Fourier component when it is in the direction of transport, as is evident in the data of Figure 5.1 and Figure 5.9 for less positive gate bias. This contradicts the simulations [1] according to which every Fourier component in 2D periodic potential contributes to PMR. These simulations do not enable us to understand the broad PMR structure at about 0.2 T in the data of Figure 5.2 and Figure 5.10 at less positive gate biases either. Thus these simulations [1] are unable to account for the experimental systematic of PMR.

5.6 Concluding remarks

Our studies of weakly modulated asymmetric stressed 2D LSSLs with rectangular lattices confirm the role of asymmetry in defining the observed magnetoresistance characteristics. The characteristics of COs are found to be in excellent agreement with the guiding centre drift model of D. E. Grant, A. R. Long and J. H. Davies [1]. The data exhibit striking confirmation of the *switching* of dominant Fourier component in the magnetic field dependent effective potential and consequent *switching* of the guiding centre drift direction that results in change of CO period between those of axial and diagonal Fourier components. The switching has been observed both by change of gate bias that changes the dominant Fourier component in the 2D periodic potential and by change of magnetic field that changes the dominant Fourier component in the effective potential. The previous semi-classical model [7] and an equivalent quantum mechanical calculation [8] are both found to be unable to account for the data, specially the phenomenon of *switching*. The experimental systematic of PMR has been presented in aid of developing a realistic working model in this regard. The work has been published [9].

5.7 References of Chapter V

[1] D. E. Grant, A. R. Long and J. H. Davies; Physical Review B **61** (2000) 13127

[2] C. W. J. Beenakker; Physical Review Letters **62** (1989) 2020

[3] E. Skuras, A. R. Long, I. A. Larkin, J. H. Davies and M. C. Holland;
Applied Physics Letters **70** (1997) 871

[4] C. J. Emeleus, B. Milton, A. R. Long, J. H. Davies, D. E. Petticrew and M.C.
Holland; Applied Physics Letters **73** (1998) 1412

[5] J. H. Davies, D. E. Petticrew and A. R. Long; Physical Review B **58** (1998) 10789

[6] I. A. Larkin, J. H. Davies, A. R. Long and R. Cuscó;
Physical Review B **56** (1997) 15242

[7] R. R. Gerhardts; Physical Review B **45** (1992) 3449

[8] F. M. Peeters and P. Vasilopoulos; In the Proceedings of the 20th International
Conference on the Physics of Semiconductors (ICPS-20), edited by E. M.
Anastassakis and J. D. Joannopoulos, (World Scientific, Singapore, 1990); p.1589

[9] S. Chowdhury, E. Skuras, C. J. Emeleus, A. R. Long, J. H. Davies, G. Pennelli and
C. R. Stanley; Physical Review B **63** (2001) 153306

Chapter VI: Transport in unstressed and stressed symmetric two-dimensional lateral surface superlattices: interplay between semi-classical and quantum mechanical Physics

6.1 Introduction

Magnetotransport data obtained from weakly modulated *asymmetric* 2D LSSLs were discussed in Chapter IV and V. It was demonstrated that the semi-classical dynamical effect of guiding centre drift [1] in asymmetric potential landscapes is enough to account in detail for almost all the features of the COs observed.

In this chapter magnetotransport data for weakly modulated *symmetric* 2D LSSLs are discussed. Symmetric potential landscapes at the 2DEG were realised in two different ways.

- Etched patterns of square symmetry were obtained on unstressed Hall bars and the resist pattern was removed after etching. Some devices were left without a gate while some were gated. The modulation at the 2DEG in the ungated samples is due to the surface effect *only* [2, 3]. The surface effect being isotropic [3], the modulations in the orthogonal principal directions in the plane of the 2DEG are equal in amplitude. Consequently, the potential landscapes in ungated unstressed superlattices of square symmetry are symmetric between the principal directions.

- In stressed superlattices, the superposition of the surface effect with the stress modulation turns the potential landscape of even square superlattices asymmetric, as discussed in Chapter IV. However, in short period superlattices the surface effect is small [4]. It can be eliminated (almost) entirely by applying a large forward gate bias, while the stress modulation remains almost unchanged, apart from any change due to change in the screening effect at the 2DEG. Moreover, since the stress modulation is present *only* along [011] and [01$\bar{1}$] directions and its magnitude is equal but opposite in sign in these two directions [5] (for square superlattices), the potential landscape of a short period stressed square superlattice (with principal axes aligned along the cleavage directions) turns symmetric for large forward gate biases. A reversal of sign is equivalent just to a half period translation of the potential distribution in one principal direction, i.e.

$$V_0 \cos(2\pi x / a) - V_0 \cos(2\pi y / a) = V_0 \cos(2\pi x / a) + V_0 \cos(2\pi y / a + \pi)$$

$$= V_0 \cos(2\pi x / a) + V_0 \cos[2\pi(y + a / 2)/a]$$

$$(6.1)$$

The way of realising weakly modulated symmetric potential landscape containing stress modulation discussed above is novel. As discussed in this chapter, to understand the magnetoresistance data of symmetric 2D LSSLs, it is necessary to invoke an interplay between semi-classical dynamical effect involving pinned guiding centre trajectories in symmetric potential landscape [1] and a quantum mechanical effect involving modulation of the density of states [6]. Moreover, as also discussed in this chapter, transport in stressed, symmetric, short period and high mobility superlattices is dominated by quantum mechanical effects and the magnetoresistances showed a characteristic amplitude modulation of COs whenever one flux quantum passed through 1, 2, 3, ... unit cells of the lattice.

6.2 Ungated unstressed devices with square superlattices

Resist patterns of about 50 nm diameter pillars arranged on square grids of 100 nm period on unstressed Hall bars were transferred to the semiconductor by shallow etching. The resist patterns were removed after etching to leave the etched patterns only. Periodic removal of material from the heterostructure surface brought the surface states periodically closer to the 2DEG and this brought about periodic modulation at the 2DEG [3]. The modulation at the 2DEG introduced by the pattern of square symmetry without a gate is essentially symmetric as already discussed.

The magnetoresistances were measured at 4 K. Data are shown in Figure 6.1 below for transport in two such devices. AFM studies of the etched pattern on the Hall bars following the measurements revealed that the depth of the valleys between the pillars (of material) was close to 18 nm.

The magnetic field values of the CO minima calculated using the mean carrier densities obtained from several high field SdH oscillations, taking the period to be 100 nm, are indicated in Figure 6.1 by the vertical bars. The strong SdH oscillations at the high magnetic fields have obscured the correct locations of the minima for k = 1 and 2. The agreement with the experimental data demonstrates that the phase factor φ in $2R_c = (k - \varphi)a$ is very close to 1/4 unlike many quoted in the literature.

There are several remarkable features in the data.

- The COs observed are very weak in amplitude compared with those in the ρ_{xx} data of 1D LSSLs [2, 3, 7].

- The COs correspond to *only* 100 nm period; there is no presence of COs of $100/\sqrt{2}$ nm period, that of diagonal Fourier components, in the data for transport along either cube axis or cleavage direction.

- There is no observable PMR, although there is a weak feature at low magnetic field indicated by the arrow.
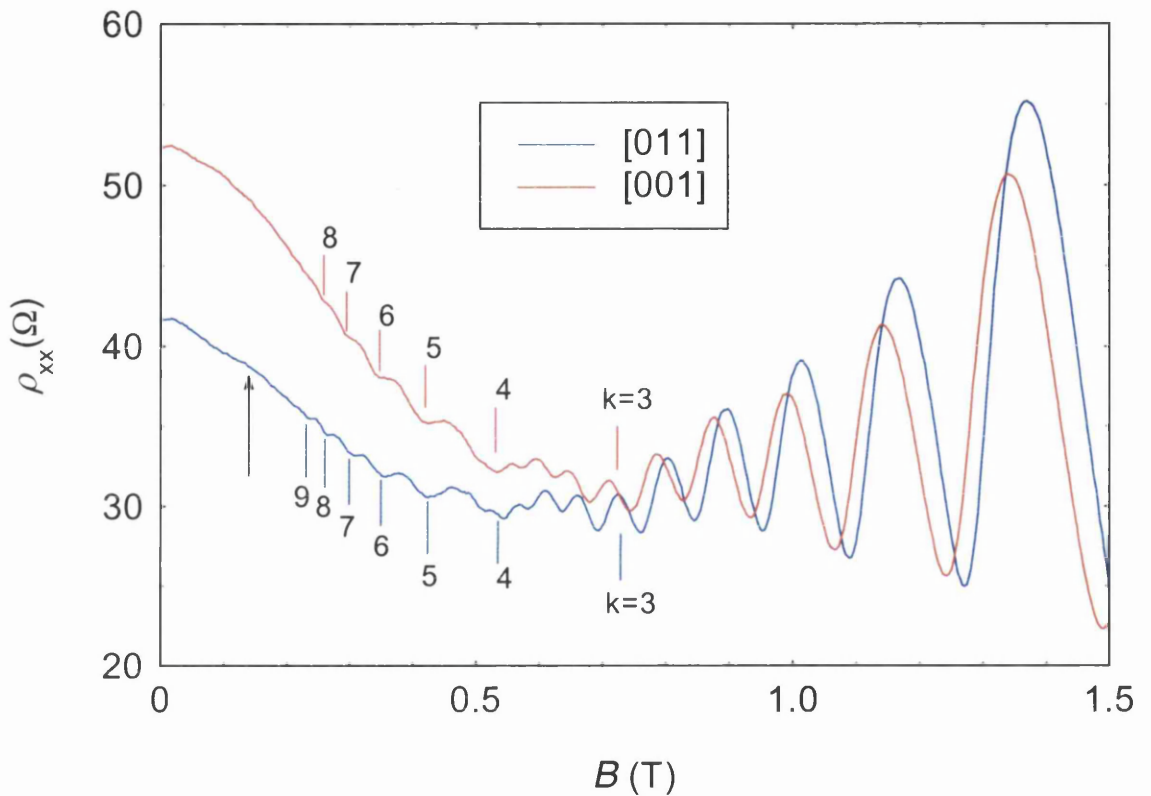
Figure 6.1
Magnetoresistivities of *ungated* unstressed devices measured at 4 K after removal of the resist. Transport is along the [011] and [001] directions in 100 nm period square lattices of 50 nm diameter pillars at the surface of Hall bars. The 100 nm period was aligned along both the [011] and [001] directions. The vertical bars, red ones for the red trace and blue ones for the blue trace, indicate the locations of predicted minima of the COs for 100 nm period, for carrier densities obtained from the respective SdH oscillations at higher magnetic field. There is no PMR in the data, although there is a weak feature indicated by the arrow.

Before discussing about the data, it is important to note that there should *not* be any reasons at all for any asymmetry in the potential landscape at the 2DEG. It is therefore expected that the crystallographic directions of transport are not of importance. This can be seen in Figure 6.1; the characteristics of the COs in the two directions are similar. The crystallographic directions of transport, although immaterial, are noted in Figure 6.1 for the sake of completeness of information.

The data of Figure 6.1 may be compared with those of R. R. Gerhardts, D. Weiss and U. Wulf [7]. They fabricated superlattices by a mask-less technique, by illuminating the heterostructure surface twice by an interference grating pattern of two coherent laser light beams, rotating the sample by 90° after the first exposure. The two-dimensional modulation produced thereby at the 2DEG is expected to be symmetric. At 4.2 K they observed suppression of COs in amplitude by about an order of magnitude compared with that in the ρ_{xx} data from 1D LSSLs realised using the same technique of holographic illumination. The suppression of COs generally observed in 2D LSSLs has been attributed [7] to suppression of band conductivity due to possible partial resolution of minigaps in the modulation broadened Landau levels, although there is no convincing evidence for the resolution of minigaps in Landau levels for temperatures above mK. In the light of the theoretical analysis of Grant, Long and Davies [1], it is natural to attribute the suppression to the symmetry between the modulations in the principal directions.

It is also of interest to compare the data of Figure 6.1 with those of the 100 nm period 1D LSSLs studied by Y. Paltiel et al. [2]. They produced gratings on GaAs-AlGaAs heterostructures by surface etching up to a depth of 10 or 20 nm with 2DEG lying 70 nm below the unpatterned surface. They noted that the etched profile brought about potential modulation at the 2DEG and the modulation is determined primarily by the etch depth and little can be added by biasing an overlying gate. With the 2DEG lying 70 nm below the unpatterned surface, the COs they observed are quite large in amplitude, comparable with that of the COs in the ρ_{xx} data of 1D LSSLs of other studies [2, 3, 7]. In our devices, the 2DEG is only 53 nm deep before patterning the Hall bars. Moreover, as the etch depth in the devices of Figure 6.1 is about 18 nm, a larger modulation at the 2DEG is expected. The observation of suppression in the amplitude of the COs in the data of Figure 6.1 is thus not attributable to any inadequacy in the modulation at the 2DEG.

The data of Figure 6.1 cannot be directly compared with those of the 1D unstressed devices of Emeleus et al. [3], because the period in their study is longer,

namely 300 nm. The modulation associated with longer period is expected to be larger [4].

The main feature of the data of Figure 6.1 that the COs are weak in amplitude conforms with the prediction of the guiding centre drift model [1] in that in symmetric potential landscape guiding centre trajectories are expected to be closed and COs are expected to be absent in the limit $\omega_c \tau \gg 1$. That weak COs are in fact observed *may* be attributed to the fact that the life-time of the carriers is in fact finite. However, the model cannot address the phase of the COs observed.

As discussed in Chapter II, a previous semi-classical model [8] and an equivalent quantum mechanical calculation [6] both predict COs as large as in the ρ_{xx} data of 1D LSSLs for transport in symmetric 2D LSSLs, unlike in the observations (see Figure 6.1). Thus the models [6, 8] are unable to account for the data. Moreover, the independence of different Fourier components as stipulated in these models [6, 8] demands simultaneous presence of COs of both 100 nm and $100/\sqrt{2}$ nm periods in the data unlike observations (see Figure 6.1). It can be argued that the diagonal Fourier components are very short in period ($100/\sqrt{2}$ nm) and are due to surface effect only, and hence are too weak to be picked up in the magnetoresistances. For example, Smith et al. [9] in their studies of very short period (hexagonal) superlattices noted that COs were not observed. *If* the diagonal Fourier components are disregarded, there is a way to fully account for the data of Figure 6.1, as discussed below, by an interplay between semi-classical effect of pinned guiding centre trajectories in symmetric potential landscape [1] and the quantum mechanical effect of modulation of density of states [6]. This is a more general way of understanding the data, because, as will be discussed in section 6.3.1, it explains the observed COs of symmetric stressed superlattices as well.

According to the quantum mechanical model [6], in a symmetric potential landscape containing two axial Fourier components only, similar COs as large in amplitude as in the ρ_{xx} data of 1D LSSLs with the phase factor also as for 1D LSSLs should be observed for transport along both the axial Fourier components. Thus the data of Figure 6.1 agree with the quantum mechanical model [6] except that the amplitude of the COs observed is not as large as in the ρ_{xx} data of 1D LSSLs. The suppression of the amplitude of the COs can be accounted for if one assumes simultaneous presence of the semi-classical effect of pinned guiding centre trajectories [1]. Thus the independent action of the quantum mechanical and semi-classical effects enables us to understand the data fully. There remains no way to fit the previous semi-classical model [8] with the data however.

According to the simulations [1], there should be a large PMR at the low magnetic field before the onset of COs even in the case of symmetric potential landscape. But as Figure 6.1 shows, there is no PMR in the data, although there is a weak feature indicated by the arrow at about 0.14 T. This adds to the experimental systematic for PMR summarised in Chapter IV and V that significant PMR is only associated with large asymmetry in potential landscape. As before, the said simulations are unable to account for the experimentally observed behaviour of PMR.

Before leaving the discussion on the ungated unstressed devices with square superlattices, it should be mentioned that magnetoresistances of gated devices were also studied. It was found that the stress of the gate turned the potential landscape a little asymmetric. Notably, there have been occasions that transport along both [010] and [001] directions with 100 nm period along these directions for forward gate biases lead to the observation of COs of the period $100/\sqrt{2}$ nm, that of the diagonal Fourier components. But there has been *no* occasion that data obtained from ungated devices (measured after removal of resist) showed COs of the period of the diagonal Fourier components. The data of *gated* "unstressed" devices are not discussed here because the potential landscapes in these devices are asymmetric to some extent, whereas the aim of this chapter is to discuss the data obtained from symmetric potential landscape.

6.3 Stressed superlattices with symmetric potential landscape

Resist patterns of about 40 nm diameter holes arranged on 80 nm period square grids on stressed Hall bars aligned along cleavage directions were transferred to the semiconductor by shallow etching. After removing the resist pattern, thick continuous gates were obtained by evaporation covering the etched areas. As already noted in section 6.1, the potential landscape in these devices turns symmetric for large forward gate bias. Data obtained for +0.4 V gate bias at 4 K and 1.6 K are shown in Figure 6.2 and Figure 6.3 respectively.

The data have been confirmed using half a dozen gated devices. AFM studies of a few devices kept without a gate showed that the depth of the etched holes is close to 20 nm, which confirms that the holes have passed through the strained layer of InGaAs and thus brought about periodic stress modulation at the 2DEG.
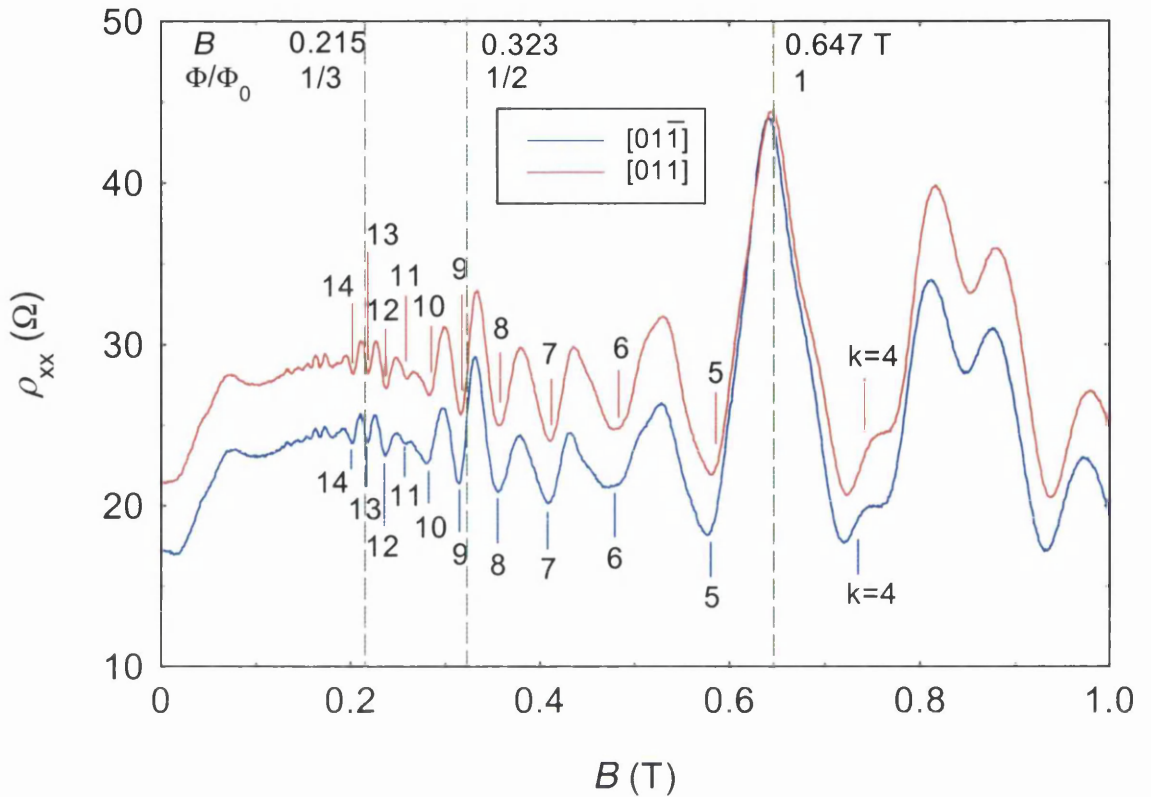
Figure 6.2

Magnetoresistivities of stressed devices measured at 4 K with +0.4 V gate bias. Transport is along the [011] and [01$\bar{1}$] directions in 80 nm period square lattices of 40 nm diameter holes at the surface of Hall bars. The 80 nm period was aligned along both [011] and [01$\bar{1}$] directions. The vertical bars, red ones for the red trace and blue ones for the blue trace, indicate the locations of predicted minima of COs for 80 nm period for the carrier densities obtained from the respective SdH oscillations at higher magnetic field. There are characteristic amplitude modulations of the COs near the green vertical lines that are at the magnetic field values whenever one flux quantum, $\Phi_0 = h/e$ passes through 1, 2 and 3 unit cells of the lattice, or in other words, whenever the number of flux quantum per unit cell, $\Phi/\Phi_0 = 1$, 1/2 and 1/3.
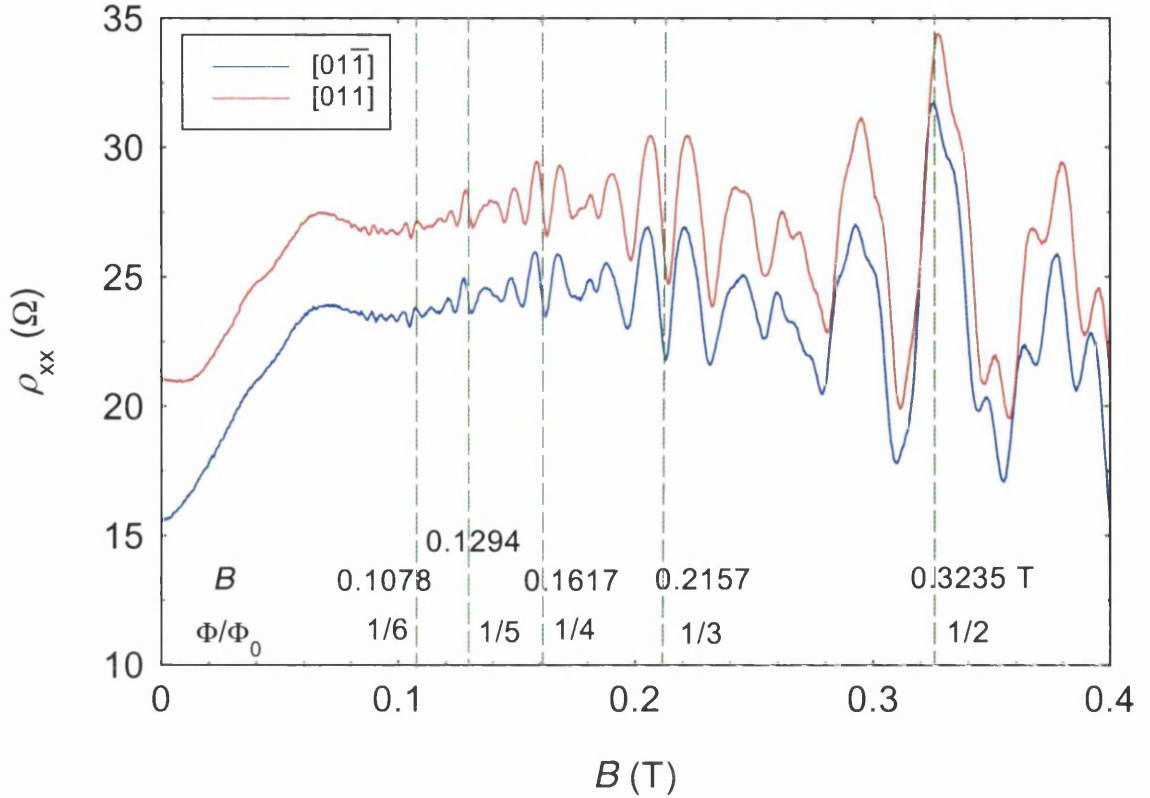
Figure 6.3
Magnetoresistivities of stressed devices measured at 1.6 K with +0.4 V
gate bias. The transport is along the [011] and [01$\bar{1}$] directions in 80 nm
period square lattices of 40 nm diameter holes at the surface of Hall
bars. The 80 nm period was aligned along both [011] and [01$\bar{1}$]
directions. There are characteristic amplitude modulations of the
magnetoresistance oscillations near the green vertical lines which are at
the magnetic field values whenever one flux quantum, $\Phi_0 = h/e$ passes
through 2, 3, 4, 5 and 6 unit cells of the lattice, or in other words,
whenever the number of flux quantum per unit cell, $\Phi/\Phi_0 = 1/2, 1/3, 1/4$,
1/5 and 1/6.

There are several remarkable features in the data.

- The magnetoresistance characteristics for transport along the two orthogonal
  directions are (almost) identical.

- The COs correspond to 80 nm period and are quite large in amplitude, comparable
  with that of the ρ_{xx} data of 1D LSSLs [2, 3, 7].

- Near the magnetic field values that correspond to one flux quantum h/e per 1, 2,
  3, … unit cells of the lattice, the amplitudes of the COs are enhanced compared
  with that of the COs in between.

One thing to note in Figure 6.3 is that oscillations have been observed down to about 0.08 T. But even in unpatterned Hall bars with similar zero field resistivities, the quantum mobility is not high enough for the SdH oscillations to be observed down to such low magnetic fields (see Figure 1.4). The quantum mobility is not expected to govern the visibility of COs. The observation may be attributed to the transport mobility that can be much larger than the quantum mobility or even an effective mobility that is some sort of combination of the two types of mobilities.

The observed COs and the amplitude modulations of these are discussed in section 6.3.1 and 6.3.2 respectively followed by a discussion of the amplitude modulation in view of Hofstadter butterfly in section 6.3.3.

6.3.1 COs of the stressed superlattices with symmetric potential landscape

The data for transport along the two axial directions of a square superlattice of 80 nm period with the principal axes aligned along the cleavage directions are shown in Figure 6.2 and Figure 6.3 for large forward gate bias. The calculated magnetic fields for the CO minima for 80 nm period are shown in Figure 6.2 by the vertical bars. Agreement with the data shows that the COs correspond to 80 nm period and that φ is close to 1/4 in $2R_c = (k - \varphi)a$, unlike many observations in the literature.

As already mentioned, a large forward gate bias eliminates the surface effect of short period superlattices. The diagonal Fourier components in the devices in question, being along [010] and [001] directions, are due to surface effect only [3]. Hence large forward gate bias (+0.4 V) "physically" eliminates the diagonal Fourier components entirely. The axial Fourier components have stress modulation as well which is not changed significantly by the gate bias. Thus for large positive gate bias, the potential landscape of the devices in question turns symmetric and contains axial Fourier components only.

The two devices of Figure 6.2 and Figure 6.3 were etched at the same time and we expect that the modulation strengths in the two superlattices are almost identical. Thus transport in the two orthogonal Hall bars is equivalent to transport in two orthogonal directions in the same superlattice. The presence of almost identical and large COs for transport in the two orthogonal directions (see Figure 6.2 and Figure 6.3) suggests that if the COs observed were due to guiding centre drift, the guiding centre must drift across both the Hall bars, i.e. along both the axial directions of the superlattice at the same time. But the potential landscapes in the two devices are symmetric and the superlattices are nominally identical. Moreover, as the potential

landscape consists only of two axial Fourier components of the same period, the effective potentials of the two Fourier components have the same magnetic field dependence. Thus the symmetry of the effective potential remains unaffected as the magnetic field is changed. According to the guiding centre drift model [1], the trajectories of the guiding centre are closed in such a symmetric effective potential and hence the COs are expected to be completely suppressed in amplitude. Although there is a degree of suppression in the amplitude of the COs between the enhanced oscillations, complete suppression is not observed (see Figure 6.2 and Figure 6.3). This cannot be attributed to $\omega_c \tau$ not being large compared with unity because the mobility in the devices is quite large, about 85 $m^2 V^{-1} s^{-1}$ corresponding to a mean free path of about 9 µm, almost as large as the width of the Hall bars. So although the semi-classical effect as envisaged in the guiding centre drift model [1] is expected to be present, it is inadequate in causing complete suppression of the CO amplitude, indicating the presence of other physics as discussed below.

As the data of Figure 6.2 and Figure 6.3 suggest, in symmetric stressed 2D LSSLs of short period and high mobility, different Fourier components *do* independently contribute to magnetoresistances. This for the first time confirms the validity of the quantum mechanical model [6] in explaining the COs of symmetric stressed 2D LSSLs of short period and high mobility. That the diagonal Fourier components are not observed is because there are no diagonal Fourier components in the potential landscape as already discussed. That the transport is quantum mechanical in nature is further supported by the observation of inverse flux quantum periodicity in the amplitude of COs discussed in section 6.3.2.

That different Fourier components *do* independently contribute to the magnetoresistances also formally agrees with the prediction of a previous semi-classical model [8]. But it is not at all clear how a given guiding centre can drift in the two orthogonal directions at the same time. This conceptual difficulty does not arise in the context of the quantum mechanical model [6] due to the probabilistic interpretation of quantum mechanical states. According to the model [6], every Fourier component in a 2D periodic potential introduces eigenstates that carry diffusive current in the direction orthogonal to the direction of modulation of the Fourier component. So there is a certain probability that a given electron will take part in the diffusive contribution to conductivity due to every Fourier component. Hence of the total number of conduction electrons near the Fermi energy, a fraction will take part in the diffusive contribution of current due to every Fourier component. Thus different Fourier

components *can* give rise to their own series of COs independently. That similar COs were observed for transport in the two orthogonal directions (see Figure 6.2 and Figure 6.3) is because the amplitude of the two (axial) Fourier components being equal, half of the total number of conduction electrons near the Fermi energy took part in the diffusive conduction due to each of the two Fourier components.

As already noted, the COs of Figure 6.2 and Figure 6.3 are in general lower in amplitude than those near the magnetic field values that correspond to one flux quantum *h/e* per 1, 2, 3, ... unit cells of the lattice. A way to account for the absence of complete suppression in amplitude is in terms of a competition between

(a) quantum mechanical effect [6] involving modulation of the density of states, which is expected to give rise to COs as large in amplitude as in the ρ_{xx} data of 1D LSSLs and (b) the semi-classical dynamical effect of closed guiding centre trajectories as envisaged in the guiding centre drift model [1], which suppresses the amplitudes of COs in symmetric potential landscape.

That the suppression this time (in Figure 6.2 and Figure 6.3) is not as much as in Figure 6.1 may be accounted for in that the quantum mechanical effect is dominant this time. Admittedly, a direct comparison of the data of Figure 6.1 with those of Figure 6.2 and Figure 6.3 is fraught with complexity as the mean free path and the potential modulation are different and there is no standard way of determining the amplitude of potential modulation of 2D LSSLs.

Before leaving the discussion on the COs of symmetric, stressed, short period and high mobility 2D LSSLs, it should be noted that the oscillations in Figure 6.3 at low field are *not* particularly regular. There are even occasional absences in expected COs. It is not clear if the low field oscillations are in fact COs or not. There are difficulties in ascertaining this. This is mainly because there is some stray magnetic field present in the experimental environment that changes as the applied magnetic field is changed. This turns it formidable to accurately analyse the data. We tried to de-magnetize the experimental environment but with limited success.

6.3.2 Amplitude modulation of COs in stressed symmetric superlattices

As noted in Figure 6.2 and Figure 6.3, there are characteristic amplitude modulations in the COs of the stressed symmetric superlattices. These occurred at the magnetic field values given by $\Phi/\Phi_0 = Ba^2/(h/e) = 1, 1/2, 1/3, 1/4, 1/5, 1/6$ where Φ is the flux through a unit cell (of area a^2) of the superlattice given by Ba^2 and $\Phi_0 = h/e$ is

the flux quantum. These are periodic in inverse magnetic field $1/B$; hence the phenomenon in question may be called inverse flux quantum periodicity.

As already mentioned, for large positive gate bias, the potential landscape of the devices in question turns symmetric and contains axial Fourier components only. Hence the amplitude modulations in the data of Figure 6.2 and Figure 6.3 cannot be explained as a result of any interference between axial and diagonal Fourier components. The possibility that this could be due to any semi-classical dynamical effect may be excluded in that it is not clear how semi-classical (nearly circular) trajectories of electrons can fit with 3 unit cells of a square lattice. Moreover, as already discussed, the symmetry of the effective potential remains unaffected as the magnetic field is changed. This excludes any possibility of any magnetic field dependent dominance of any Fourier component that could break the symmetry of the effective potential.

The inverse flux quantum periodicity was also observed at the correct magnetic fields in the amplitude of COs of stressed 100 nm period 2D LSSLs of square symmetry for large positive gate bias. These superlattices although larger in period (100 nm) were realised without introducing a large surface effect in the etching process. Hence for large forward gate bias the potential landscape turned symmetric as in the case of 80 nm period. Some data are shown in Figure 6.4 and Figure 6.5. It is important to note that the magnetic field values for $\Phi/\Phi_0 = 1$ in the superlattices of 80 nm and 100 nm periods, being 0.647 T and 0.414 T respectively (see Figure 6.2 and Figure 6.5), are different by about 50%. The observation of the effect near these correct magnetic fields for two different periods is a significant support to the idea that the effect results from flux quantization.

In 100 nm period samples, the inverse flux quantum periodicity was only clearly apparent at mK temperature, unlike in 80 nm period samples. This is mainly because the magnetic field value for $\Phi/\Phi_0 = 1/3$ in 100 nm period superlattices is below 0.2 T (see Figure 6.4) while it is above 0.2 T in 80 nm period superlattices (see Figure 6.2). This brings in a mobility constraint that prevents the observation of the effect in 100 nm period samples above mK temperature. But the effect at higher magnetic fields is in fact thermally robust. The amplitude modulations for $\Phi/\Phi_0 = 1$ and 1/2 were observed up to 9 K for 80 nm period superlattices as shown in Figure 6.6. The effect is also pronounced near $\Phi/\Phi_0 = 1$ for 100 nm period superlattices even at 5 K as shown in Figure 6.5.
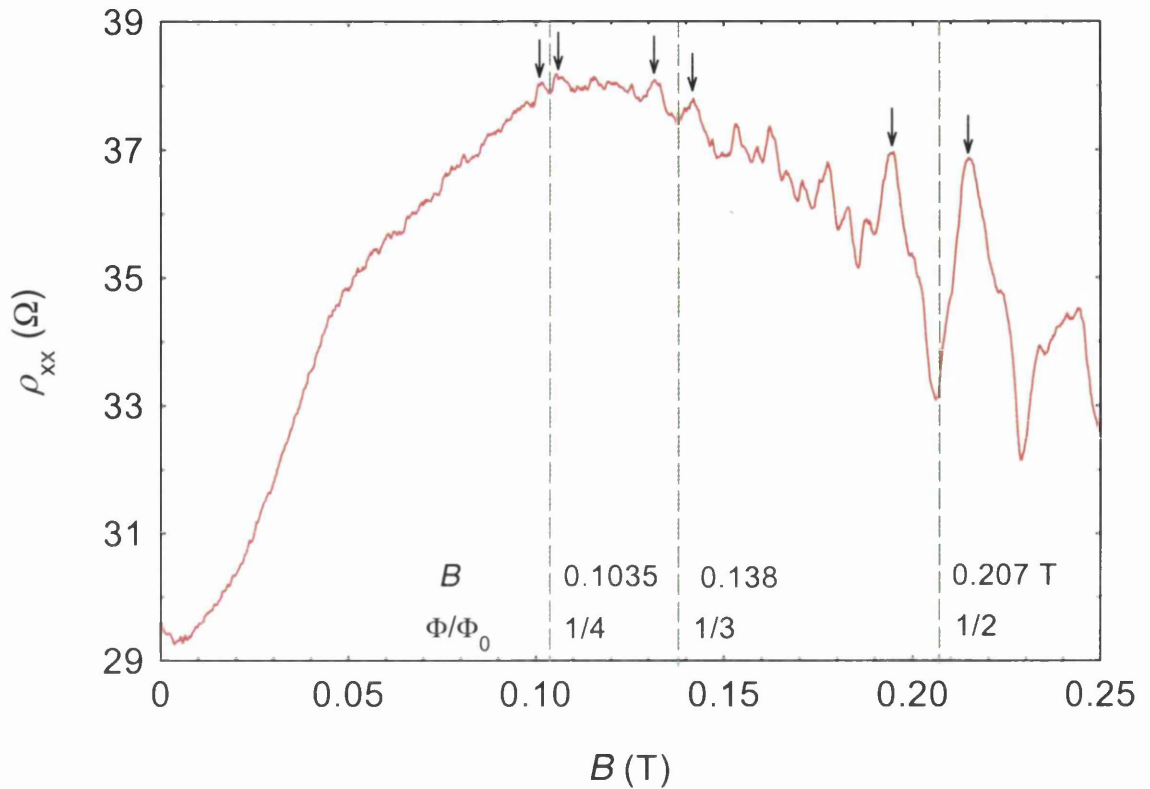
Figure 6.4

Magnetoresistivities of a stressed device measured at 30 mK with +0.3 V gate bias. Transport is along the [011] direction in a 100 nm period square superlattice of 50 nm diameter pillars at the surface of the Hall bar. The 100 nm period was aligned along the [011] direction. There are characteristic amplitude modulations of COs near the green vertical lines that are at the magnetic field values whenever one flux quantum h/e passes through 2, 3, 4 unit cells of the lattice. Arrows indicate the magnetoresistance oscillations that are enhanced. The trace contains 1000 data points and was confirmed to be reproducible.

Chapter VI Transport in unstressed and stressed symmetric two-dimensional lateral surface
superlattices: interplay between semi-classical and quantum mechanical Physics

190
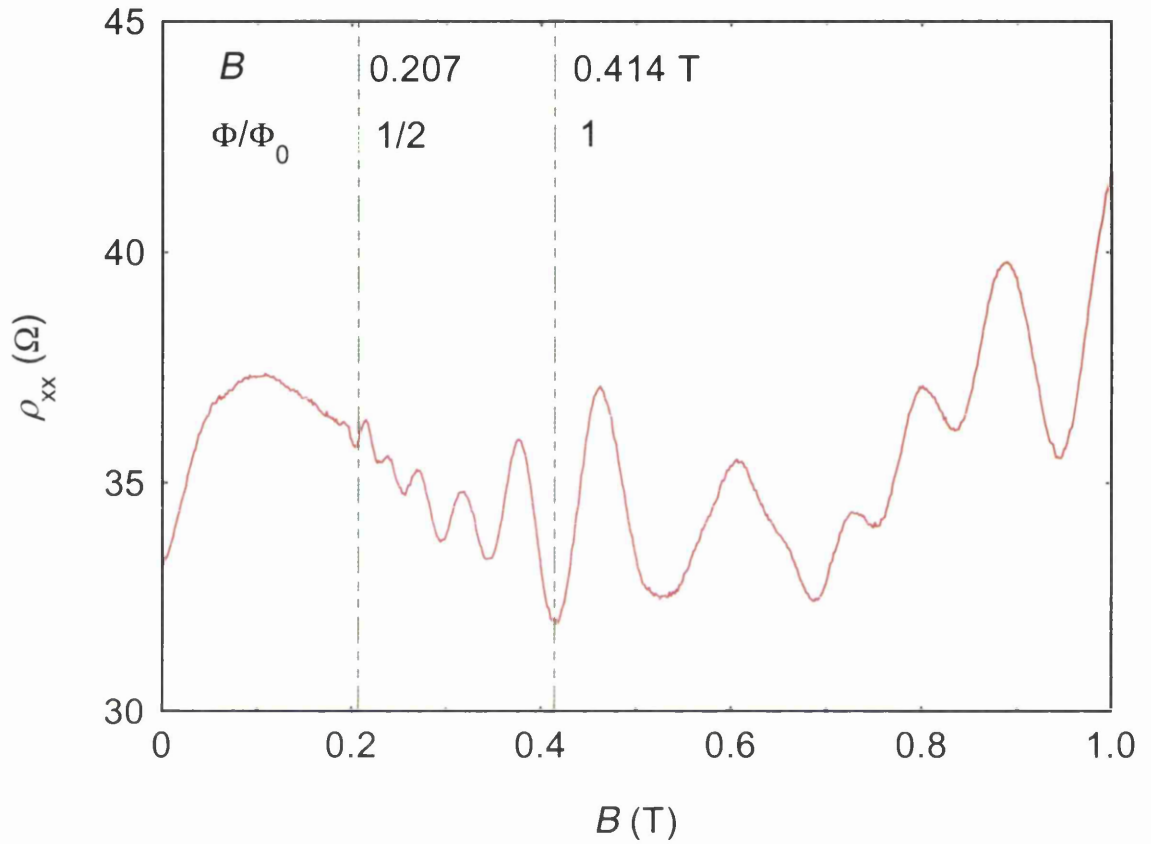
Figure 6.5
Magnetoresistivities of the device of Figure 6.4 measured at 5 K and
+0.3 V gate bias. There are characteristic amplitude modulations of COs
near the green vertical lines that are at the magnetic field values
whenever one flux quantum h/e passes through 1 and 2 unit cells of the
lattice. Below about 0.2 T the oscillations could not appear due to
thermal smearing as the temperature was high, 5 K.
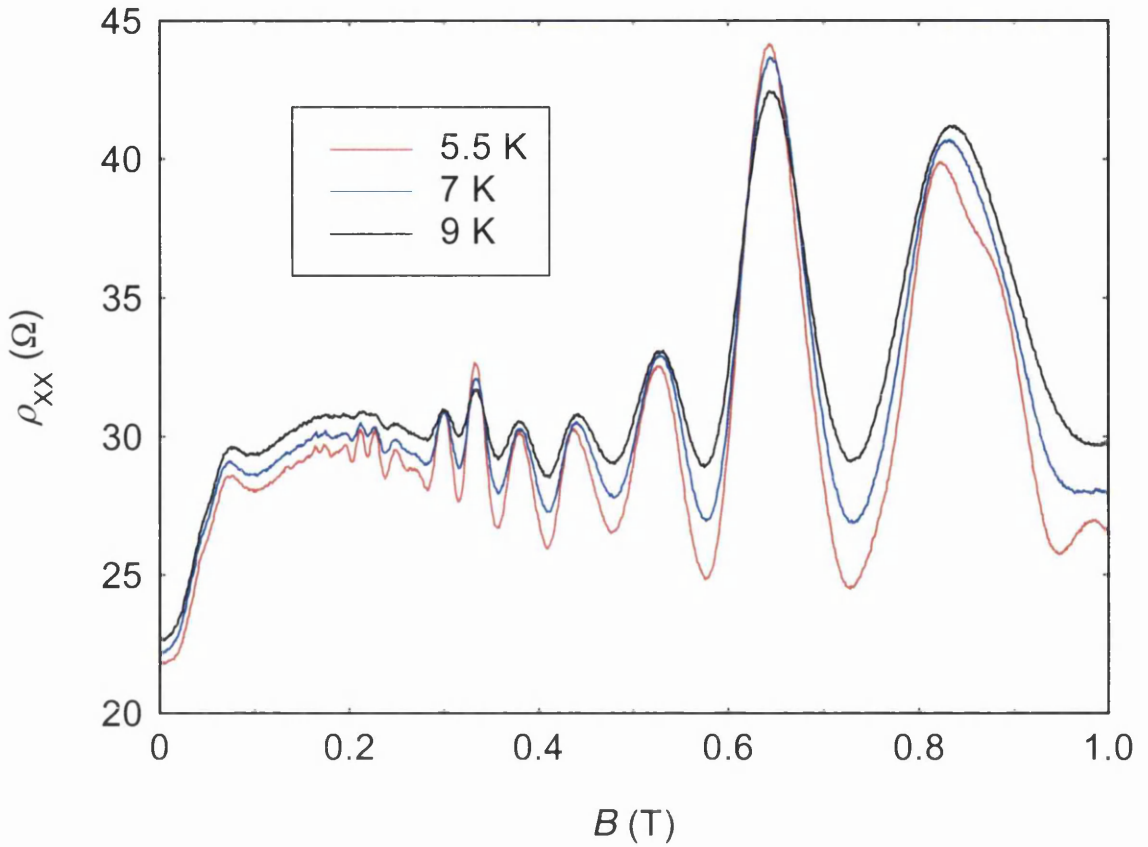
Figure 6.6
Magnetoresistivities of the [011] device of Figure 6.2 measured at +0.4 V gate bias and different temperature as indicated. Data for the [01$\bar{1}$] device of Figure 6.2 were similar.

A theoretical calculation by P. Rotter, M. Suhrke and U. Rössler [10] shows that the number of flux quantum per unit cell can affect the magnetoresistances of 2D LSSLs. Their quantum mechanical calculation on the resistivity of a 2DEG in a strongly modulated two-dimensional periodic potential and a perpendicular magnetic field revealed fascinating structures at 1, 3/2, 2 and 3 magnetic flux quanta per unit cell. They identified the structures as quantum oscillations. The main parameters used in the calculation are 100 nm period, 5 meV potential amplitude and 4 to 12 meV Fermi energy. For mobility of about 50 $m^2V^{-1}s^{-1}$, they asked for lattice period of about 100 nm as the most important requirement for experimental observation. Theoretically they found the effect to persist to 4 K and even to 15 K. COs are not considered in their calculation. If both COs and the quantum oscillations they predicted are present in the data, the quantum oscillations are expected to appear as amplitude modulations of COs. They calculated the effect for $\Phi/\Phi_0 = 1$ and above assuming strong modulation at the 2DEG, while we observed amplitude modulation for $\Phi/\Phi_0 = 1$ and lower values i.e. 1/2,

1/3, 1/4, 1/5 and 1/6 and the potential modulation in our superlattices is expected to be weak. If the amplitude modulation we observed is due to the effect found by Rotter et al., then it is expected that if the calculation is extended to $\Phi/\Phi_0 < 1$ assuming weak potential modulation, the effect may be found at $\Phi/\Phi_0 = $ 1/2, 1/3, 1/4, 1/5 and 1/6. Thus the effect considered by Rotter et al. [10] stands as a possible candidate in explaining the amplitude modulations we observed.

Before concluding this section, it should be noted that the amplitude modulations involving inverse flux quantum periodicity are not at all as clear in Figure 6.1 as in Figure 6.2 and Figure 6.3. There may be several reasons for this.

- Firstly, the potential landscape of the devices of Figure 6.2 and Figure 6.3 contains stress modulation whereas that of the devices of Figure 6.1 does not contain any stress modulation at all. In short period superlattices, one cannot rely on the surface effect to obtain significant potential modulation.

- Secondly, the period of the stressed devices studied is 80 nm whereas that of the unstressed devices studied is 100 nm. Quantum mechanical effects are expected to be more pronounced in shorter period superlattices.

- Thirdly, the mobility in the stressed devices was much larger than that in the unstressed devices studied. In the stressed devices, a large forward gate bias turned the potential landscape symmetric and raised the mobility as well, whereas in the unstressed devices large forward gate biases diminish the potential modulation, which is undesirable.

6.3.3 Amplitude modulation of COs in light of the Hofstadter butterfly

The observed amplitude modulation of COs in the magnetoresistances of symmetric, stressed, short period and high mobility 2D LSSLs has been discussed in detail in section 6.3.2. As it is a possibility that the amplitude modulations observed are related to density of states, in this section the phenomenon is discussed as a possible manifestation of the well-known Hofstadter butterfly.

D. R. Hofstadter [11] calculated the energy spectrum of an electron in a two-dimensional periodic potential of square symmetry and a perpendicular uniform magnetic field. His plot of the energy E of the electron as a function of a wide range of rational values of flux quantum per unit cell Φ/Φ_0 gave rise to a recursive spectrum, the large gaps of which form a pattern somewhat resembling a butterfly. This is known as the Hofstadter butterfly (see Figure 6.7).
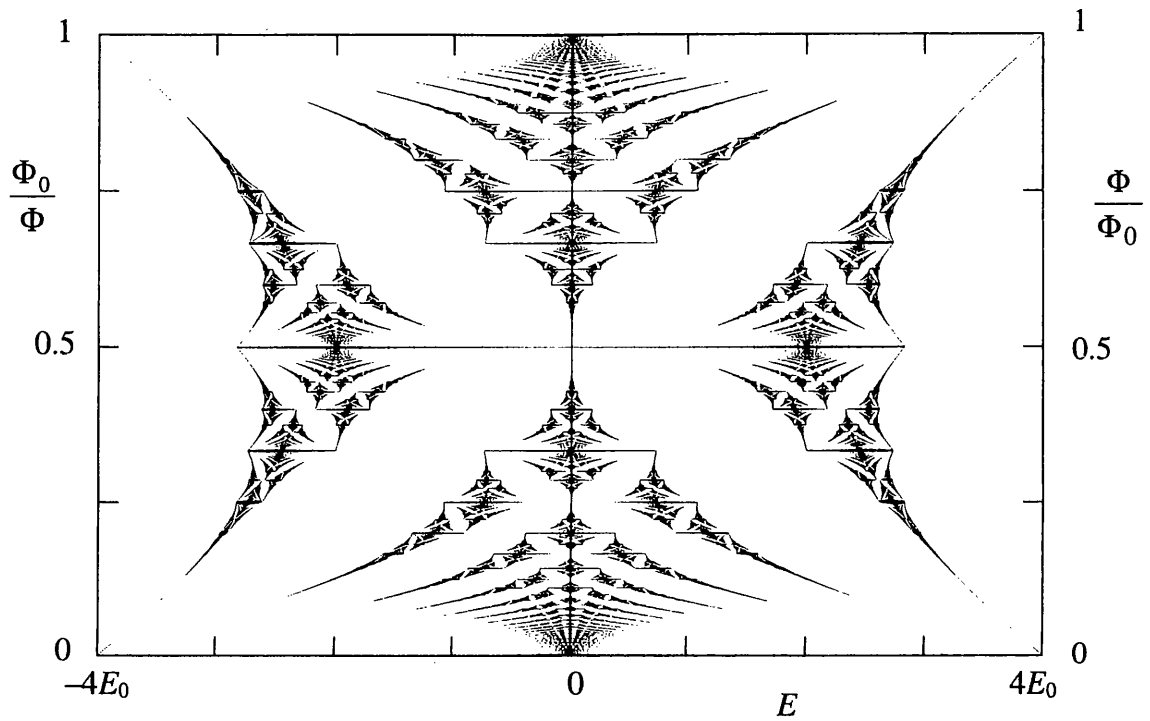
Figure 6.7
Hofstadter butterfly that looks the same for rational values of both Φ_0/Φ and Φ/Φ_0 versus energy E of an electron in a two-dimensional periodic potential of square symmetry and a perpendicular magnetic field.

Chapter VI Transport in unstressed and stressed symmetric two-dimensional lateral surface superlattices: interplay between semi-classical and quantum mechanical Physics

194

It is important to note that the energy spectrum has been calculated for two complementary situations, namely a) strong potential modulation and weak magnetic field [11] and b) weak potential modulation and strong magnetic field [12]. Although the energy spectra obtained in the two calculations look similar, there are two important differences.

- In the original work [11] the energy spectrum was plotted as energy against the rational values of Φ/Φ_0, while in the latter work [12] the plot was energy against rational values of Φ_0/Φ.

- The original calculation [11] has nothing to do with Landau levels while the latter calculation [12] related the gap structures in the energy spectrum to the internal structures of modulation broadened Landau levels due to the resolution of minibands.

It is arguable if the physical situation in our experiment corresponds to strong potential modulation and weak magnetic field or weak potential modulation and strong magnetic field. This is because it is a relative matter and also because there is no standard way of determining the potential amplitude in 2D LSSLs.

There are two different ways to look at the observed amplitude modulations of COs in view of the two calculations of Hofstadter butterfly. The observed amplitude modulations occurred at Φ/Φ_0 = 1, 1/2, 1/3, 1/4, 1/5 and 1/6. Looking at the Hofstadter butterfly as calculated by D. R. Hofstadter [11], these magnetic fields are not symmetric with respect to Φ/Φ_0 = 1/2. Amplitude modulations have not been observed at the symmetrically located fields given by Φ/Φ_0 = 1-1/3, 1-1/4, 1-1/5 and 1-1/6. An arguable way to understand the absence of amplitude modulation of COs at these fields is that, as Figure 6.2 shows, there are only 2 or 3 COs in the data in this magnetic field range (between about 0.4 T and 0.65 T). So there is not much room for the amplitude modulation to show up. If one fabricates shorter period (e.g. 60 nm) superlattices, one might expect to observe larger number of COs giving greater room for the amplitude modulations near Φ/Φ_0 = 1-1/3, 1-1/4, ... to show up. But as the potential modulation in shorter period superlattices is expected to be weaker, one may need to introduce greater stress, perhaps using a thicker strained layer of InGaAs. One may need to use heterostructures grown on (111) GaAs substrate. The stress modulation on (111) GaAs is expected to be nearly isotropic [4] and hence both surface effect and stress modulation can be utilized to produce sufficient modulation at the

2DEG for short period superlattices. It will not be necessary to eliminate the surface effect to get symmetric potential landscape, unlike the case with (100) GaAs wafer.

The perspective is different if one looks at the observed amplitude modulations in the context of Hofstadter butterfly calculated by D. Pfannkuche and R. R. Gerhardts [12]. The Hofstadter butterfly shown in Figure 6.7 for $0 < \Phi_0 / \Phi < 1$ in fact repeats itself for $1 < \Phi_0 / \Phi < 2$, $2 < \Phi_0 / \Phi < 3$ and so on. The amplitude modulations were observed at $\Phi_0 / \Phi = 1, 2, 3, 4, 5,$ and 6. These magnetic field values are at the edges of each repetition of the butterfly structure and do not correspond to the internal structures of the Hofstadter butterfly. Individual Landau levels are not themselves resolved in the (low field) data of Figure 6.2 and Figure 6.3 let alone their internal structures.

The internal structure of Hofstadter butterfly [12] has been searched for [13] in the Landau levels as dips in the peaks of SdH oscillations. These dips are expected to appear when the Fermi energy passes through the expected gaps in the internal structure of the Landau levels. We have looked for similar effect as well by studying 100 nm period square superlattices at mK temperature. Only one or two instances of splitting of SdH peaks could arguably be related to the Hofstadter butterfly, but a large number of splittings were also observed which could not be ascribed to the internal structures of Hofstadter butterfly. Our observations in this context are inferior to those of T. Schlösser et al. [13] (who also found some splitting that could not be ascribed to Hofstadter butterfly). Our data do *not* provide any advancement in the experimental search for internal structure of Hofstadter butterfly and are not discussed.

6.4 Transport in nearly symmetric potential landscapes

As discussed in section 6.1, a large forward gate bias in short period stressed square superlattices turns the potential landscape symmetric. However, as the positive gate bias is reduced, the surface effect comes into play and breaks the symmetry of the potential landscape. The surface effect is small, as the period of the superlattices is short. Hence the asymmetry introduced is not very large. Magnetoresistance data obtained under such a condition are discussed in this section. Some data are shown in Figure 6.8 below.

The calculated locations of the CO minima for 80 nm period are shown by vertical bars in Figure 6.8. Agreement with the experimental data demonstrates that the phase factor φ in $2R_c = (k - \varphi)a$ is close to 1/4. Moreover, the amplitude modulation of COs is still visible particularly near 0.647 T that corresponds to $\Phi/\Phi_0 = 1$ and to some

extent near 0.323 T corresponding to $\Phi/\Phi_0 = 1/2$. So the quantum mechanical effect related to flux quantization observed in symmetric potential landscapes persists to some extent even when the symmetry of the potential landscape is somewhat lowered.
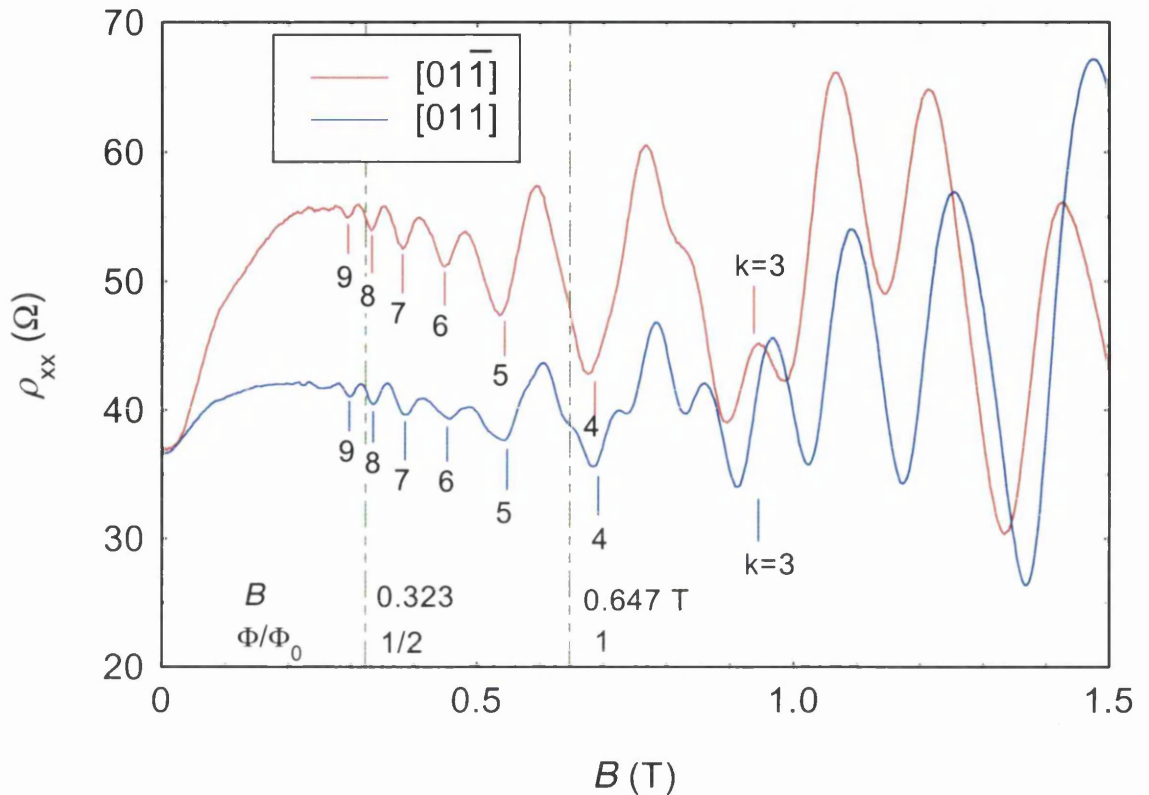
Figure 6.8
Magnetoresistivities of gated stressed devices measured at 4 K without gate bias. Transport is along the [011] and [01$\bar{1}$] directions in 80 nm period square lattices of 40 nm diameter shallow etched holes at the surface of Hall bars. The 80 nm period was aligned along both the [011] and [01$\bar{1}$] directions. The vertical bars, red ones for the red trace and blue ones for the blue trace, indicate the magnetic field values of the CO minima for 80 nm period, calculated using the carrier densities obtained from the respective SdH oscillations at higher magnetic fields. The green vertical dashed lines show the magnetic fields for $\Phi/\Phi_0 = 1$ and 1/2.

The two devices of Figure 6.8 were etched at the same time and hence the modulation strengths in the two devices are expected to be the same. This is supported by the fact that the zero field resistivity, mobility and carrier density of the two devices of Figure 6.8 are (almost) identical. The surface effect adds to the stress modulation along [01$\bar{1}$], while the two types of modulations partially cancel each other in [011]

direction. Thus [01$\bar{1}$] is the direction of stronger modulation. The modulation associated with the diagonal Fourier components being along [010] and [001] are due to the surface effect only and, being of short period, are weaker. According to the guiding centre drift model [1], guiding centre should drift *only* along the direction orthogonal to the direction of modulation of the dominant Fourier component. Hence guiding centre should drift only along [011] and hence there should be large COs for transport along [01$\bar{1}$] and no COs for that along [011]. As the data of Figure 6.8 reveal, the COs in [01$\bar{1}$] are large as expected but those in [011], although weak, are not entirely suppressed. It cannot be argued that at the effective potential minima of the dominant Fourier component along [01$\bar{1}$] that along [011] turns dominant and causes guiding centre drift along [01$\bar{1}$] producing COs for transport along [011] as well. This is because the minima (or maxima) of the effective potentials along both [01$\bar{1}$] and [011] directions occur at the same magnetic field (see Figure 6.9 below). Moreover, as already noted, the superlattices on the two Hall bars are nominally identical. These exclude the option of magnetic field dependent switching of guiding centre drift direction in explaining the COs observed for transport along [011]. Thus the guiding centre drift model [1] is unable to fully account for the data.

At this point it is imperative to compare the data of Figure 6.8 or Figure 6.9 with those of Figure 4.12. The mobility is comparable in the two sets of data, although the COs in [011] data are much more suppressed in Figure 4.12 than in Figure 6.8 or Figure 6.9. The difference can be accounted for in that the surface effect in the devices of Figure 4.12 is so much that even for +0.3 V gate bias, there is appreciable asymmetry in the potential landscape. Moreover, the superlattices of Figure 4.12 being of larger period (100 nm) than those of Figure 6.8 or Figure 6.9, a larger surface effect is expected in the former under similar conditions. This suggests that it is the *asymmetry* that suppresses the COs that are not expected from semi-classical models. This conforms with the conclusion reached in Chapter IV and Chapter V that transport in asymmetric 2D LSSLs is semi-classical in nature. The observation of COs in [011] in Figure 6.8 or Figure 6.9 is thus attributable to *weak* asymmetry and consequent quantum mechanical effect of modulation of density of states [6] that was observed in symmetric potential landscapes and discussed in section 6.3.1. Quantum mechanical effects are suppressed if the potential landscape has *strong* asymmetry as found in Chapter IV and Chapter V. *Asymmetry suppresses quantum mechanical effects in asymmetric 2D LSSLs.*
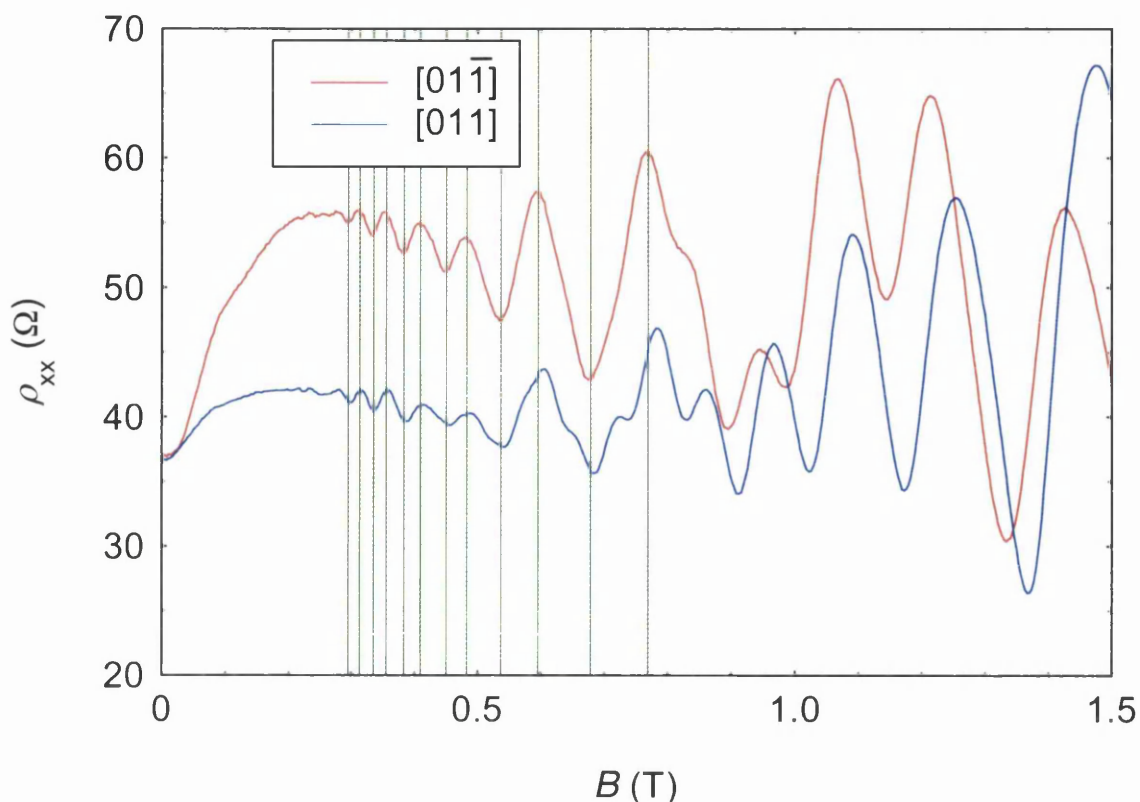
Figure 6.9
Data of Figure 6.8 shown with the green *vertical* lines that pass through
the maxima and minima of the COs. The vertical green lines that pass
through the maxima of one trace pass through those of the other as well.
Again, the vertical green lines that pass through the minima of one trace
pass through those of the other as well. This confirms that for square
superlattices the minima (or maxima) of the effective potentials along
both $[01\bar{1}]$ and $[011]$ directions occur at the same magnetic field.
Although a cursory glance at the SdH oscillations suggests that the
carrier densities in the two devices are different, calculations using the
standard Equation (1.2) reveal that the carrier densities are 3.98×10^{15} m^{-2}
for the $[01\bar{1}]$ and 4.03×10^{15} m^{-2} for the $[011]$, identical within error of
calculation. The mobilities are also (almost) equal, as are the zero field
resistivities.

Before leaving the discussion of the data of nearly symmetric 2D LSSLs, it
should be mentioned that similar magnetoresistance features were observed for
transport in a set of stressed square superlattices of pillars with 100 nm period, that
were realised without introducing a large surface effect in the etching process. Data are
shown in Figure 6.10. Because the process latitude of the pattern of pillars was small,
the modulation strengths in the two devices are *not* identical. As such the carrier
densities and mobilities in the two devices are also appreciably different. Thus, as

expected, for a given value of k, the CO minima in the two traces occurred at different magnetic fields. There are amplitude modulations of COs of both the devices near 0.414 T that corresponds to one flux quantum per unit cell of 100 nm period square superlattice.
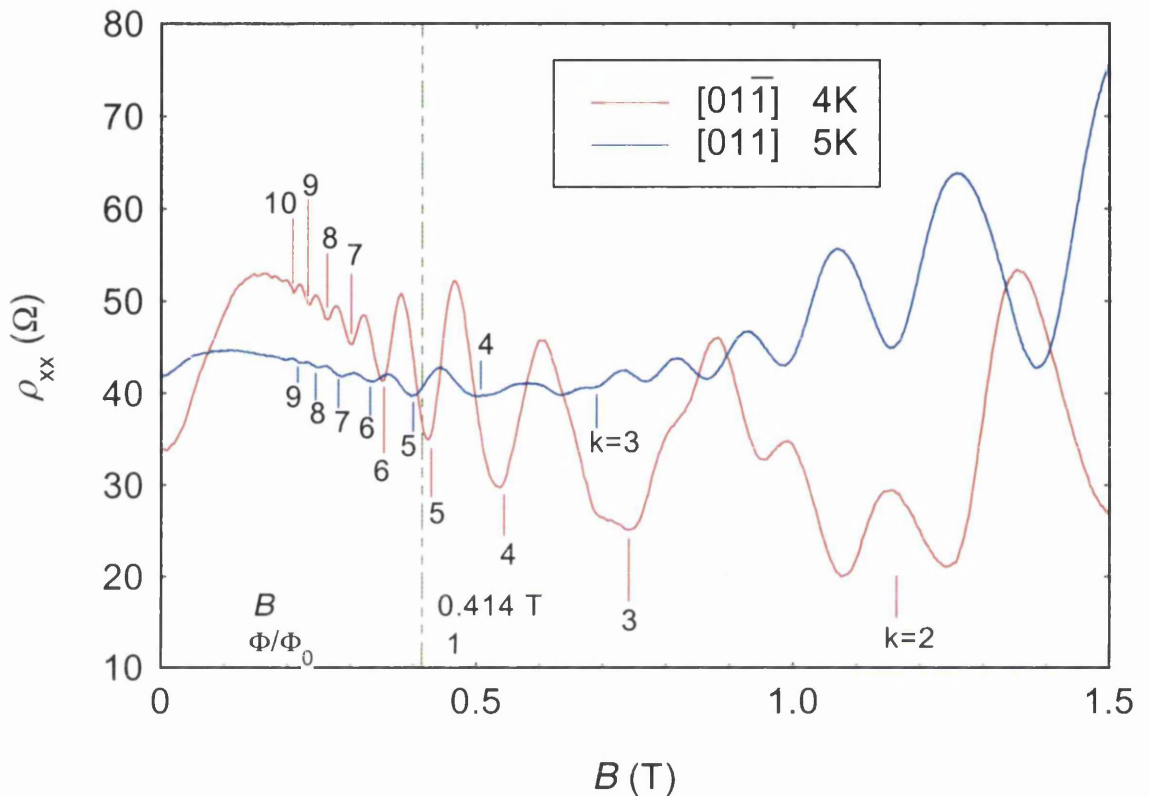
Figure 6.10
Magnetoresistivities of gated stressed devices measured at 4 or 5 K without any gate bias. Transport is along the [011] and [01$\bar{1}$] directions in 100 nm period square lattices of 50 nm diameter pillars at the surface of Hall bars. The 100 nm period was aligned along both [011] and [01$\bar{1}$] directions. The vertical bars, red ones for the red trace and blue ones for the blue trace, indicate the magnetic field values of the CO minima for 100 nm period calculated using the carrier densities obtained from the respective SdH oscillations at higher magnetic fields, and using $2R_c = (k - \varphi)a$ and taking $\varphi = 1/4$. The green vertical dashed lines show the magnetic field for $\Phi/\Phi_0 = 1$.

As one goes from a pattern of holes to a pattern of pillars, the sign of both surface effect and stress modulation changes. Thus [01$\bar{1}$] is the direction of dominant Fourier component in the superlattices of pillars as well in conformity with the observation in Figure 6.10.

6.5 Unstressed rectangular superlattices revisited

Now that a lot of ideas have been gathered, before finishing off the discussion on the data altogether, it may be worth revisiting the complex magnetoresistance structures observed for transport in unstressed 100 nm by 170 nm period rectangular superlattices for transport along 100 nm period. The data were introduced in Figure 4.27 in section 4.2.2 and are shown again in Figure 6.11.
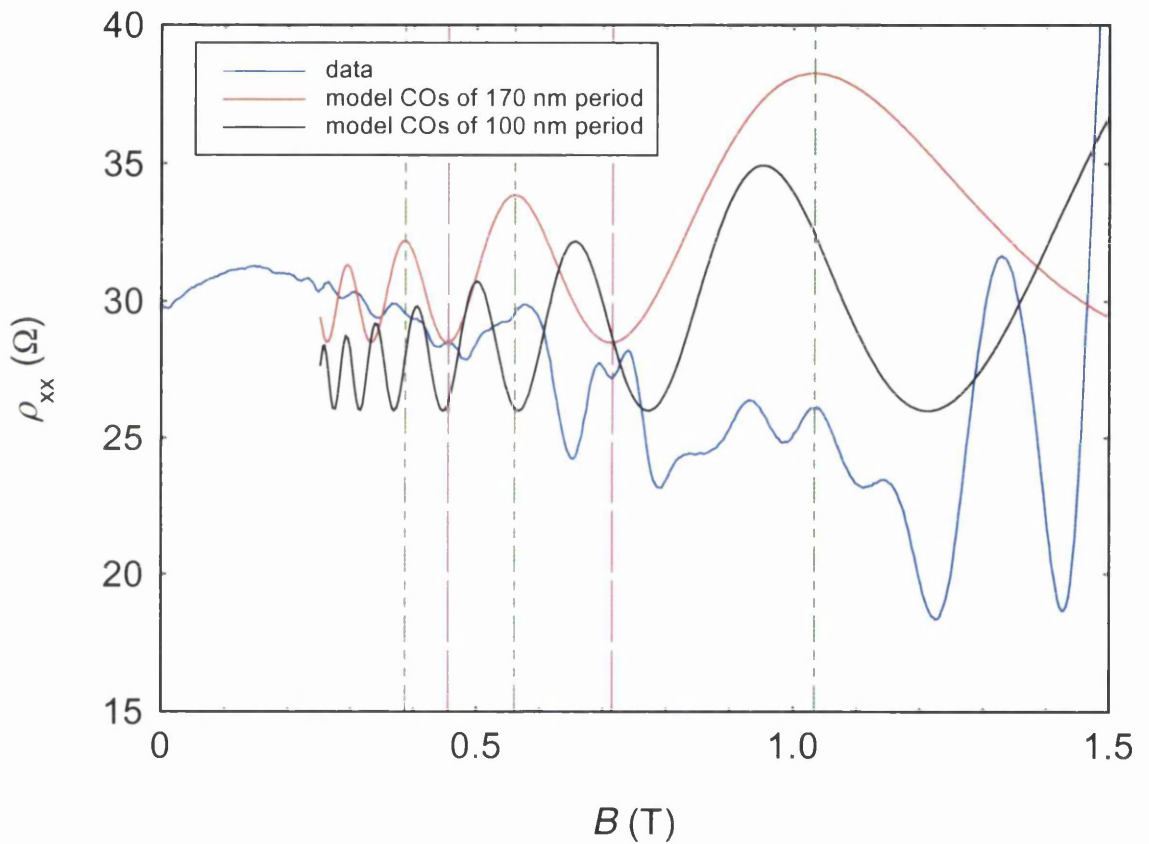
Figure 6.11
The data of Figure 4.27 are shown again classifying some of the COs into two sorts. The CO peaks in the data round the vertical dashed purple and green lines are at the minima and maxima respectively of the effective potential associated with 170 nm period indicated by the model COs of 170 nm period. The model COs have been calculated using 1D formulation [14].

As noted in section 4.2.2, the data contain oscillations (COs) that do not correspond to any certain period of the superlattice and seem unclassifiable. However, the ideas introduced in Chapter V and VI enable one to classify some of the oscillations as follows.

As discussed in section 4.2.1, the dominant Fourier component in the potential landscape in the superlattice in question corresponds to the longest period i.e. 170 nm. But the 170 nm period is across the Hall bar of Figure 6.11. Some of the maxima of the effective potential associated with the 170 nm period are seen at the magnetic fields indicated by the vertical dashed green lines in Figure 6.11. At these magnetic fields, guiding centre drifts along the Hall bar because it is the direction orthogonal to the direction of modulation of the dominant Fourier component [1]. As this drift has no component across the Hall bar, the CO peaks in the data for the magnetic fields at the green vertical dashed lines are expected to be suppressed completely. As can be seen in Figure 6.11, indeed these peaks are suppressed, although not entirely.

Some of the minima of the dominant Fourier component in the effective potential associated with 170 nm period are indicated by the purple dashed vertical lines in Figure 6.11. At these magnetic fields, the Fourier component of the 100 nm period although minimal is non-zero, as can be seen in Figure 6.11. As its direction of modulation is along the Hall bar, the guiding centre drifts across the Hall bar [1] producing the peaks in the data at the purple dashed vertical lines. Thus these peaks in the data could be explained using the concept of magnetic field dependent switching of guiding centre drift direction (from along the Hall bar to across the Hall bar) as envisaged by the guiding centre drift model [1]. It is important to note that these peaks are in anti-phase with the 170 nm period model COs shown in Figure 6.11 calculated using the 1D formulation [14].

Now let us return to the CO peaks at the green vertical dashed lines. As already noted, as expected from the guiding centre drift model [1], these are suppressed but not entirely. Unfortunately, these peaks are at the maxima of the dominant Fourier component of 170 nm period which is across the Hall bar. The period along the Hall bar is 100 nm instead. Hence these peaks cannot be attributed to the quantum mechanical effect as envisaged in the existing model [6]. The data appear to suggest that modulation across a Hall bar influences the transport along the Hall bar as well. No existing model on 2D LSSLs suggests this. So a fresh quantum mechanical analysis may be necessary to investigate the effect of a Fourier component for transport in the direction orthogonal to its direction of modulation. Such an analysis might have

implications for the magnetoresistances of symmetric and nearly symmetric 100 nm and 80 nm period superlattices discussed earlier in this chapter.

6.6 Concluding remarks

Admittedly, some of the reasoning put forward in the discussion of the data in this chapter is tentative and many arguments are subtle. Detailed reasoning and studies on the magnetoresistance characteristics of symmetric 2D LSSLs *by the existing models* reveal a fascinating interplay between semi-classical and quantum mechanical physics. Independent presence of both the semi-classical effect of pinned guiding centre trajectories in symmetric potential landscape [1] and the quantum mechanical effect of modulation of the density of states [6] is found to be necessary to account for the COs in the magnetoresistances in any detail. It is found that it is a question of dominance between semi-classical and quantum mechanical effects that determines whether an observation is to be accounted for by a semi-classical or a quantum mechanical model.

The magnetoresistances of symmetric, stressed, short period and high mobility 2D LSSLs showed characteristic amplitude modulations whenever one flux quantum passed through 1, 2, 3, ... unit cells of the lattice. Several possibilities were excluded to conclude that the phenomenon is related to flux quantization. The amplitude modulations have been discussed in terms of a theoretical formulation of Rotter et al. [10] and also as a possible manifestation of the Hofstadter butterfly [11, 12].

The studies of the data also enabled to conclude that *asymmetry* suppresses the COs that are not expected from semi-classical models. Quantum mechanical effects are suppressed if the potential landscape has *strong* asymmetry. This conforms with the conclusion reached in Chapter IV and Chapter V that transport in asymmetric 2D LSSLs is semi-classical in nature.

As has been the case, the model that can explain the COs of strongly asymmetric 2D LSSLs quite well fails to fully account for the COs when the potential landscape is symmetric or when the asymmetry is small, while the model that can account for the COs of symmetric 2D LSSLs fails in asymmetric case. Ideally one would therefore call for a fresh theoretical analysis for the resistivities of weakly modulated 2D LSSLs that can explain the COs of both asymmetric and symmetric 2D LSSLs. Also both theoretical and experimental efforts are required to clarify the conduction mechanism responsible for the amplitude modulation of COs involving flux quantization.

6.7 References of Chapter VI

[1] D. E. Grant, A. R. Long and J. H. Davies; Physical Review B **61** (2000) 13127

[2] Y. Paltiel, D. Mahalu, H. Shtrikman, G. Bunin and U. Meirav;
   Semiconductor Science and Technology **12** (1997) 987

[3] C. J. Emeleus, B. Milton, A. R. Long, J. H. Davies, D. E. Petticrew and M.C.
   Holland; Applied Physics Letters **73** (1998) 1412

[4] J. H. Davies, D. E. Petticrew and A. R. Long; Physical Review B **58** (1998) 10789

[5] E. Skuras, A. R. Long, I. A. Larkin, J. H. Davies and M. C. Holland;
   Applied Physics Letters **70** (1997) 871

[6] F. M. Peeters and P. Vasilopoulos; In the Proceedings of the 20th International
   Conference on the Physics of Semiconductors (ICPS-20), edited by E. M.
   Anastassakis and J. D. Joannopoulos, (World Scientific, Singapore, 1990); p.1589

[7] R. R. Gerhardts, D. Weiss and U. Wulf; Physical Review B **43** (1991) 5192

[8] R. R. Gerhardts; Physical Review B **45** (1992) 3449

[9] C. G. Smith, W. Chen, M. Pepper, H. Ahmed, D. Hasko, D. A. Ritchie, J. E. F.
   Frost and G. A. C. Jones;
   Journal of Vacuum Science and Technology B **10** (1992) 2904

[10] P. Rotter, M. Suhrke and U. Rössler; Physical Review B **54** (1996) 4452

[11] D. R. Hofstadter; Physical Review B **14** (1976) 2239

[12] D. Pfannkuche and R. R. Gerhardts; Physical Review B **46** (1992) 12606

[13] T. Schlösser, K. Ensslin, J. P. Kotthaus and M. Holland;
   Europhysics Letters **33** (1996) 683

[14] C. W. J. Beenakker; Physical Review Letters **62** (1989) 2020

Chapter VII: Summary of the results, conclusions and suggestion for future work

7.1 Summary of the results

In this thesis magnetoresistances of both stressed and unstressed asymmetric and symmetric weakly modulated 2D LSSLs have been studied and the data have been extensively analysed on the basis of the existing models with a view to clarifying theoretical understanding of the conduction process.

Devices were realised by shallow etching of patterns on the surface of Hall bars. Some of the Hall bars contained a strained layer close to the surface. After patterning the surface of the Hall bars containing the strained layer, not only the isotropic surface effect, but also anisotropic stress modulation was produced at the 2DEG. The combination of the two types of modulations gave rise to *asymmetric* potential landscapes even for etched patterns of square symmetry. Stressed superlattices containing rectangular patterns, which also gave rise to asymmetric potential landscape, were also studied. In stressed asymmetric 2D LSSLs, it was possible to change the relative dominance of Fourier components in the potential landscape by biasing a thick and continuous overlying gate. Asymmetric potential landscapes were also realised by etching patterns of rectangular symmetry on unstressed Hall bars.

Symmetric potential landscapes were also realised in two different ways. Firstly, an etched pattern of square symmetry without a gate, fabricated on unstressed Hall bars, provides a symmetric potential landscape. Secondly, the surface effect of gated stressed short period superlattices of square symmetry was eliminated by a large forward gate bias, leaving behind equal and opposite stress modulations along the cleavage directions. This also gave rise to a symmetric potential landscape. The results obtained from both asymmetric and symmetric 2D LSSLs are summarised below.

7.1.1 Results obtained from stressed devices containing square superlattices

The characteristics of the magnetoresistances observed for transport in stressed square superlattices containing *strong* asymmetry in the potential landscape are as follows. These were discussed in detail in Chapter IV.

- Transport along $[01\bar{1}]$ [on a (100) GaAs wafer] with 100 nm period along this direction showed pronounced COs of *only* 100 nm period, as large in amplitude as in the ρ_{xx} data of 1D LSSLs, for all gate biases. The minima of the COs observed

for all gate biases are found to agree well with the commensurability condition $2R_c = (k - \varphi)a$ with phase factor $\varphi = 1/4$ and $a = 100$ nm.

- Transport in the orthogonal direction, [011] with 100 nm period along this direction showed no COs for any gate bias.

- Transport along [010] and [001] with 100 nm period along these directions for appreciable forward gate bias (+0.3 V) showed weak COs of *only* $100/\sqrt{2}$ nm period, that of the diagonal Fourier components of 100 nm period square lattices. There is no presence of COs of the 100 nm period in the data. The magnetoresistance characteristics for transport in these two directions are almost identical. The minima of the COs agree quite well with the commensurability condition $2R_c = (k - \varphi)a$ with phase factor $\varphi = 1/4$ and $a = 100/\sqrt{2}$ nm.

- For less positive gate bias, transport along [010] and [001] with 100 nm period along these directions showed weak COs of both 100 nm and $100/\sqrt{2}$ nm periods interfering with each other. The magnetoresistance characteristics for these two directions are almost identical.

- PMR is found to be primarily associated with large asymmetry in the potential landscape and with the dominant axial Fourier component, when it is in the direction of transport.

As discussed in Chapter IV, the characteristics of the COs observed are defined by the asymmetry in the potential landscape. As also discussed in Chapter IV, these characteristics are in striking agreement with the new guiding centre drift model [1]. Only the dominant Fourier component in the potential landscape is found to give rise to COs, in striking agreement with the guiding centre drift model [1]. Different Fourier components are *not* found to contribute independently to the COs in contradiction with a previous semi-classical model [2] and an equivalent quantum mechanical formulation [3].

7.1.2 Results obtained from unstressed devices containing rectangular superlattice

The characteristics of the magnetoresistances observed for transport in unstressed rectangular superlattices of 170 nm by 100 nm periods with 170 nm period along the directions of transport are as follows. These were also discussed in detail in Chapter IV.

- Transport in both ungated and gated devices showed fairly large COs *only* of 170 nm period.

- The period of the COs observed is 170 nm irrespective of the crystallographic direction of transport as long as 170 nm period is along the direction of transport.

- The minima of all the COs observed irrespective of the crystallographic direction of transport agree with the commensurability condition $2R_c = (k - \varphi)a$ with phase factor $\varphi = 1/4$ and $a = 170$ nm.

- PMR is observed, associated as before with large asymmetry in the potential landscape.

As discussed in Chapter IV, the characteristics of the COs observed are defined by the asymmetry in the potential landscape. As also discussed in Chapter IV, these characteristics are in agreement with the guiding centre drift model [1]. Only the dominant Fourier component in the potential landscape is found to give rise to COs in agreement with the guiding centre drift model [1].

Data for transport along 100 nm period in similar superlattices show that the COs observed do *not* correspond to any certain period of the superlattice. This reveals that different Fourier components do *not* contribute independently to the COs in contradiction to a previous semi-classical model [2] and an equivalent quantum mechanical formulation [3].

7.1.3 Results obtained from stressed devices containing rectangular superlattices

The magnetoresistances observed for transport along the [010] and [001] directions in stressed rectangular superlattices of both 130 nm by 100 nm and 170 nm by 100 nm periods have been studied. These were discussed in detail in Chapter V. In 130 nm by 100 nm period 2D LSSLs, 130 nm period was aligned along [010] and 100 nm period along [001]. In 170 nm by 100 nm period 2D LSSLs, 170 nm period was aligned along [001] and 100 nm period along [010] and vice versa.

In the 130 nm by 100 nm period stressed superlattices, the following phenomena were observed.

- Magnetoresistances for transport along both [010] and [001] directions for large forward gate bias (+0.4 V) showed weak COs of *only* 79 nm period, that of the diagonal Fourier components of 130 nm by 100 nm period rectangular lattices. There is no sign of the axial Fourier components of 100 nm and 130 nm periods in the data. The minima of the COs agree with the commensurability condition $2R_c = (k - \varphi)a$ with phase factor $\varphi = 1/4$ and $a = 79$ nm.

- As the gate bias was appreciably reduced (to +0.1 V), transport along the longer 130 nm period showed COs of 130 nm period and that along the shorter 100 nm period showed no COs of 130 nm or 100 nm periods.

- Transport along the shorter period (100 nm) at +0.1 V gate bias picked up some CO peaks of 79 nm period, near the minima of the effective potential associated with the dominant axial Fourier component of 130 nm period.

- For intermediate gate biases, magnetoresistance features were observed which, as demonstrated in Chapter V, correspond to *magnetic field dependent switching* of CO period between 79 nm and 130 nm.

Transport in 170 nm by 100 nm period stressed superlattices revealed similar phenomena.

- Magnetoresistances for transport along both [010] and [001] directions, for large forward gate bias showed weak COs of *only* 86 nm period, that of the diagonal Fourier components of 170 nm by 100 nm period rectangular lattices. There is no sign of the axial Fourier components of 100 nm and 170 nm periods in the data. The minima of the COs agree with the commensurability condition $2R_c = (k - \varphi)a$ with phase factor $\varphi = 1/4$ and $a = 86$ nm.

- As the forward gate bias was appreciably reduced, transport along the longer 170 nm period showed COs of 170 nm period and that along the shorter 100 nm period showed no COs of 170 nm or 100 nm periods.

- Transport along the shorter period (100 nm) for less positive gate bias picked up some COs of 86 nm period, that are particularly large at the magnetic fields where there are minima of the dominant axial Fourier component of 170 nm period. The resulting COs are in anti-phase with conventional 170 nm period COs.

- For intermediate gate biases, magnetoresistance features were observed which, as demonstrated in Chapter V, correspond to *magnetic field dependent switching* of CO period between 170 nm and 86 nm.

As discussed in detail in Chapter V, these results provide a striking confirmation of *switching* of guiding centre drift direction in asymmetric 2D LSSLs, a phenomenon predicted by the guiding centre drift model [1]. *Switching* was observed by varying both gate bias and magnetic field. Change in gate bias changed the dominant Fourier component in the potential landscape, while change in magnetic field changed the dominant Fourier component in the magnetic field dependent effective potential. It is found that different Fourier components do *not* independently contribute to COs, in striking agreement with the guiding centre drift model [1] and in

contradiction with a previous semi-classical model [2] and an equivalent quantum mechanical calculation [3].

7.1.4 Results obtained from devices containing symmetric potential landscapes

The characteristics of the magnetoresistances observed for transport in unstressed and stressed square superlattices containing symmetric potential landscapes are as follows. These were discussed in detail in Chapter VI.

- Transport in ungated unstressed devices containing superlattices of square symmetry with 100 nm period along the directions of transport showed weak COs of 100 nm period. The weakness of the COs is in agreement with the expectations of the guiding centre drift model [1]. The minima of the COs are found to agree with the commensurability condition $2R_c = (k - \varphi)a$ with phase factor $\varphi = 1/4$ and $a = 100$ nm. As expected, the characteristics of the COs observed are independent of crystallographic direction of transport.

- Transport along [011] and [01$\bar{1}$] in stressed devices of square symmetry and 80 nm period, with 80 nm period along the directions of transport, for large forward gate biases showed quite *large* COs of 80 nm period. Moreover, the COs for transport in these two orthogonal directions are almost identical. That the COs are large *and* similar in the two orthogonal directions are as expected from a quantum mechanical calculation [3]. The CO minima are found to agree with the commensurability condition $2R_c = (k - \varphi)a$ with phase factor $\varphi = 1/4$ and $a = 80$ nm. COs observed are in general suppressed in amplitude, but there are characteristic amplitude modulations whenever the number of flux quantum per unit cell is 1, 1/2, 1/3, ...

- The amplitude modulation was also observed at the expected magnetic fields for transport in 100 nm period stressed square superlattices for large forward gate bias, but only clearly at 30 mK.

- When the potential landscape is neither strongly asymmetric nor perfectly symmetric, then magnetoresistance data suggest that the quantum mechanical effects observed in the symmetric potential landscapes persist to some extent.

As discussed in Chapter VI, an interplay between semi-classical dynamical effect of closed guiding centre trajectories that suppresses COs in symmetric potential landscape [1] and quantum mechanical effect of modulation of density of states [3] that gives rise to COs as large as in the ρ_{xx} data of 1D LSSLs is found to be necessary to account for the COs in the data. The amplitude modulation has been shown to be related to flux quantization.

7.2 Conclusions

Detailed studies of the magnetoresistance data obtained from weakly modulated asymmetric and symmetric 2D LSSLs based on the *existing models* lead to the following conclusions.

- In 2D LSSLs of *strongly* broken symmetry, the characteristics of the COs are determined by the asymmetry of the potential landscape.

- Transport in 2D LSSLs of *strongly* broken symmetry is explained well by the guiding centre drift model of D. E. Grant, A. R. Long and J. H. Davies [1].

- In 2D LSSLs of *strongly* broken symmetry, different Fourier components do *not* independently contribute to COs, in striking agreement with the guiding centre drift model of D. E. Grant, A. R. Long and J. H. Davies [1]. A previous semi-classical model [2] and an equivalent quantum mechanical calculation [3] are both unable to account for this conclusion.

- In 2D LSSLs of *strongly* broken symmetry, a change of dominant Fourier component changes the guiding centre drift direction which changes the period of the COs in the magnetoresistances, in complete accord with the guiding centre drift model of D. E. Grant, A. R. Long and J. H. Davies [1]. A previous semi-classical model [2] and an equivalent quantum mechanical calculation [3] both are unable to account for the observations in question.

- An interplay between the semi-classical dynamical effect of closed guiding centre trajectories that suppresses COs in symmetric potential landscape [1] and quantum mechanical effect of modulation of density of states [3] that gives rise to COs as large in amplitude as in the ρ_{xx} data of 1D LSSLs is found to be necessary to account for the COs of symmetric 2D LSSLs in any detail.

- Asymmetry suppresses quantum mechanical effects in asymmetric 2D LSSLs.

- Semi-classical and quantum mechanical effects prevail independently. It is a matter of dominance of one that determines whether a phenomenon is semi-classical or quantum mechanical.

- The magnetoresistances of symmetric, stressed, short period and high mobility 2D LSSLs are dominated by quantum mechanical effects. That COs observed for transport in two orthogonal directions in symmetric 2D LSSLs are large *and* similar confirm the validity of the quantum mechanical calculation of F. M. Peeters and P. Vasilopoulos [3] in the case of symmetric 2D LSSLs.

- The magnetoresistances of symmetric, stressed, short period and high mobility 2D LSSLs show a quantum mechanical phenomenon — characteristic amplitude modulations involving inverse flux quantum periodicity.

- As an experimental systematic, PMR is primarily associated with large asymmetry in the potential landscape and with the dominant axial Fourier component when it is in the direction of transport.

7.3 Suggestion for future work

Following is a list of suggestions for further work on weakly modulated 2D LSSLs.

- According to the simulations [1], every significant Fourier component in 2D LSSLs contribute to PMR. But as an experimental systematic, PMR is primarily associated with large asymmetry in the potential landscape and dominant axial Fourier component when it is in the direction of transport. Isotropic scattering is used in the simulations [1], whereas it is well known that in high mobility 2DEG at semiconductor interfaces the basic scattering mechanism is due to long range Coulomb interactions due to impurities, which lead predominantly to small angle scattering of electrons [4]. In reality scattering is anisotropic [4]. Thus a realistic working model for PMR in 2D LSSLs needs to be developed giving due importance to anisotropic scattering.

- Magnetoresistances of unstressed symmetric 2D LSSLs of 100 nm period have been studied in this project. With larger period, e.g. 300 nm, one can introduce larger modulation at the 2DEG. This may allow one to ascertain if the quantum mechanical effect [3] observed in 80 nm period stressed devices of square superlattices at forward gate bias discussed in Chapter VI is due to any larger modulation only or due to a combination of short period and larger modulation. This experiment will suffer complication from difference in mobility. The etching process will reduce the mobility and unlike in short period stressed devices, application of a forward gate bias in unstressed devices will reduce the modulation, which is undesirable in this context. The inverse flux quantum periodicity is not expected to be clearly seen for these larger periods, because the number of COs will be smaller and consequently there will not be much room for the amplitude modulations to show up at the expected magnetic field values.

- An attempt could be made to realise shorter period, e.g. 60 nm period, stressed 2D LSSLs of square symmetry to look for amplitude modulation of COs in the

magnetoresistances at forward gate bias. Of course the stress modulation in shorter period lattices is expected to be weaker and one may need to use a thicker strained layer, e.g. 10 nm thick InGaAs instead of 6 nm used in this project. One may also need to use (111) GaAs wafer in which the stress modulation is nearly isotropic [5]. Hence the surface effect and stress modulation will reinforce in all directions and stronger modulation will be realised without having to apply forward gate bias to achieve symmetry in the potential landscape as in the case of square superlattices on (100) GaAs wafer.

- As has been the case, the theoretical framework that explains the data of asymmetric 2D LSSLs fails to fully account for the data of symmetric 2D LSSLs and vice-versa. Hence efforts are necessary to achieve a theoretical formulation that can fully explain the data of both asymmetric and symmetric 2D LSSLs. Theoretical efforts are also necessary to clarify the conduction mechanism responsible for the observed amplitude modulation of COs involving flux quantization.

- One can also vary the parameters and realise asymmetric 2D LSSLs of other periods and geometries. For example, one can realise a lattice of diamond pattern, i.e. diagonals of a square lattice aligned along and across the length of Hall bars. One can also realise rectangular lattices of other periods.

- One may experimentally investigate the properties of (111) GaAs surface.

7.4 References of Chapter VII

[1] D. E. Grant, A. R. Long and J. H. Davies; Physical Review B **61** (2000) 13127

[2] R. R. Gerhardts; Physical Review B **45** (1992) 3449

[3] F. M. Peeters and P. Vasilopoulos; In the Proceedings of the 20th International Conference on the Physics of Semiconductors (ICPS-20), edited by E. M. Anastassakis and J. D. Joannopoulos, (World Scientific, Singapore, 1990); p.1589

[4] A. Manolescu, R. R. Gerhardts, M. Suhrke and U. Rössler; Physical Review B **63** (2001) 115322

[5] J. H. Davies, D. E. Petticrew and A. R. Long; Physical Review B **58** (1998) 10789

Appendix I

The Maple worksheets used to produce the resistivity traces in section 2.3.1 are presented in the following five sections.

AI.1 Maple worksheet used to calculate the resistivities of 1D LSSLs

```
> e:=1.6e-19:
> m:=0.067*9.1e-31:
> hbar:=evalf(6.626e-34/(2*Pi)):
> omegac:=e*B/m:
> n2D:=4e15:
> mu:=50:
> R:=evalf(hbar*sqrt(2*Pi*n2D)/(m*omegac)):
> tau:=mu*m/e:
> a:=100e-9:
> Vx:=1/1000*1.6e-19:
> Vy:=0:
> Vd1:=0:
> Vd2:=0:
>
deltasigmaxx:=evalf((tau*e^2/(Pi*m*(hbar*omegac)^2))*0.5*(2*Pi/a)^2*(Vy^2*(Bess
elJ(0,2*Pi*R/a))^2+Vd1^2*(BesselJ(0,2*Pi*sqrt(2)*R/a))^2+Vd2^2*(BesselJ(0,2*Pi*s
qrt(2)*R/a))^2)):
>
deltasigmayy:=evalf((tau*e^2/(Pi*m*(hbar*omegac)^2))*0.5*(2*Pi/a)^2*(Vx^2*(Bess
elJ(0,2*Pi*R/a))^2+Vd1^2*(BesselJ(0,2*Pi*sqrt(2)*R/a))^2+Vd2^2*(BesselJ(0,2*Pi*s
qrt(2)*R/a))^2)):
> deltasigmaxy:=evalf((-tau*e^2/(Pi*m*(hbar*omegac)^2))*0.5*(2*Pi/a)^2*(Vd1^2-
Vd2^2)*(BesselJ(0,2*Pi*sqrt(2)*R/a))^2):
> deltasigmayx:=-deltasigmaxy:
> sigma0:=n2D*e^2*tau/m:
> sigmaxx:=sigma0/(1+omegac^2*tau^2)+deltasigmaxx:
> sigmayy:=sigma0/(1+omegac^2*tau^2)+deltasigmayy:
> sigmaxy:=-sigma0*omegac*tau/(1+omegac^2*tau^2)+deltasigmaxy:
> sigmayx:=sigma0*omegac*tau/(1+omegac^2*tau^2)+deltasigmayx:
> rhoxx:=sigmayy/(sigmaxx*sigmayy-sigmaxy*sigmayx):
> rhoyy:=sigmaxx/(sigmaxx*sigmayy-sigmaxy*sigmayx):
>
plot([rhoxx,rhoyy],B=0.2..1,colour=[red,blue],font=[TIMES,ROMAN,15],axes=BOXE
D,view=[0.2..1,0..450],ytickmarks=10);
```

AI.2 Maple worksheet used to calculate the resistivities of symmetric 2D LSSLs: *coskx+cosky*

```
> e:=1.6e-19:
> m:=0.067*9.1e-31:
> hbar:=evalf(6.626e-34/(2*Pi)):
> omegac:=e*B/m:
> n2D:=4e15:
> mu:=50:
> R:=evalf(hbar*sqrt(2*Pi*n2D)/(m*omegac)):
> tau:=mu*m/e:
> a:=100e-9:
> Vx:=1/1000*1.6e-19:
> Vy:=1/1000*1.6e-19:
> Vd1:=0:
> Vd2:=0:
>
deltasigmaxx:=evalf((tau*e^2/(Pi*m*(hbar*omegac)^2))*0.5*(2*Pi/a)^2*(Vy^2*(Bess
elJ(0,2*Pi*R/a))^2+Vd1^2*(BesselJ(0,2*Pi*sqrt(2)*R/a))^2+Vd2^2*(BesselJ(0,2*Pi*s
qrt(2)*R/a))^2)):
>
deltasigmayy:=evalf((tau*e^2/(Pi*m*(hbar*omegac)^2))*0.5*(2*Pi/a)^2*(Vx^2*(Bess
elJ(0,2*Pi*R/a))^2+Vd1^2*(BesselJ(0,2*Pi*sqrt(2)*R/a))^2+Vd2^2*(BesselJ(0,2*Pi*s
qrt(2)*R/a))^2)):
> deltasigmaxy:=evalf((-tau*e^2/(Pi*m*(hbar*omegac)^2))*0.5*(2*Pi/a)^2*(Vd1^2-
Vd2^2)*(BesselJ(0,2*Pi*sqrt(2)*R/a))^2):
> deltasigmayx:=-deltasigmaxy:
> sigma0:=n2D*e^2*tau/m:
> sigmaxx:=sigma0/(1+omegac^2*tau^2)+deltasigmaxx:
> sigmayy:=sigma0/(1+omegac^2*tau^2)+deltasigmayy:
> sigmaxy:=-sigma0*omegac*tau/(1+omegac^2*tau^2)+deltasigmaxy:
> sigmayx:=sigma0*omegac*tau/(1+omegac^2*tau^2)+deltasigmayx:
> rhoxx:=50+sigmayy/(sigmaxx*sigmayy-sigmaxy*sigmayx):
> rhoyy:=sigmaxx/(sigmaxx*sigmayy-sigmaxy*sigmayx):
>
plot([rhoxx,rhoyy],B=0.2..1,colour=[red,blue],font=[TIMES,ROMAN,15],axes=BOXE
D,view=[0.2..1,0..450],ytickmarks=10);
```

AI.3 Maple worksheet used to calculate the resistivities of asymmetric 2D LSSLs: *coskx+0.5 cosky*

```
> e:=1.6e-19:
> m:=0.067*9.1e-31:
> hbar:=evalf(6.626e-34/(2*Pi)):
> omegac:=e*B/m:
> n2D:=4e15:
> mu:=50:
> R:=evalf(hbar*sqrt(2*Pi*n2D)/(m*omegac)):
> tau:=mu*m/e:
> a:=100e-9:
> Vx:=1/1000*1.6e-19:
> Vy:=0.5/1000*1.6e-19:
> Vd1:=0:
> Vd2:=0:
>
deltasigmaxx:=evalf((tau*e^2/(Pi*m*(hbar*omegac)^2))*0.5*(2*Pi/a)^2*(Vy^2*(Bess
elJ(0,2*Pi*R/a))^2+Vd1^2*(BesselJ(0,2*Pi*sqrt(2)*R/a))^2+Vd2^2*(BesselJ(0,2*Pi*s
qrt(2)*R/a))^2)):
>
deltasigmayy:=evalf((tau*e^2/(Pi*m*(hbar*omegac)^2))*0.5*(2*Pi/a)^2*(Vx^2*(Bess
elJ(0,2*Pi*R/a))^2+Vd1^2*(BesselJ(0,2*Pi*sqrt(2)*R/a))^2+Vd2^2*(BesselJ(0,2*Pi*s
qrt(2)*R/a))^2)):
>     deltasigmaxy:=evalf((-tau*e^2/(Pi*m*(hbar*omegac)^2))*0.5*(2*Pi/a)^2*(Vd1^2-
Vd2^2)*(BesselJ(0,2*Pi*sqrt(2)*R/a))^2):
> deltasigmayx:=-deltasigmaxy:
> sigma0:=n2D*e^2*tau/m:
> sigmaxx:=sigma0/(1+omegac^2*tau^2)+deltasigmaxx:
> sigmayy:=sigma0/(1+omegac^2*tau^2)+deltasigmayy:
> sigmaxy:=-sigma0*omegac*tau/(1+omegac^2*tau^2)+deltasigmaxy:
> sigmayx:=sigma0*omegac*tau/(1+omegac^2*tau^2)+deltasigmayx:
> rhoxx:=sigmayy/(sigmaxx*sigmayy-sigmaxy*sigmayx):
> rhoyy:=sigmaxx/(sigmaxx*sigmayy-sigmaxy*sigmayx):
>
plot([rhoxx,rhoyy],B=0.2..1,colour=[red,blue],font=[TIMES,ROMAN,15],axes=BOXE
D,view=[0.2..1,0..450],ytickmarks=10);
```

AI.4 Maple worksheet used to calculate the resistivities for a periodic potential of the form *0.25 cosk(x+y)*

```
> e:=1.6e-19:
> m:=0.067*9.1e-31:
> hbar:=evalf(6.626e-34/(2*Pi)):
> omegac:=e*B/m:
> n2D:=4e15:
> mu:=50:
> R:=evalf(hbar*sqrt(2*Pi*n2D)/(m*omegac)):
> tau:=mu*m/e:
> a:=100e-9:
> Vx:=0:
> Vy:=0:
> Vd1:=0.25/1000*1.6e-19:
> Vd2:=0:
>
deltasigmaxx:=evalf((tau*e^2/(Pi*m*(hbar*omegac)^2))*0.5*(2*Pi/a)^2*(Vy^2*(Bess
elJ(0,2*Pi*R/a))^2+Vd1^2*(BesselJ(0,2*Pi*sqrt(2)*R/a))^2+Vd2^2*(BesselJ(0,2*Pi*s
qrt(2)*R/a))^2)):
>
deltasigmayy:=evalf((tau*e^2/(Pi*m*(hbar*omegac)^2))*0.5*(2*Pi/a)^2*(Vx^2*(Bess
elJ(0,2*Pi*R/a))^2+Vd1^2*(BesselJ(0,2*Pi*sqrt(2)*R/a))^2+Vd2^2*(BesselJ(0,2*Pi*s
qrt(2)*R/a))^2)):
> deltasigmaxy:=evalf((-tau*e^2/(Pi*m*(hbar*omegac)^2))*0.5*(2*Pi/a)^2*(Vd1^2-
Vd2^2)*(BesselJ(0,2*Pi*sqrt(2)*R/a))^2):
> deltasigmayx:=-deltasigmaxy:
> sigma0:=n2D*e^2*tau/m:
> sigmaxx:=sigma0/(1+omegac^2*tau^2)+deltasigmaxx:
> sigmayy:=sigma0/(1+omegac^2*tau^2)+deltasigmayy:
> sigmaxy:=-sigma0*omegac*tau/(1+omegac^2*tau^2)+deltasigmaxy:
> sigmayx:=sigma0*omegac*tau/(1+omegac^2*tau^2)+deltasigmayx:
> rhoxx:=5+sigmayy/(sigmaxx*sigmayy-sigmaxy*sigmayx):
> rhoyy:=sigmaxx/(sigmaxx*sigmayy-sigmaxy*sigmayx):
>
plot([rhoxx,rhoyy],B=0.2..1,colour=[red,blue],font=[TIMES,ROMAN,15],axes=BOXE
D,view=[0.2..1,30..55],ytickmarks=5);
```

AI.5 Maple worksheet used to calculate the resistivities of asymmetric 2D LSSLs: *0.3 coskx+0.3 cosky+0.8 cosk(x+y)+0.4 cosk(x-y)*

```
> e:=1.6e-19:
> m:=0.067*9.1e-31:
> hbar:=evalf(6.626e-34/(2*Pi)):
> omegac:=e*B/m:
> n2D:=4e15:
> mu:=50:
> R:=evalf(hbar*sqrt(2*Pi*n2D)/(m*omegac)):
> tau:=mu*m/e:
> a:=100e-9:
> Vx:=0.3/1000*1.6e-19:
> Vy:=0.3/1000*1.6e-19:
> Vd1:=0.8/1000*1.6e-19:
> Vd2:=0.4/1000*1.6e-19:
>
deltasigmaxx:=evalf((tau*e^2/(Pi*m*(hbar*omegac)^2))*0.5*(2*Pi/a)^2*(Vy^2*(Bess
elJ(0,2*Pi*R/a))^2+Vd1^2*(BesselJ(0,2*Pi*sqrt(2)*R/a))^2+Vd2^2*(BesselJ(0,2*Pi*s
qrt(2)*R/a))^2)):
>
deltasigmayy:=evalf((tau*e^2/(Pi*m*(hbar*omegac)^2))*0.5*(2*Pi/a)^2*(Vx^2*(Bess
elJ(0,2*Pi*R/a))^2+Vd1^2*(BesselJ(0,2*Pi*sqrt(2)*R/a))^2+Vd2^2*(BesselJ(0,2*Pi*s
qrt(2)*R/a))^2)):
> deltasigmaxy:=evalf((-tau*e^2/(Pi*m*(hbar*omegac)^2))*0.5*(2*Pi/a)^2*(Vd1^2-
Vd2^2)*(BesselJ(0,2*Pi*sqrt(2)*R/a))^2):
> deltasigmayx:=-deltasigmaxy:
> sigma0:=n2D*e^2*tau/m:
> sigmaxx:=sigma0/(1+omegac^2*tau^2)+deltasigmaxx:
> sigmayy:=sigma0/(1+omegac^2*tau^2)+deltasigmayy:
> sigmaxy:=-sigma0*omegac*tau/(1+omegac^2*tau^2)+deltasigmaxy:
> sigmayx:=sigma0*omegac*tau/(1+omegac^2*tau^2)+deltasigmayx:
> rhoxx:=50+sigmayy/(sigmaxx*sigmayy-sigmaxy*sigmayx):
> rhoyy:=sigmaxx/(sigmaxx*sigmayy-sigmaxy*sigmayx):
>
plot([rhoxx,rhoyy],B=0.2..1,colour=[red,blue],font=[TIMES,ROMAN,15],axes=BOXE
D,view=[0.2..1,0..300],ytickmarks=6);
```

Appendix II

Following is the list of contributions made during the project. Copies of some of the papers follow the list.

(1) A paper has been **published** in **Physical Review B** as **rapid communication**

Physical Review B **62** (2000) R4821

"Importance of symmetry breaking in two-dimensional lateral-surface superlattices"

S. Chowdhury, C. J. Emeleus, B. Milton, E. Skuras, A. R. Long

Department of Physics and Astronomy, Glasgow University, Glasgow G12 8QQ, U.K.

J. H. Davies, G. Pennelli and C. R. Stanley

Department of Electronics and Electrical Engineering, Glasgow University, Glasgow G12 8QQ, U.K.

(2) A paper has been **published** in **Physical Review B**

Physical Review B **63** (2001) 153306

"Switching of guiding center-drift direction in asymmetric two-dimensional lateral surface superlattices"

S. Chowdhury, E. Skuras, C. J. Emeleus, A. R. Long

Department of Physics and Astronomy, Glasgow University, Glasgow G12 8QQ, U.K.

J. H. Davies, G. Pennelli and C. R. Stanley

Department of Electronics and Electrical Engineering, Glasgow University, Glasgow G12 8QQ, U. K.

(3) A paper has been **published** in the *Proceedings of the 25th International Conference on the Physics of Semiconductors 2000* (ICPS25), Osaka, Japan, edited by Noboru Miura and Tsuneya Ando, (Springer-Verlag Berlin Heidelberg, 2001); Part I, p.757.

"Transport in asymmetric two-dimensional lateral surface superlattices"

S. Chowdhury, A. R. Long, J. H. Davies[+], D. E. Grant, E. Skuras and C. J. Emeleus

Department of Physics and Astronomy, Glasgow University, Glasgow G12 8QQ, U.K.

[+]*Department of Electronics and Electrical Engineering, Glasgow University, Glasgow G12 8QQ, U.K.*

(4) A paper has been **accepted** for publication in the "Journal of the Korean Physical Society".

"Transport of Electrons in two-dimensional Square and Rectangular Lateral Surface Superlattices"

S. Chowdhury, A. R. Long, E. Skuras, C. J. Emeleus

Department of Physics and Astronomy, Glasgow University, Glasgow G12 8QQ, U.K.

J. H. Davies

Department of Electronics and Electrical Engineering, Glasgow University, Glasgow G12 8QQ, U.K.

(5) An abstract has been **accepted** for **ORAL** presentation in the *International Conference on Superlattices, Microstructures and Microdevices* **(ICSMM-2000)**, 25-27 September 2000, Kyongju, Korea.

"Transport of electrons in two-dimensional square and rectangular lateral surface superlattices"

S. Chowdhury, A. R. Long, J. H. Davies, E. Skuras, C. J. Emeleus

Nanoelectronics Research Centre, University of Glasgow, Glasgow G12 8QQ, U. K.

(6) An abstract has been **accepted** for POSTER presentation in the *25th International Conference on the Physics of Semiconductor* **(ICPS25)**, 17-22 September 2000, Osaka, Japan.

M119 "Transport in asymmetric two-dimensional lateral surface superlattices"

S. Chowdhury, A. R. Long, J. H. Davies, D. E. Grant, E. Skuras and C. J. Emeleus--

Nanoelectronics Research Center, University of Glasgow, Glasgow G12 8QQ, U. K.

(da781TK1, D064)

(7) An abstract has been **accepted** for POSTER presentation in the *14th International Conference on the Electronic Properties of Two-Dimensional Systems* **(EP2DS-14)**, 30 July-03 August 2001, Prague, Czech Republic.

"Inverse flux quantum periodicity in the amplitudes of Weiss oscillations in two-dimensional lateral surface superlattices"

S. Chowdhury, A. R. Long, J. H. Davies, K. Lister, E. Skuras and C. J. Emeleus

Nanoelectronics Research Centre, University of Glasgow, Glasgow G12 8QQ, U. K.

(8) A POSTER in *Condensed Matter and Materials Physics Conference 1999* (CMMP99), 19-22 December 1999, Leicester, England. Abstract number SEMa.P1.10.

"The importance of broken symmetry in explaining the magnetotransport in 2-dimensional lateral surface superlattices"

S. Chowdhury, C. J. Emeleus, B. Milton, J. H. Davies and A. R. Long

Nanoelectronics Research Centre, University of Glasgow, Glasgow G12 8QQ, U.K.

(9) A POSTER in *Condensed Matter and Materials Physics Conference 2000* (CMMP-2000), 19-21 December 2000, Bristol, England. Abstract number SMp.P2.28

"Switching of the direction of guiding centre drift in asymmetric two-dimensional lateral surface superlattices"

S. Chowdhury, A. R. Long, J. H. Davies, E. Skuras, C. J. Emeleus

Nanoelectronics Research Centre, University of Glasgow, Glasgow G12 8QQ, U. K.

(10) A POSTER in *Condensed Matter and Materials Physics Conference 2000* (CMMP-2000), 19-21 December 2000, Bristol, England. Abstract number SMp.P2.29

"Enhanced magnetoresistance oscillations in two-dimensional lateral surface superlattices - evidence for inverse flux quantum periodicity"

S. Chowdhury, A. R. Long, J. H. Davies, K. Lister, E. Skuras, C. J. Emeleus

Nanoelectronics Research Centre, University of Glasgow, Glasgow G12 8QQ, U. K.

Appendix III

The following two prizes were received in recognition of the contribution made by the project.

1. Thomson experimental prize (2000)

Awarded by the University of Glasgow. Details are in the enclosed award letter.

2. A prize for the best poster presentation in the Condensed Matter and Materials Physics Conference 2000 (CMMP-2000).

Awarded by the Institute of Physics (IOP).

The abstract number in question is SMp.P2.29.

The title was "Enhanced magnetoresistance oscillations in two-dimensional lateral surface superlattices — evidence for inverse flux quantum periodicity"

Further details are in the accompanying certificate.